



# LUND UNIVERSITY

## Microfluidic Cell and Particle Sorting using Deterministic Lateral Displacement

Holm, Stefan

2018

*Document Version:*

Publisher's PDF, also known as Version of record

[Link to publication](#)

*Citation for published version (APA):*

Holm, S. (2018). *Microfluidic Cell and Particle Sorting using Deterministic Lateral Displacement*. [Doctoral Thesis (compilation), Solid State Physics]. Department of Physics, Lund University.

*Total number of authors:*

1

*Creative Commons License:*

CC BY-NC

**General rights**

Unless other specific re-use rights are stated the following general rights apply:

Copyright and moral rights for the publications made accessible in the public portal are retained by the authors and/or other copyright owners and it is a condition of accessing publications that users recognise and abide by the legal requirements associated with these rights.

- Users may download and print one copy of any publication from the public portal for the purpose of private study or research.
- You may not further distribute the material or use it for any profit-making activity or commercial gain
- You may freely distribute the URL identifying the publication in the public portal

Read more about Creative commons licenses: <https://creativecommons.org/licenses/>

**Take down policy**

If you believe that this document breaches copyright please contact us providing details, and we will remove access to the work immediately and investigate your claim.

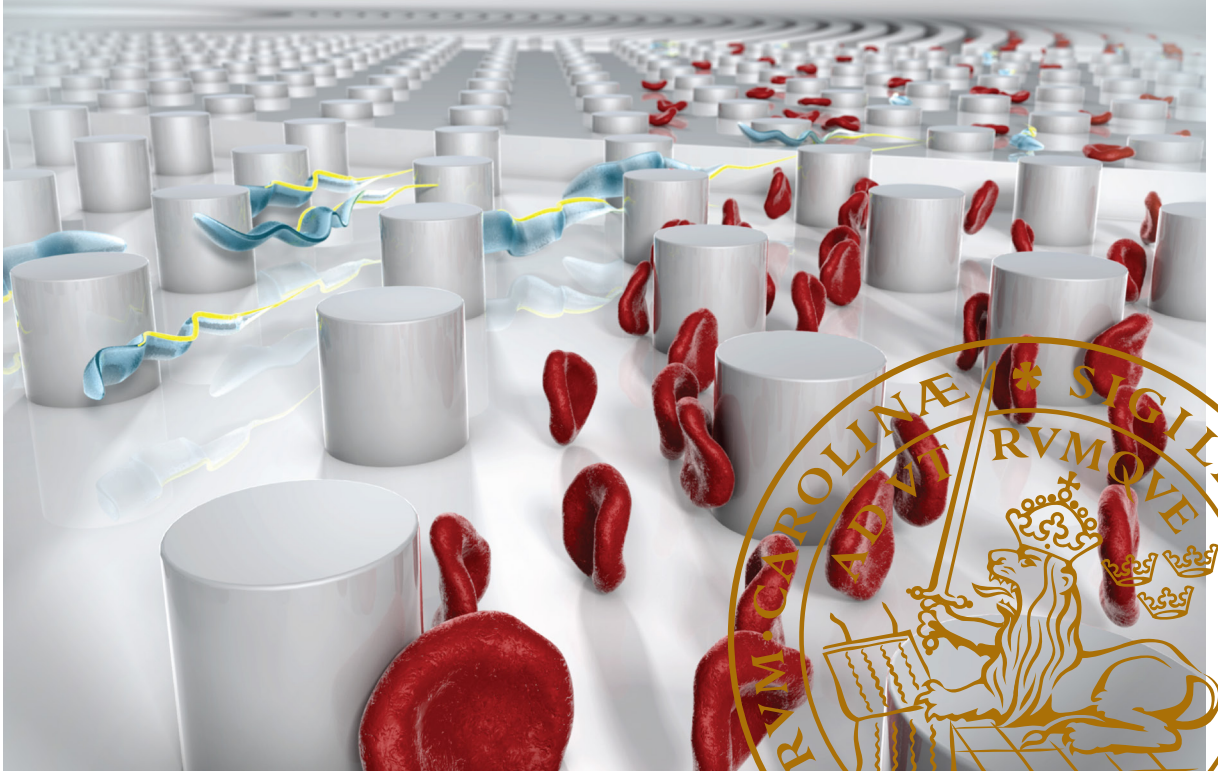
LUND UNIVERSITY

PO Box 117  
221 00 Lund  
+46 46-222 00 00

# Microfluidic Cell and Particle Sorting using Deterministic Lateral Displacement

STEFAN HOLM

DEPARTMENT OF PHYSICS | LUND UNIVERSITY



# Microfluidic Cell and Particle Sorting using Deterministic Lateral Displacement

Stefan Holm



**LUND**  
UNIVERSITY

DOCTORAL DISSERTATION

by due permission of the Faculty of Engineering, Lund University, Sweden.

To be defended at Rydbergssalen, Sölvegatan 14.

Friday 16<sup>th</sup> of March 2018 at 14.15.

*Faculty opponent*

Brian Kirby, Cornell University, New York, USA

Organization LUND UNIVERSITY	Document name	
	Date of issue	
Author(s)	Sponsoring organization	
Title and subtitle Microfluidic Cell and Particle Sorting using Deterministic Lateral Displacement		
<p>Microfluidics is a field which has the potential to revolutionize medical diagnostics. The ability to sort and analyse cells by the use of portable handheld devices has the potential to enable sensitive devices for point-of-care diagnostics. This could play a major role in diagnosis of a wide range of diseases which are prevalent in remote areas in developing countries where a majority of the people live without access to modern health care.</p> <p>One focus of this thesis is the development of such a tool for diagnosis of human African trypanosomiasis, a deadly disease which requires accurate and rapid diagnosis in order to start treatment at an early stage for better chances of survival. The way the disease is normally diagnosed is by microscopic examination of blood smears in order to see if the blood parasite which causes HAT is present in the patient or not. This is a tremendously difficult task as in a single drop of blood there can be 500 million red blood cells (RBC) while at the same time the number of parasites can be less than 10. The vast majority of background cells makes finding the parasite as difficult as finding a needle in a haystack. To help in diagnosis we present a way by which we separate out the blood parasites, if present, from the blood so they can be easily detected.</p> <p>The method which we use to achieve sorting is called deterministic lateral displacement (DLD), a continuous and passive particle sorting technique which relies on flowing the sample through an array of obstacles. The separation of particles relies on the positioning of these obstacles such that small particles are not affected by the obstacle array while large particles are, and travel at a different angle. The cut-off size between small and large particles is known as the critical diameter and is relatively well characterized for spherical particles. However, the sorting of irregular shaped particles such as RBCs and the long slender parasites has been proven difficult in DLD device. In order to achieve sorting we present a method by which we can control the orientation of particles in order to accentuate their morphological differences. Using this method we present a tool with which we, with high accuracy are able to achieve sorting between these otherwise indistinguishable particles; a tool which could find use in the field-diagnosis of HAT (Paper I and II).</p> <p>We build on the finding of how non-spherical particles, RBCs, behave in DLD devices and combine that with an investigation of how forces exerted on deformable particle act to deform them. This results in the ability to sort based on the size, shape and deformability of a particle, and the successful sorting of normal RBCs and chemically induced, pathologically relevant, forms of RBCs (Paper III). Further on, RBCs are known to undergo cyclic dynamic events such as tumbling and tank-treading. We address this and show that the sorting in DLD is highly dependent on the dynamic behaviour of RBCs which opens up for new sorting schemes based on for example the internal viscosity of RBCs, a factor which is known to influence the choice of dynamic mode (Paper IV). Microfluidic particle sorting has, due to small length scales, often low throughput. This is addressed by investigating the effects of sample concentration on sorting efficiency (Paper V). By changing the sorting behaviour of particles depending on their vertical position in the device, we implement density-based sorting in DLD (Paper VI).</p> <p>DLD can be used to separate any particle mixtures, not only naturally occurring biological particle systems. In Paper VII, we expand the scope to also include thermoresponsive microgel clusters generated by droplet microfluidics which allows for the encapsulation at ~10 kHz frequencies. By allowing the aqueous content of the droplet to evaporate we force the microgels into close contact and can subsequently crosslink them. With the microgel particles which makes up these clusters having temperature dependent interactions we have a way to selectively tune the interaction sites on the clusters. In combination with DLD we can sort out clusters of interest consisting of a specific number of microgel particles which opens up for new types of particles with interesting properties which is highly suitable for interaction studies and the development of novel materials.</p> <p>Microfluidics draws benefit from differences in scaling between variables when length scales decreases from macroscale to microscale, such as the increased surface area-to-volume ratio. This acts to introduce new phenomena which can be exploited as in the examples above. Additional benefits to microfluidics include the ability to handle smaller volumes, faster energy dissipation, precise spatial and temporal control and the ability to integrate multiple preparative and analytical functionalities on a single chip, a so-called lab-on-a-chip, which is a major driving force for the microfluidic field and definitely the direction that I have endeavoured to push the projects within this thesis. For example, the continued development of the parasite sorting device has the potential to not only separate RBCs and parasites but also detect the result, and consequently enable a complete handheld sample-to-answer device dedicated for field-use.</p>		
Key words Separation science, Deterministic Lateral Displacement, Microfluidics, Lab-on-a-chip, Point-of-Care, concentration, morphology, deformability, cell dynamics, droplet microfluidics		
Classification system and/or index terms (if any)		
Supplementary bibliographical information		Language
ISSN and key title		ISBN
Recipient's notes	Number of pages 282	Price
	Security classification	

I, the undersigned, being the copyright owner of the abstract of the above-mentioned dissertation, hereby grant to all reference sources permission to publish and disseminate the abstract of the above-mentioned dissertation.

Signature



Date 2018-02-13

# Microfluidic Cell and Particle Sorting using Deterministic Lateral Displacement

*Doctoral Thesis*

Stefan Holm



**LUND**  
UNIVERSITY

Front cover: Illustration of RBCs and trypanosomes in a DLD, Y. Naderi

Back cover: Livia, 1 year old, enjoying sunshine (and this thesis)

Copyright 2018 Stefan Holm


Division of Solid State Physics  
Department of Physics  
Lund University

ISBN 978-91-7753-598-0 (print)

ISBN 978-91-7753-599-7 (pdf)

Printed in Sweden by Media-Tryck, Lund University  
Lund 2018



MADE IN SWEDEN 

Media-Tryck is an environmental-  
ly certified and ISO 14001 certified  
provider of printed material.  
Read more about our environmental  
work at [www.mediatryck.lu.se](http://www.mediatryck.lu.se)

*Dedicated to Erling Holm, pappa*





# Abstract

Microfluidics is a field which has the potential to revolutionize medical diagnostics. The ability to sort and analyse cells by the use of portable handheld devices has the potential to enable sensitive devices for point-of-care diagnostics. This could play a major role in diagnosis of a wide range of diseases which are prevalent in remote areas in developing countries where a majority of the people live without access to modern health care.

One focus of this thesis is the development of such a tool for diagnosis of human African trypanosomiasis, a deadly disease which requires accurate and rapid diagnosis in order to start treatment at an early stage for better chances of survival. The way the disease is normally diagnosed is by microscopic examination of blood smears in order to see if the blood parasite which causes HAT is present in the patient or not. This is a tremendously difficult task as in a single drop of blood there can be 500 million red blood cells (RBC) while at the same time the number of parasites can be less than 10. The vast majority of background cells makes finding the parasite as difficult as finding a needle in a haystack. To help in diagnosis we present a way by which we separate out the blood parasites, if present, from the blood so they can be easily detected.

The method which we use to achieve sorting is called deterministic lateral displacement (DLD), a continuous and passive particle sorting technique which relies on flowing the sample through an array of obstacles. The separation of particles relies on the positioning of these obstacles such that small particles are not affected by the obstacle array while large particles are, and travel at a different angle. The cut-off size between small and large particles is known as the critical diameter and is relatively well characterized for spherical particles. However, the sorting of irregular shaped particles such as RBCs and the long slender parasites has been proven difficult in DLD device. In order to achieve sorting we present a method by which we can control the orientation of particles in order to accentuate their morphological differences. Using this method we present a tool with which we, with high accuracy are able to achieve sorting between these otherwise indistinguishable particles; a tool which could find use in the field-diagnosis of HAT (Paper I and II).

We build on the finding of how non-spherical particles, RBCs, behave in DLD devices and combine that with an investigation of how forces exerted on deformable particle act to deform them. This results in the ability to sort based on the size, shape and deformability of a particle, and the successful sorting of normal RBCs and chemically induced, pathologically relevant, forms of RBCs (Paper III). Further on, RBCs are known to undergo cyclic dynamic events such as tumbling and tank-treading. We address this and show that the sorting in DLD is highly dependent on the dynamic behaviour of RBCs which opens up for new sorting schemes based on for example the internal viscosity of RBCs, a factor which is known to influence the choice of dynamic mode (Paper IV). Microfluidic particle sorting has, due to small length scales, often low throughput. This is addressed by investigating the effects of sample concentration on sorting efficiency (Paper V). By changing the sorting behaviour of particles depending on their vertical position in the device, we implement density-based sorting in DLD (Paper VI).

DLD can be used to separate any particle mixtures, not only naturally occurring biological particle systems. In Paper VII, we expand the scope to also include thermoresponsive microgel clusters generated by droplet microfluidics which allows for the encapsulation at  $\sim 10$  kHz frequencies. By allowing the aqueous content of the droplet to evaporate we force the microgels into close contact and can subsequently crosslink them. With the microgel particles which makes up these clusters having temperature dependent interactions we have a way to selectively tune the interaction sites on the clusters. In combination with DLD we can sort out clusters of interest consisting of a specific number of microgel particles which opens up for new types of particles with interesting properties which is highly suitable for interaction studies and the development of novel materials.

Microfluidics draws benefit from differences in scaling between variables when length scales decreases from macroscale to microscale, such as the increased surface area-to-volume ratio. This acts to introduce new phenomena which can be exploited as in the examples above. Additional benefits to microfluidics include the ability to handle smaller volumes, faster energy dissipation, precise spatial and temporal control and the ability to integrate multiple preparative and analytical functionalities on a single chip, a so-called lab-on-a-chip, which is a major driving force for the microfluidic field and definitely the direction that I have endeavoured to push the projects within this thesis. For example, the continued development of the parasite sorting device has the potential to not only separate RBCs and parasites but also detect the result, and consequently enable a complete handheld sample-to-answer device dedicated for field-use.

*Keywords:* Separation science, Deterministic Lateral Displacement, Microfluidics, Lab-on-a-chip, Point-of-Care, morphology, deformability, cell dynamics

# List of publications

This thesis is based on the work presented in the following papers, denoted as Papers I-VII in the text.

## **I. Separation of Parasites from Human Blood using Deterministic Lateral Displacement**

Stefan H. Holm, Jason P. Beech, Michael P. Barrett and Jonas O. Tegenfeldt  
*Lab on a Chip*, 2011, 11, 1326-1332

I designed the device while the fabrication and measurements were a joint effort together with Beech. I developed the particle tracker and did the analysis. I wrote the paper together with my co-authors.

## **II. Simplifying Microfluidic Separations for Field-Diagnosis**

Stefan H. Holm, Jason P. Beech, Michael P. Barrett and Jonas O. Tegenfeldt  
*Analytical Methods*, 2016, 8, 3291-3300

Based on findings in Paper I, together with my co-authors I implemented ideas for how the device could be improved. I fabricated the device which was designed together with my co-authors. I did all the experiments and data analysis. I wrote the paper together with my co-authors.

## **III. Sorting Cells based on Size, Shape and Deformability**

Jason P. Beech, Stefan H. Holm, Karl Adolfsson and Jonas O. Tegenfeldt  
*Lab Chip*, 2012, 12, 1048-1051

Based on the findings in Paper I and II together with previous research by Beech and Adolfsson we develop a method of how DLD can be used for mapping a sample in terms of size, shape and deformability. I designed the device and fabricated it together with Beech. I helped to carry out the experimental part and the analysis. I contributed to writing the paper.

#### **IV. Sorting Cells by their Dynamic Properties**

Ewan Henry, Stefan H. Holm, Zunmin Zhang, Jason P. Beech, Jonas O. Tegenfeldt, Dmitry A. Fedosov and Gerhard Gompper

*Scientific Reports*, 2016. 6: p. 34375.

Based on the findings in Paper III and previous research by Zhang, Fedosov and Gompper on RBCs in microchannels we further investigate RBC dynamics in DLD. I designed the devices which were fabricated together with Beech. I did all experiments and did the data analysis together with Henry who did all computer simulations. I contributed to writing the paper.

#### **V. Concentration Effects in Deterministic Lateral Displacement devices**

Stefan H. Holm, Zunmin Zhang, Jason P. Beech, Dmitry A. Fedosov, Gerhard Gompper and Jonas O. Tegenfeldt

*Manuscript* (2018)

Based on previous findings on particle behaviour in DLD, mainly Paper II, we investigated how sample concentration affects DLD separations. I designed and fabricated the devices. I performed all experiments involving RBCs and particles and did the analysis. I contributed to writing the manuscript.

#### **VI. Density-based Sorting in Deterministic Lateral Displacement Devices**

Stefan H. Holm<sup>\*</sup>, Jason P. Beech and Jonas O. Tegenfeldt

*Manuscript* (2018)

I designed the device together with my co-authors, I fabricated the devices, carried out the measurements and did the data analysis. I contributed to writing the manuscript.

## **VII. Thermoresponsive Colloidal Molecules Prepared using Droplet-based Microfluidics**

Feifei Peng\*, Stefan H. Holm\*, Linda K. Månsson, Somnath Ghosh, Jérôme J. Crassous, Peter Schurtenberger and Jonas O. Tegenfeldt

*Manuscript* (2018)

I designed and fabricated the devices. Peng and I carried out the droplet experiments. Månsson was responsible for microgel synthesis and characterization. Peng carried out the confocal analysis. Peng and Ghosh optimized the washing protocol. I contributed to writing the manuscript.

## **VIII. Microfluidics-Based Approaches to the Isolation of African Trypanosomes** (Not within the scope of this thesis)

Michael P. Barrett, Jon M. Cooper, Clément Regnault, Stefan H. Holm, Jason P. Beech, Jonas O. Tegenfeldt, Axel Hochstetter

*Pathogens*, 2017, 6(4), 47;

# Acknowledgements

Time truly flies. It feels as if it could have been only last year when Jonas passionately presented an idea about a problem which he had found out about. Apparently there was a blood parasite, which was really difficult to detect due to its low concentration, a task truly suited for DLD, right? I did not hesitate and was soon thereafter working hard on what became the major part of my PhD thesis.

The project grew as Jonas was granted a substantial sum of money to realize the EU project LAPASO, consisting of a strong team of experimentalists, theoreticians, and biomedical collaborators within Europe and Africa, with one of the overall goals of the project being to bring new point-of-care diagnostic devices to Africa. This was well in line with my thesis work and sparked several interesting collaborations.

I have also had the opportunity to visit the parts of Africa where the HAT disease is endemic; meeting the people living in these areas and workers in field clinics who desperately try to give a correct diagnosis with the very limited resources available. This had a significant impact on me, and confirmed the urgent and crucial need for new diagnostic tools which can be used under these conditions, and gave me a strong motivating factor for the long nights in the lab.

Jonas, I am truly grateful that you have always believed in me and for all the opportunities you have given me during my PhD, making me grow as a researcher.

During the course of the PhD I have worked with several people. Past and present members of the Biogroup at FTF have all contributed to creating a great work atmosphere, which I have been fortunate enough to be a part of, Martina, Cassie, Inga, Christelle, Mattias T, Bao, Kushagr, Greger, Oskar, Trung, Mattias B, Heiner, Mercy, Frida, Regina, Damiano, Laura, Elke, Martin, Anders, Johanna, Anastasia, Dmitry and Gaëlle. A few people have made significant contributions to this thesis. First and foremost Jason, who has long been a close colleague and made several important contributions leading to the realization of Paper I-V. Kalle, whom I worked closely with during his master thesis, a work that later developed into Paper III. Henrik contributed to cell culturing and cell staining. Fredrik helped with preparing

cells for SEM. Zhen, who helped to acquire confocal images for Paper II. In addition to the collaborations within the division I am very happy for the exciting collaboration with Peter Schurtenberger, Physical Chemistry, and his skilled team, Feifei, Linda, Jérôme, Somnath and Alfredo who made Paper VII possible. Further, the collaboration with Gerhard Gompper, Forschungszentrum Jülich, and his team, Ewan, Zunmin and Dmitry has with their powerful simulations given us a unique insight into particle behaviour in DLD which made Paper IV and V possible. The collaboration with Mike Barrett, University of Glasgow, and his team of parasitologists, Clément, Gordon, Federica and Axel with whose knowledge and expertise Paper I, II and VIII became possible.

The LAPASO collaboration provided a great open research climate with sharing of ideas and knowledge. This has had a significant impact on my PhD, and has led to several of the collaborations listed above. I would like to collectively thank all members of this organization, with a special mention to Hywel Morgan, University of Southampton and his team, Dan, Carlos and Miguel, with whom we have an exciting, ongoing collaborations together with Monica Brivio and Simone Tanzi at Micronit Microtechnologies in order to further push the limits in field-diagnosis of blood parasites.

Several people at the Department of Biomedical Engineering in Lund have over the years contributed in terms of lending equipment (high speed camera, DAQ systems), sample (microspheres, biosamples) and lab space (plasma bonding and UV mask fabrication) in addition to interesting discussions, namely Thomas, Johan, Christian, Anke, Pär, Pelle, Simon, Maria, Anette and Mikael.

I would like to thank all people, students, researchers, technical staff, administrative staff and faculty, at the division of Solid State Physics collectively for contributing to its special research environment. People who have gone above and beyond to help in my work whom I would like to thank personally include Gerda, Håkan, George, Mariusz, Ivan, Anders, Lena, Mona, Janne and Johanna.

Most important in all of this has been my family whose immense support has made this journey possible. Mamma and Pappa, Thomas, Karin, Kenneth, Gustaf, Anna, Valérie, Amanda, Fredrika, Christer, Andreas, Beatrice, Kathryn, Michael, George, Roger, Clare and my extended family Leo, Hanne Marie, Jesper, Sameera, Nicolai and Kristoffer.

And lastly, my fiancé Lærke who has always stood by me and (together with our daughter Livia) given me moral support. I love you.

# List of acronyms and notations

$\alpha$	correction factor
$a$	acceleration
A	surface area
AO	acridine orange
$\beta$	flow stream width
BBB	blood-brain barrier
$Bo$	Bond number
$c$	concentration
$C$	viscosity contrast
$Ca$	Capillary number
CATT	card agglutination test for trypanosomiasis
CBC	complete blood count
$CH_3$	methyl group
CNS	central nervous system
CSF	cerebrospinal fluid
CTC	circulating tumour cells
$CV$	coefficient of variation
$D$	diffusion coefficient
$D_p$	particle diameter
$D_{post}$	post diameter
$\Delta A_0$	relaxed area difference
$\Delta\lambda$	row-shift
$d$	device depth
$D_c$	critical diameter
$D_H$	hydraulic diameter
DLD	deterministic lateral displacement
$\varepsilon$	row-shift fraction
EMF	erythrocyte membrane filtration
$E$	enrichment
$\Phi$	flow rate
$\phi$	flow rate ratio
$f$	force



FACS	fluorescence activated cell sorting
$\gamma$	interfacial tension
$G$	gap
GC	Gas chromatography
$\eta$	viscosity
$h$	channel height
HAT	human African trypanosomiasis
Ht	hematocrit
$k_B$	Boltzmann constant
$\lambda$	centre-centre distance of obstacles
$l$	length
$L$	characteristic length, channel length
LNA	lymph node aspirate
LOC	lab-on-a-chip
$L_p$	period length
$\mu$ TAS	micro-total-analysis-system
$m$	mass
mAECT	mini-anion-exchange centrifugation technique
MCV	mean corpuscular volume
MHCT	microhematocrit centrifugation technique
$N$	period
O/W	oil-in-water
$p$	pressure
$Pe$	Péclet number
$P_w$	wetted perimeter
PFOTS	1H,1H,2H,2H-Perfluorooctyl-trichlorosilane
PNIPAM	poly-N-isopropylacrylamide
PNIPMAM	poly-N-isopropylmethacrylamide
POC	point-of-care
QBC	quantitative buffy coat
$\rho$	density
$R$	radius
RBC	red blood cell
$Re$	Reynolds number
$R_h$	hydraulic resistance
RTDC	real-time deformability cytometry
$\sigma$	viscosity ratio
SAV	surface-area-to-volume
SEM	scanning electron microscopy
SiOH	silanol group

$t$ .....	time
TAS.....	total-analysis-system
$\theta$ .....	array inclination
$v$ .....	velocity
$w$ .....	channel width
W/O.....	water-in-oil
WBC.....	white blood cell
We.....	Weber number
WHO.....	World Health Organization
VSG.....	variant surface glycoprotein
$x, y, z$ .....	rectilinear spatial coordinates

# Contents

Abstract .....	i
List of publications .....	iii
Acknowledgements .....	vi
List of acronyms and notations .....	viii
1. Introduction .....	1
1.1. Advantages of microfluidics .....	2
1.2. Particle separation .....	3
1.3. Microfluidics for particle sorting .....	4
2. Fluidics at the microscale .....	9
2.1. Laminar flow .....	11
2.2. Hydraulic resistance .....	13
2.3. Diffusion .....	14
3. Deterministic lateral displacement .....	17
3.1. Critical diameter .....	18
3.2. Factors affecting the critical diameter .....	21
3.3. Mixed modes .....	25
4. Device design and fabrication .....	29
4.1. Single or multiple sections .....	30
4.2. Single or multiple inlets .....	31
4.3. Connecting channels .....	32
4.4. Throughput .....	34
4.5. Device fabrication .....	37
5. Blood .....	41
5.1. Composition .....	42
5.2. Red blood cells .....	43
5.3. Methods to examine RBCs .....	44
5.4. Bilayer-couple theory .....	47
6. Human African Trypanosomiasis .....	49
6.1. Pathogenesis .....	50
6.2. Epidemiology .....	53
6.3. Life cycle .....	54
6.4. Evading the immune response .....	55

6.5. Treatment.....	55
6.6. Diagnosis.....	56
7. Droplet microfluidics.....	61
7.1. Dimensionless numbers.....	63
7.2. Surface energy.....	64
7.3. Surfactants.....	64
7.4. Droplet generation.....	65
7.5. Pressure or flow-rate-driven pumping.....	69
7.6. Particle synthesis.....	70
8. Appendix 1 Software.....	71
9. Appendix 2 Device overview.....	73
9.1. Device used in Paper I, III and IV.....	73
9.2. Device used in Paper II.....	75
9.3. Device used in Paper V.....	77
9.4. Device used in Paper VI.....	78
9.5. Device used in Paper VII.....	79
10. Discussion and Conclusion Paper I-VII.....	81
10.1. Paper I Separation of parasites from human blood using deterministic lateral displacement.....	82
10.2. Paper II Simplifying microfluidic separation towards field-detection of blood parasites.....	84
10.3. Paper III Sorting cells by size, shape and deformability.....	87
10.4. Paper IV Sorting cells by their dynamical properties.....	90
10.5. Paper V Concentration effects in Deterministic Lateral Displacement.....	93
10.6. Paper VI Density based sorting in deterministic lateral displacement devices.....	95
10.7. Paper VII Thermoresponsive colloidal molecules prepared using droplet-based microfluidics.....	98
11. Concluding remarks.....	101
11.1. Future directions.....	102
12. Populärvetenskaplig sammanfattning.....	109
13. References.....	115

# 1. Introduction

This thesis concerns the area of microfluidics, a research area dealing with the behaviour, precise control, and manipulation of fluids that are physically constrained to a small scale; typically, at least one dimension is of submillimetre size. It is a truly multidisciplinary field which stems from the 1950s when efforts were made to dispense small amount of liquids, with volumes in the nanolitre to picolitre range, something which laid the basis for ink-jet printing [1] and fluorescent activated cell sorting (FACS) [2]. A major milestone for the realization of today's microfluidics was made by the evolution of another sorting technique, namely chromatography. The first step was taken when Terry *et al.* were able to realize a miniaturized gas chromatograph (GC) for the analysis of air on a silicon (Si) wafer [3]. In 1990, Manz *et al.* published a high-pressure liquid chromatography column device which had been integrated onto a silicon chip, for the first time realizing a true microfluidic device [4]. The paper further exemplifies the efforts at that time toward automation in analytical chemistry, in what became known as total analysis systems (TAS) [5]. In TAS devices, it was carrier streams of fluid, and not human hands, which transported sample fluid between different manipulation steps. Later, the term micro total analysis system ( $\mu$ TAS) was coined to refer to smaller versions of these devices, which were handling  $\mu$ L or even submicrolitres of liquid. Manz's groundbreaking paper is often seen as the spark that ignited the microfluidic field. Similar to the field in general, the work presented in this thesis has relied on advances in micromachining technologies for fabrication of devices on the relevant length scales of microfluidics. Recently the field has become known as the 'lab-on-a-chip' (LOC) or 'microfluidics' field, names which highlight the applicability and usability of microfluidic devices outside of analytical chemistry. Here we will use the name 'microfluidics'.

## 1.1. Advantages of microfluidics

Microfluidics focuses on building networks of interconnecting submillimetre channels. In this way, small volumes of solutions may be introduced from one channel into another, making the controlled interaction of reactants possible. Further, it can draw benefit from the scaling between different properties as the devices are miniaturized, leading to a high surface area-to-volume (SAV) ratio. Consequently, surface effects will dominate in microfluidics as opposed to what we are used to within the macro world in our own reference frame. One major example is laminar flow, which is present in most microfluidic devices. The laminar flow refers to how the flow is ordered and predictable, unlike the turbulent flow, which is present for example when we are pouring water into a glass.

The microfluidic field has grown considerably since its dawn and today physicists and engineers are creating devices with exciting functionality, with the aim of constructing highly integrated compact devices. Chemists are using such tools to synthesize new molecules and particles while biologists use them to study complex cellular processes. Additionally, diagnostic microfluidic devices could potentially revolutionize medicine by the creation of accurate, cheap and portable instruments well suited for point-of-care (POC) diagnostics. Similar devices are also being developed for industrial applications or environmental monitoring.

Microfluidics, in addition to being able to exploit the new phenomena arising at the microscale also offers several advantages over traditional instruments:

- **Portability** - the small length scales allows for the fabrication of small devices, which can be used in for example POC settings.
- **Costs** - microfluidic devices are in general easy to fabricate and do not rely on expensive equipment to operate, as compared to traditional tools *e.g.* FACS and hematology analysers. In addition the small volumes ensure a low liquid consumption.
- **Multiplexing** - microfluidics offers the ability to create integrated LOC devices that can analyse and manipulate samples based on multiple parameters. The ability to create devices with integrated reference systems without human intervention eliminates the risk of contamination.

- **Low liquid consumption** - due to the small length scales devices do not require large volumes of liquids, which is important when sample is scarce or expensive.
- **Rapid** - the shorter length scales and faster reaction times lead to short processing time.

The focus of this thesis is deterministic lateral displacement (DLD), a particle sorting technique which would be a prime example of how new physical phenomena arising at the microscale can be exploited in new types of processes. The ordered and predictable flow often present in microfluidics, laminar flow, is a cornerstone in how particle separation is achieved. DLD was first introduced in 2004 by Huang *et al.* [6] at Princeton University and has since been shown to sort a wide range of particle types from nanometre to centimetre sized particles [7-16]. In the original paper the authors showed an unprecedented, for comparable methods, size-based resolution of 1% for submicron particles. At its introduction DLD was viewed as a purely size-based particle separation method. This has been one of the main foci of this thesis, to expand the applicability of DLD to new types of samples by opening up for separation based on additional parameters.

## 1.2. Particle separation

*"Separation is as old as the earth" [17]*

The first particle separation occurred already at formation of our Earth. The denser elements in the cloud of dust and gases which made up protoearth sedimented inwards and condensed to form our planet while the lighter elements aggregated at the top and today they make up the earth's crust and atmosphere.

Viewed in light of these separations, the development of modern particle separation is a very recent phenomenon. It is usually considered to stem from the development of chromatography in Russia by the Italian-born scientist Mikhail Tsvet in 1900. Chromatography was initially used for the separation of plant pigments, and this is also what has given name to the method. Chromatography was later developed substantially during the 1940s and 1950s by Martin and Synge [18] for which they were jointly awarded the 1952 Nobel Prize in chemistry.

## **Preparative and analytical separations**

The motivation to sort particles can differ significantly. An initial classification of the separation is to divide it into either being preparative or analytical depending on the general goal of the process. In preparative separations the goal is to purify and collect a specific product from all other particles in the sample for future use. This could for example be research related purposes where one wants to study a specific component in the initial sample. In analytical separations the information is instead given directly as a result of the separation. Particles are sorted according to a certain pre-decided criterion giving quantitative or qualitative distribution about the properties of the particles in the sample. This could for example be a diagnostic test which sorts particles present in the blood based on their sizes.

Which of these two categories the end goal of the separation in question belongs to has in general a significant effect on the design of the device, and will affect factors such as the required sensitivity (fraction of false negatives to false negatives and true positives), the specificity (fraction of false positives to false positives and true negatives) and the throughput, as further discussed in context of device designing in Chapter 4.

### **1.3. Microfluidics for particle sorting**

Several general advantages of microfluidics have been outlined, all of which can be exploited for microfluidic particle sorting. The use of microfluidics for the manipulation and analysis of cells and other bioparticles is to a great extent attributed to the matching length scales, Figure 1. This enables sensitive separations and analysis on the single-cell level, instead of bulk averaging which is a common measure of traditional instruments. For example, a doctor will often request a complete blood count test, which among other parameters evaluates the red blood cells (RBCs) in terms of their average volume, known as mean corpuscular volume (MCV). This parameter, while it might on occasion help a doctor give a diagnosis, is severely limited in information. It does not accurately describe the complete distribution of RBCs sizes in the blood. With microfluidics allowing for accurate sorting on the single-cell level the sample heterogeneity is revealed providing a wealth of hidden information.



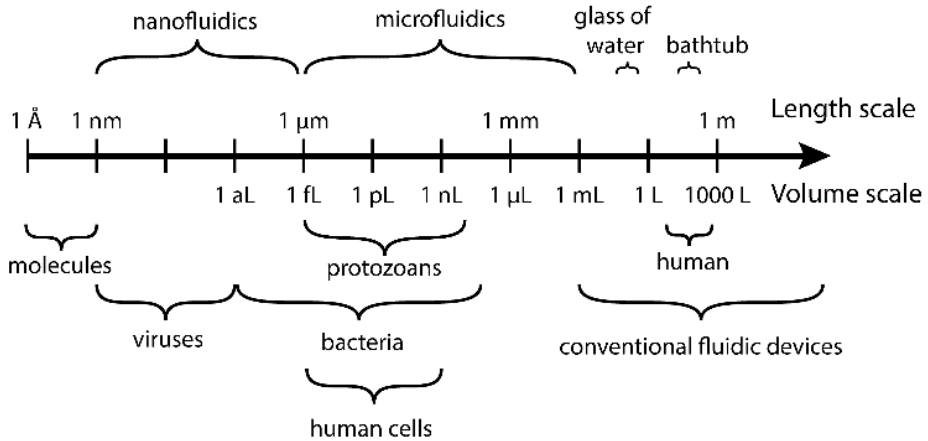


**Figure 1**  
 Approximation of lengths and volumes of a few typical particles. One major benefit of microfluidics is that the length scales match with the many biological particles of interest, making highly sensitive single-cell sorting and analysis possible. Figure adapted from [19].

There are many microfluidic particle-sorting techniques. One major distinction to be made is between active and passive methods. Active techniques require an external force field for functionality, which could be any force which is able to take advantage of the disparities in the intrinsic properties including ultrasonic standing waves [20], homogenous [21] or inhomogeneous [22] electric fields, magnetic fields [23] and optical forces [24]. The other particle-sorting category encompasses the passive methods, which rely solely on the channel geometry and inherent hydrodynamic forces to achieve separation. Several different methods exist, including margination [25, 26], inertial microfluidics [27], hydrodynamic filtration [28], pinched-flow fractionation [29], hydrodynamic chromatography [30] and, the focus of this thesis, DLD [6-8, 10, 31-36]. Several reviews are available which outline the differences between both the aforementioned methods and additional microfluidic particle separation methods [37-40].

Another important distinction is made between continuous and bulk sorting of particles which is based on how sorting is achieved [41]. In bulk sorting, which often includes chromatography, particles get separated along the same axis as they travel the device. Consequently, due to some intrinsic property, particles arrive at the outlet at different time points. As the sample can only be injected at a specific time point, it is often difficult to integrate these techniques with other devices; something that is often desirable in microfluidics systems. As a consequence, many of the more attractive microfluidic sorting techniques are instead continuous. In these devices the

sample is introduced at a single point and while being transported forward through the device is subjected to a secondary force at an angle, often perpendicular, to the direction of the flow and are thus deflected from the direction of flow. With the particles responding differently to the applied force the sorted particles can be collected at different outlets.

## **Deterministic Lateral Displacement**

DLD is a continuous and passive particle sorting technique. It relies only on the hydrodynamic forces to achieve separation. At the same time particles are deflected at an angle with respect to the flow and can be collected in separate outlets, which enables the integration with other tools for analysis and manipulations on-chip. This is reflected in the name, the particles are *laterally displaced* with respect to the flow. *Deterministic* comes from the fact that the separation in a DLD does not, in principle, involve any random processes, as will be discussed in later chapters. DLD relies on the aforementioned laminar flow, which is often present in microfluidics. With laminar flow, the movement of the fluid is ordered and predictable, and as a consequence, so is the outlet position of a particle with a specific size.

While this thesis is mainly focused on the sorting of bioparticles in DLD, its high sorting sensitivity can also be taken advantage of in other systems. In Paper VII we demonstrate such a system by the fabrication of, *so-called*, colloidal molecules by using droplet microfluidics. Colloidal molecules have been used extensively in the past decade as a model system to explore analogies between colloids, atoms and molecules and to investigate various phenomena in condensed matter physics and material sciences [42-45]. The use of droplets microfluidics allows us to generate a library of colloidal molecules consisting of a small number of precursor particles (governed by the Poisson distribution). For studies where clusters consisting of a specific number of precursor particles are required, DLD offers the ability to, with high precision, select subpopulations within the sample for further use.

# Thesis structure

**Chapter 1** gives an introduction to microfluidics, dealing with its past, present and future. Further on, particles and the motivation for particle separation in various settings is discussed.

**Chapter 2** deals with the theory of fluid confined in micrometre size channels and discusses some of the effects that dominate in this fluid regime due to the different scaling between variables. The understanding of the fluid physics lays a foundation for the understanding of DLD devices.

**Chapter 3** will further expand on DLD and present how it can be used to achieve particle separation based on parameters such as size, shape and deformability. Parameters additional to size, that affect the separation and that are a central aspect of this thesis, are discussed.

**Chapter 4** presents design considerations of microfluidic devices, depending on the aim of the separation and particles involved. Device fabrication and the analysis of experimental results are discussed.

**Chapter 5** focuses on blood, its constituents, and their respective properties and importance in disease models. Rheology of blood and the intrinsic properties of single cells are discussed. This relates to Paper I-V where we sort and analyse blood cells based on their size, shape, deformability (Paper III), and further on, based on their dynamic properties (Paper IV)

**Chapter 6** will focus on the epidemiology of human African trypanosomiasis. The current options for diagnosis, staging and confirmation of infection are discussed together with the alternatives for treatment. The development of DLD devices as diagnostic tools capable of discriminating between blood cells and the trypanosome parasite is the focus of Paper I and II.

**Chapter 7** will introduce droplet microfluidics and its wide range of applications, important to Paper VII in which we generate *so-called* colloidal molecules.



## 2. Fluidics at the microscale

*A fluid - a material that deforms continuously under shear stress or more specifically, with the application of an external force attempting to displace part of the fluid elements at its boundary layer (i.e. surface) [19].*

We all have an intuitive sense of how fluids around us behave - when we stir a coffee to mix it with milk, when we open the faucet and let the water run or when we go for a swim in the lake. To us these interactions with fluids are intuitive and we have a sense of how we expect them to act and how the fluid should react when we apply a force to it. However, the fluids in our normal macroscale reference frame behave in many cases in stark contrast to fluids at the microscale. We are used to the motion of fluids being controlled to a large degree by body forces, such as gravity and inertial forces. However fluid flow at the microscale in general behaves significantly different. Decreasing length scales leads to surface forces dominating the behaviour of fluids, which due to scaling differences act to introduce new phenomena in microfluidics according to

$$\frac{\text{surface forces}}{\text{body forces}} \propto \frac{l^2}{l^3} = l^{-1} \xrightarrow{l \rightarrow 0} \infty. \quad (1)$$

The movement of an object can be described by Newton's second law, which relates the mass,  $m$ , and acceleration,  $a$ , to the applied force,  $F$ ,

$$m\mathbf{a} = \sum \mathbf{F}_i. \quad (2)$$

This can for example be used to describe how the centre of mass of a discrete object such as a raindrop falls to earth. However as the fluid inside the raindrop instead is a continuous liquid and not a discrete entity it needs to be described in terms of continuous fields such as density and force density that are defined per unit volume instead of discrete quantities such as mass and force. The motion of a viscous fluid substance is described by the Navier-Stokes equation, which essentially is a continuum version of Newton's second law on a per unit volume basis. The equation is used for vastly different applications such as the modelling of ocean currents, airflow

around a wing or, as in this case, the analysis of fluid flows on the microscale. For a Newtonian fluid the equation can be expressed by

$$\rho \left( \frac{\partial \mathbf{v}}{\partial t} + (\mathbf{v} \cdot \nabla) \mathbf{v} \right) = -\nabla p + \eta \nabla^2 \mathbf{v} + \mathbf{f} \quad (3)$$

together with

$$\nabla \cdot \mathbf{v} = 0. \quad (4)$$

with Eq. 4 being the continuity equation which is valid for an incompressible fluid where  $\rho$  is constant in both time and space. For Eq. 3, the inertial term on the left consists of local acceleration,  $\partial \mathbf{v} / \partial t$ , and convective acceleration,  $(\mathbf{v} \cdot \nabla) \mathbf{v}$ . The force terms consist of the pressure gradient ( $-\nabla p$ ) and the viscous effects ( $\eta \nabla^2 \mathbf{v}$ ), the final term,  $\mathbf{f}$ , represents the body forces.

The nonlinear term of Eq. 3,  $(\mathbf{v} \cdot \nabla) \mathbf{v}$ , makes a general analytical solution not possible. However, under certain conditions, the equation can be simplified in order to arrive at solutions, given later in this chapter. However, in order to get a sense of the fluid behaviour and its properties, several dimensionless parameters are used to quantify the relative importance of different physical quantities, with a few outlined in Table 1.

**Table 1**  
Dimensionless parameters in microfluidics used to describe flow behaviour

Symbol	Name		Physical meaning
$Re$	Reynolds number	$\rho v D_H / \eta$	Inertial force/viscous force
$Pe$	Péclet number	$vL/D$	Convection/diffusion
$Ca$	Capillary number	$\eta v / \gamma$	Viscous force/interfacial tension
$We$	Weber number	$\rho v^2 L / \gamma$	Inertial force/interfacial tension
$EO$	Eötvös number	$\Delta \rho g L^2 / \gamma$	Buoyancy/interfacial tension
$\eta_R$	Viscosity ratio	$\eta_d / \eta_c$	Dispersed viscosity/continuous viscosity
$\Phi_R$	Flow rate ratio	$\Phi_d / \Phi_c$	Dispersed flow rate/continuous flow rate

## 2.1. Laminar flow

Fluid flow can be categorised as either being laminar, Figure 2, or turbulent with microfluidic devices almost exclusively operating under conditions which favour the former. These two regimes are characterized by the relative importance of inertial forces and viscous forces, which is typically expressed by the Reynolds number,  $Re$  [46]. Turbulent flow is chaotic and it is, as a consequence, impossible to predict where a particle will be positioned in the fluid as a function of time. Laminar flow, on the other hand, is predictable and a particle's position and velocity is not a random function of time (if we neglect diffusion). For cylindrical channels, laminar flow is typically present for  $Re \lesssim 2300$ .

$$Re \equiv \frac{\rho v_o L_o}{\eta} \quad (5)$$

with  $\rho$  being the density,  $v_o$  the characteristic velocity,  $\eta$  the viscosity and  $L_o$  the characteristic length scale, which often can be considered as the hydraulic diameter,  $D_H$ , given by

$$D_H = 4 \frac{A}{P_w} \quad (6)$$

where  $P_w$  is the wetted perimeter of the cross-section. The Reynolds number can be derived by converting the Navier-Stokes equation to its non-dimensional form and thereafter comparing the magnitude of the inertial term ( $\rho v_o^2/L_o$ ) to the viscous term ( $\eta v_o/L^2$ ). As  $Re$  scales with the length, the small length scales present in microfluidics often lead to  $Re < 1$ .

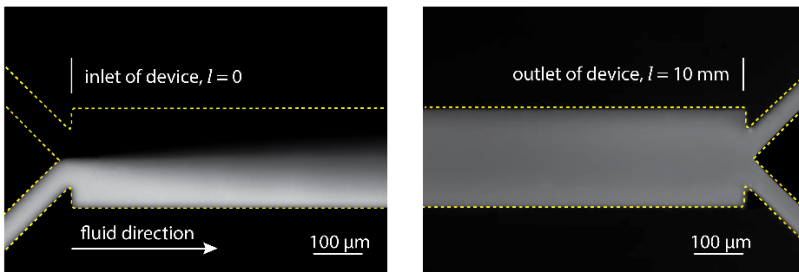


**Figure 2**

Laminar flow; two streams enter a wide channel and flow side by side in an ordered fashion, no turbulent mixing occurs. The width of the centre channel is  $w = 200 \mu\text{m}$  and has a depth of  $d = 30 \mu\text{m}$ , at the same time the average flow velocity is  $v \sim 0.2 \text{ mm/s}$ , considering density and viscosity of water we have  $Re \approx 0.01 \ll 1$  with laminar flow present as a result.

In the intermediate Reynolds number range  $1 \lesssim Re \lesssim 100$ , non-turbulent inertial effects such as Dean flow or non-turbulent vortices may be present, effects which have been shown useful for the manipulation particles [27].

Laminar comes from the Latin word *lāmina* meaning "thin sheet of material". This is also good description of laminar flow, where the fluid can be said to consist of non-mixing parallel flows. For the separation of particles in DLD, due to being a separation method relying on hydrodynamic interactions, the presence of laminar flow is required. Figure 3 shows a microfluidic device consisting of two inlets with identical flow rates. Fluorescent polystyrene particles have been added to the bottom inlet to visualize how these two streams are able to flow next to each other in an ordered predictable manner. With an average flow velocity of  $v_o = 0.2$  mm/s and a channel geometry of  $w = 200$   $\mu\text{m}$  by  $d = 30$   $\mu\text{m}$  we have a Reynolds number, considering the properties of water,  $Re \approx 0.01 \ll 1$  and consequently laminar flow is present as the viscous forces are dominating the system. However in the same figure, even in the absence of turbulent chaotic mixing, the outlet distribution of the particles have adopted a uniform concentration profile. This is due to diffusion, which is the random movement of particles which acts to redistribute them from areas of high concentration to low concentration, as discussed later in this chapter.

An important feature of laminar flow is the velocity profile which has a central role in the separation of particles in DLD devices, as seen in the next chapter. Due to the viscous drag exerted by the channels walls, the flow at the boundary is often considered static, in what is called the no-slip boundary condition, Figure 3. At the same time, the maximum velocity is when fully developed found in the centre of the channel acting to create a parabolic flow profile.

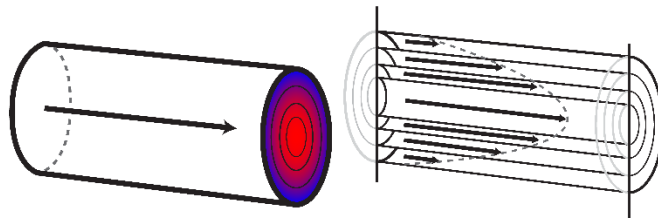


**Figure 3**

Laminar flow consists of non-mixing parallel flows. These separated layers in combination with the no-slip condition at the boundaries of the channel create a velocity profile across the channel, with a maximum flow velocity in its centre.



## 2.2. Hydraulic resistance

Depending on the size and cross sectional shape of the channel, the flow rate will be an effect of the applied pressure according to

$$\Phi = \frac{\Delta P}{R_h} \quad (7)$$

with  $P$  being the pressure,  $\Phi$  the flow rate and  $R_h$  the fluidic resistance. This leads to an equation which is analogous to ‘Ohm’s law’ and electric resistance, connecting the potential of two points to the flow rate between them.

The hydraulic resistance constitutes an important parameter during device designing when channels from the inlet and outlet need to be connected to the DLD array in order to ensure the desired flow ratios. The correct relative hydraulic resistances between the inlet channels negates the need for precise adjustments of the applied pressures, and further it enables the correct bifurcation of the flow at the end of the device and ensures that the samples are diverted into the correct outlet.

Poiseuille flow is when an incompressible, Newtonian fluid is driven through a long, straight, and rigid channel by imposing a pressure difference between the inlet and the outlet. These conditions allows for several simplifications to the Navier-Stokes equation allowing for an analytical solution for certain cross-sections.

For the devices in this thesis, fabricated by 2D photolithographic techniques, the channels are of rectangular cross-sections. In this case there is no analytical solution to the hydraulic resistance, instead the closest to an analytical solution is a Fourier sum [47] given by

$$R_h = \frac{12\eta L}{wh^3} \left[ 1 - \frac{192h}{\pi^5 w} \sum_{i,odd}^{\infty} \frac{\tanh\left(\frac{i\pi w}{2h}\right)}{i^5} \right]^{-1} \quad (8)$$

where  $w > h$ . The part within brackets is given in Figure 4 as the correction factor. Here we can see that for a channel of square cross section the expression simplifies to

$$R_h = \frac{29\eta L}{w^4}. \quad (9)$$

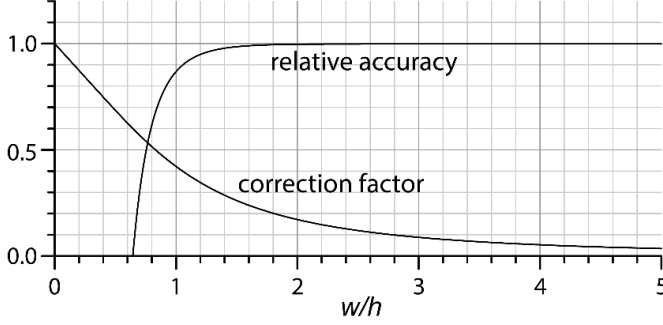


**Figure 4**

Hydraulic resistance in a channel of rectangular cross-section. A correction factor is used to compensate for the varying aspect ratio (the factor within brackets in Eq. 8). For channels of higher aspect ratios an approximation, Eq. 10, can be used with high accuracy. For aspect ratios  $w > 2h$ , the error is less than 0.2%.

For high aspect ratio channels, Eq. 8 can be approximated with

$$R_h = \frac{12\eta L}{wh^3} \left(1 - 0.63 \frac{h}{w}\right)^{-1}. \quad (10)$$

Figure 4 also gives the relative accuracy for this approximation showing an error less than 0.2% in channels where  $w \geq 2h$ .

## 2.3. Diffusion

Diffusion is the process by which particles, by Brownian motion, spread out over time. Particles from areas of high particle concentration are on average displaced to areas of lower particle concentration acting to generate a uniform concentration profile. The mean square displacement of a particle due to diffusion is given by

$$\langle r^2 \rangle = 2nDt \quad (11)$$

with  $n$  being the dimensionality of the diffusion process,  $t$  is the time and  $D$  is the diffusion coefficient given by the Stokes-Einstein equation

$$D = \frac{k_B T}{6\pi R \eta} \quad (12)$$

with  $k_B$  being Boltzmann's constant,  $T$  is the temperature,  $R$  is the particle radius and  $\eta$  the viscosity of the medium.

**Table 2. Average distance of diffusion for spherical particles under Stokes flow**

Particle diameter	$t = 1 \text{ s}$ [ $\mu\text{m}$ ]	$t = 10 \text{ s}$ [ $\mu\text{m}$ ]	$t = 100 \text{ s}$ [ $\mu\text{m}$ ]	$t = 1000 \text{ s}$ [ $\mu\text{m}$ ]
10 nm	6.6	21	66	210
100 nm	2.1	6.6	21	66
1 $\mu\text{m}$	0.66	2.1	6.6	21
10 $\mu\text{m}$	0.21	0.66	2.1	6.6
100 $\mu\text{m}$	0.066	0.21	0.66	2.1

The significance of diffusion depends to a large extent on the aim of the measurements and the sample. However, as a general rule, considering the time to diffuse a distance equal to its diameter together with the typical time scales involved in a measurement, diffusion typically starts to become significant for particles with a diameter below 1  $\mu\text{m}$ . Although diffusion can be useful for the separation of particles in certain settings [48, 49], in general the stochastic movement of particles lead to a decreased resolution of the separation. For sorting of cells, such as RBCs, their large size together with typical residence times in the device makes the effect of diffusion limited. However, for the sorting of smaller objects such as DNA and extracellular vesicles, diffusion must be considered [50].

The dimensionless Péclet number is used to describe the relative importance of advective transport to diffusive transport, which can be considered in terms of the time it takes to transport a particle a specific distance by axial advection and radial diffusion respectively. If we consider two liquids flowing side by side in an H-filter, Figure 5, then the time to achieve full mixing is approximately when the particles on average have diffused a distance equal to half the channel width. Comparing this to the time required to transport the fluid the same distance we arrive at the Péclet number

$$Pe = \frac{L^2/D}{L/v} = \frac{Lv}{D} \quad (13)$$

where  $L$  and  $v$  are the characteristic length and velocity of the system.

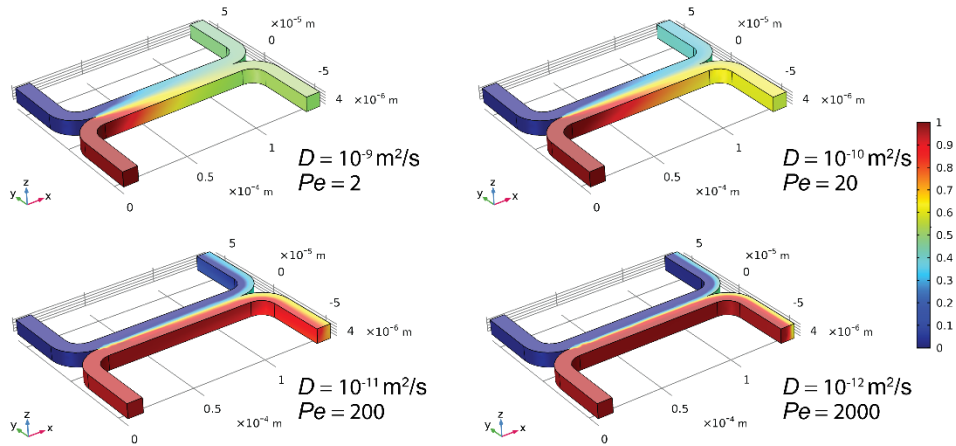


**Figure 5**

Results of FEM simulation using COMSOL Multiphysics showing the impact of the Péclet number on mixing in an H-filter where all inlet and outlet channels have the same widths. With a lower diffusion coefficient we get, together with a constant flow rate and device geometry, a decrease in the mixing in the device, as reflect in the increased  $Pe$  number. In this situation  $Pe$  can be considered the number of device lengths the particles has to be moved by advective transport before complete mixing by diffusion has occurred.

As seen above, depending on the application diffusion can either be a requirement or act to decrease the performance of the system. In situations where fast mixing times is a requirement the combination of laminar flow with the relatively slow process of diffusion can be a problem and act to limit how quickly *e.g.* chemical reactions can take place. To counteract this, several methods have been developed, either active approaches which rely on an external field to perturb the sample or passive methods which amplify the effect of diffusion by using chaotic mixing to decrease the involved diffusion lengths [51].

However, for the general case of particle sorting diffusion acts to decrease the sorting efficiency. While diffusion can be limited to some degree by increasing the viscosity of the medium or decreasing the temperature, it will always be present and can, especially for sorting of smaller particles, constitute a serious issue. As DLD is a passive particle sorting technique, it is not dependent on the time an external field is applied. As a result, the flow rates can be increased (within reasonable limits) in order to suppress the detrimental effects of diffusion. Consequently, while active particle sorting techniques suffer when throughput is increased, the resolution of sorting in a DLD is instead improved.

### 3. Deterministic lateral displacement

Deterministic Lateral Displacement was first introduced in 2004 by Huang *et al.* [6] displaying an, for fluidic separations, unprecedented resolution of  $\sim 10$  nm for the separation of submicron polystyrene spheres. Further, bacterial artificial chromosomes (dsDNA with lengths 61 kbp and 158 kbp) were separated in 10 minutes with a resolution of 12%. The method relies on the predictability of laminar flow which is often present in microfluidics. Due to hydrodynamic and steric interaction with an array of obstacles, particles are separated based on their size, Figure 6.

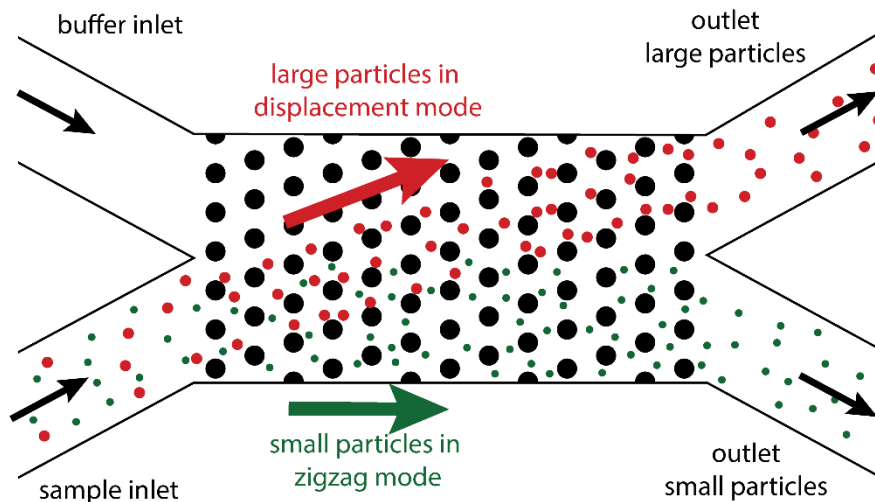


**Figure 6**  
Schematic illustration of a DLD device showing separation between large particles (red) and small particles (green). This specific device consists of two inlets with particles injected from the bottom left inlet while a clean buffer is injected from the top left inlet. The small green particles thereafter travel through the device in the direction of the fluid and exit at the same lateral position as where they entered. The larger red particle, however, interact with the obstacle array and travel at an angle to the flow so that they are laterally displaced away from the green particles. At the end of the device they exit to a separate outlet and can be collected.

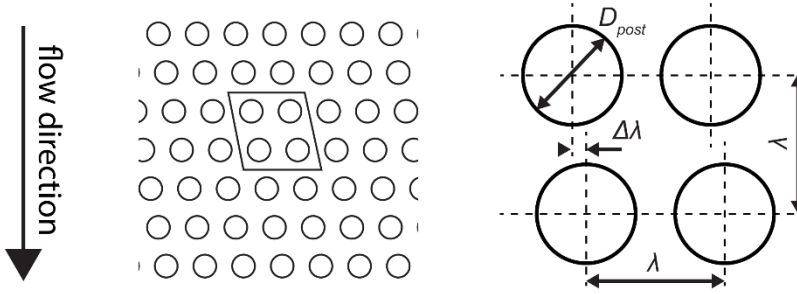


**Figure 7**

A rhombic unitcell within a DLD post array. The most important parameters in deciding the cut-off size between small and large particles include the centre-to-centre distance between the posts,  $\lambda$ , the post diameter,  $D_{post}$ , and the row shift,  $\Delta\lambda$ , which is the distance by which every row in the array is shifted laterally with respect to its previous row. The distance between two neighbouring posts, the gap, is given by  $G = \lambda - D_{post}$ .

### 3.1. Critical diameter

In DLD the separation of particles relies on the specific arrangements of posts in a channel. The posts make up a symmetric array with which particles interact in such a way that particles above a certain size travel at an angle with respect to the fluid flow while particles below this size travel in the overall direction of the fluid. This cut-off size between small and large particles is known as the critical diameter,  $D_c$ , and vary depending on several variables of the post array geometry, given in the unit cell in Figure 7. Important parameters include the centre-to-centre distance between two neighbouring posts,  $\lambda$ , the post diameter,  $D_{post}$ , and the row shift,  $\Delta\lambda$ , which is the distance by which every row in the array is shifted laterally with respect to its previous row, and the period of the array which is given by  $N = \lambda/\Delta\lambda$ . Often the gap is used instead of the post diameter. This is the distance between two neighbouring posts and is given by  $G = \lambda - D_{post}$ .

Within a DLD device the flow can be divided into multiple laminae each with the same volumetric flow rate. By choosing the widths so that each laminae transport  $\Phi = \Phi_{gap}/N$ , where  $\Phi_{gap}$  is the total volumetric flow rate through a gap between two neighbouring posts within the same row we arrive at the situation in Figure 8. Here one lamina is diverted around a post for each row in the device. After  $N$  rows, the laminae are back to their original relative positions. The basis for the critical diameter, and the separation, is whether a particle is able to fit within the same lamina throughout the device or if it is, through interactions with the posts, forced away into the neighbouring

laminae. The gap between two posts within the same row is where the laminae are the narrowest. As a consequence, this is the decision point for whether a particle can continue to reside in a specific laminae.

Shown in Figure 8 are two separate DLD arrays where one has a period of  $N = 3$  and the other of  $N = 5$ . The widths of the laminae,  $\beta_n$ , in the gap are non-uniform due to the parabolic flow profile, resulting in the laminae closest to the posts being the widest, while the central laminae are narrower. If the centre of a particle, with a diameter  $D_p$ , is able to reside within the first flow stream in the gap ( $D_p < 2\beta_1$ ), exemplified by the particle in the  $N = 3$  array in Figure 8, then the particle is able to reside in this laminae throughout the device and its lateral position at the outlet is identical to its lateral position at the inlet. If the particle is too large so its centre is not able to reside within the first laminae at the gap ( $D_p > 2\beta_1$ ), exemplified by the particle in the  $N = 5$  array in Figure 8, then through interactions with the post and the fluid it will be pushed out into the neighbouring laminae for every row in the device, resulting in that large particles travel at angle with respect to the fluid flow.

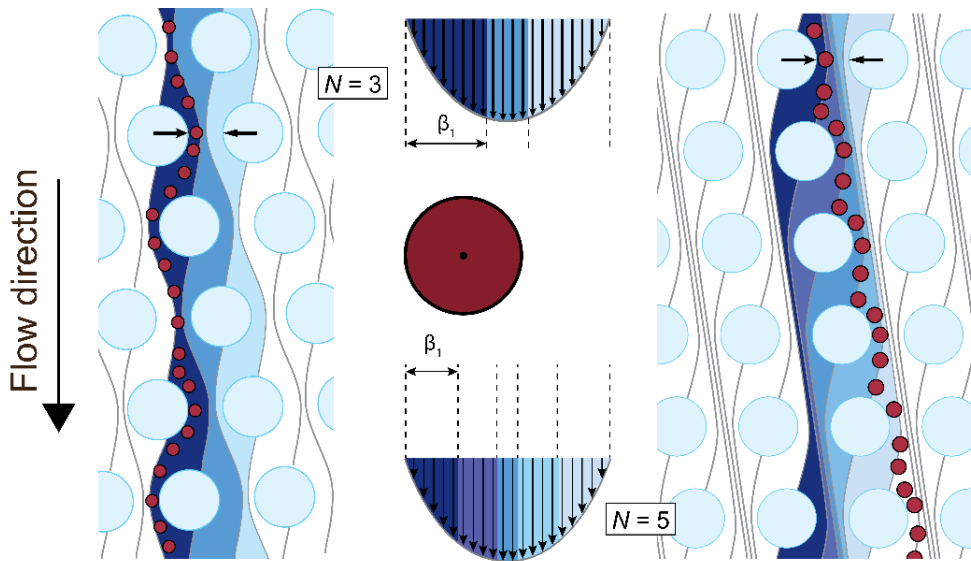


**Figure 8**

Separation in DLD relies on the widths of laminae which each transport the same volumetric flow rate. Particles with a diameter larger than twice the width of the first laminae at the decision point (between two neighbouring posts) are forced out into the adjacent flowstream. This process is repeated for each row in the device and gives rise to a separation of particles based on a critical diameter. The laminae widths are non-uniform due to the parabolic flow profile, resulting in a larger width of the first and last lamina compared to the centre laminae.

Consequently, if a particle is smaller than the critical diameter it will follow the bulk flow of the fluid, in what is commonly referred to as (zigzag mode). Particles with a size which is above the critical diameter will on the other hand be laterally displaced for each row in the device and travel at a resulting angle which is dictated by the array geometry. This mode is commonly referred to as displacement mode. The critical diameter is given by

$$D_c = 2\beta_1 = \alpha \frac{G}{N} \tag{18}$$

where  $\alpha$  is a dimensionless parameter used to correct for the flow profile which is a function of the post shape and device geometry. For a parabolic flow profile given by

$$v(x) = k(Gx - x^2) \tag{19}$$

with  $k$  being a constant, and  $x$  the relative position across the channel, Eq. 18 can be approximated with  $\alpha = 2(N/3)^{0.5}$  with minor error for periods  $N > 10$  [52].

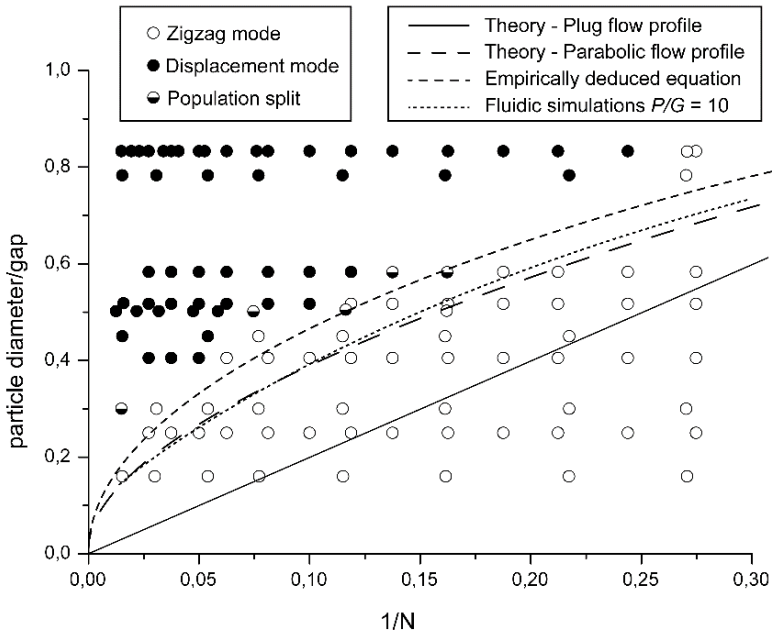


**Figure 9**

A collection of our experimental results showing the transition between zigzag mode and displacement mode. Particle sizes have been normalized to the gaps used in the specific measurements and this is plotted as a function of the inverse period of the device. Lines represent theoretical plug-flow and parabolic flow profiles in the device together with the empirically deduced formula,  $D_c = 1.4GN^{0.48}$ , and CFD simulations by COMSOL, at a post-to-gap ratio of 10.



However, an empirically deduced formula [53] has been shown better at predicting the critical diameter, and is consequently often used for estimating the critical diameter in a device,

$$D_c = 1.4GN^{-0.48}. \quad (20)$$

The reason to why analytical solutions to the critical diameter has shown discrepancies to experimental separation results is believed to be in part due to the flow perturbation caused by particles as they flow through the gap, an effect which increases for large particles in relationship to the gap. Eq. 20 agrees reasonably well with our results, Figure 9. Here it can be seen that while the theoretical parabolic flow profile agrees well with fluidic simulations, they both underestimate the critical diameter. The empirically deduced critical diameter instead shows a better agreement with experimental results, with a discrepancy for lower  $N$ , which can be attributed to the aforementioned flow perturbation caused by large particles in relation to the gap. The plug flow profile has a much smaller critical diameter due to having a much higher flow velocity closer to the boundaries.

Fluid perturbations due to a large particle size in relation to the gap is one factor which can affect the critical diameter, however, other parameters related to the device geometry can also act to alter the critical diameter as discussed in the next section.

## 3.2. Factors affecting the critical diameter

Factors which are not included in Eq. 20 can act to alter the critical diameter, and consequently this formula may be oversimplified to encompass device geometries outside the norm. By carrying out 3-dimensional fluidic CFD simulations using COMSOL Multiphysics 5.3 this section points out factors which can act to influence the critical diameter in a device. While basing the critical diameter on simple fluid flow without particles is not ideal, it provides a reliable way to show the relative trends when different parameters of the device geometry is changed.

### **Post shape**

The effect of post shape and also the post-to-gap ratio ( $P/G$ ) is exemplified in Figure 10 by three circular posts  $P/G = 0.1, 1$  and  $10$ , and further two equilateral triangular posts angled differently with respect to the overall flow direction. The flow in the figure is up, while the displacement direction is to

the right. The period in each device is  $N = 5$ . The velocity magnitude (normalised here to the maximum velocity) is colour coded for easy visualization. By measuring the flow profiles across the gap, Figure 10f-g, the differences become apparent. The flow profiles have here been normalised to the average flow rate. The large circular posts  $P/G = 10$  reveal a much better agreement with parabolic flow theory than the small posts  $P/G = 0.1$ , which is believed to be related to entrance effects where the fluid has to travel a certain distance in order to fully develop the parabolic flow profile. Additionally, the equilateral triangular posts show significant differences depending on their orientation angle. The cumulated flow rate graph can be used to find the critical diameter,  $D_c = 2\beta_1$ , where  $\beta_1$  is given as the width of the first laminae, with a flow rate of  $\Phi_1 = \Phi_{gap}/N$ . For the circular posts this was found to be  $0.446G$  and  $0.470G$  for  $P/G = 0.1$  and  $10$  respectively. For the triangles the inverted had a critical diameter of  $0.430G$  while the other had  $0.487G$ , and consequently a 13% increase depending on its angle.

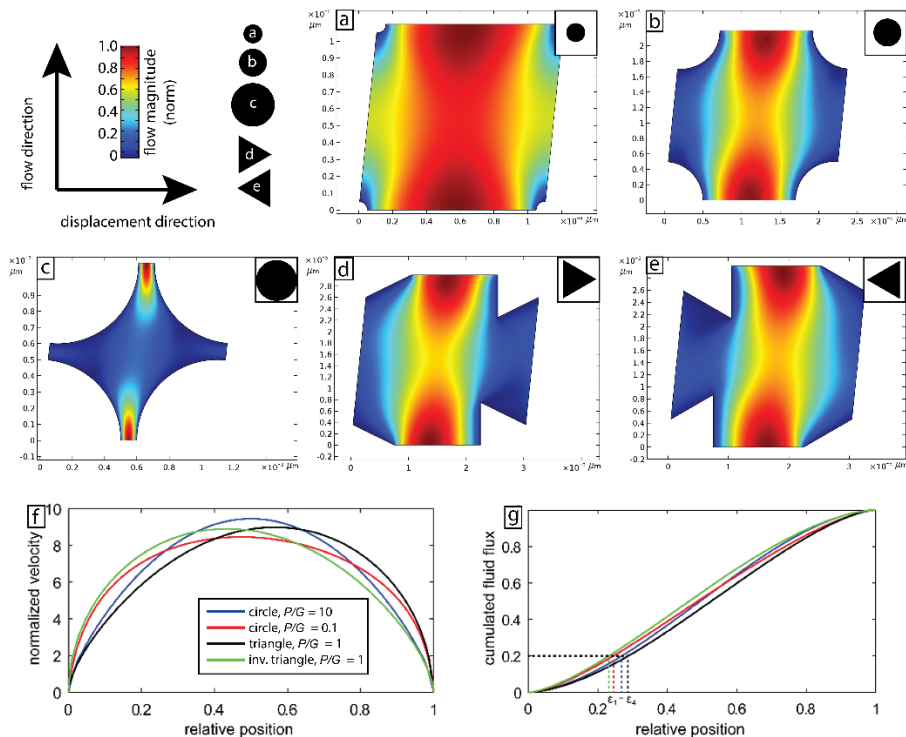


**Figure 10** Fluidic simulations using COMSOL showing the impact of post shape on the flow field and, as a result, the critical size. **(a)-(c)** flow field of circular posts of increasing post-to-gap ratio,  $P/G = 0.1, 1$  and  $10$ , **(d)** equilateral triangle and **(e)** inverted equilateral triangle. **(f)** The flow profiles along the gap show significant differences which effect on the critical diameter can be quantified by considering the width of the first laminae (with a flow rate of  $\Phi_{gap}/N$ ). **(g)** The largest difference is between the two triangles, where the normal triangle has a 13% higher critical diameter than the inverted.

The influence of post shape on critical size have been studied to some extent by Wei *et al.* [54] who proposed the addition of a shape-dependent factor to Eq. 20 to expand its use to arbitrary post shapes. However, experimental results have shown significant deviations [55]. As a result, a generic formula has been proposed [56]

$$D_c = \alpha GN^\beta \quad (21)$$

where the dimensionless parameters  $\alpha$  and  $\beta$  are geometric factors determined by the shape and arrangements of posts.

## Device depth

Another factor which affects the flow profile is the device depth as first reported by Beech [52]. In a normal, relatively deep, DLD device the velocity profile is parabolic, or close to being parabolic at the decision point (depending on for example factors outlined above). However, when decreasing the device depth the flow profile is modified so that the flow velocity is increased close to the posts. A 3D FEM simulation, Figure 11, of a unit cell with  $G = 10 \mu\text{m}$ ,  $P = 10 \mu\text{m}$  and  $N = 10$  shows a saddle point at the centre of the gap at a depth of  $d = 1 \mu\text{m}$ . The effect is also apparent above this depth but to a smaller degree. Comparing the width of the first streamline,  $\beta_1$  given at  $\Phi = \Phi_{gap}/10$ , there is a significant difference between the deepest device ( $d = 6 \mu\text{m}$ ,  $D_c = 0.36G$ ), and the shallowest device ( $d = 0.1 \mu\text{m}$ ,  $D_c = 0.18G$ ). Consequently, the critical diameter decreases with decreasing depth, which in turn could allow for shorter devices, however the throughput would be limited due to the depth. In Paper II, a part of the device was made shallow ( $d = 3.5 \mu\text{m}$ ) in order to orient RBCs and blood parasites to increase their effective size. This effect would likely be visible in this section and act to decrease the critical size. As the goal of this specific section was to displace all cells it should act to increase device performance.

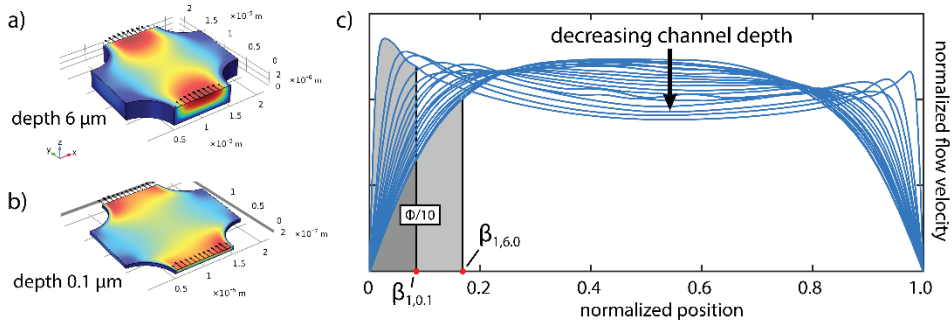


**Figure 11**

CFD simulation of device depth effect on critical size. For a normal relatively deep device (a) the flow profile adapts a close to a parabolic profile. However, for decreasing channel height (b) the flow is higher closer to the posts than in the centre of the gap. Already at  $2\ \mu\text{m}$  the flow profile is close to that of plug flow. The width of the first flow stream (c) between a device with a depth of  $6\ \mu\text{m}$  ( $\beta_{1,6.0}$ ) and a device of  $0.1\ \mu\text{m}$  ( $\beta_{1,0.1}$ ) is shown. The resulting critical sizes is  $D_{c,6} = 0.36G$  and  $D_{c,0.1} = 0.17G$ . This simulation was carried out at  $P/G = 1$ . The noise in the lines at lower depth is introduced due to the mesh.

The inherent simplicity of the DLD, which allows it to benefit from a constant and stable critical size may be a drawback during the design stage due to the above mentioned difficulties in predicting the resulting separation characteristics. Our approach to this has been to base the device design on theory and simulation to a certain extent, but in the end focus on the experimental results. Consequently, we use analytical DLD devices consisting of multiple critical sizes in series in order to investigate the particle behaviour in DLD devices of certain geometries at various shear rates and buffer viscosities and thereafter specific, optimized, devices can be constructed based on the experimental results. This was for example carried out in Paper I and II where the initial paper presents the behaviour of RBCs and trypanosomes in DLD devices of different critical sizes and at different depths. Building on the knowledge of which critical size gives rise to the best separation an improved device with a much increased throughput in combination with simplicity of use was presented in Paper II. However, there are both passive and active approaches to tuning the critical size in a DLD. Active approaches include the use of dielectrophoresis [57] by which the relative polarizability of a particle with respect to the medium can be used to affect its trajectory in the DLD. Passive approaches have been shown by exploiting the elastic properties of polydimethylsiloxane (PDMS) [58], non-Newtonian liquids [59] and varying the ionic concentration of the buffer [60].

### 3.3. Mixed modes

The trajectories of particles in a DLD device is often thought of in terms of pure zigzag mode or pure displacement mode, which is a simplified model of the particle behaviour. Several factors can lead to changes in particle behaviour as it flow through the device, include shape and softness. For a non-spherical particle the orientation as it passes through the decision point in the array will decide if it will travel in displacement mode or zigzag mode. Consequently, if the orientation of non-spherical particles is not controlled, they can display a stochastic behaviour in the device. Another effect is the shear forces exerted on soft particles by the fluid flow. These will lead to deformation of the particle resulting in a smaller effective size. If the shear forces vary in the device or if there is anisotropy to the deformability of the particle, this could also lead to mixed modes. However, even for rigid spherical particles, so-called mixed modes have been shown both experimentally [6] and theoretically [56]. Kulrattanarak *et al.* [61, 62] proposed that the underlying reason is an asymmetric flow lane distribution at the decision point. Instead of the symmetric profile as expected from a fully developed parabolic flow profile the first and last streamline differed significantly, an effect which results in a separation of the first streamline width and the critical diameter,  $D_c \neq 2\beta_1$ . Several factors which can lead to this non-anisotropic permeability in DLD devices have been pointed out in a recent paper by Vernekar *et al.* [63], including the traditionally parallelogram array geometry, as opposed to the tilted-square and the ratio between the axial-and-lateral post distance.

Other factors which can induce non-ideal flows in DLD devices include boundary effects [64, 65]. If the device edges is fabricated as a straight line, the widths of the first and last gap will vary along the device and act to distort the flow pattern. By assuming the fluid flux to be proportional to the gap squared, the lengths of the gaps closest to the edge can be adjusted to decrease this effect. In order to account for this all devices within this thesis have been fabricated with the following gap sizes

$$G_{zigzag,n} = G \sqrt{\frac{n}{N}} \quad (24)$$

$$G_{displacement,n} = G \sqrt{1 - \frac{n}{N}} \quad (25)$$

where  $G_{displacement}$  is the gap between the edge of the device and the first post in a row on the side to which particle are laterally displaced, while  $G_{zigzag}$  is

the first gap on the opposite side of the device and  $n$  is the row number in the period going from  $n = 1$  to  $n = N$ .

It should also be pointed out that fabrication limitations may introduce defects which can give rise to mixed modes in the device and which in turn decrease the separation efficiency. These could for example be introduced during the photolithography step in the case of non-uniform illumination, resulting in areas partially being underexposed while others, on the same device, may be overexposed. Consequently, the resulting post diameters would vary and as a result the critical size. The result would be similar if the walls of the posts are not vertical, an effect which in general is increased with increasing aspect ratios or due to device elasticity [66] depending on device material. The separation of a particle would consequently be dependent on its vertical position in the device, an effect which has been shown useful if controlled in density-based particles sorting in DLD [33, 34].

Diffusion is also a stochastic effect which act to decrease the resolution of a separation. The influence of diffusion is different for a particle in zigzag mode and a particle in displacement mode [50]. For a very small particle the outlet distribution is completely dominated by diffusion and the outlet distribution is given by the 1D transverse diffusion during the time the particle spends in the device. Due to the position of a large particle being reset at each row when it interacts with a posts, it can only undergo a lane swapping event if diffusion can move it into the first flow stream as it passes between two posts. Measurements conducted at elevated Reynolds number have been shown that the typical operation of a DLD breaks down at  $Re > 70$  [67], which would for a typical DLD device geometry translate into flow velocities in the centimetre-to-meter per second range. If we consider a flow velocity of  $v = 10$  cm/s, together with  $\lambda$  ( $\sim 10$   $\mu\text{m}$ ) as the characteristic length scale over which diffusion competes with fluid transport, we would for a RBC ( $D_p \approx 10$   $\mu\text{m}$ ) have  $Pe \sim 10^5$  while for a 10 nm particle  $Pe \sim 100$ . Depending on the device geometry, the flow velocities could be increased even further. This could also be compared in terms of the relative effect of the lateral particle transport mediated by the DLD and diffusion. With the same characteristic length,  $\lambda$ , we arrive at

$$\frac{l_{DLD}}{l_{diffusion}} = \frac{v_{DLD}t_0}{\sqrt{Dt_0}} \sim \frac{v}{\lambda/\Delta\lambda} \sqrt{\frac{\lambda/v}{D}} = \sqrt{\frac{v\lambda}{DN^2}} \quad (26)$$

where  $t_0$  is given by  $\lambda/v$ , and  $v_{DLD}$  is the lateral velocity of a particle due to interactions with the DLD array.

One often overlooked parameter to achieve high-throughput sorting of particles is the sample concentration. The effect has been noticed [8], and to some extent evaluated numerically [68] but never thoroughly investigated experimentally. To address this we in Paper V quantify the effect on sorting at different particle concentrations. If the volumetric flow rate is set, then the throughput would be proportional to the particle concentration in the sample. Samples in DLD are often diluted in order to avoid particle-particle interactions acting to skew separation and further, particle-post interaction which act to clog the device. One effect that may play a role is the hydrodynamic effect, wherein smaller particles are able to reside closer to the wall. As a consequence, they on average flow slower than the large particles. At high particle concentration, an effect which we have observed is that the posts get decorated with small particles, which forces the larger particles to the centre of the gap and consequently they on average displace more. Stochastic effects at high concentration, such as the particle-particle interactions increase the probability that a normally displacing particle swap flow lanes and goes into zigzag mode or that a particle which normally is in zigzag mode swap lanes and gets displaced. If these events occur at the same rate, the effect of the particle normally in displacement mode would be more significant than for the particle in zigzag mode. A particle failing to zigzag in a row where it was supposed to have consequently been shifted to the neighbouring streamline, an error of  $\sim G/N$ . At the same time, a particle failing to displace in a row will have shifted  $\lambda$  from its intended position. For soft particles, depending on the flow conditions and device geometry the Fåhræus effect might play a role as this will act to focus soft particles to the areas of highest flow velocity.

From what has been discussed above, it is apparent that there exist numerous parameters which influence the behaviour of particles in a DLD device. Theoretical predictions for critical size and the particle behaviour have been shown, but these can mainly be applied to ideal cases. An increased knowledge is required in order to improve the sorting abilities of DLD.

In Paper I we investigate the effect on particle shapes and in Paper II we further develop this method in combination with initial studies relating the separation efficiency of soft particles to the flow rates. In Paper III we show how sorting schemes can be developed which probe specific properties of soft particles, which is further extended with the dynamic properties of the RBCs in Paper IV. This ability, to sort according to certain particle properties of interest in the sample is decided already at the device design stage, making it crucial to the results of a measurement.





# 4. Device design and fabrication

Particle sorting in DLD relies almost exclusively on the device geometry, as it is a passive separation method. Consequently, the separation is in general fixed and cannot be tuned and optimized during measurements. Exceptions exist such as in Paper II where we show that separation is affected by tuning the flow rates leading to variations in the shear stresses asserted on deformable particles, and Paper III where the viscosity of the medium can be modified in order to change the dynamic properties of RBCs. Although the device geometry can be modified post-fabrication in order to change the sorting in DLD to some degree [58], the overall performance of the device is determined during device designing, making it the most important step for the end results of an experiment. Several factors play a role when deciding on the design of the device including the size range of particles, the required purity of the sorted fractions, the fraction of particles of interest that needs to be collected, the throughput of the device and the simplicity of operation.

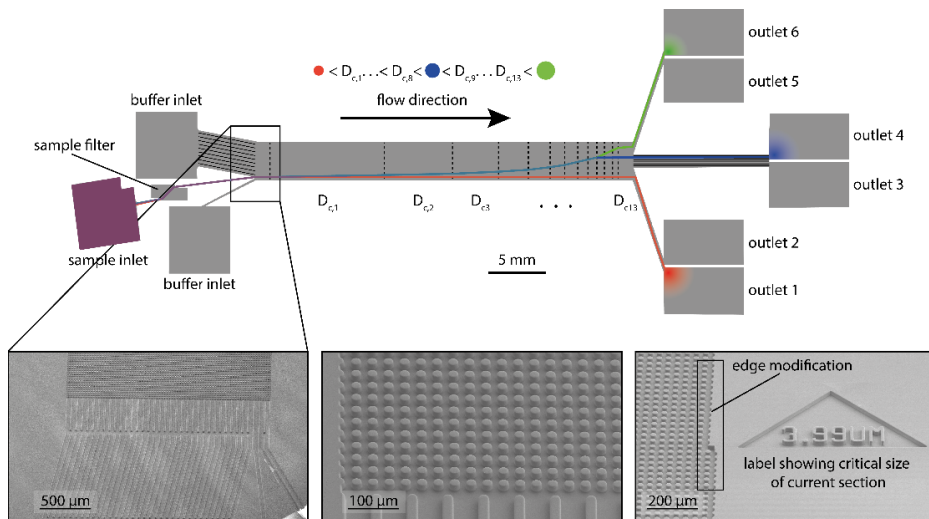


**Figure 12**  
The device that was used in Paper I, III and IV. This device has 13 sections in series of increasing critical diameter. Each section displaces the particles  $5\lambda = \sim 160 \mu\text{m}$ . At the end of the DLD array the particles can be extracted from any of the six outlets, depending on their size. A sample filter is used to remove particles which could potentially clog the device.

## 4.1. Single or multiple sections

An initial distinction can be made between devices consisting of single or multiple sections, *i.e.* one critical diameter or multiple critical diameters in series. Figure 13a-b. If the device consists of a single section the result is a bimodal separation where the position of particles with a size above the critical diameter is laterally shifted at an angle with respect to the flow. The remaining particles below the critical diameter follow the fluid and have an outlet distribution corresponding to its inlet distribution plus any stochastic effects such as diffusion acting to disperse the particles. An alternative to the single-section device is the multiple-section device consisting of multiple sections of different critical diameters. Having multiple sections allows for the sorting of a sample into additional bins, which can provide a more thorough description of the particle distribution. A device consisting of  $n$  sections can sort the sample in up to  $n+1$  bins at the outlet.

There are multiple ways of achieving different sections. As discussed in Section 3, the critical diameter is mainly seen as dependent on the gap,  $G$ , and the period,  $N$ . These two parameters could be varied along the device to achieve sorting in multiple steps. The most common approach is to alter the period, since decreasing the gap in the device could potentially lead to clogging. With the period being strongly connected to the angle at which particles are sorted, the sections with a low critical diameter often occupy a major part of the device if all sections are to laterally displace particles the same amount, as can be seen in Figure 13b and discussed in later sections of this chapter.

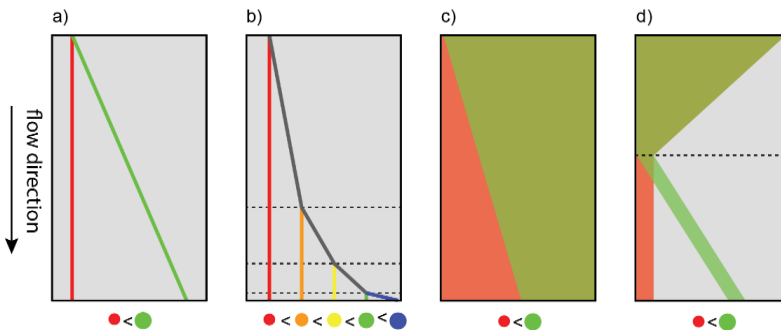


**Figure 13**

General device designs. Different strategies are used depending on the overall goal of the separation. (a) A DLD device consisting of a single inlet gives rise to a bimodal separation. (b) By instead designing the DLD device to consist of multiple sections, the sample at the outlet can be sorted into multiple bins. (c) In devices consisting of only one single inlet and one section, larger particles can be enriched relative to a background of smaller particles. (d) To enable a high level of purification in a single-inlet device we developed a device, presented in Paper II, which initially focuses all cells along the edge of the device followed by separation of the particles of interest.

Sections can be defined in other ways than by their critical diameter. As we have shown in Paper I-IV height plays a major role in determining the particle behaviour in the device. Also the effect of varying the flow rate by varying the total cross sectional area (width or height) is investigated in Paper II-III showing a strong contribution to the behaviour of soft particles. Consequently, both these parameters can be altered between sections in order to achieve a separation into multiple subpopulations.

## 4.2. Single or multiple inlets

An important aspect of the device performance is how particles enter the device, as this sets the starting condition for separation. Most commonly devices consists of multiple inlets where the particles are injected approximately at the centre with sheath fluid on each side, which ensures two things.

Firstly, the stream of particles can be well-focused. This is important as the inlet distribution is reflected in the outlet distribution, meaning that a well-focused inlet stream gives rise to a higher resolution of the separation since there will be less overlap, given the same device length. As a result, this device design is often referred to as an analytical DLD.

Secondly, the sheath fluid ensures that the particles are not close to the edges of the devices, which due to boundary effects, can lead to broadening of the sample stream. As discussed in Chapter 3, by making careful adjustments to the geometry, the device can be designed to ensure symmetric flow also at the edges of the device.

Another type of device consists of only one single inlet. With this design the initial particle distribution is uniform across the device. While particles can still be laterally displaced, the result at the outlet is an enrichment of those particles with a larger effective size. Particles smaller than the critical size are not affected by the post array and their distribution at the outlet is identical to the inlet distribution. The volumetric enrichment of the larger particles is only related to the widths of the streams given by

$$E_v = \frac{w_i}{w_o} \tag{26}$$

with  $w_i$  and  $w_o$  being the inlet and outlet widths in the distribution of the displaced larger particles respectively. At the same time the number enrichment is given by

$$E_n = \frac{\frac{c_1}{c_1 + \frac{w_o}{w_i} c_2}}{\frac{c_1}{c_1 + c_2}} = \frac{c_1 + c_2}{c_1 + \frac{w_o}{w_i} c_2} \quad (27)$$

with  $c_1$  and  $c_2$  being the initial concentrations of the larger and smaller particles respectively. The numerator reflects the number fraction of the large particles at the outlet and the denominator the same number at the inlet. For situations where  $c_2 \gg c_1$  Eq. 27 can be approximated as the former  $w_i/w_o$ . This is true for the sorting of trypanosomes from blood, where extremely focused particles in the outlet are necessary in order to achieve high enrichment.

The issues outlined above were addressed in Paper II where we developed a new type of sorting scheme combining the simplicity of single-inlet devices in terms of device preparations and fluid actuation, with the purity of a multiple inlet design, like that illustrated in Figure 13d. By using a device design where the critical diameter is below the effective size of all particles in the sample, the particles are laterally displaced and focused along the edge of the device. This opens up a clear particle-free stream in the centre into which particles of interest in the subsequent sections can be displaced.

### 4.3. Connecting channels

In a complete device, inlets and outlets need to be connected with the DLD arrays. Due to the sizes of the inlet and outlet connectors, there exists a minimum distance that the inlet and outlet areas can be positioned from each other, which depends on the fabrication method as discussed later in this chapter, and typically for the devices presented in this thesis, fluidic reservoirs are positioned on-chip with a spacing of 5 mm. Channels are laid out to connect the inlet and outlets with the DLD array, allowing for liquid to enter and exit the device. In order to ensure that the fluid carries the particles into their designated outlets at the end of the device the resistances of the outlet channels need to be chosen carefully. This, in general, also holds true for the inlet of the device, although tuning of the inlet pressures can be used to optimize the flow. The device used in Paper II is shown in Figure 14, detailing the channels connecting different sections of the device.

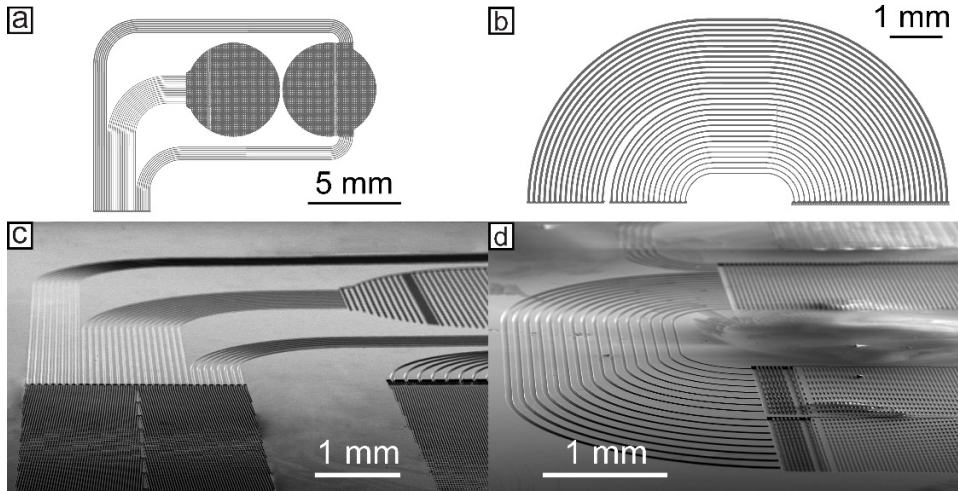


**Figure 14**

Channels of equal hydraulic resistance used to maintain the symmetric flow and the relative positions of particles so that they are sorted into their designated outlet. (a) and (b) show the CAD designs of the corresponding SEM micrographs in (c) and (d). These are sections of the device used in Paper II.

By modifying the channels so that the hydraulic resistance, Eq. 8 p. 12, between the array and the reservoir is inverse proportional to the fraction of array width occupied by that reservoir,  $R_h \propto w^{-1}$ , constant relative lateral positions of the particles is ensured, with no diverging or converging flows at the beginning or end of the DLD array. For example the device used in Paper I, Figure 12, consists of six outlets where the flow at the end of the DLD array is split evenly into these six reservoirs and so the hydraulic resistances between the array and each of these outlets is designed to be equal. With channels of different lengths, the widths need to be adjusted such that the correct resistances can be achieved.

The same device consists of three inlets with a total width of  $w = 81\lambda$ . The large buffer inlet accommodates  $w_1 = 74.5\lambda$ , the small buffer inlet  $w_2 = 4.5\lambda$  and the sample inlet  $w_3 = 2\lambda$ . By having inlet channels with hydraulic resistances given by  $R_{h,1} = k/74.5$ ,  $R_{h,2} = k/4.5$  and  $R_{h,3} = k/2$  respectively, where  $k$  is a constant there is no need for any adjustment of the relative pressures in order to achieve a symmetric and ordered flow. The same method was used to connect different DLD sections in Paper II. Due to the length of the device, and with an overall size limitation of a regular glass slide, curved channels which connected subsequent sections were used to obtain a meandering DLD device which could fit within this area. At each end of a section multiple channels of equal hydraulic resistance were used to preserve the relative position of the particles while transporting them to the next section.

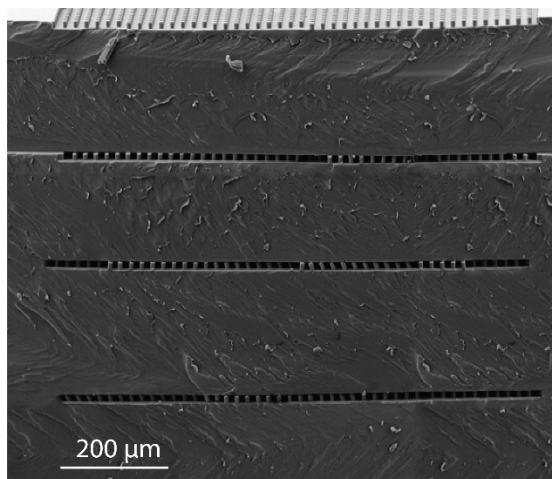


**Figure 15**

SEM micrograph showing a cross-section of multiple identical DLD devices, each with a thickness of  $\sim 200\ \mu\text{m}$ , bonded on top of each other in order to create a high throughput device by parallelization. Stacking of devices allows for increasing the throughput while still maintaining a specific aspect ratio or device depth. The device is identical to what was used in Paper II. Sample is fed through the different layers by making an inlet hole through all layers, and outlets where made in a similar fashion. Precise alignment was achieved by bonding the films under microscope.

## 4.4. Throughput

Depending on the sample to be sorted, throughput might be a concern. This is certainly true for rare-cell sorting where the particles of interest only exist in miniscule amounts. Although microfluidics is a very powerful tool, as shown in previous chapters, the small length scales can lead to limited flow rates. Several strategies can however be used to increase the throughput in DLD devices. For example parallelization, Figure 15, or to fabricate deep devices. The depth at which a device can be fabricated is restricted ultimately by the aspect ratios that can be achieved with the selected fabrication method. Furthermore, flow rates can be increased as long as reasonable Reynolds numbers are maintained [67] and the device integrity is not at risk (*e.g.* by delamination or pressure induced inflation [66]). Deformable particles are also affected by the increased shear stresses at elevated flow rates, as shown in Papers II and III. At a certain point, the increasing shear stresses exerted on the particles are expected to affect cell viability. For RBCs, the reported threshold value for the onset of lysis is  $\dot{\gamma} = 1500\ \text{dyne/cm}^2$  [69, 70]. In Paper III, where the deformability of RBCs was studied, we approximated the maximum shear stresses exerted on the cells (at the edge of the posts), to  $\sim 60\ \text{dyne/cm}^2$ , highlighting the opportunity of

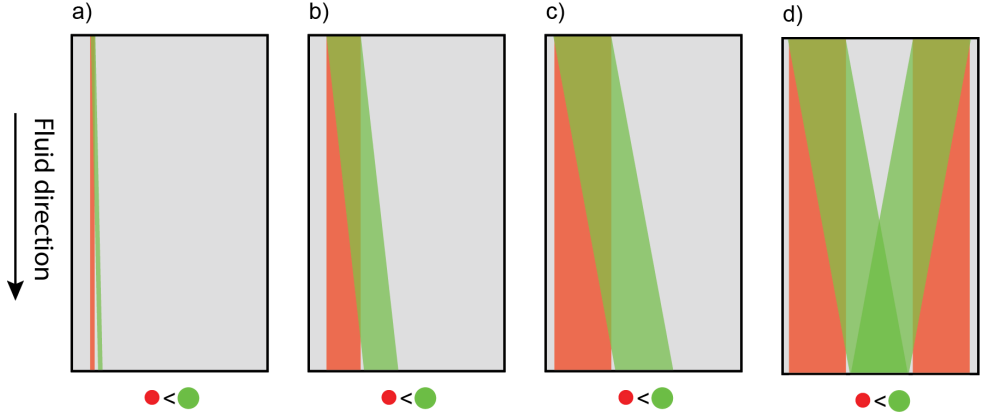


**Figure 16**  
 Relationship between inlet width and the device throughput. (a)-(c) A larger displacement angle enables a wider inlet given a certain device length and consequently a higher throughput. (d) By mirroring the device the throughput can be increased by a factor of 2, as we show in Paper II.

increasing throughput further without affecting the cell viability. Further, the shear stresses exerted on the particles can be limited to a degree by careful consideration of the post shape, as this will have an effect on the flow profile.<sup>f</sup>

One important factor, which can be affected during the design stage of the device is the width of the inlet, as this parameter is proportional to the throughput. However, a wider inlet also requires a longer device in order to sort out the particles of interest given that the particles are sorted at an angle with respect to the fluid flow. By increasing the sorting angle, the throughput can be increased, Figure 16.

Given the empirical formula for the critical size, equation 20, we can deduce the maximum inlet width,  $w_{max}$ , for a certain device length,  $l$

$$\frac{l}{w_{max}} = N \rightarrow w_{max} \approx \frac{l}{2} \left( \frac{G}{D_c} \right)^{-2} \quad (28)$$

showing, as expected, the throughput to be proportional to the device length and additionally approximately inverse square to the gap-to-critical diameter ratio. It is apparent that decreasing this ratio can lead to a significant increase in the throughput. However, a larger critical diameter (and consequently larger particles) in relation to the gap would increase the risks of device clogging depending on the size distribution of the sample. At the same time particles that are large in relation to the gap size are expected to cause increased disturbances to the flow field, and may as a result affect

the deterministic nature of the device. The device length can be increased in order to enable wider inlets and consequently a higher throughput in terms of particles sorted per unit time. However, it should be noted that the time for a particle to travel through a longer device also increases, a fact that can be important to consider for time dependent effects such as cell viability or changes in gene expression. As a result, depending on the sample volume, the flow rates, and the sorting angle, an optimum inlet width in relation to device length might exist. For the devices used in this thesis, we have conformed to the size of a common glass slide. This allows us to use cheap and readily available glass slides as support for the device while the devices fit to standard microscope stages. To achieve higher throughput in a final optimized device by scaling up the sizes the same fabrication methods could be used. Additionally, methods relying on thermoplastics such as hot embossing, roller imprinting or injection moulding could be used. These fabrication methods, would in addition to facilitating higher throughputs allow for larger volume productions [71].

Increasing the particle concentration would be a possibility to achieve higher throughput. In Paper I the sorting results for whole blood were similar to blood diluted ten times. However, due to a very small sample inlet the sample was effectively diluted in the device by the buffer. In relation to Paper II, we investigated the effect of whole blood in this single inlet device and could conclude that the focusing of particles to the device edge, in section 2, decreases at elevated RBC concentrations. With whole blood having a concentration of 45% (v/v), it could theoretically be focused into a stream equal to 45% of its initial width. By diluting the sample, a narrower stream can be achieved which in turn would increase the specificity of the sorting in this device. However, this would at the same time be at a cost of lowering the throughput. Consequently, there is a relationship between sample concentration and device performance, as investigated in Paper V.

Other approaches, which also have been outlined in Chapter 3, include alterations to the flow profile. For the purpose of increasing the throughput this would be done so that a higher migration angle can be realized at a specific gap-to-critical diameter ratio. This has been shown by the use of non-Newtonian fluids [59], specific post shapes [72, 73] and the modification of electrostatic interactions between particles and posts [60]. In Paper II we show how mirroring of a DLD device can be achieved, Figure 16d, doubling the throughput for a given device length.

Several DLD devices have been used in the work related to this thesis, as outlined in Table 3. The analytical device with 13 multiple sections used in Paper I, III and IV has proven to be highly versatile. With multiple sections,



**Table 3. DLD devices used in the work presented in this thesis**

	Critical diameter $D_c$ [ $\mu\text{m}$ ]	Row shift $\Delta\lambda_n$ [ $\mu\text{m}$ ]	post diameter $P$ [ $\mu\text{m}$ ]	Gap $G$ [ $\mu\text{m}$ ]	Period $N_n$
Paper I,III,IV	3.0-9.0	0.8-8.8	20	12	40-3.6
Paper II					
Array 1	7.1	2	20	22	21
Array 2	3.5	1.2	20	12	26.67*
Array 3	3.5	1.2	20	12	26.67*
Paper V	6.1	4	20	16	9
Paper VI	2.86	0.8	20	12	40
Paper VII**	1.6	1.0	24	6.0	30

\* For the array in section 2-3 of Paper II, the period is cyclic starting with  $N = 26$  for one set of rows and then increases to  $N = 27$  for the remaining two sets of rows.

\*\* More detail on this device is given in Figure 43.

each with relatively small critical diameter increments (0.5  $\mu\text{m}$ ), the resulting outlet distribution is closely linked to the particles' effective sizes, *i.e.* the size resolution of the separation is high. The other devices used for the work in this thesis have been designed with a specific sorting application in mind. For example, in order to achieve higher throughput the DLD arrays consist of a single section. On overview of all devices used is given in Appendix 2.

## 4.5. Device fabrication

Fabrication of a DLD device can be done in many different ways depending on requirements such as rigidity to withstand high pressures, maximum aspect ratio, fabrication time and cost. The devices within this thesis all have a similar fabrication method with only smaller variations. The Papers contain the individual specific details but in general device were fabricated by replica moulding using PDMS, a.k.a. soft lithography, Figure 17. This is a widely popular method due to its relative rapid turn-around time in combination with a low cost [74-76]. Further advantages of using PDMS for the work within this thesis include its high gas permeability, which was used in Paper VII to allow for the evaporation of solvent content of droplets in order to force the formation of microgel clusters. Other important properties of PDMS include its good thermal stability, the optical transparency and having a wide range of surface modifications available for minimizing sticking of particles and controlling the surface wettability. While PDMS is relatively chemically stable, several solvents can permeate the polymer and cause it to swell [77] which affects the sorting properties of a DLD. Many

alternatives do however exist for fabricating microfluidic devices, both in terms of the material and in the fabrication process as further discussed in several reviews [78-85]. An interesting method, although most likely suited for device prototyping, is 3D-printing, which in addition to going almost directly from drawing board to device offers the ability for true three-dimensional features [86-88].

As outlined in table 4, the most time-consuming steps are typically the device designing which often include CFD simulations using COMSOL Multiphysics 5.3a (COMSOL Inc.) to ensure device functionality, and the device fabrication. Following these two steps a replica moulding master (or multiple) have been realized and they can thereafter be used to fabricate multiple devices relatively fast. The devices used in this thesis were drawn in Tanner L-Edit 2010-2016 (Mentor Graphics). Photomasks were either produced in-house using a direct laser writer (DWL-66 Heidelberg Instruments) or by outsourcing the fabrication (Delta Mask B.V.). The negative photoresist SU8 (2005-2100, MicroChem Corp.) has been used and applied on 2-4 inch wafers using a spincoater. Subsequent soft-baking was carried out on a hotplate at 65 °C followed by 95 °C. UV exposure (365 nm @ 20mW/cm<sup>2</sup>) was carried out using an MJB3 (Karl Süss) in vacuum mode. Post exposure baking was done mainly by temperature ramping (10 °C/min) from 65 °C to 95 °C and back down again.

**Table 4. Device fabrication**

<b>Fabrication step</b>	<b>Time</b>	<b>Fabrication step</b>	<b>Time</b>
<b>1. Device design</b>	~2 days	<b>3. Soft lithography</b>	~5 h
calculations/simulations	~1 days	Silanization of master	~3 h
drawing single/multi-layered device	~1 days	PDMS Sylgard 184 mix/degas/apply	~1 h
<b>2. Photolithography</b>	~2 days	Cure at 80°C	~1 h
Expose, develop and etch photomask	~1 day	Peel of PDMS and cut out device	~5 min
Pre-treat wafer	~1 h	<b>4. Device finalization</b>	
Spin coat SU8	~5 min	Clean surfaces prior to bonding	~5 min
Soft-bake	~5 min	O <sub>2</sub> Plasma etch	~30 s
Exposure (365 nm)	~10 s	Surface treatment	~5 min
Post-exposure bake	~10 min	Attach inlet and outlet reservoirs	~1 h
Develop	~5 min	<b>5. Pre-treat final device</b>	30 min
Hard bake	~1 h		
Characterization (profilometer/SEM)	~1 h	<b>Total time going from idea to measurement</b>	~5 days

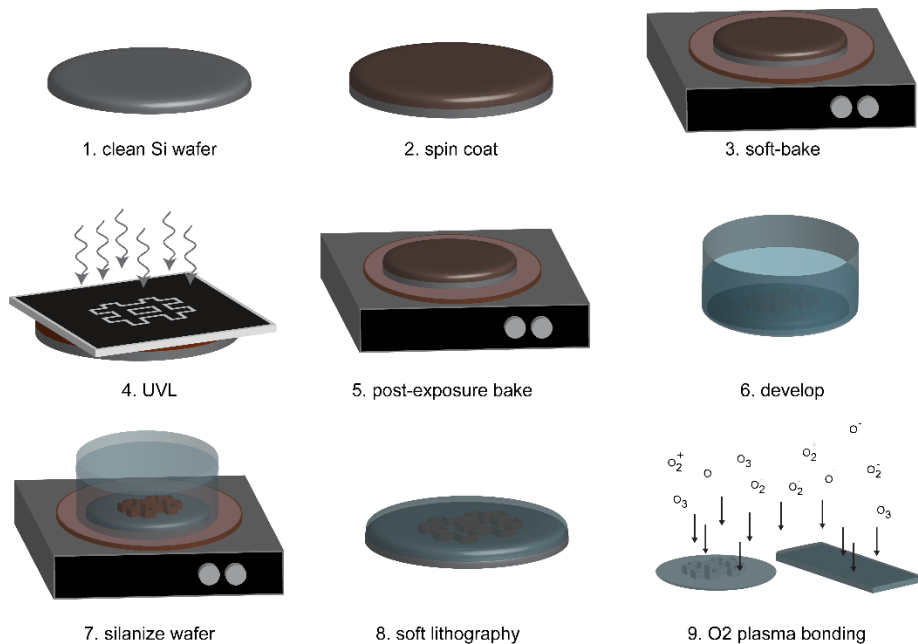


**Figure 17**

Typical fabrication steps in UVL and soft lithography. 1) A silicon wafer, preferably Si [111] is cleaned in acetone and IPA, dried with filtered nitrogen gas and heated on hotplate for ~15 min at 100 °C. 2) After cooling down SU8 at desired viscosity is applied at specific rotation speed by spin coater. 3) sample is soft baked to evaporate excess solvent. 4) UVL performed at 365 nm for a time corresponding with a dose suitable for the thickness and resist. 5) PEB to allow for polymerization of resist. 6) develop to get rid of non polymerized areas 7) silanize wafer using PFOTS. 8) carry out soft lithography using PDMS. 9) bond to a PDMS-coated glass slide to seal the device.

Development was carried out under mild stirring in mr-Dev 600. Following drying in purified nitrogen gas, the wafers were inspected using profilometer and optical microscope. Hard bake was done in an oven by ramping up the temperature to 200 °C and waiting 1 h for the wafer to cool down. The surface of the wafers were treated in a dehumidified glove-box using 1H,1H,2H,2H-Perfluorooctyl-trichlorosilane (PFOTS, Aldrich) to allow for lift-off during soft lithography. This is the general procedure of photolithography. Times, exposure doses, and temperatures have been individually optimized for the devices used in this thesis to achieve vertical walls, desired thicknesses and correct feature sizes. Detailed descriptions of the processes used for specific devices are available in their respective publications.

Soft lithography was carried out using Sylgard 184, with monomer and curing agent mixed at a 10:1 ratio. Following thorough mixing, bubbles are removed by degassing in a desiccator in vacuum for a minimum of 30 minutes. After applying the polymer to the silicon master, it is heat-cure in

an oven at 85 °C for 1 h. In order to fabricate a sealed device, the cured PDMS slab was bonded following treatment in an oxygen plasma etcher (Plasmatic Systems) together with either a normal glass slide or a PDMS coated glass slide. Following this, devices were surface treated depending on their application. For the generation of W/O droplets, Paper VII, device surfaces are required to be hydrophobic and these devices were therefore treated with PFOTS similar to the silicon master [89]. For DLD devices used for sorting of the colloidal clusters in the same paper 5% v/v PEG-silane in anhydrous acetone was flushed immediately following plasma bonding for 10 minutes [90]. The devices used in the other papers were instead treated by flushing 0.1% w/v PLL-g-PEG in milliQ water solution to minimize sticking [91, 92].

The sorting efficiency for the work presented within this thesis was mainly characterized by analysing the individual particle positions at the outlets. While it can be time-consuming to determine the position of a high number of particles, this gives the most accurate reading of the DLD performance and it does not require the fluorescence staining of cells, which might affect their characteristics and consequently their behaviour in the DLD. To correctly determine the position of a high number of particles, a particle tracker, built on an available core [93], was developed together with a GUI using MATLAB R2014b, Figure 18. This tracker was used in Paper I, II and III. The tracker is able to go through several files simultaneously in order to produce plots over the relative outlet position of particles. Particles are identified by removing the static background followed by carrying out a FFT band pass to sort out noise. The identified particle positions are linked between subsequent frames based on their separation distance in relation to the expected flow velocity. The lateral displacement of particles with respect to the inlet is measured at a certain position and plotted. The MATLAB code for the tracker together with the GUI is available in Appendix 1.

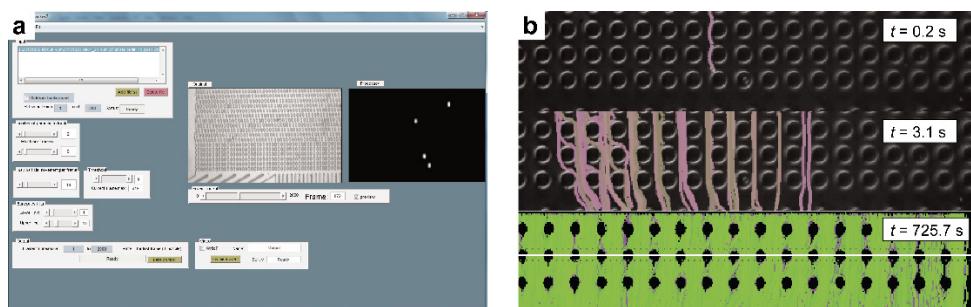


**Figure 18**  
Particle tracker enabling the correct determination of the outlet positions of  $\sim 10\,000$ s of particles per measurement. Based on available code, the software was developed together with a GUI for simple and accurate detection of the lateral position of a large number of particles. Further description in Appendix 1, together with the code.

# 5. Blood

Blood is a complex fluid that is responsible for several, mostly vital, tasks in the human body. It supplies all cells in the human body with essential nutrients and oxygen while also taking care of their waste products, *e.g.* carbon dioxide and lactic acid. Further, blood is an important part of the homeostasis, it protects the body from foreign compounds using antibodies and white blood cells (WBC) and at the same time it has its own self-repairing mechanism, which in the first stage is carried out by platelets and fibrin. Due to the vast number of functions of blood, it contains a wealth of information about the physiological state of an individual making it an ideal target in clinical diagnosis. In addition, the extraction of the required amounts of blood for microfluidic diagnostics can easily be carried out by simple finger pricking. This makes the sample to be analysed being readily available and consequently portable diagnostic device targeting blood are well-suited in a point-of-care setting.

For this thesis, the understanding of blood has been an important part in Paper I and II for the separation of blood cells and parasites. Further on, blood is in focus in Paper III and IV where their morphology, deformability and dynamic properties are studied in order to elucidate a connection to their behaviour in DLD devices. Finally, in Paper V, the sorting of particles from a background of RBCs was investigated at varying hematocrit (Ht) and pressure aimed at achieving high throughput blood separations. This chapter will mainly focus on the properties of RBCs and methods by which these can be probed.

**Table 5. Content of blood [94]**

Cell type	amount ( $\mu\text{L}^{-1}$ )	size ( $\mu\text{m}$ )	shape	number fraction
<b>RBC</b>	$5.1 \cdot 10^6$	7.2 – 8.4 by 2.5	biconcave	0.94
<b>WBC</b>	7 000		~spherical	$1.3 \cdot 10^{-3}$
Lymphocyte	2 185	6-8		$4.0 \cdot 10^{-5}$
Neutrophil	4 150	9-16		$7.6 \cdot 10^{-5}$
Eosinophil	165	12-17		$3.0 \cdot 10^{-4}$
Basophil	44	10-14		$8.1 \cdot 10^{-5}$
Monocyte	456	12-20		$8.4 \cdot 10^{-3}$
<b>Platelets</b>	350 000	2-3	biconvex	$6.4 \cdot 10^{-2}$

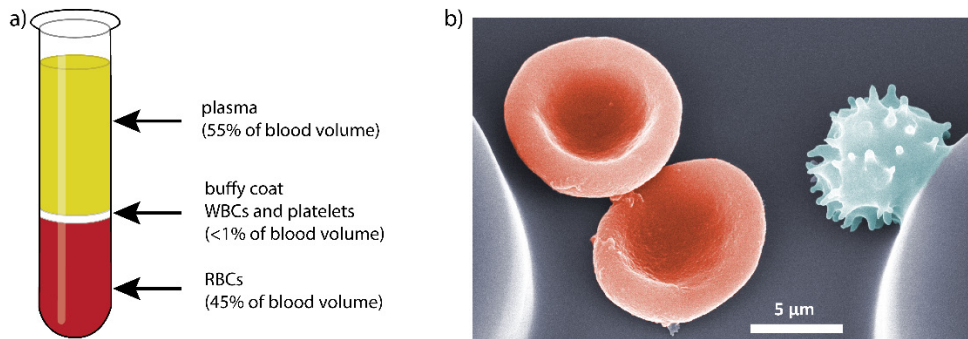


**Figure 19**

Blood constituents. (a) Typical tube showing the result of separation in a centrifuge, where the blood cells are separated according to the density. The RBCs, found at the bottom, are the most abundant cells and account for 45% of the total volume. The buffy coat layer is just above the RBC layer and consists of WBCs and platelets. The total volume is less than 1%, making the RBCs account for ~94% of the total number of cells. The top layer is the plasma, a yellowish liquid made up of mainly water (~95%). (b) Scanning electron micrograph showing fixated RBCs next to a WBC inside a DLD device. Image kindly provided by Jason Beech.

## 5.1. Composition

Blood cells are a major component of the human body. Estimations are that the hematopoietic lineage accounts for ~90% of the total number of cells in the human body (with only the RBCs accounting for ~84%) [95]. At the same time, due to their relatively small size, in terms of mass the numbers are more moderate with RBCs making up 3-4% of the total body mass [96].

A common way to separate the blood components is through centrifugation, which separates the constituents based on their densities, Figure 19a. The major part of blood, ~55% v/v consists of plasma of which ~95% v/v is water. It contains dissolved proteins, *e.g.* serum albumins, globulins and fibrinogen, and hormones, electrolytes and nutrients. Below the plasma layer is the buffy coat layer, named after its colour. This layer consists of WBC and the platelets and makes up less than 1% v/v of the total blood volume. The remaining part of the blood consists of the RBCs which normally make up around 45% v/v of the blood, depending on factors such as age, sex, environment, and health status.

## 5.2. Red blood cells

Mature RBCs are distinct from other cells in the human body in that they have no nucleus. Their sole purpose is to deliver oxygen to tissues and carbon dioxide back to the lungs. While also dissolved in the cytosol the main carrier is the haemoglobin hetero tetramer where each subunit contains a central ( $\text{Fe}^{2+}$  coordinating) *heme* group capable of associating one molecule of oxygen, and consequently, the entire haemoglobin complex can carry four molecules of oxygen in total.

In their resting state RBCs display a typical biconcave shape with a diameter of 6-8  $\mu\text{m}$  and a thickness of 2-3  $\mu\text{m}$  [94], Figure 20. A shape which is a factor in its ability to undergo high deformations in the small capillaries of the circulatory system and further to maximize the oxygen and carbon dioxide exchange in the lungs and tissues. A contributing factor to its shape has been shown to be the lower membrane bending energy [97].

The life span of RBCs starts when they are released into the blood stream as reticulocytes, a slightly larger cell which contains ribosomal RNA and organelles. After  $\sim 1$  day they are matured into normal biconcave RBCs and circulate the body for around 120 days before they are recycled in the liver and spleen due to a decrease in their elasticity [98].

RBCs are considered a typical soft biomaterial, exhibiting viscoelasticity, with both elastic energy-storing properties as well as viscous energy-dissipating characteristics. They are the most deformable cell in the human body, a property which is attributed to several factors.

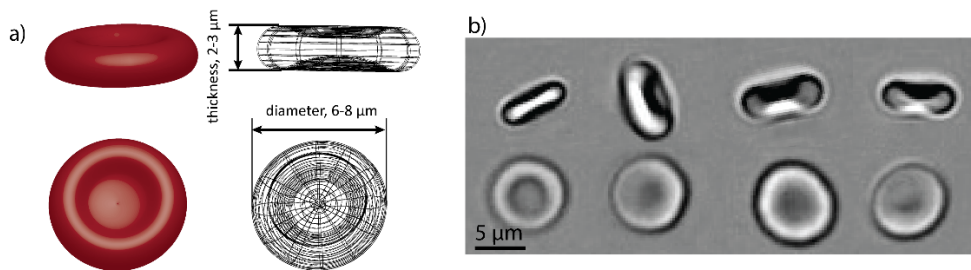


**Figure 20**  
The biconcave shape of discocytic RBCs. (a) Illustrations and (b) mosaic image of optical micrographs showing RBCs from the side and top. Although under physiological conditions, slight variations in size and morphology can be noted. Individual factors, in addition to health status, are known to affect the size but a common accepted average is  $\sim 7.6$   $\mu\text{m}$  in diameter and  $\sim 2.3$   $\mu\text{m}$  in width [94]. This is reflected in the mean corpuscular volume and red cell distribution width, two common parameters which are quantified during a normal complete blood count.

Firstly, as mentioned, their specific morphology is connected to having a significant excess surface area. While their mean corpuscular volume is  $\sim 90 \mu\text{m}^3$  [94], their mean surface area is  $\sim 135 \mu\text{m}^2$ , significantly larger than the area of a sphere ( $97 \mu\text{m}^2$ ) encapsulating the same volume.

Secondly, the cytoplasmic viscosity, which in the absence of a nucleus and most organelles, is mainly dependent on the internal Hb level. It has been measured by dynamical membrane fluctuation studies to be in the range 5-6 mPa·s at physiological conditions, which is five times the viscosity of plasma [99]. While blood is a non-Newtonian fluid, with shear-thinning properties, the cytoplasm of the RBC is considered to be independent of shear strain or shear stress [68]. Further, the reduced deformability of aged cells is correlated with an increase in hemoglobin content [100].

Thirdly, the behaviour of RBCs is affected by the viscoelastic properties of its membrane-cortex structure consisting of an outer carbohydrate-rich layer, a tightly packed phospholipid bilayer with a thickness of 4-5 nm embedded with transmembrane proteins and a membrane skeleton (MS) made up of a dense spectrin network anchored to the membrane proteins [101].

In characterization of the viscoelastic properties of the RBCs membrane cortex it is usually treated as a continuum due to being only a few molecules thick. The elastic properties are characterized by the area expansion, shear and bending moduli, while its viscous properties are related to the membrane viscosity [101, 102].

The RBCs are known to exist in other shapes than the normal biconcave discocytes due to a wide range of pathological conditions as further outlined in several reviews and books [103-105]. The precise structural and mechanical basis for these shapes, as well as their underlying reason to deviate from their normal discocytic shape remains to be answered [106]. RBCs are often used as a model for cell membrane studies due to, in relation to other cells, being a simple system without a nucleus, organelles or large cytoskeletal structures.

### 5.3. Methods to examine RBCs

As mentioned, the wealth of available information in combination with ease of access makes measurements on blood and RBCs a common practise for medical diagnosis. An initial step in diagnosis is often to perform a complete blood count (CBC), mainly carried out by Coulter counters relying on the



impedance change as cells pass a constriction [107]. They allow for the classification of cells with respect to multiple variables including the hematocrit (the packed volume of RBC), the RBC distribution width (variation in the cellular volume of the RBC) and the mean corpuscular volume (the average volume of RBCs) [108]. While providing a simple means of measuring these basic characteristics of blood, it does not provide the ability to probe single cells in terms of morphology and deformability, factors which are known clinical indicators and have been in focus for the past decades to reveal the connection between cell shape, the cell membrane cortex and their overall function.

The morphology of cells has traditionally been determined by microscopic examination of blood smears. A time consuming method has been made simpler with the advent of image cytometers [109]. This has been implemented in many clinical settings to provide additional information in relation to the traditional CBC. However, they are unable to catch anisotropy in cell morphology, and it is not possible to sort cells for further analysis using this method [110]. Flow cytometry is a common practice used for cell sorting. However, the sorting mainly relies on fluorescent labelling, as it is not able to give a correct representation of the cell morphology.

Over the past decades several different methods have been developed in order to measure the deformability of RBCs. Conventional methods such as the rotational viscometer [111], the ektacytometer [112] or erythrocyte membrane filtration (EMF) [113-115] have to some degree been proven useful in a clinical setting but these approaches are limited to bulk averaging.

Methods for single-cell measurements include micropipette aspiration [116], atomic force microscopy [117], flickering analysis [118] and optical tweezers [119]. These have been used extensively to characterize RBCs and have given new insights into the biomechanical properties of RBCs but they have a low throughput making them of limited use in a clinical setting.

Several microfluidic approaches have been developed to probe the deformability of RBCs [120]. These mainly rely on studying how easily an RBC can squeeze through a constriction; its filterability. This is similar to EMF, however microfluidics offers the ability to perform single-cell analysis, and further, the constrictions can be fabricated to exact specifications. The RBCs are studied while they pass the constriction and the time or threshold pressure to allow for passage is recorded. While this method has been shown useful in a lab setting to the diagnosis of late ring stage malaria samples [121], the filterability is a parameter which is influenced by both the cell size and deformability.

Another microfluidic method, real-time deformability cytometry (RTDC) is based on image analysis as the particle passes through a channel where the shear stresses and the pressure gradient act to deform the cells without the cells being in contact with the walls. RTDC performs at moderate throughputs,  $\sim 100$  cells/s are probed without the risk of clogging [122]. It offers a simple approach to deformability studies, although it would be sensitive to deformation anisotropy and is not yet able to sort cells for further characterization. A few microfluidic approaches for sorting based on deformability have been shown. Recently Park *et al.* [123] showed a device consisting of microfluidic filters in series which were combined with ratcheting flow in order to achieve separation. This method was applied to the sorting of circulating tumour cells (CTC) from blood cells. It may also be of use for sorting different RBCs, but the separation would again be based on a combination of size and deformability. Bagnall *et al.* [124] showed a proof-of-principle device, with limited throughput, where RBC filterability was combined with a fluorescent detection of surface markers and a microchannel resonator to measure the cells buoyant mass. Another microfluidic approach to deformability-based sorting with higher throughput is to use deformability-induced lift forces, similar to the process of WBC margination in the human body [125]. This was recently used for malaria diagnosis in order to discriminate between ring-stage trophozoites and normal RBCs by their difference in stiffness during an infection [126]. The focusing positions of particles in a channel is in addition to being affected by their deformability also a consequence of their size, making it difficult to target the viscoelastic properties of RBCs specifically [126, 127].

In order to address the issues of the aforementioned techniques we explore how the RBC transit modes in a DLD are affected by their morphology, deformability and dynamic properties (Papers III and IV), in order to open up for sorting and characterization based on targeting these properties specifically as separate parameters. This was carried out by controlling their orientation through the tuning of channel depth in combination with the imposing of a range of shear stresses onto the RBCs. In Paper IV, the influence of dynamic modes on the sorting behaviour in DLD was investigated, a property which has been very little exploited for cell sorting.

This was carried out by altering the viscosity contrast (ratio between cytosolic viscosity and the plasma viscosity,  $C_i/C_o$ ) which is known to have a considerable effect to RBC dynamics [128]. In Paper III, separations were performed on samples consisting of RBCs, which had been chemically modified to induce clinically relevant shape changes, Figure 21, in order to demonstrate the ability of DLD to correctly capture their individual biophysical properties.

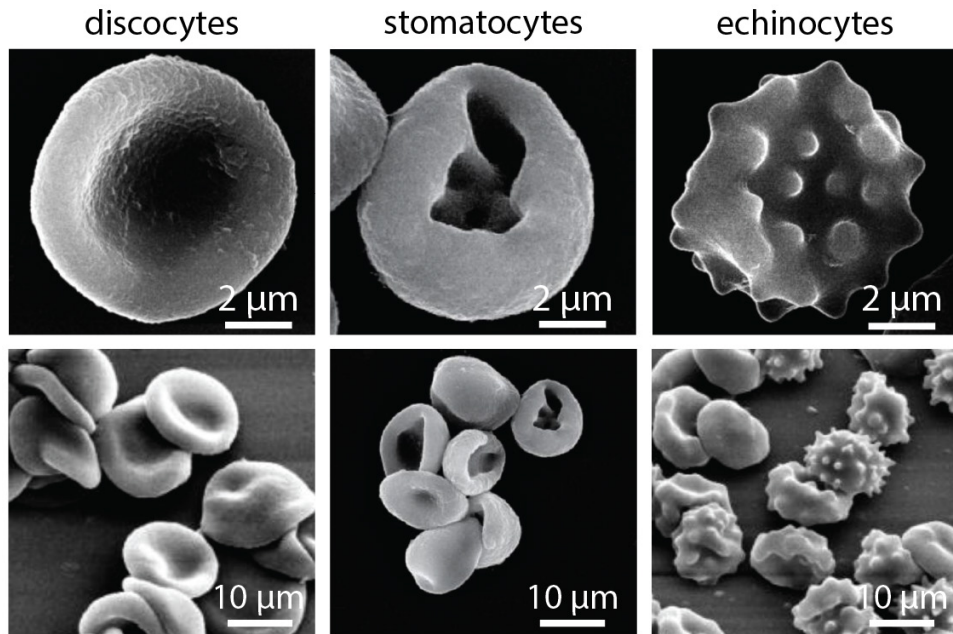


**Figure 21**

SEM micrographs showing RBCs of three separate shapes at two different magnifications. The discocytes are the normally occurring RBCs with a biconcave shape. The other two types are known to exist in various pathological conditions. Here, the stomatocytes have been chemically induced by the use of 580 ppm Triton™ X-100, which mainly intercalates into the inner leaflet of the cell membrane leading to concave membrane shapes. Echinocytes have been formed by using 16 mM sodium salicylate which mainly affects the outlet layer of the cell membrane by causing convex, spikes on the cell surface. Images acquired together with Jason Beech and Karl Adolfsson (unpublished work).

## 5.4. Bilayer-couple theory

An important factor contributing to shape changes in RBCs, and which was exploited in Paper III, is the relaxed area differences between the inner and outer leaflet of the cell membrane ( $\Delta A_o$ ), as first proposed 1974 by Sheetz and Singer [129] in the so called bilayer couple hypothesis. In fact, it has been shown that even a small change of 0.4 percentage points to the normal ratio ( $A_{inner} / A_{outer} \approx 0.98$ ) is sufficient to induce these shape changes, Figure 21.

Any process that either expands the outer leaflet area or decreases the inner leaflet area (increasing  $\Delta A_o$ ) acts to form convex structures on the cell surface in order to accommodate the extra area, leading to echinocytes. For the opposite situation, if the area of the inner leaflet of the membrane is increased or the area of the outer leaflet is decreased (increasing  $\Delta A_o$ ), concavities will be formed resulting in stomatocytes. If the area difference

between the leaflets continue to grow, the cells become more spherical and eventually they lyse.

The cell membrane has an asymmetry with an increased fraction of anionic lipids in the inner leaflet, while the outer leaflet is neutral. Consequently, the partitioning of amphiphilic molecules will be significantly different depending on their charge. In general, cationic compounds accumulate in the inner leaflet while anionic compound accumulate in the outer leaflet [98]. As a result, different chemicals can be used to induce specific shape changes to RBCs. In Paper III we used 580 ppm Triton™ X-100 in order to induce stomatocytes as it will mainly be incorporated into the inner leaflet [130]. In the same paper 16 mM sodium salicylate was used to induce echinocytes as it will mainly be incorporated into the outer leaflet [131]. This provides a simple means by which the shape can be controlled. Other methods by which the RBC shape can be controlled include changing buffer osmolarity [132] (leading to a change in RBC volume) or pH [133] (affecting the chemical properties). While leading to similar shapes, these methods would alter the cytosolic viscosity while the leaflet ratio is believed to be unchanged. It is however worth pointing out that although modifications of the ratio between the leaflets are capable of reproducing these pathological shapes present in the human body the shape changes are believed to be an interplay between this ratio and changes to the underlying membrane skeleton [134]. The resulting trajectories in the DLD due to these changes to cell morphologies and their dynamic properties were characterized in Paper III and IV, Figure 22.

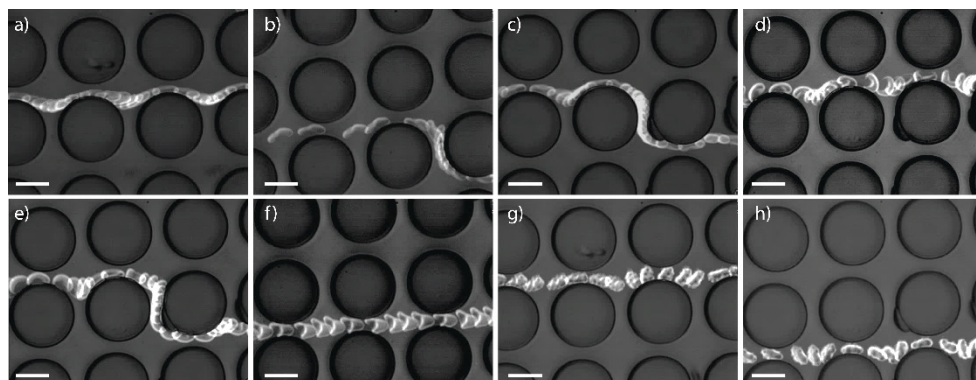


**Figure 22**

Stroboscopic micrographs of various shapes of RBCs in a DLD device under different applied shear rates. (a)-(c) show normal biconcave discocytes which are being displaced and zigzag. (d) show stomatocytes which are laterally displaced and (e) zigzag. (f) show parachute-shaped RBCs, which mainly are present at high shear rates. (g)-(h) show echinocytes flipping and being laterally displaced. These figures are shown to give the reader a sense of the RBCs behaviour in a DLD. Their overall behaviour in a DLD cannot correctly be assessed using these short sequences. Scale bars are 10  $\mu$ m.

# 6. Human African Trypanosomiasis

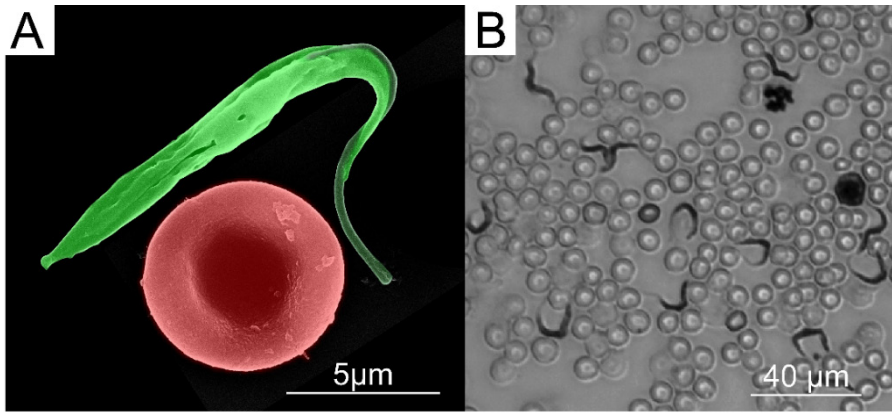


**Figure 23**

Size comparison of RBCs and trypanosomes. **(A)** Composite image of false-coloured scanning electron micrographs showing *T. cyclops* and a human RBC. Micrographs acquired together with J. P. Beech. **(B)** Giemsa-stained blood culture of *T. b. brucei*, showing trypanosomes at a much higher, 1000s times, concentration than for an HAT infected individual. (unpublished images)

Human African Trypanosomiasis, also known as sleeping sickness, is a vector-borne parasitic disease caused by a protozoan belonging to the *Trypanosoma* genus [135]. It is a fatal disease if not correctly diagnosed and treated at an early stage. The disease is caused by two subspecies of *Trypanosoma brucei*, which give rise to distinct disease patterns. *Trypanosoma brucei gambiense* (*T. b. gambiense*) causes West African trypanosomiasis (WAT), characterized by a longer chronic phase with increasingly severe symptoms until death, while *Trypanosoma brucei rhodesiense* (*T. b. rhodesiense*) causes East African trypanosomiasis (EAT) characterized by an acute disease progression with an average survival time around 9 months following infection [136]. It is estimated that a significant majority of infected cases is caused by the West African variant of the disease [137]. The name trypanosome comes from the ancient Greek word τρύπανον (*trúpanon*, “borer”) and σῶμα (*sôma*, “body”) derived from the corkscrew-like motion that propels them. The morphology of the parasite

differs depending on strain and also during the course of its life cycle. The trypomastigote form which is present in vertebrate hosts is reported to have a size ranging between 16-42  $\mu\text{m}$  in length and 1-3  $\mu\text{m}$  in width [138], Figure 23. The smallest dimension of the parasite, its width, overlaps with the smallest dimension of the RBC. Consequently, separation in a traditional DLD where particles are sorted according to their smallest dimension would not be possible. In Paper I we present a way to accentuate the morphological differences between the trypanosomes and RBC in order to achieve separation of these otherwise indistinguishable particles.

## 6.1. Pathogenesis

*T. b. gambiense* gives rise to a chronic form of the disease in Western and Central Africa with a disease pattern characterized by increasingly severe symptoms. The survival time, if not treated, varies due to individual factors but survival for up to four years has been shown [137]. The vector is *Glossina palpalis*, which mainly transfers the parasite between human hosts. Animals can occasionally get infected but will then only act as a reservoir for the disease [137]. The other variant of the parasite *T. b. rhodesiense*, is a zoonosis which gives rise to an acute form of the infection in the southern and eastern parts of Africa. The vector is *Glossina morsitans*. The disease progression is characterized by a rapid onset following infection with an average survival time around nine months. It has been reported that the *T. b. gambiense* subspecies accounts for as much as 98% of the detected cases [139] with the Democratic Republic of Congo accounting for 75% of known cases [140].

Other important subspecies include *T. b. brucei*, *T. b. vivax* and *T. b. congolense* whose primary hosts are domestic and wild animals, Figure 25. Although rare cases of human infection have been shown [137], their major impact on society is through Animal trypanosomiasis, nagana, which has a devastating socioeconomic effect in areas of disease foci [141]. Further species within the Trypanosomatida order include *T. b. cruzi* which causes American trypanosomiasis, Chagas disease, in Central America and South America with an estimated 6.6 million infected in 2015 [142]. In this case the triatomine bug (Hemiptera order) is the vector. Another example is leishmaniasis, which is caused by at least 20 different species within the *Leishmania* genus. Currently the disease is affecting several millions with an estimated 0.9-1.6 million new infections occurring per year in large parts of the world [143].

HAT is characterized by two distinctly separate stages. During the initial, haemo-lymphatic stage, the parasites multiply in the subcutaneous tissue, lymph and blood stream. Although, for the East African variant a visible chancre is present in 19% of cases [137], the occurrence of symptoms are at this stage low and they are often non-specific to HAT, including fever, headache and itching. Especially African natives can have first stage gambiense HAT without any symptoms and infections often remain unnoticed [144]. In the second stage of the disease the parasite crosses the blood brain barrier (BBB) and invades the central nervous system (CNS). It has been proposed that the trypanosomes are able to cross the BBB as extracellular parasites by the release of cysteine proteases, which interact with host endothelial cell G-protein receptors. This is expected to generate an increased permeability of the BBB which promotes parasite crossing [145]. This acute, so called meningo-encephalatic, stage is characterized by more distinct and specific symptoms including changes in behaviour, sensory difficulties and disturbances to the sleep-awake pattern – which is what gives the disease its common name (sleeping sickness). For *T. b. rhodesiense* more than 80% of deaths occur within 6 months of the onset of illness [146].

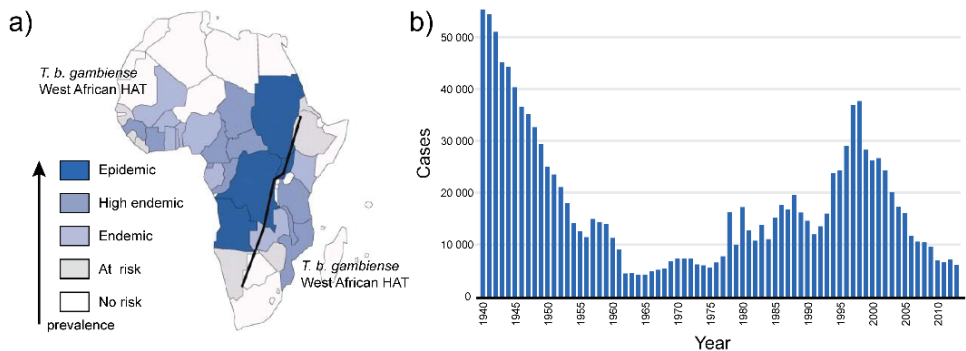


**Figure 24** Geographic distribution of HAT cases 2000-2009 together with the historical number of reported cases. **(a)** The black line divides the areas in which *T. b. gambiense* prevails and those where *T. b. rhodesiense* predominates. **(b)** Historical number of reported cases showing a time where HAT was close to being eliminated. Times of neglect led to an increase in number of cases until the disease was put in focus by WHO. Today, once again, we are close to eliminating the disease as a general health problem. New diagnostic tools combined with screening efforts can potentially lead to the complete elimination of the disease. Figures adapted from reference [137] with permission from Elsevier.

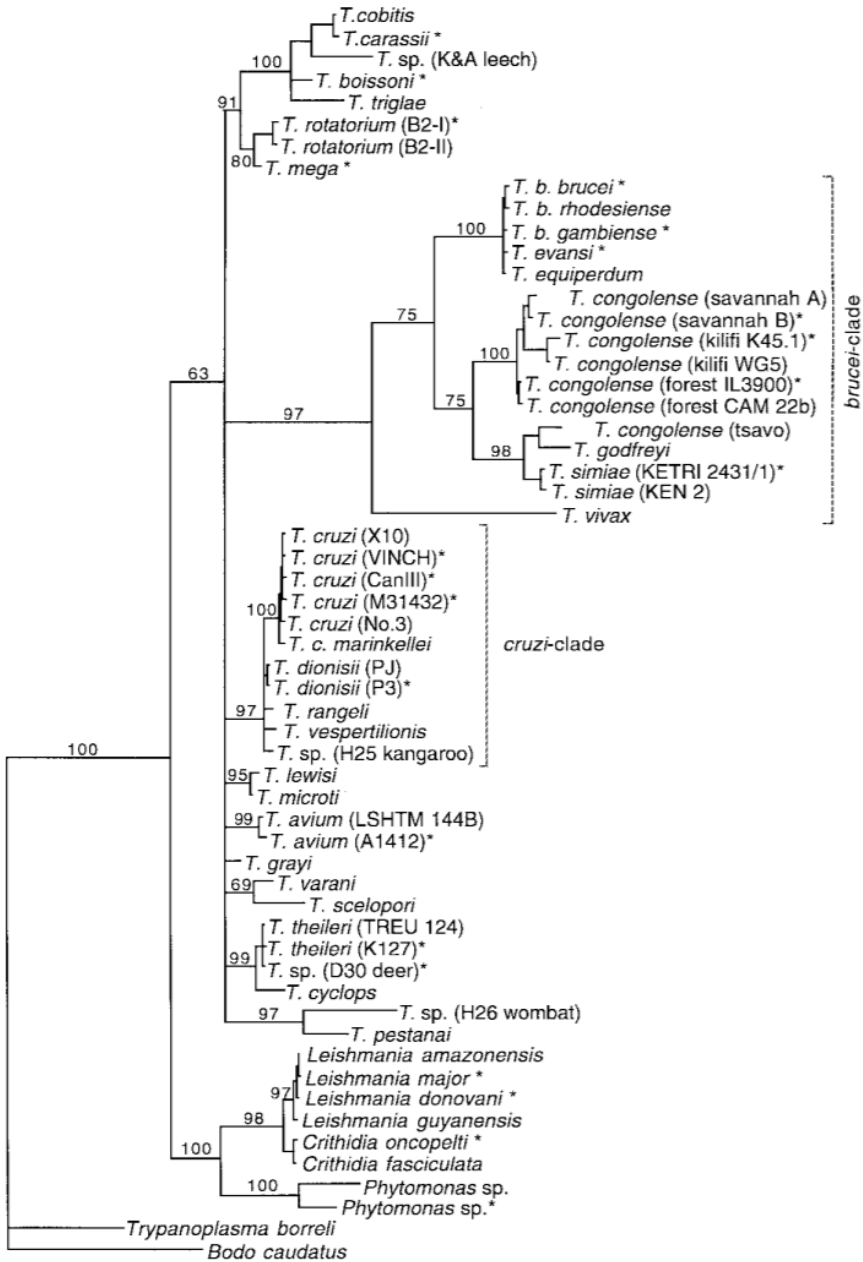


**Figure 25**

Phylogenetic tree showing relationships between various species within the Trypanosomatidae family. The for human infective *T. b. gambiense* and *T. b. rhodesiense* can be seen together with multiple specie within the brucei clade which are not infectious to humans. Further, the cruzi clade includes *T. cruzi*, which causes Chagas disease in South America with the triatomine bug as the vector. The tree also includes a few species within the Leishmania genus causing leishmaniasis with sand fly as the vector. *T. cyclops* was used in Paper I and II as a model system for *T. brucei*. Reprinted from reference [147] under CC license [148].



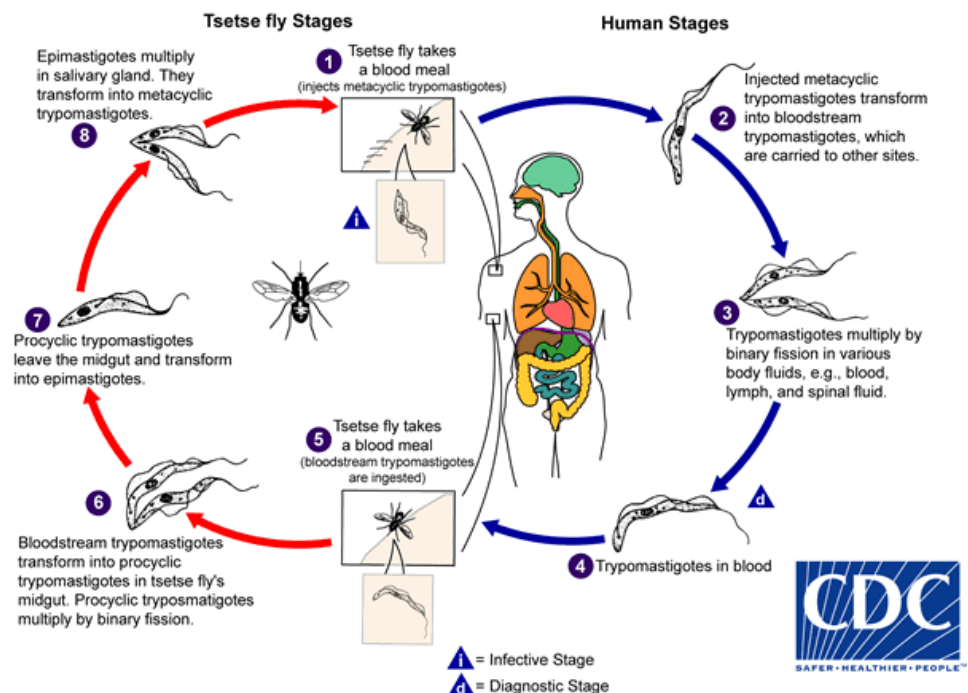


**Figure 26**

The life cycle of a trypanosome parasite. (1) While an infected tsetse fly takes a blood meal the protozoan can successfully be injected into a new host. A metacyclic form of the protozoan is injected into skin tissue from where it enters the lymphatic system and eventually the blood stream. (2) The bloodstream form can spread throughout the host and into for example the lymph fluid and cerebrospinal fluid (CSF). It continues to multiply by binary fission. (4,5) In order to complete a full life cycle the bloodstream form of the Trypomastigote is taken up by a tsetse fly during a blood meal. (6) Here, it resides in the fly's midgut and is transformed into its procyclic form, which is adapted to its new environment. (7,8) Leaving the midgut it transforms into its epimastigote form and continues to multiply in the salivary glands by binary fission. Here, it waits for its fly vector to take a blood meal in order to complete a life cycle. Figure from reference [149] used under CC-BY-4.0

## 6.2. Epidemiology

HAT is considered a neglected tropical disease, which is a group of diseases characterized as primarily affecting the poorest people living in remote rural areas of tropical and subtropical countries [150]. The role of HAT as a neglected tropical disease stems from the 1960s when it appeared that HAT was under control with a low, constantly declining number of new cases detected. However, due to several decades of neglect the number of infected individuals in the beginning of the 2000s was estimated to around 300 000, which lead to the deployment of several projects targeting HAT, mainly by the WHO, in order to regain control of the disease. By 2012 the number of reported new cases had dropped to around 8000. Although the number of

infected individuals is higher, WHO has an aim at eliminating West African trypanosomiasis as a public health problem by 2020. Elimination is defined as having the number of annual new cases below 2000 [151]. Further, WHO has set a target of complete elimination of the disease by 2030 [139]. If these visions are to be realized, then new, diagnostic tools that offer an increased sensitivity and specificity compared to what is being used today are crucial. Furthermore, these new tools must be made substantially cheaper to make use of the very limited resources available.

### 6.3. Life cycle

The most common life cycle of the trypanosome parasite is outline in Figure 26. Other paths of transmission are known, such as mother-to-child or sexual contact, however the most common route to infection is transmission with a tsetse fly (*Glossina* genus, *Diptera* order) as the vector. Transmission occurs when the fly takes a blood meal of a human causing the parasite to be transmitted to a new host. A metacyclic form of the protozoan is injected into the skin tissue from where it enters the lymphatic system and eventually it reaches the blood stream. The bloodstream form of the parasite can spread throughout the host in the blood or lymph fluid. Eventually it may cross the BBB in order to invade the CNS of the host. In the blood the parasite continues to multiply by longitudinal binary fission (i.e. cytokinesis takes place along the longitudinal axis). To successfully transfer to a new host it is taken up by a tsetse fly during a blood meal. The uptake has been shown to have a very low success rate with only 2-5% of trypanosomes continuing to multiply in the fly [152].

When a successful uptake occurs the parasite initially resides in the fly's midgut and is transformed into its procyclic form, which is adapted to the new environment. Eventually, when the parasite concentration has increased, it transforms into its epimastigote form, which continues to multiply in the salivary glands of the tsetse fly. Here, it awaits the vector taking another blood meal in order to spread to a new host. One complete life cycle is estimated to take around 3 weeks.

## 6.4. Evading the immune response

In order to successfully create a chronic infection the trypanosomes have developed an intricate method by which they evade the immune response of the host. The entire surface of the parasite is covered by a dense layer of highly immunogenic variant surface glycoproteins (VSG), making this the only part of the parasite that is visible to the host's immune system. Consequently, when a response is triggered, the VSG will be targeted [153]. However, the VSG coating spontaneously undergoes a stochastic gene mutation which gives rise to a small population of parasites that express a different VSG. The immune response will be directed towards the VSG of the major fraction of parasites while a small fraction of parasites can continue to multiply unnoticed. Eventually, when the number of parasites expressing the new VSG is sufficient, a new immune response will be triggered. However, again there will be a small fraction with a differing VSG, which can escape the immune system. The periodic fevers, a characteristic symptom of the disease, are a result of these reoccurring triggering of an immune response. The importance of the VSG to the trypanosome parasite is reflected in the fact that 10% of the *T. brucei* genome is estimated to comprise genes related to the VSG surface coating which by far outnumbers antigenic variation gene families elsewhere [154].

## 6.5. Treatment

The most commonly used drug for treatment of HAT is melarsoprol, an arsenic derivative which has been reported of having a mortality rate of 2-10% from the treatment itself, in addition to other severe side effects [155]. Today there exist a few alternatives, which although they are to prefer over melarsoprol, they do display severe side effects together with drawbacks during administering. Further, the options for treatment is dependent on whether the disease has progressed to the second acute stage (by crossing the BBB) or not and further if it is caused by *T. b. gambiense* or *T. b. rhodesiense*.

For first-stage treatment WHO advises the use of recurring intravenous administering of Pentamidine isethionate and Suramin for West African HAT and East African HAT respectively. Both of these drugs have been used for a long time with Pentamidine being introduced in the 1940s. The recommended regimen is to give seven to ten intramuscular doses per day. Side effects are usually not severe and mainly include hypotension and

hypoglycemia. Suramin was introduced in the 1920s and is given in weekly intravenous injections. Side effects are more common and severe; they include renal-failure, neurotoxic signs and anaphylactic shock. For second stage treatment melarsoprol has been used widely for both types of HAT. The side effects are severe, with its high mortality rate having the highest negative impact. For East African HAT no other treatment has been shown to be successful, making this drug, introduced in the 1940s, the best option for treatment. Recent reports suggest that there are strains that have developed increased drug resistance for melarsoprol with an increased therapeutic failure rate as a consequence [156, 157]. For West African HAT the situation improved in recent years when nifurtimox-eflornithine combination therapy (NECT) was introduced. This treatment combines multiple daily doses of nifurtimox given orally and eflornithine given intravenously. Severe side effects do exist and include vomiting, psychosis and convulsions [158]. The main hindrance to widespread adoption is however that this treatment is cumbersome and expensive to administer. As a consequence, melarsoprol is also given to a large fraction of these patients. For relapsing West African HAT patients, melarsoprol is the advised drug. To conclude, many of the drugs that today are used to treat HAT are outdated and show severe side effects. The treatment for second stage disease is difficult and it possesses highly severe side effects, including a high mortality rate for melarsoprol.

As a result of the severe side effects, including death, treatment is not administered before an ongoing HAT infection has been clinically confirmed. Non-specific symptoms or serological tests are commonly used for patient screening of HAT, but the only way to confirm the disease without false positives in order to initiate treatment is by finding the actual parasite in the patient. Consequently, there is a strong and compelling motivation for portable, improved diagnostic tools to aid in the diagnosis of HAT.

## 6.6. Diagnosis

Clinical symptoms can be used to indicate HAT but they have shown to be of too low sensitivity and specificity for use during confirmation and staging of the disease. Further, patients can often carry multiple infections (malaria, HIV, TB) or other infections, which show similar symptoms to HAT. As a consequence, the diagnosis of suspicious HAT cases needs to be confirmed by laboratory tests.

Complete diagnosis consists of three separate steps; screening, confirmation and staging. There are different requirements on the test parameters for these steps. In screening a large number of people need to be tested. Important factors therefore include low cost and a low number of false negatives (high sensitivity) while an elevated number of false positives (lowered specificity) can, at this stage, be tolerated. For the confirmation of a suspected HAT infection, because of the severe side effects and costs related to treatment, false positives are not tolerated (100% specificity is required). The sensitivity at this stage should be as high as possible in order to capture infections at low parasitaemia. The most used test for initial screening of people in endemic areas is the serological card agglutination test for trypanosomiasis (CATT). This test has shown a sensitivity of 87-98% for whole blood however the specificity is limited due to for example antibodies present in the blood from earlier infections or infections of strains not expressing the gene (LiTat 1.3) for the target epitope.

A similar test (LATEX) was developed which also uses LiTat 1.5 and LiTat 1.6. The results so far show that the specificity is higher while the sensitivity, often considered the most important factor during screening, is lower than CATT. Further, the CATT test can show false-positives with patients infected by other parasites (e.g. the *Plasmodium* malaria parasites) or transient infection by non-human trypanosomes strains.

Consequently, these suspected HAT cases need to be confirmed by other methods that rely on finding the actual parasite. It is however estimated that the commonly used techniques for parasite detection misses 20-30% of cases [159]. Parasite detection can be carried out by analysis of cerebrospinal fluid (CSF) and lymph node aspirate (LNA), however, it is most commonly carried out by analysing blood. The most common method is microscopic examination of blood smears, a very time consuming method with a very limited sensitivity. The difficulties are due to the parasitaemia, the concentration of parasites in blood, which varies from 10 000 per mL, which can easily be detected, down to below 10 per mL, which is extremely difficult to detect. The parasitaemia depends on individual factors but will fluctuate due to the recurring triggering of the host's immune response against the major VSG antigen. During periods of low parasitaemia, detection is a major problem, especially when considering that the number of normal blood cells is around 5 billion per mL with the majority being red blood cells.

Given the low abundance of parasites in blood, several methods have been developed to concentrate trypanosomes prior to microscopic examination each with its limitation as reviewed by Chappuis *et al.* [160].

Table 6 methods available for field-diagnosis of HAT in blood

Name	Method	Purpose	Equipment requirements	portability	Detection limit	time	Cost	sens.	spec.
microhematocrit centrifugation technique (mHCT)[160, 161]	centrifuge	Confirmation, staging	Medium, 220V, centrifuge	Low	500		USD[162]	46%[163] 48.3-64.5%[162] 95% at 7500/ml[164]	
quantitative-buffy coat (QBC)[164, 165]	centrifuge fluo. mic.	Confirmation, staging	High (USD 6000[166]) (fluorescent microscope setup, staining, reagents, buffers, capillary tubes, high speed centrifuge, filter cubes, dark room,	Low	<500/ml[167]	15-20 min[162, 168]	3-4 USD[166]	77%[164] 69-92[168] 88%[163] 95% at 450/ml[164]	
mini-anion-exchange centrifugation technique[169]	Chromat. centrifuge	Confirmation, staging	Fridge, columns	Low	100[160]	30-45 min[162, 168]	USD 2.5[168]	75.3%[162]	
Thick blood films[167]	Mic. G/AO	Confirmation, staging	Low, reagents	High	10000/ml with AO[170]	1 h + 0.5 h preparation and examination[163]		31%[163]	
RBC lysis[171]	Mic.	Confirmation, staging	Low, reagents		500/ml[172]	~45 min[171]		58% at 200/ml[173]	92.5%
CATT[174, 175]	LiTat 1.3 antigen	Screening <i>T. b. gambiense</i>	Medium, Cold chain			~1 min			
wb-LATEX[174, 175]		Screening <i>T. b. gambiense</i>						96-99% 91%	71-100%
GIATT[176]		Screening <i>T. b. gambiense</i> + rhodesiense							61-98%

\*Costs only include device and material costs. Additional costs for running the operation, i.e. personnel, surrounding equipment and vehicles are not included but are further discussed in a recent paper by Lutumba *et al.*[177]

Currently, the mini-anion-exchange centrifugation technique (mAECT) is considered the best trypanosome separation technique, and has been reported of having a detection limit of around 100 trypanosomes per mL of blood [160, 169]. This technique takes advantage of the negative surface charge of RBCs, which can be sorted out from the remaining sample by using a charged stationary phase in the chromatography column. This is followed by a centrifugation step focusing parasites into the bottom of a special glass tube, which is then analysed by microscopy. While the technique offers a low limit of detection the drawback is that the columns require an unbroken cold chain, a relatively long analysis time, a high price per test and the need for surrounding equipment.

Additional techniques include microhematocrit centrifugation technique (MHCT), often referred to as the Woo test, so named for its inventor in the 1970s [161, 178]. This technique uses small capillary tubes by which blood samples are drawn. The capillary tubes are centrifuged which concentrates the trypanosomes together with the white blood cells in the buffy coat layer. After centrifugation the capillary tubes are analysed in a microscope to check for the presence of a trypanosome infection. The detection limit is slightly higher than mAECT, around 500 trypanosomes per mL. The detection limit is related to the number of analysed capillary tubes, as the volume in each tube is limited. Normally 6-8 tubes are analysed, however a higher detection limit can be achieved (together with a longer analysis time) by using more tubes. MHCT is cheaper and faster than mAECT and does not require a cold chain.

Quantitative Buffy Coat (QBC) is a technique that is considered to have a limit of detection between mAECT and MHCT [164]. The technique combines high-speed centrifugation with fluorescent microscopy where trypanosomes are stained with acridine orange (AO). This makes the technique require a fluorescent microscopy setup together with a stable power and dark room to operate in. By using special capillary tubes containing AO, EDTA and a float, trypanosomes can be identified by their fluorescent kinetoplasts in an expanded buffy coat layer. The required equipment together with their fragility makes this technique difficult for transportation into the field and the price per test is relatively high. However, it can be used to detect concomitant infections, such as malaria.

An alternate method to these separation techniques is to selectively lyse the RBCs [171]. This method has been estimated to also have a detection limit of ~500 trypanosomes per mL of blood but has been difficult to implement and has not received widespread use in field diagnosis of HAT [172, 173].





# 7. Droplet microfluidics

*Droplet - a diminutive form of drop usually referring to drops with a diameter smaller than 500  $\mu\text{m}$ .*

Droplet microfluidics is a wide spanning field encompassing the manipulation of two-phase flows in microfluidic channels. It concerns mainly liquid-liquid flows although liquid-gas flows have been studied extensively [179-181].

Similar to how reactions in nature are often performed in micron-sized compartments in the form of cells and their organelles, droplet microfluidic offers a possibility for compartmentalization and to perform reactions and molecular processes within individual femto-to-picolitre-sized reaction chambers. A major advantage with the compartmentalization offered by droplet microfluidics is that it can be used to overcome one of the main limitations with continuous flow microfluidics - scaling up by parallelization. For many applications, the throughput of continuous flow microfluidics may be a limitation. To solve this, devices can easily be fabricated in parallel with a throughput that is proportional to the number of devices in parallel. However due to the traditional 2D fabrication techniques, mainly based on lithography, the device size also scales linearly with the throughput. Although there are hopes for the future in what many consider to be a coming microfluidic revolution based on 3D printing [86] the current options for scaling up stand in stark contrast to the parallelization inherent to droplet microfluidics which has the ability to perform a great number of reactions in parallel without significantly increasing the size or complexity of the device.

Droplet microfluidics takes advantage of the dimensional scaling in microfluidics and allows for the rapid formation (100 Hz – 100 kHz) of a large number of separate micro reactors with precise control over their size and content. The small length scales lead to smaller liquid consumptions, faster energy dissipation, and faster reagent mixing resulting in shorter reaction times. The droplet devices used in Paper VII is shown in Figure 27.

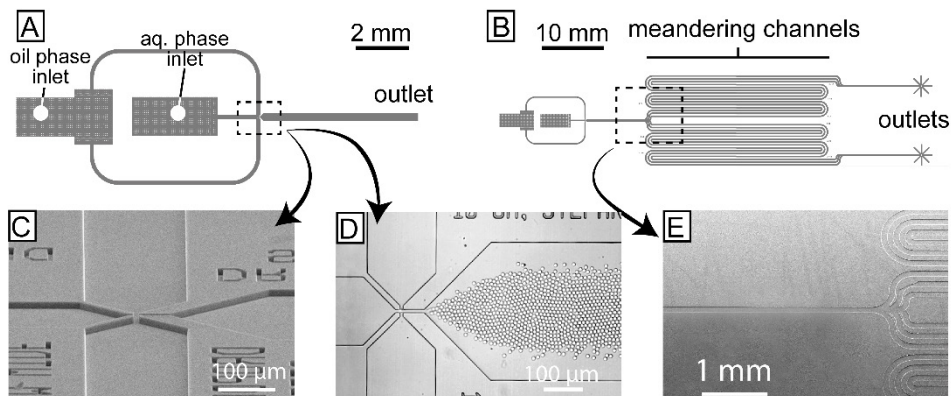


**Figure 27**

Droplet device used in Paper VII for the generation of temperature sensitive clusters, so-called colloidal molecules. A flow focusing droplet device geometry was used which a nozzle size of  $10\ \mu\text{m}$ . As a result of the small nozzle and a low capillary number, droplets were consistently formed in squeezing mode. (a) short device used for high frequency droplet generation. (b) longer meandering device which allowed for the study of *in-situ* droplet shrinkage. (c) SEM-micrograph and (d) optical micrograph of droplet forming region which had a nozzle size of  $10\ \mu\text{m}$  while keeping other channels large in order to maintain a low hydraulic resistance. (e) SEM micrograph showing the part where droplets are split into the meandering channels, in order to increase the residence time in the device and allow for complete *in-situ* shrinking.

While conventional methods for the generation of emulsions include shearing of immiscible fluids or the grinding of polymeric materials resulting in a wide particle distribution, droplet microfluidics has the ability to produce droplets of very low size variation, usually with a coefficient of variation ( $CV$ , defined as the standard deviation of the droplet diameter over its arithmetic mean)  $<5\%$ . Consequently, droplet microfluidics has shown great potential in areas where the monodispersity of emulsions is of paramount importance. These areas include for example particle synthesis, drug delivery and bio sensing where the biological and chemical properties of the particles often are decided by their volume and composition [139, 182, 183].

Several methods have been developed to extend the use of droplet microfluidics by controlling and manipulating droplets both in active and passive device, including splitting, fusing, sorting and mixing of their content as further demonstrated in a recent review by Simon *et al.* [184] Polymerization has been used to change the phase [185], encapsulation have been shown for a wide range of samples including cells [186], proteins [187] and DNA [188] and finally direct synthesis of micro and nanoparticles have been shown by the use of droplet microfluidics [189-191].

## 7.1. Dimensionless numbers

Droplet microfluidics can, like other areas of fluid dynamics, be characterized by various dimensionless numbers. These numbers are useful in order to gain an understanding of the relative importance of different effects and can be used to compare different flow regimes in parameter space and make prediction of the performance of a specific droplet system. Table 1 outlined the most important numbers for general microfluidics. For droplet formation, the Capillary number is an important number as it compares viscous stresses to the interfacial tension.

$$Ca = \frac{\eta v}{\gamma} \quad (29)$$

where  $\gamma$  is the interfacial tension,  $v$  is the characteristic velocity and  $\eta$ , the larger viscosity acting on the system. With a high Capillary number the viscous stresses exceeds the stresses due to the interfacial tension. When droplets are generated under this condition they tend to be heavily deformed with non-asymmetrical shapes as a result. Contrary, if the droplets are formed under low capillary number conditions the interfacial tension exceeds the viscous stresses and consequently the droplets will minimize their surface area with spherical shapes being the result.

It has been shown that there exists a certain critical capillary number above which droplets are formed. The critical capillary number is dependent on the specific system but can be used to predict the required relationship between the parameters (stated above) for droplet formation to occur. There are two additional dimensionless numbers, which are important in droplet microfluidics, the viscosity ratio,  $\sigma$ , and the flow rate ratio,  $\varphi$ , of the dispersed and the continuous fluid which are defined as

$$\sigma = \frac{\eta_d}{\eta_c} \quad (30)$$

and

$$\varphi = \frac{\Phi_d}{\Phi_c} \quad (31)$$

These dimensionless numbers will, together with the Capillary number, determine the mode of droplet formation [19], as discussed further in this chapter.

## 7.2. Surface energy

The introduction of a secondary phase results in a new interface that in turn gives rise to an interfacial tension. This is a force per unit length, which pulls the interface with a magnitude  $\gamma$  (N·m<sup>-1</sup>) in order to minimize the surface area and the free energy of the system. As mentioned, the interfacial tension acts to produce a spherical droplet while the viscous stress acts to deform it. The Laplace pressure is the pressure drop between the inside and the outside of a droplet and is given by the Young-Laplace equation

$$\Delta P = \gamma \left( \frac{1}{R_1} + \frac{1}{R_2} \right) \quad (32)$$

where  $R_1$  and  $R_2$  are the two principal radii of the droplet. From this equation it is apparent that the high surface-area-to-volume-ratio (SAV) of smaller droplets require more energy to form. The generation of oil-in-water (O/W) or water-in-oil (W/O) droplets depends mainly on how well the two phases respectively wet the channel walls, and this will furthermore have a big importance in controlling the adhesion of the dispersed-phase to the channel walls, something that is usually to be avoided. In order to generate W/O droplets the channel walls need to be hydrophobic while O/W droplets are generated in hydrophilic channels.

Various methods of surface treatment have been developed in order to control the surface properties of devices. Plasma treatment, which is normally used during soft lithography, renders the naturally hydrophobic surface of PDMS hydrophilic by incorporating silanol groups (-SiOH) at the expense of methyl groups (-CH<sub>3</sub>) [192]. To counteract this we in Paper VII used a coating of fluorosilane to render the droplet device hydrophobic [89]. Other methods such as PVA coating [92] and PEG-silane [90] have also been shown successful in modifying the surface properties of microfluidic devices

## 7.3. Surfactants

The word surfactant is a contraction of ‘surface active agent’ [193] and refers to molecules of amphiphilic nature which consist of a polar head group and a non-polar tail. They are commonly used in droplet microfluidics in order to facilitate droplet formation and further to stabilize the droplets once formed [194]. Due to its amphiphilic nature such a molecule prefers to be

positioned in the interphase, bridging between the water and the oil phase. As a result the surface tension (between the oil and water phases) will decrease.

In order for a microfluidic droplet system to be biocompatible the continuous phase needs to allow gas exchange [186]. The only oil type to have shown continued cell survival and proliferation with long-term incubation is fluorinated oils. Their high gas exchange was exploited in Paper VII where the dispersed water phase was allowed to evaporate through the oil phase in order to force precursor particles to form clusters. Due to this interest in fluorinated oils, several compatible surfactants have been developed for microfluidic studies. It has been shown that both the head and the tail group affect the final biocompatibility of the surfactant [195]. Today, the most promising type of molecule for increased biocompatibility in microfluidic droplet devices using fluorocarbon oils is amphiphilic molecules with a block copolymer of perfluoropolyether and polyethylene oxide [194].

## 7.4. Droplet generation

There exists a multitude of droplet generation techniques, each with its advantages and disadvantages. Important parameters are often considered to be a low polydispersity, a high generation frequency and the ability to tune droplet size and generation frequency. The two main routes to droplet formation are active and passive, where the former relies on external actuation in order to promote interfacial instabilities while the latter relies on hydrodynamic forces to form droplets [196, 197].

### **Active droplet generation**

Active droplet generation can be achieved in two ways, either by applying external forces, including electric, magnetic and centrifugal fields or by modifying intrinsic properties of the flow or the fluid in terms of viscosity, velocity, interfacial tension and channel wettability [197].

Advantages with active droplet generation include that the size and generation frequency of droplets can be independently tuned while for passive droplet devices these are related to the flow ratio between the dispersed and continuous phase. The faster response time and higher control in active droplet generation allow for simple tuning of the encapsulated number of particles (governed by Poisson distribution) [198].

## Passive droplet generation

Passive droplet generation allows for simpler mode of operation and often higher formation frequencies. Apart from actuating the fluid, no external force is needed for droplet formation. At the same time they often allow for higher generation frequencies and have been shown capable of generating smaller droplets than active droplet generation methods. Within passive droplet generation several different device configurations can be used in order to generate droplets with the most common ones, cross-flow, co-flow and flow-focusing shown in Figure 28. Several review papers are available which details their individual advantages and disadvantages [199-203]. The following pages will give a brief overview of their individual properties.

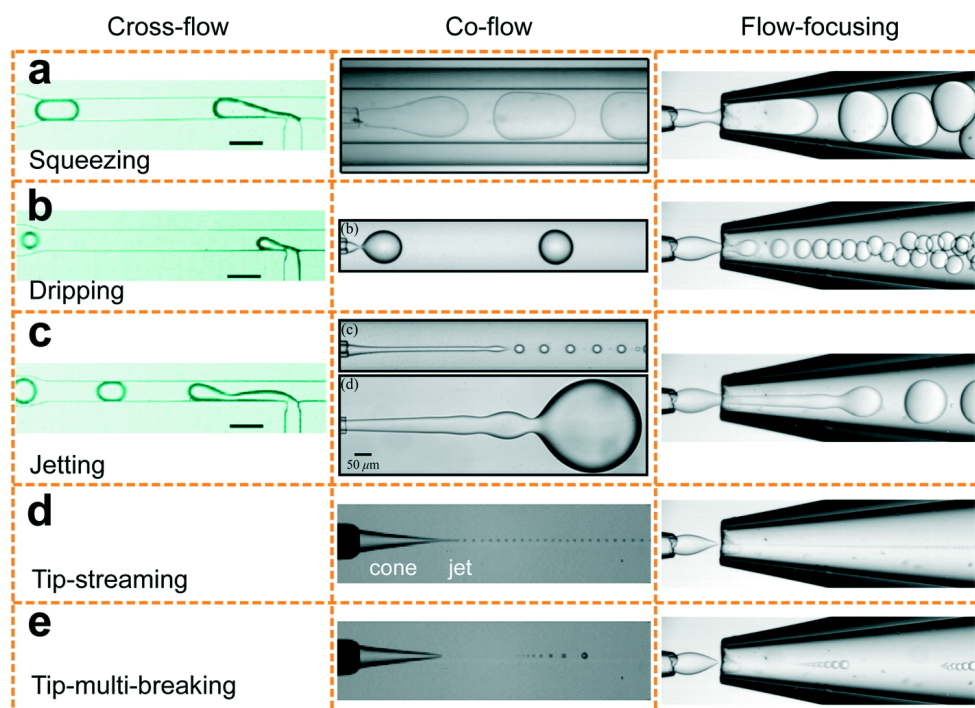


**Figure 28**

Modes of droplet break-up in cross-flow, co-flow and flow focusing devices. Cross-flows of (a)–(c) are reprinted with permission from ref. 131. Copyright 2010, American Chemical Society. Co-flow of (a) is reprinted with permission from ref. 133. Copyright 2007, American Physical Society. Co-flows of (b) and (c) are reprinted with permission from ref. 15. Copyright 2007, American Physical Society. Co-flows of (d) and (e) are reprinted with permission from ref. 58. Copyright 2013, Cambridge University Press. Flow-focusing (a)–(e) are reprinted with permission from reference [196]

In cross-flow devices the dispersed phase is injected at an angle, often perpendicular, into the channel containing the continuous phase [204]. The shear force of the continuous phase causes the liquid thread of the dispersed phase to be elongated into the main channel with the size of its neck decreasing until a single droplet is formed. The size of the droplet depends on the channel sizes, the flow rates and the relative viscosity of the two phases. The main advantage with the cross flow configuration is its simplicity, both in terms of fabrication and droplet generation. It has been shown to be able to generate droplets with a CV <2% [205].

In a co-flow configuration, the channels of the dispersed and the continuous phases are aligned [182]. A common way of fabricating these types of devices is to insert a tapered glass capillary tube into a standard microfluidic channel of rectangular cross-section. Similar devices have, however, been fabricated using standard lithographic methods. The size distribution varies depending on the droplet regime with dripping mode (see further below) showing a low size variation with a CV <3% [182].

First proposed by Anna *et al.* [206] and Dreyfus *et al.* [207], flow focusing has traditionally been the most common way to generate droplets in passive droplet devices [208, 209]. Here, the dispersed phase and the continuous phase are forced through a narrow constriction where droplets are formed. In comparison to cross-flow devices the symmetric shearing of the liquid thread results in a more stable droplet generation with a lower polydispersity at higher frequencies. Further, the symmetric shearing allows for smaller droplets [196].

Step emulsification is, unlike the other techniques mentioned, driven by interfacial tension instead of hydrodynamic shearing of the dispersed phase [202, 210-213]. The name is due to the method relying on variations in channel confinement through which a sharp change in capillary pressure occurs, leading to droplet formation by interfacial tension. The method is characterized with low size variation, CV ~ 1% [210], although CV ~ 0.1% has been achieved [212]. Further, droplets of the same size can be generated with varying frequencies as long as the flow ratio,  $\phi$ , is kept constant [211]. By parallelization, in what is known as EDGE devices, it has been shown to generate droplets up to ~300 kHz, although with large size variations, CV ~ 10% [214].

## Droplet regimes

The process of droplet formation is due to fluid instabilities. Depending on factors such as device geometries, interfacial tension, channel wetting and fluid viscosities the process can be categorized into one of the five droplet generation modes: squeezing [215], dripping [216], jetting [216], tip-streaming [217] or tip-multi-breaking [218]. These breakup modes are all present in co-flowing and flow-focusing configuration while only squeezing, dripping and jetting has been reported for devices with a T-junction configuration.[196] The squeezing regime relies mainly on the channel confinement whereas the other regimes rely on the Plateau-Rayleigh instability [219, 220] to form droplets, similar to how the liquid from a slow running faucet breaks up into droplets before touching the sink. This process relies on the interfacial tension acting to minimize the interfacial energy by decreasing the surface area. At the same time the viscous and inertial forces (if present) act to deform the liquid interface and counteract interfacial tension forces, which resist deformation. The interplay between these forces determines the specific breakup mode.

Squeezing mode occurs at low capillary numbers,  $Ca_c < 10^{-2}$ . It is often referred to as the geometry-controlled mode due to how the droplet formation relies on confining the dispersed phase into a small channel. This leads to a pressure build-up in the continuous phase, which increases until it overcomes the internal pressure of the droplet, and squeezes the droplet to deform and neck it into a droplet.

In dripping mode, the droplets are formed before they have grown large enough to touch the channel walls and they are consequently spherical at formation. The capillary number  $Ca_c$  is elevated compared to the squeezing regime resulting in higher viscous shearing forces acting on the dispersed phase, ultimately necking the thread and forming a single droplet. The scaling of the final droplet size can be estimated by balancing the viscous stress,  $\sim \eta_c v_c / L$ , with the Laplace pressure  $\sim \gamma / D$ , yielding  $D/L \sim Ca_c^{-1}$  [204].

At an elevated flow rate of either the dispersed or the continuous phase, the droplet generation can transform from the dripping regime into jetting regime [216]. This regime is characterized by the creation of a long protrusion, a jet, of the dispersed phase, which ultimately breaks up by Plateau-Rayleigh instability. Due to capillary perturbation droplet generation in jetting regime often results in a relatively large size variation in the final droplet size.



If the flow rate of the continuous phase is increased sufficiently the dispersed phase will take on a conical shape where droplets are formed at the apex of the tip in a regime known as tip-streaming. The droplets can be several orders of magnitude smaller than that of the dispersed phase channel [217]. In this way sub-micrometre droplets can be formed in regular microfluidic channels, however the fraction of dispersed phase to the continuous phase is low compared to other regimes which can be a drawback when using expensive continuous phase liquids.

A final droplet regime known as tip-multi-breaking has recently been identified [218, 221]. In this mode droplets are formed in a periodic manner with a certain number of droplets forming in sequence with their sizes linearly decreasing. Droplets are believed to form due to an expansion of the dispersed phase downstream of the constriction. The enlarged dispersed phase thread is subjected to a significant shearing force from the continuous phase which elongates the thread and breaks it into a sequence of  $n$  droplets one by one until the entire dispersed phase liquid downstream of the constriction has been consumed. Following this, the same process is repeated leading to a periodic droplet breakup. In most applications, the formation of monotonic droplets of low size variation is preferred. However in certain applications droplets of different, but still controlled, sizes are preferred such as multi-volume droplet digital polymerase-chain-reaction [222]

## 7.5. Pressure or flow-rate-driven pumping

The use of pressure driven or flow-rate driven pumping can also have an impact on droplet formation. Little research has been carried out to find out the quantitative differences between these two ways of actuating the fluid. Ward *et al.* recently used a flow focusing device and reported qualitative agreements between the two setups in terms of size, frequency and flow rate fractions but major quantitative differences [223]. Most notably is that for pressure driven flow there exists a minimum pressure below which no droplet generation occurs while the same is not true for flow-rate driven devices. It seems as likely that below a certain pressure ratio ( $P_d/P_c$ ), the forces exerted by the dispersed phase at the interface is lower than what is exerted by the continuous phase in the form of normal stress and shear stress, suppressing droplet formation and resulting in static flow.

## 7.6. Particle synthesis

As discussed, there are two different aspects that make droplet microfluidics particularly attractive. First, the compartmentalization realizes the formation of reaction-chambers with high control over the chemical composition and its environment. Further, droplet microfluidics has the ability to generate monodisperse emulsions at kHz range. This has opened up a wide range of applications based on droplet microfluidics, as previously discussed in this chapter. In Paper VII, we show how microgels clusters with temperature sensitive interactions can be generated through droplet microfluidics. The generation of monodisperse particles with novel functionalities has been made possible by employing droplet microfluidics. The individual reaction chambers allow for the creation of particles with interesting properties while the low size distribution of the droplets results in precise control of the content and consequently, control over the precursors for particle synthesis. The success of droplet microfluidics for particle generation is reflected in the wide range of particle types that have been realized using the technique, as discussed further in several reviews covering this area, including biodegradable particles for food industry [224], anisotropic micro- and nanoparticles [190, 225], polymeric microparticles [191] and photonic crystals [226].

# 8. Appendix 1 Software

## **Automated DLD array generator**

The designing of DLD devices can be a time-consuming step. To accurately position the posts and in addition to generate the channels connecting the post array with the inlet and outlets can often take longer than clean room fabrication of devices. Ordered arrays can be created in CAD software, but the edge correction, Chapter 3.3, which is dependent on the post parameters has to be manually positioned. For the creation of multiple devices, often with several critical sizes, a code was developed in Java which automated the process. This was later converted into C++ by Bao Dang Ho [227] and implemented directly into L-edit (Mentor graphics). The code is available under CC BY-NC-SA 4.0 and can be downloaded from <http://bit.ly/Stefan2018>

## **Particle analyser**

In order to quantify the behaviour of the DLD performance in Paper I, II and III the lateral position of particles at the outlet was determined. To manually count the 100s or 1000s of particles needed for good statistics would be a tedious task. Consequently a MATLAB (MathWorks) software was used which could determine the correct position of 10 000s particles within seconds. The software can scan through a folder of micrograph stacks acquired at the outlet and will provide the tracks of particles together with an outlet distribution. It is equipped with a GUI to allow the user to tune the parameters needed to accurately capture the particles. This includes the removal of the background by the difference to a median projection of the stack and a FFT band-pass between 1 pixel (removing noise) and the size of the particles (acting to further remove background). The code is available and free to use under CC BY-NC-SA 4.0 and can be downloaded from <http://bit.ly/Stefan2018>



# 9. Appendix 2 Device overview

## 9.1. Device used in Paper I, III and IV

Section	$\Delta\lambda$	$N$	Rows	$D_C$	Displacement ( $\mu\text{m}$ )
1	0.8	40.00	200	2.86	160
2	1.2	26.67	130	3.47	316
3	1.6	20.00	100	3.99	476
4	2.0	16.00	80	4.44	636
5	2.6	12.31	60	5.04	792
6	3.2	10.00	50	5.56	952
7	3.8	8.42	40	6.04	1104
8	4.4	7.27	35	6.48	1258
9	5.2	6.15	30	7.02	1414
10	6.0	5.33	25	7.53	1564
11	6.8	4.71	20	7.99	1700
12	7.8	4.10	20	8.53	1856
13	8.8	3.64	15	9.04	1988

$G = 12 \mu\text{m}$

$\lambda = 32 \mu\text{m}$

Each section consists of 5 periods.

Width:  $81 \lambda = 2.59 \text{ mm}$

Total length:  $804 \lambda = 25.73 \text{ mm}$

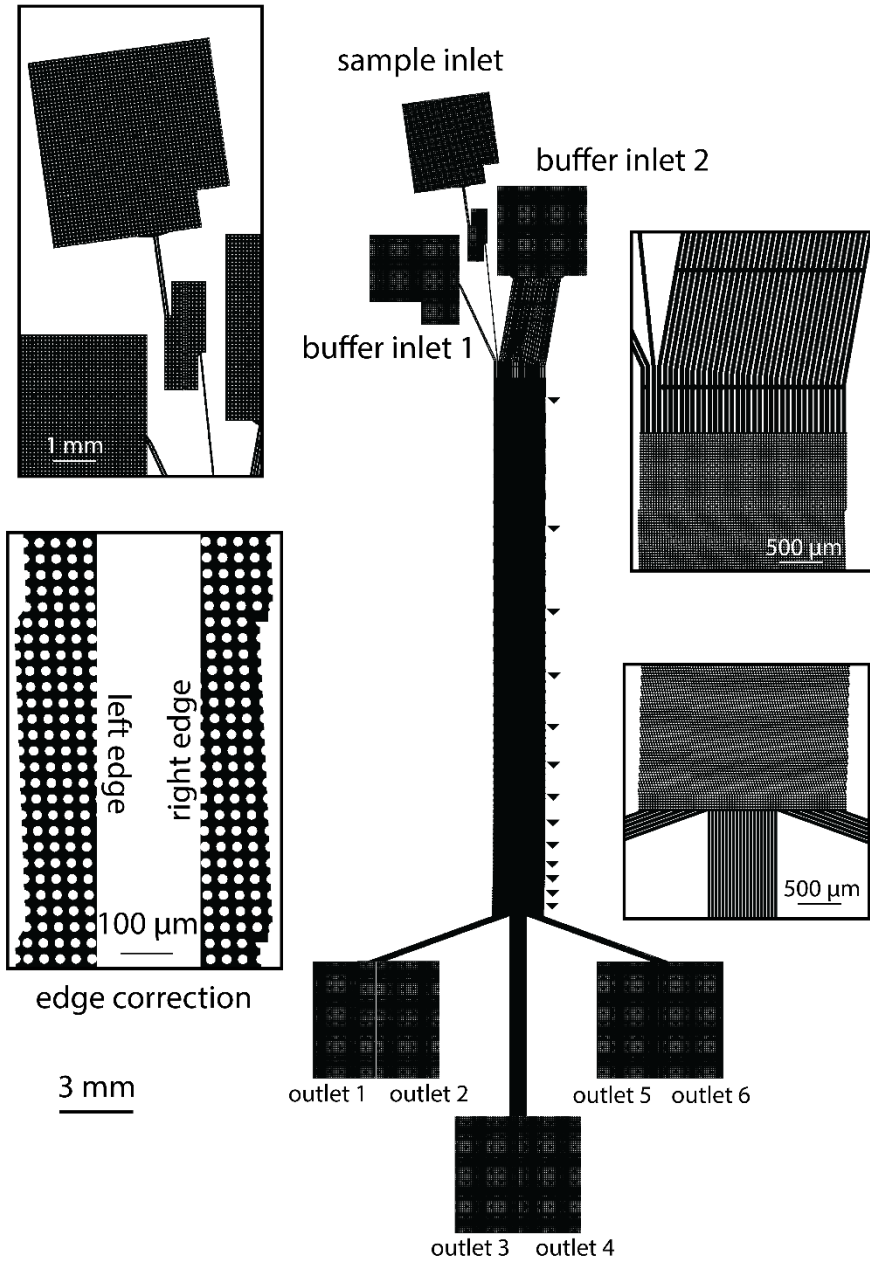
Buffer 1 inlet width:  $4.5 \lambda$

Sample inlet width:  $2 \lambda$

Buffer 2 inlet width:  $74.5 \lambda$

All six outlet widths are  $13.5 \lambda$

# Device used in Paper I, III and IV



## 9.2. Device used in Paper II

<b>section</b>	<b>1</b>	<b>2</b>	<b>3</b>
$D_c$ ( $\mu\text{m}$ )	7.14	3.47	3.47
$d$ ( $\mu\text{m}$ )	26	3.5	9
$G$ ( $\mu\text{m}$ )	22	12	12
$\lambda$ ( $\mu\text{m}$ )	42	32	32
$\Delta\lambda$ ( $\mu\text{m}$ )	2	1.2	1.2
$N$	21	26.67	26.67
repeats	45	48	48
length ( $\mu\text{m}$ )	39690	40960	40960
width ( $\mu\text{m}$ )	1890	3072	3072

At the end of section 1, 20% of the flow is bifurcated into the WBC outlet while the remaining flow continuous to section 2. The widths are proportional to their respective flow rates.

WBC outlet width:  $9\lambda$

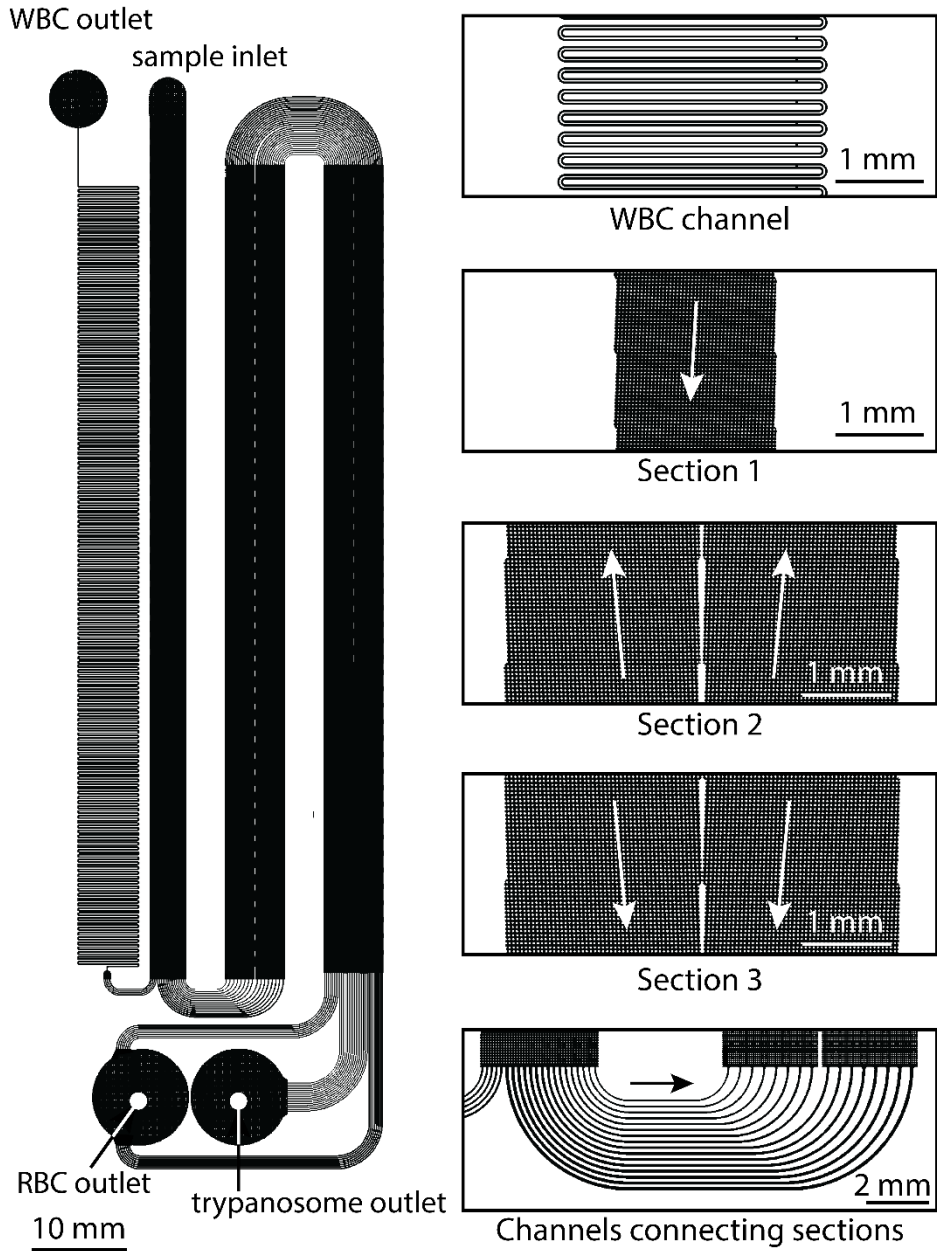
Section 2 outlet width:  $36\lambda$

At the end of the device, the flow is split up evenly between the RBC and trypanosome outlet with the trypanosome outlet occupying the centre half and the two RBC outlets 25% on each side of the device.

RBC outlet width:  $2 \cdot 24\lambda$

Trypanosome outlet width:  $48\lambda$

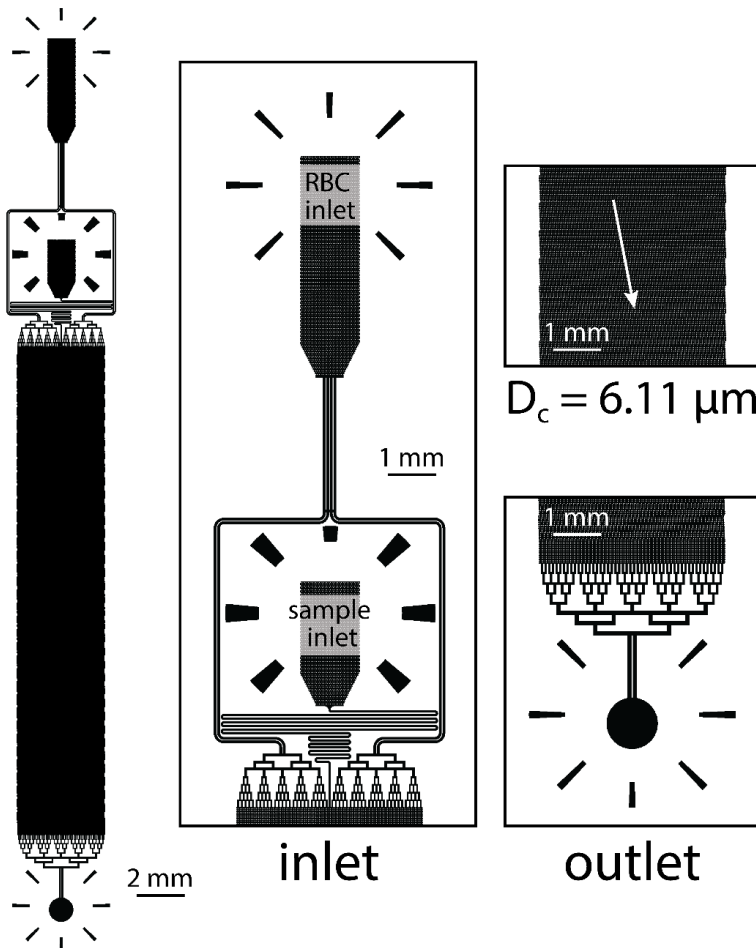
# Device used in Paper II





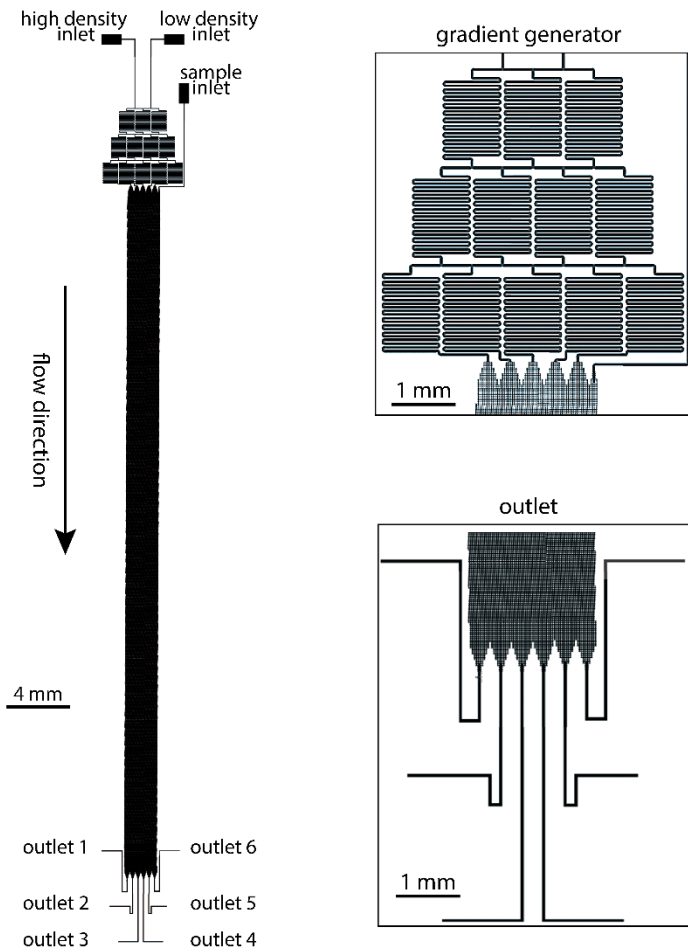
### 9.3. Device used in Paper V

$\lambda$ ( $\mu\text{m}$ )	36
$G$ ( $\mu\text{m}$ )	16
$N$	15
$D_c$ ( $\mu\text{m}$ )	6.11
Repeats	36
Length ( $\mu\text{m}$ )	19440
Width	$3636 \mu\text{m} = 101\lambda$
sample inlet	$36 \mu\text{m} = 1\lambda$
RBC inlet	$3600 \mu\text{m} = 100\lambda$

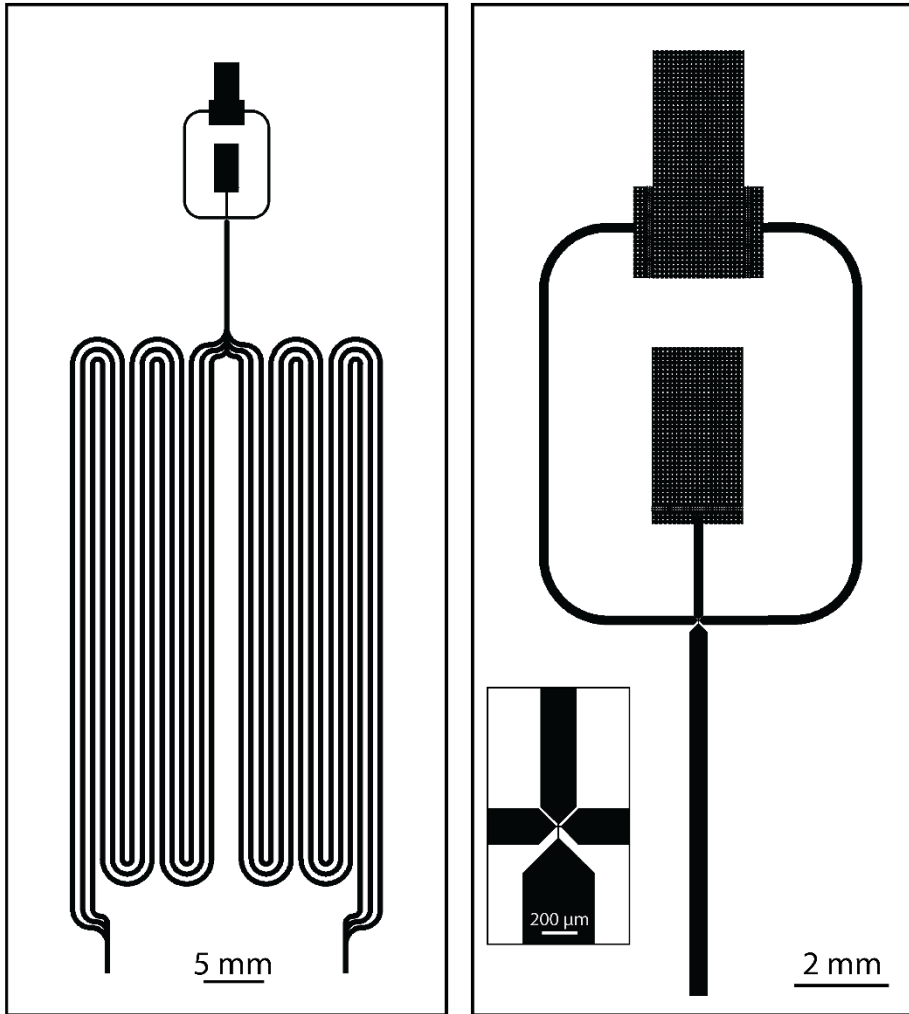


## 9.4. Device used in Paper VI

$\lambda$ ( $\mu\text{m}$ )	32
$G$ ( $\mu\text{m}$ )	12
$N$	40
$D_c$ ( $\mu\text{m}$ )	2.86
Repeats	34
Length ( $\mu\text{m}$ )	43520
Width	1984 $\mu\text{m}$ = $62\lambda$
sample inlet	160 $\mu\text{m}$ = $5\lambda$
buffer inlet	1824 $\mu\text{m}$ = $57\lambda$



## 9.5. Device used in Paper VII



meandering device  
for *in-situ* droplet shrinking

short device  
for high throughput



# 10. Discussion and Conclusion

## Paper I-VII

The main focus of this thesis work has been on particle sorting by deterministic lateral displacement (DLD). In addition, the thesis also presents particle generation by droplet microfluidics, which has large potential for novel applications in combination with the sorting capabilities of DLD. One of the main goals regarding the work related to DLD has been to extend its sorting abilities by incorporating sorting based on new parameters, and by the quantification of how various phenomena affect sorting in DLD. In this way we show how DLD, while simple to operate, can achieve high sensitivity in the separation of particles. This opens up for the fabrication of simple diagnostic devices, capable of operating in the field, targeting HAT, as described in Paper I and II. Further, we show schemes for sorting RBCs based on their size, morphology, elasticity and their dynamic properties, as described in Paper III and Paper IV. In Paper V sorting at high hematocrit is explored, targeting future applications in high-throughput sorting such as rare-cell detection or whole-blood processing. Paper VI presents an approach where density based particle sorting can be achieved in DLD devices. Two methods are presented, first a method which is sensitive to both size and density followed by another approach where separation is based only on density. Paper VII presents an approach for the realization of a new type of colloidal particles which allows for interaction tuning by temperature. All figures in this chapter is from the respective paper, and they are reprinted with permission from the publisher.

## 10.1. Paper I Separation of parasites from human blood using deterministic lateral displacement

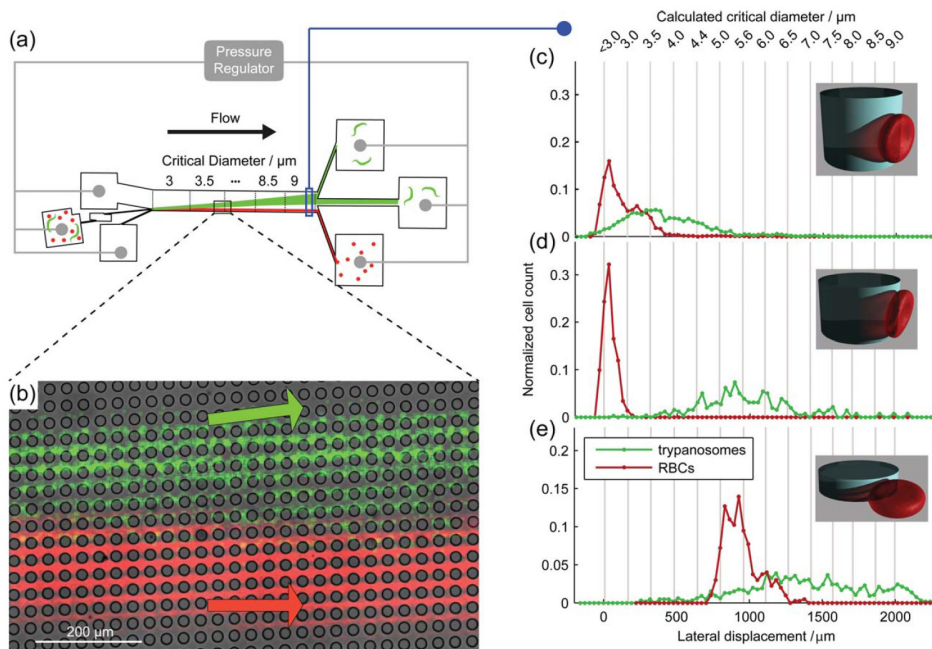


**Figure 29**

Shape-based sorting in DLD devices. **(a)** Overview of our DLD device with a focused stream of particles entering from the sample inlet to the left. Particles larger than the critical diameter are laterally displaced (upwards in the figure) and can be collected at the end of the device. The distributions of RBCs and *T. cyclops* are measured at the end of devices of three different depths. **(b)** A time-integrated micrograph showing a mixture of RBCs and parasites imaged in brightfield and coloured red. Overlaid on this image, in green, is an epifluorescence micrograph in which only the DAPI-stained trypanosomes can be seen having been displaced out of the stream of blood cells. **(c)** **(d)** and **(e)** Device depth has a large effect on the distributions of RBCs and parasites at the end of the device, with the 11  $\mu\text{m}$  deep device **(d)** showing the best separation.

DLD is an excellent candidate for portable blood tests as it is a passive particle sorting technique, *i.e.* separation does not rely on an external field such as electrophoresis or centrifugation. Instead the separation is based on hydrodynamics, which offers simplicity and portability while at the same time having a high sensitivity in size-based particle sorting.

Separation of RBC and trypanosomes in a traditional deep DLD device would however be challenging as these separations depend to a great extent on the smallest feature of the particles, which for RBC and trypanosomes is similar,  $\sim 2.5 \mu\text{m}$ . In Paper I we present a method that accentuates the

morphological differences of the cells and show how we can achieve sorting between RBCs and trypanosomes, an approach that in addition to being essential for this application opens up for shape-based sorting of otherwise indistinguishable particles in DLD. The approach uses channel depth to orient particles. Our main finding is that device depth has a significant impact on the behaviour of non-spherical particles in DLD devices. By carefully tuning this parameter we show how the orientation of non-spherical particles can be controlled. Our findings open up for morphology-based separations.

In brief, a chirped device consisting of 13 different sections with critical diameters ranging from 3-9  $\mu\text{m}$  in steps of 0.5  $\mu\text{m}$  was designed, fabricated and tested, Figure 29a. The device was fabricated at different depths and the effects of device depth on separation performance were explored.

In the deep device (33 $\mu\text{m}$ ) both RBCs and trypanosomes are free to rotate under the influence of shear forces. They present their smallest dimensions to the device and have overlapping effective sizes. This overlap is reflected in a low purified fraction,  $F_p$ , (the fraction of trypanosomes captured with a lateral displacement chosen such that 99% of the RBCs are rejected) of 14.0%.

In the shallowest device, 4  $\mu\text{m}$ , both RBCs and trypanosome have larger effective sizes and are displaced considerably more. In this device the overlap was also large. While the separation was better the purified fraction was still poor with  $F_p = 53\%$ .

In an 11  $\mu\text{m}$  deep device, the effective size of parasites was maximized while that of the RBCs was kept to a minimum. This allowed us to achieve a significant increase in the purified fraction,  $F_p = 99.5\%$ .

As well as showing a new type of separation, several new phenomena are described and practical solutions presented. E.g. Movement of trypanosomes through our devices was studied and they were observed to move in a variety of modes, several of which lead to an increase in their effective size. Combinations of surface treatment and buffer solution were developed to allow the running of blood and parasite sample for extended times.

While the throughput in the device presented in Paper I was too low to reach our goal of detecting a target parasitaemia of 100  $\text{mL}^{-1}$  (within a practical time limit), we were able to propose strategies, based on our results, for the improvement of the method that we then implemented in the work presented in Paper II.

## 10.2. Paper II Simplifying microfluidic separation towards field-detection of blood parasites

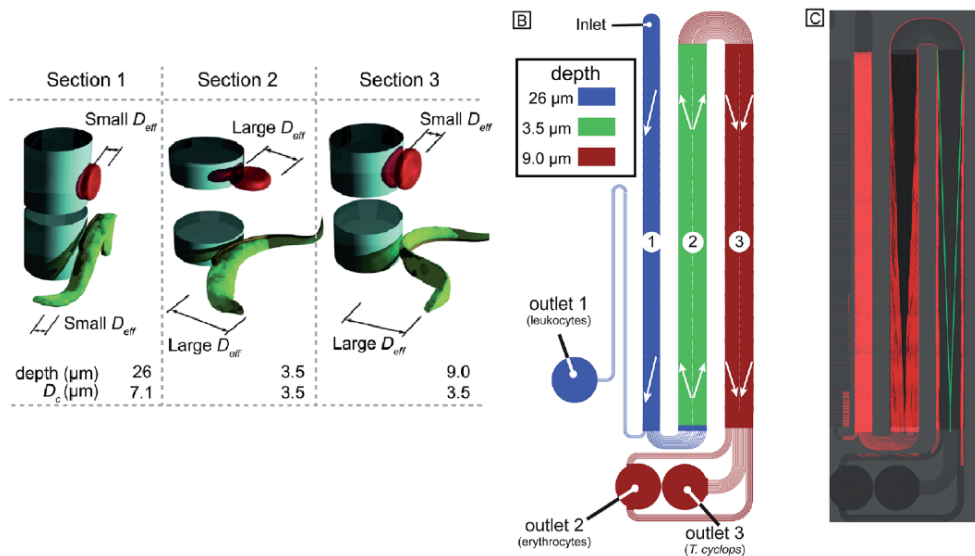


**Figure 30** Outline of device functionality. (A) Basic principle of how orientation changes the effective size of particles of different shape. (B) Schematic overview with the three different sections colour coded. Arrows represent the direction of displacement in each section. (C) False-coloured mosaic image consisting of 34 time-integrated micrographs showing the trajectories of erythrocytes and the parasites through the device.

This paper builds on the findings presented in Paper I and focuses on fabricating a device that meets the requirements of the resource-deprived areas where the HAT disease is prevalent namely, it needs to be cheap, simple to use, portable, require low or no power and it needs to be able to detect a low concentration of parasites in a background of human blood. Many of the devices that show great promise in the lab are doomed to fail because they do not fully address these points.

By the incorporation of several DLD arrays in series, Figure 30, each with its own specific depth, we were able to perform the following steps in one device: (1) removal of leukocytes in order to avoid clogging of subsequent steps, (2) creation of a cell-free plasma and (3) migration of the parasites into this cell-free stream for detection. The device has high specificity and sensitivity and with only a single inlet has no need for complex flow controllers and instead uses a simple hand-held syringe to drive the fluid. As such, it is an ideal approach for POC detection in resource-limited settings.



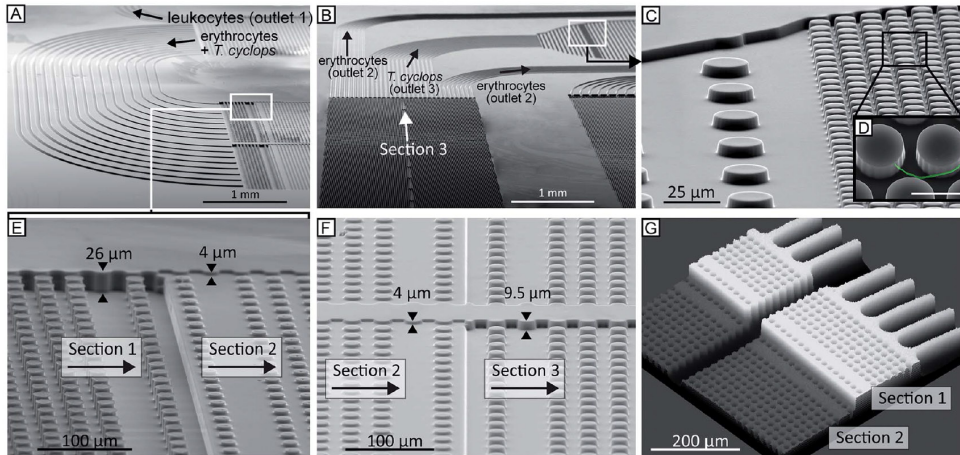


**Figure 31**

SEM and confocal images of the device. Channels connecting different sections of the device are designed to be of equal fluidic resistance in order to maintain the relative positions of particles, allowing for longer and more complex devices to be created. **(A–B)** Separate rounds of photolithography enabled device sections of specific depths, which was used in order to alter the individual effective sizes of the particles. **(E–F)** After the final section in the device, section 3, the trypanosomes have been focused to the centre and thus exit to the trypanosome outlet where a dense array of pillars **(C–D)** is defined with the purpose of capturing the parasites. Note the inset **(D)** where a parasite is highlighted (coloured green). Scale bar is 10  $\mu\text{m}$ . **(G)** Confocal micrograph of a fluorescent solution (0.1% rhodamine B in H<sub>2</sub>O) passing through the step-change in depth between section 1 and 2.

Furthermore, the device we present can be fabricated in cheap materials, has no moving parts or power requirements and by being no larger than a microscope slide it is highly portable. Compared to the devices in Paper I, these are easier to use, with a significantly increased throughput. Our method provides a dramatically simpler and cheaper alternative to existing methods with the potential of enabling a fast and cheap point-of-care device that will have significant impact on field diagnosis.

As well as 30-fold enrichment of parasites at  $2\mu\text{l min}^{-1}$  in a self-contained separation device requiring no external power or pumping, other specific developments presented in Paper II involve the designing of channel systems to join together multiple DLD arrays with minimal perturbations to the fluid flow and the fabrication of multi-depth DLD devices using soft lithography.

We believe the proof-of-principle device shown in Paper II holds great promise as a point-of-care test for tropical diseases. While offering several advantages over current options for field-diagnosis there is still work to be done towards a fully-functional diagnostic device. Most notably, the current

device would benefit from a method for portable detection, such as cell-phone based microscopes [228] or integrated electronic cell counting based on impedance spectroscopy [229]. Finally, while soft lithography offers rapid prototyping of microfluidic devices, alternative fabrication methods, such as foil-based fluidics [230] or injection-moulding [78] would allow for mass fabrication.

Lastly, our method is not limited to the detection of HAT but could potentially also aid in diagnosis of related parasitic diseases. This could both include species within the same genus, such as *T. vivax* and *T. Congolense*, which mainly affect livestock and consequently puts a significant socioeconomic burden on endemic areas, and *T. cruzi* which is responsible for Chagas disease, also known as American trypanosomiasis. Further potential lies in diagnosis of leishmaniasis, affecting several millions worldwide and additional macroparasites and microfilarial worms responsible for diseases such as river blindness and elephantiasis.

### 10.3. Paper III Sorting cells by size, shape and deformability

Cell morphology is a key characteristic in biology and pathology, to identify different species and strains as well as to identify abnormalities. Typically, microscopy is used to characterize cell samples. On the other hand, for sorting, image cytometry [231] exists, but these instruments are limited by their resolution and speed of sorting.

Deformability is another parameter which has shown to be highly connected to the underlying state of a cell and it is an important clinical indicator of a wide range of medical conditions. Most commonly, deformability is measured in bulk using ektacytometry [232], resulting in loss of information about the heterogeneity among the cells. To address this issue a few microfluidic methods have been developed such as optical tweezer [233], RTDC [122], margination [234] and inertial focusing [27]. These methods, while allowing for single-cell studies, would at varying degrees be unable to map the morphology with high resolution of a large number of cells. Further, they would not be suitable to assess anisotropic behaviour.

By using DLD we present a method to probe the size, shape and deformability, demonstrated on three types of RBCs. The relative contribution of these parameters to the final behaviour in the DLD device is investigated, which opens up for sorting and analysis schemes where these parameters can be targeted individually or combined. RBC is an interesting cell type to use for demonstrating this sorting principle, as RBC has an unusual non-spherical shape and is soft. A wide range of diseases are known to affect these properties of the RBCs, adding strong clinical relevance.

We demonstrate how the orientation of a non-spherical particle is of paramount importance to its displayed effective diameter,  $D_{eff}$ , in a DLD. For a normal discocyte (disc-shaped) RBC which is  $\sim 2.5 \mu\text{m}$  thick with a diameter of  $\sim 7.5 \mu\text{m}$  this means that in a deep DLD device, this non-spherical particle would tend to, under the influence of the shear field of the fluid, be aligned so that it presents its smallest dimension to the posts – its thickness of  $\sim 2.5 \mu\text{m}$ . However, when decreasing the channel depth below the diameter of the RBC the effective diameter of this particle increases and it will depend on both its thickness and diameter. At sufficiently strong confinement, at a depth close to its thickness, the effective size is entirely determined by the overall diameter.

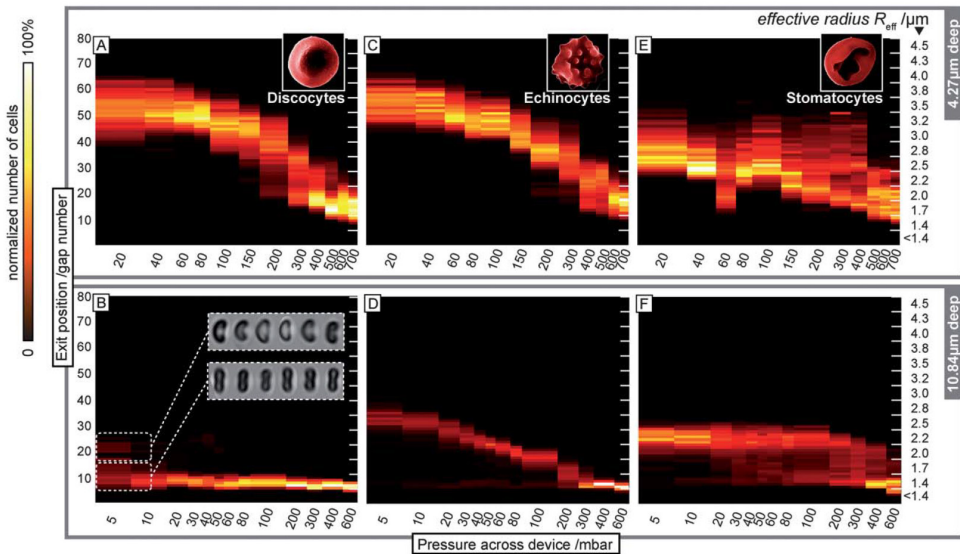


**Figure 32**

The exit position (reflecting the measured effective radius,  $R_{eff}$ ) as a function of applied pressure (and therefore shear rate and resulting shear stress) constitutes a cell type fingerprint. Here three red blood cell types are shown in devices of 4.27 mm depth (A, C and E) and 10.84 mm depth (B, D and F).

Further, due to shear forces exerted by the fluid and normal forces from the stationary posts, a deformable particle will assume an increasingly elongated shape as the shear forces increase, which in turn will decrease its effective diameter. Consequently, by sweeping the driving pressure of the fluid across a certain range and register the outlet distribution of the particles we essentially acquire a stress-strain measurement from which, together with the ability to orient the cells, we can extract information about the mechanical properties of the cell.

In conclusion, we have demonstrated a scheme where we add morphology-based sorting to the size-based sorting inherent to DLD by controlling the particle orientation, and deformability-based sorting by varying the shear rates in the device in order to affect the effective sizes of the particles as a function of deformability. Compared to the standard image cytometry we demonstrate a passive approach to sort cells at high throughput based on their morphological and mechanical properties, including the anisotropy of these properties. Since the method does not rely on imaging it is not limited by diffraction, and could be applicable to sorting of very small particles. The method would be a good candidate for *e.g.* extraction of circulating tumour cells from blood. Further studies in order to couple the properties of the

underlying cell architecture to the behaviour of cells in the device is needed to couple the shear stresses exerted by the device and how it is related to the change in the critical diameter. Another factor which is important is to connect the shearing time scales with cell deformation and relaxation as this would open up for characterization of the viscous properties of the cells.

## 10.4. Paper IV Sorting cells by their dynamical properties

We employ the combination of numerical and experimental investigations of RBCs in DLD devices to quantitatively describe the full trajectories of RBCs through the DLD device. By careful analysis and comparisons between experiments and simulations we target essential physical mechanisms to make quantitative predictions of how cell dynamics affects transit behaviour of bioparticles in DLD devices.

The RBC dynamic behaviour is studied during lane swapping events in order to deduce a relationship between their trajectory, their dynamic behaviour and the hydrodynamic interactions. Further, measurements were conducted at varying ratios between the internal viscosity and the external viscosity ( $C = v_i/v_o$ ) of the RBC, as this has been shown to affect the dynamic behaviour of RBCs [128], with a decrease in viscosity ratio leading to a preference of tank-treading over tumbling motion [235, 236]. Consequently, by tuning the viscosity contrast we were able to assess the individual contributions of cell morphology, elasticity and cell dynamics to the transit modes in DLD devices.

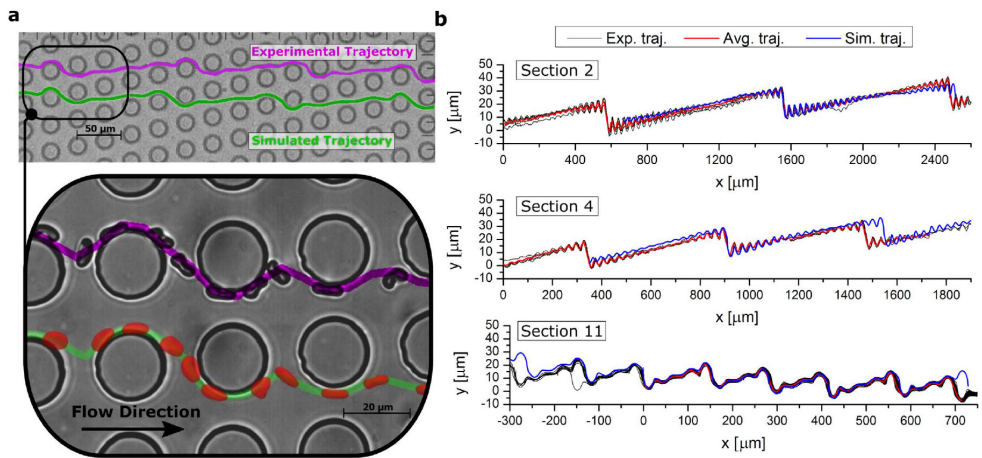


**Figure 33**

Experimental and simulated trajectories for RBCs at viscosity contrast  $C = 5$ . (a) The trajectories of the experimental and simulated RBCs are obtained by following their centre of mass through the pillar array. (b) Experimental and simulated RBC trajectories for several sections of the thick device. Black lines show multiple aligned experimental RBC trajectories and red lines correspond to average experimental trajectories. The blue lines show the RBC trajectories found in simulations. Section 2 shows an approximately neutral zigzag mode, section 4 illustrates a positive zig-zag mode, and section 11 leads to a negative zig-zag mode.

An interesting revelation in the results were that pure zigzag and displacement modes, often used to describe particle motion in DLD devices, were not enough to correctly describe the trajectories of these deformable and anisotropic bioparticles. Instead, the observed zigzag modes displayed a variety of net displacements, including positive, neutral and negative. The trajectories are however not random. Instead very consistent periodic behaviour was found (Figure 33b).

The simulated and experimental RBC trajectories in general show very good agreement, suggesting that the simulations are able to adequately capture the hydrodynamic effects and RBC deformation and dynamics. There is a tendency for a discrepancy in the final sections of the device which is believed to be an effect due to disturbances in the flow field close to the outlets of the device.

Figure 34 shows the thick device at viscosity contrast  $C = 5$  and  $C = 1$ . In addition to showing a good agreement between the behaviour of experimental and simulated (red) RBCs it is also worth noticing how the tumbling and rolling behaviour which are present at  $C = 5$  lead to an induced zigzag event. The RBC dynamics is closely related to these events, as it is directly precedes and follows lane-swapping events. The tank-treading RBC shown in Figure 34b is subject to local shear-flow alignment which act to suppress tumbling motion and consequently lane-swapping consistent with the results from the thick device.

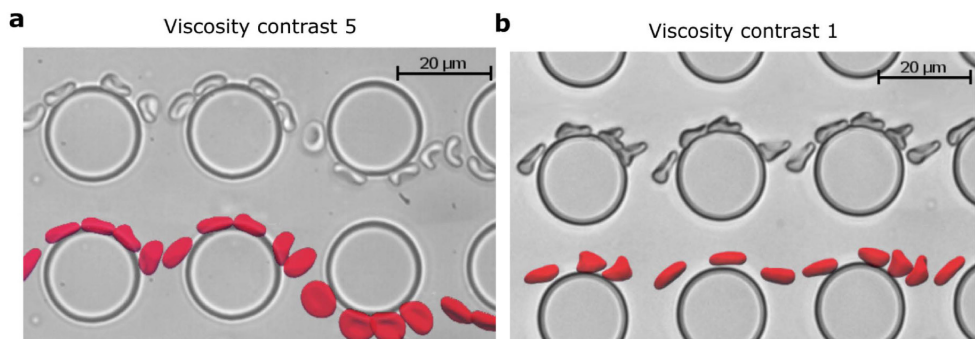


**Figure 34**  
Combined images showing simulated and measured RBCs in section 2. (a) RBC lane swapping is promoted by tumbling when  $C = 5$ . (b) Tank-treading type dynamics occurs at  $C = 1$  resulting in the RBC favouring displacement mode.

Our results suggest that in order to design an ideal device for sorting deformable particles, not only neutral zigzag and complete displacement can be considered but also the net displacement from negative and positive zigzag modes. Further, our results from sorting of RBC at varying viscosity contrasts show that it would be possible to sort based on particles' internal viscosity given that the viscosity of the medium is carefully chosen. Such a sorting scheme would best be performed in a thick device which allows the cells to explore their full range of particle dynamics induced by the viscosity contrast.

An interesting aspect of this work is also that sorting based on elasticity may be improved at decreased viscosity contrasts in order to suppress the effects of cell dynamics. Similarly, the thin device shows difference in the later sections between viscosity contrast  $C = 1$  and  $C = 2-5$  which is believed to be due to the deformability of the RBCs due to the limited RBC dynamics allowed due to the constrained environment.

Our results reveal that the combined effects of the particles dynamic behaviour and the hydrodynamic interactions they experience near obstacles give rise to a more complex behaviour in DLD devices than that found for rigid spherical particles. Still, the transit modes detected in this study are not random but deterministic, and are determined by fluid flow and the mechanical properties of deformable particles.

Consequently, we believe that this method can be a powerful tool for the design of novel sorting schemes which utilize the dynamic behaviour and intrinsic mechanical characteristics of bioparticles as a quantitative separation parameter or biomarker. In addition to blood related diseases (*e.g.* malaria and sickle-cell anaemia), it would also benefit other areas including bacteriology, parasitology, and oncology.



## 10.5. Paper V Concentration effects in Deterministic Lateral Displacement

Microfluidics, and especially DLD, offers the sensitivity and specificity needed for rare cell capture, which has a high potential in for example clinical diagnostics. However, in order to enable rare-cell capturing within reasonable time limits, focus has to be put on the often limited throughput of microfluidics where separation are mainly carried out at a significant sample dilution in order to decrease particle-particle interactions. To allow for high throughput separations we here present a quantitative investigation of the relationship between sample concentration and the performance of DLD arrays using experiments and simulations.

While most microfluidic analysis techniques require a diluted sample, we show that DLD can be operated at whole-blood concentrations. We demonstrate that white blood cells can be enriched from whole blood at least 200 times in a DLD device.

To better understand the underlying mechanisms of the changing behaviour of the DLD as a function of hematocrit and to elucidate the quantitative changes of the trajectories of particles in a DLD with changing hematocrit, we performed careful experiments and simulations. We ran a standard DLD device with blood at different concentrations and observed the trajectories of microsphere particles with sizes above and below the critical size of the DLD array.

The blood has two main effects on the trajectories of the particles. Smaller particles that normally zigzag in aqueous solutions through the device deviate towards the displacement direction. Larger particles that are normally displaced in the DLD deviate towards the zigzag directions, i.e. the direction of the liquid flow through the device. The deviation increases with blood concentration for both particle sizes. However, for very large particles (50% larger than the critical size) we could not observe any deviation. Surprisingly, increasing the flow rate would allow us to almost reverse the effect of the blood, Figure 35.

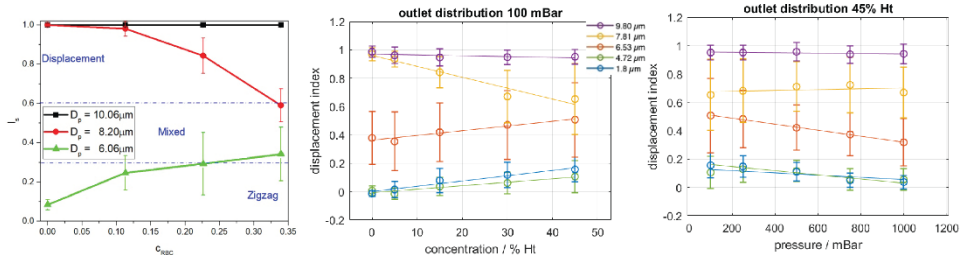


**Figure 35**

Trajectories of microspheres in DLD as a function of haematocrit. The displacement index gives the degree of displacement of the particles (0 – zigzag mode, and 1 – displacement mode). (A) Experimental data on the displacement index of beads of different sizes as a function of haematocrit. (B) Experimental data on the displacement index of beads of different sizes as a function of applied pressure across the device. The data was acquired for 45% haematocrit (whole blood). (C) Simulations of particle trajectories presented as displacement index as a function of haematocrit for different sizes of microspheres.

To explain the behaviour, we turned to several different mechanisms. We could reject margination as an important factor since the interaction length along the posts is very short. Through simulations we could also barely see any change in the velocity profile of the flow between the posts. Therefore, change in the trajectories could not be explained by this factor.

Simulations reveal that the concentration of RBCs at the posts increase. This gives increased effective sizes of the pillars that affect the trajectories of the small particles such that they move away from the liquid flow in the device, thereby increasing the displacement index. For larger particles, collisions with the RBCs lead to deviation from the displacement mode and decreased displacement index. We also find that for smaller particles, collisions may have opposite effect, and the net effect would be determined by a balance by these two types of collisions. An interesting effect that is observed both in simulations and in experiments is that the variation in the trajectories increases with increasing haematocrit. This is consistent with the trajectories changing due to collisions between the particles and the RBCs.

To summarize, we have clearly shown that DLD arrays can be operated successfully at whole-blood concentrations for particle sorting. This opens up for high-throughput analysis of blood, and it provides important simplifications because no dilution is necessary. Since higher flow rates can be used to counteract the deterioration of the performance, we expect the approach to be useful for most conceivable applications except those where the uttermost in resolution is required. We have established a putative model of the underlying mechanisms to the changes in particle trajectories that will allow us to optimize the technique further.

## 10.6. Paper VI Density based sorting in deterministic lateral displacement devices

In microbiology and molecular biology, density is a central parameter for sorting. Typically, centrifugation is used. For miniaturization this poses problems as it requires rotating the sample. While the centrifugal force creates an enhanced sedimentation, another approach is to use the sedimentation afforded by the gravitational pull and amplify it by different geometrical structures. To this end we have developed two types of devices. (1) A DLD is designed with T-shaped posts, Figure 36. The gap between the posts is now different for particles that are lighter than the liquid medium and the ones that are denser than the liquid medium. The different gaps will give different critical sizes. The trajectories of particles with sizes within the range of these two critical sizes will now depend on the buoyancy of the particles. The device is very simple in terms of design, fabrication and operation. However, it only provides a crude separation as a function of density and poor resolution.

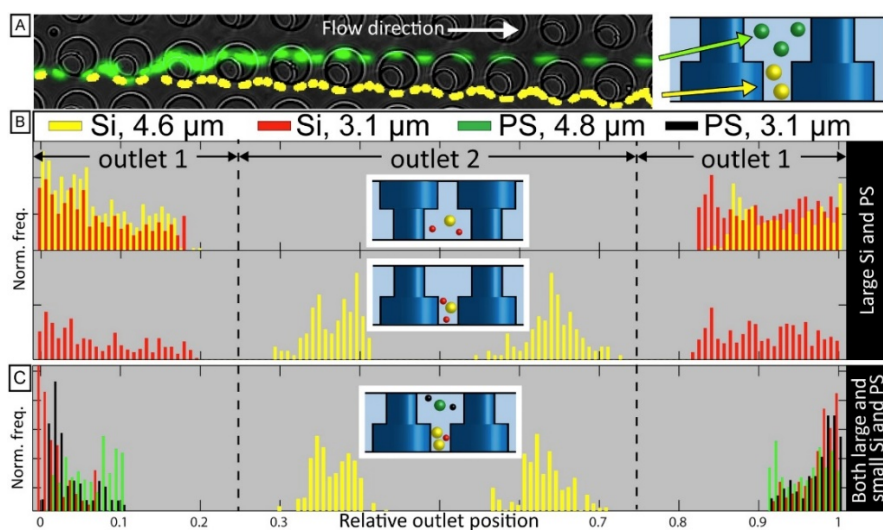


**Figure 36**

(A) False-colored time-integrated micrograph of a 4.87 μm PS bead (green) and a 4.63 μm Si sphere (yellow). The different lateral position can clearly be seen with the green particle above the small gaps. (B) Graph showing the distribution of silicon (Si) microspheres, 3.13 μm (red) and 4.63 μm (yellow), in DI water at the outlet of the device. The illustrations in the middle show how the device was oriented. When the device is flipped over the Si spheres sediment into the level with smaller gaps and the larger spheres are laterally displaced into outlet 2. (C) Outlet distribution of both large and small Si (yellow, red) and PS (green, black) microspheres in 15% sucrose solution. The buoyancy of the PS microspheres forces them into a vertical position with large gaps while the silicon microspheres sediment into a vertical position with small gaps. Combining of size and density-based separation allows for the sorting out a single specific particle type.

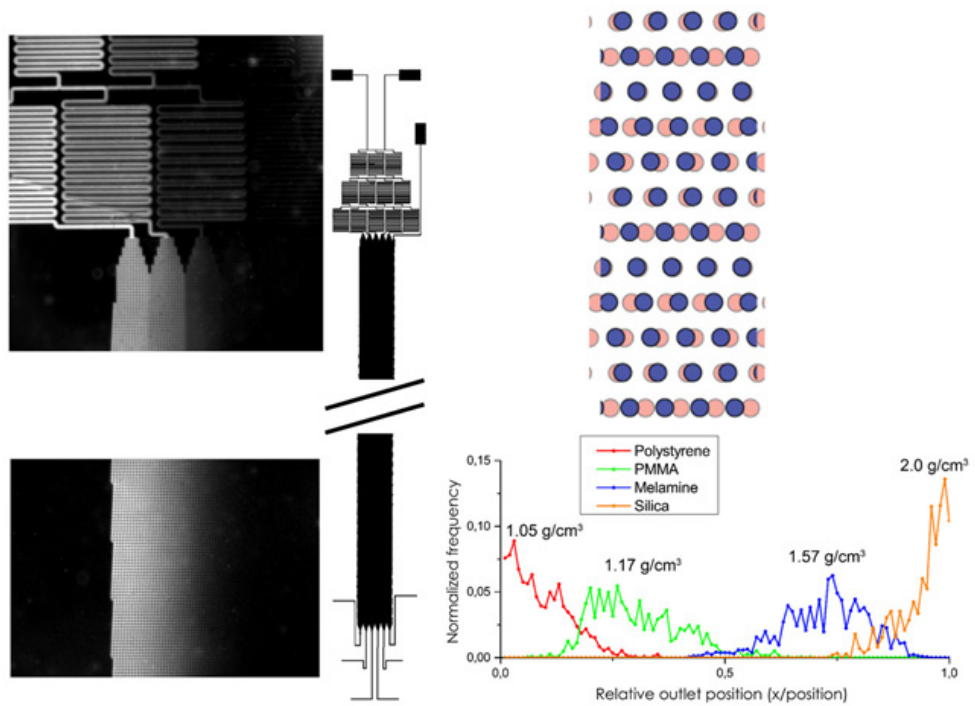


**Figure 37**

Overview of main components of the density DLD based on isopycnic focusing. By mixing the high and low density buffers in multiple steps a density gradient across the device is created. Particles are injected along the edge at low density and migrate into areas of higher density. Eventually the particles sediment to the lower level DLD when the surrounding buffer density is higher than their own density.

(2) To address the shortcomings of the above device, we developed an enhanced approach based on a device with two DLD arrays on top of each other, facing each other, combined with a gradient generator, Figure 37. The requirements for density sorting is now that the particles are larger than the critical size of the DLD arrays. The role of the DLD is to send the particles to the left or the right depending on the sign of the buoyancy of the particles. The gradient determines where the particles of different densities can be collected at the end of the device. While this approach requires more careful design and fabrication as well as slightly more complicated experimental conditions, it has the potential to provide high-resolution sorting based on solely the density of the particles. The sorting range is here determined by the gradient across the device. By selecting a large gradient, a wide range of densities can be separated. By selecting a narrow gradient, higher resolution is expected.

To summarize, we have successfully demonstrated density-based sorting in simple and passive devices without any moving parts. In contrast to other approaches to density-based sorting and characterization[237, 238], our method does not require any monitoring nor any additional driving force except the pressure driven flow necessary to drive the sample through the device. The devices can be made using simple cost-effective methods such as injection moulding, in a single piece of plastic.

While the results are promising, we look forward to more detailed studies of the limits of resolution of the device based on the density gradient combined with DLD. The density gradient can easily be decreased, and the challenge will be to find suitable reference particles to carefully characterize the attainable resolution.

## 10.7. Paper VII Thermoresponsive colloidal molecules prepared using droplet-based microfluidics

We demonstrate a method for fabricating colloidal molecules with tuneable interactions, exemplified by the use of two thermoresponsive polymeric colloids, so-called microgels, poly-N-isopropylacrylamide (PNIPAM) and poly-N-isopropylmethacrylamide (PNIPMAM). Because the temperature response for PNIPAM differs from PNIPMAM we can tune their interaction individually, from soft repulsive to short-range attractive through an increase in temperature.

Droplet microfluidics is used to generate the thermoresponsive colloidal molecules, as outlined in Figure 38. A microfluidic droplet generation device, with a flow-focusing geometry, is used to produce a W/O emulsion of low size-variation. The aqueous phase contains modified PNIPAM and PNIPMAM particles which have methacrylate (MA) groups incorporated to enable crosslinking of particles. A fluorinated oil which, together with PDMS, allows for evaporation of the dispersed aqueous phase, forcing the microgels into close contact in the shrinking droplets. When in the close-packed state the clusters are crosslinked by ultra-violet (UV) light activation of the photoinitiator 2-hydroxy-2-methylpropio-phenone (HMPP) and thereafter these colloidal molecules are transferred to an aqueous phase by several rounds of washing using a combination of hexane and surfactants.

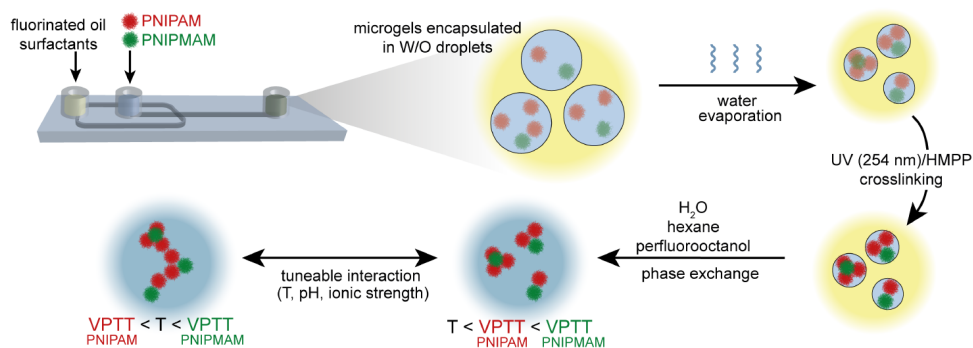


**Figure 38**

Schematic illustration showing the microfluidic generation of thermoresponsive colloidal molecules. A microfluidic flow focusing device is used to form monodisperse water droplets containing microgels. Through evaporation of the water content of the droplets, the microgel particles are forced into close contact. At this stage, the clusters can be made permanent through photocrosslinking. Following this, the clusters are washed and transferred from the oil into water where the interactions between different clusters can be studied..

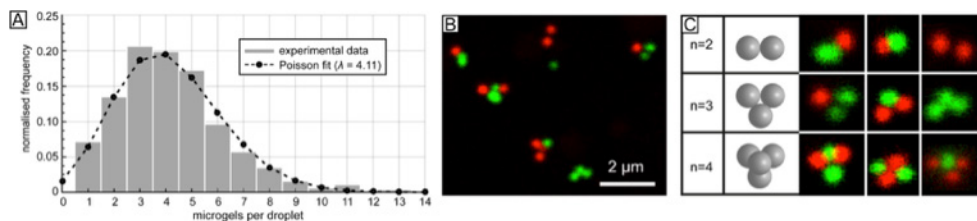


**Figure 39**

Distribution of microgels per cluster. (A) Poisson fit shows the expected number of microgels per droplet at formation, calculated from the zero-truncated Poisson distribution. (B) Chemically crosslinked clusters of PNIPAM (red) and PNIPMAM (green) in water. (C) At maximum shrinking of the droplets, clusters are forced to adopt certain conformations in order to maximise the packing efficiency, which are retained after crosslinking and transfer to water.

The number of microgels per formed droplet adopted as expected a Poisson distribution. With an aim of producing colloidal molecules with a low number of interaction sites, an average number of microgels per droplet  $n = 4$  was chosen. Dimers, trimers and tetramers with varying numbers of PNIPAM-co-MA and PNIPMAM-co-MA particles are shown, Figure 39. Depending on the final application of the thermoresponsive clusters, the method can be tuned to fabricate a library of clusters where the number of microgels per cluster can be altered by adjusting the initial concentrations of the microgels as well as by tuning the droplet volume in order to maintain a constant average ratio between the microgels.

Our results demonstrate a method for the fabrication of colloidal molecules with tuneable interaction-sites based on the spontaneous evaporation of water-in-oil emulsion droplets. The inherent thermo- and pH-responsive properties of the microgels give us the ability to finely tune the interactions between different patches/interaction sites with temperature, pH and ionic strength. With droplet microfluidics allowing for well-defined control over droplet size and composition, the resulting colloidal molecules can be tuned in terms of the average number and ratio of interaction-sites. Further, by adjusting the conversion rate for the incorporation of MA groups, the temperature-dependency of the interaction-sites can be individually tuned.

Based on the realization of colloidal molecules with tuneable patchy interactions, future work will address the quantitative investigation of the resulting directional interactions, the phase behaviour and the self-assembly of mixtures of colloidal clusters as a function of concentration.





# 11. Concluding remarks

Since deterministic lateral displacement was first presented in 2004 by Huang *et al.* [6] it has gained widespread attention and there have been numerous research studies based around this method. Already in this initial paper the inherent high sensitivity of DLD in size-based particle sorting was shown with the discrimination of submicron particles with a resolution of 10 nm. In order to further extend its capabilities we have strived towards the implementation of sorting based on additional parameters such as morphology, deformability and the dynamic properties of cells and particles.

We have shown how sorting based on shape can be realized in DLD by limiting the orientational freedom of particles. This has been used to achieve separation of *T. cyclops* and RBCs which would be indistinguishable in a traditional, deep, DLD. By tuning the device depth we can accentuate the morphological differences between these particles in order to achieve sorting by high specificity. A greatly improved device for the detection of HAT was developed with a much increased throughput while simultaneously simplifying device operations by the use of an intricate design consisting of multiple DLD arrays of different depths in series. With projected material costs being negligible, this allows for a cheap device which is capable of field-use.

We have further presented a scheme where the orientation of particles has been used in combination with deformability probing by varying the applied shear stress. In this way we achieve 'fingerprints' based on the size, shape and deformability of cell samples. This work was exemplified with normal discocytic RBCs together with chemically treated RBCs to induce the formation of stomatocytes and echinocytes. This is an interesting model system due RBCs being soft, anisotropic particles together with stomatocytes and echinocytes being potential clinical markers. The approach could be extended to clinical samples for diagnosis of diseases which are known to affect morphology and deformability of RBCs such as malaria and sickle-cell anaemia, or other areas such as parasitology, oncology or bacteriology.

The ability to sort deformable particles based on their dynamical properties has been investigated experimentally in combination with full 3D-simulations in order to provide insights into the physical mechanisms behind the cell dynamics and the resulting behaviour in the DLD. By altering the viscosity contrast of the cells and the suspending medium we promote different cell dynamics, which we show can lead to a significant change in the cell behaviour and the resulting lateral displacement. This opens up for precise sorting based on cell viscosity, and further, provides a means of controlling RBC dynamics in DLD which can be used in *e.g.* elasticity based sorting.

A scheme for the generation of thermo-responsive colloidal molecules, based on microgels has been developed. We achieved clusters consisting of a small number of microgel particles, governed by the Poisson distribution, by the evaporative removal of aqueous phase solvent followed by crosslinking and phase-exchange. An elegant approach which, depending on the final application, can be expanded to include sorting of fabricated clusters by DLD to achieve clusters of specific number of microgel particles. The ability to tune the directional patchy interactions of the formed clusters opens up several exciting opportunities for the creation of several new materials.

## 11.1. Future directions

Several interesting directions can be outlined for future work. Continuing cell sorting and analysis using DLD towards medical diagnostics would be a very exciting route to pursue. The results presented in this thesis show how sorting using DLD can be made sensitive to parameters which are known to be influenced by several blood related diseases and disorders. Potential would be in *e.g.* the sorting and detection of intracellular parasites which causes diseases such as malaria and leishmaniasis which are expected to influence the mechanical properties of cells during an invasion, opening up for the important early-stage diagnosis [239, 240]. Another subpopulation of RBCs with clinical relevance include fetal nucleated RBCs which provide an easy means of non-invasively extracting fetal genetic information for genetic diagnosis [241]. Other interesting cell types which could draw benefit from sorting schemes outlined in this work include label-free sorting of circulating tumours cells [242, 243] and peripheral blood stem cells [244, 245].

While the final sorting scheme depends on the application, designing DLD devices in series in order to fractionate particles based on multiple properties could be realized. For example, an initial size based-sorting could be used in order to separate the particles into a second stage DLD where sorting based on another parameter takes place.

Several interesting findings presented in this thesis could potentially be realized to improve the sorting abilities of DLD. Similar to how the rotational effect observed in Paper I has been exploited by using different post-shapes in a recent paper by Zeming *et al.* [55], the effect of parasites getting trapped in a U-shape configuration could also be investigated further. This configuration was seen to be very stable and once a parasite was trapped in this position, it was not observed to leave it, leading to a significant increase in lateral displacement. The distance between posts together with limiting their orientational freedom is likely to increase the significance of this effect. If realized it would potentially allow for sensitive sorting based on length of long-slender particles. This could for example include the sorting of bacteria according to chain length which is known virulence factor [246].

Another interesting area which could be investigated further is parasite sorting in other types of samples. For trypanosomes this include LNA for patients which, during palpation, display enlarged lymph glands, and additionally the examination of CSF which is a common approach to HAT stage determination.

For the temperature sensitive particles ongoing measurements are conducted to sort out clusters of specific numbers of microgels for further interaction studies. By the combination with DEP the sorting could in addition be made sensitive to charge which in turn allows for not only sorting based on the number of microgels, but also the type of microgel allowing for the precise selection of a specific type of subpopulation. The presented work allows for the fabrication of a new type of particle exhibiting thermoresponsiveness which would be highly interesting for interaction studies. For other types of applications, such as photonic materials these particles are of limited use due to their low optical density. However, this could be realized by instead using core-shell particles which, while retaining the patchy interaction of the shell, can have modified optical properties of the core.

## Throughput

Throughput is in general a limiting factor for microfluidic devices. Due to the small length scales the volumetric flow rates are often limited. Exceptions of high-throughput sorting in DLD exists [13], however by using shallow channels to enable sorting based on cell morphology we decrease the throughput, which when the particle of interest is scarce, *e.g.* for rare-cell detection, increases analysis times. Increasing the flow rates [67], would lead to an increase in shear stresses and affect the behaviour of soft particles. This could however be counteracted by modifying the shear field of the fluid, by altering the post shape, as discussed in section 3 and further in references [54, 56, 72], or the use of non-Newtonian fluids [59]. Both of these methods would alter the flow field which have the ability to, if chosen correctly, lead to a decrease of the exerted shear stresses together with an increase in throughput. Another, maybe more elegant approach would be to apply an additional force to orient non-spherical particles. Potential methods include acoustophoresis [247] and DEP [248] which have been shown capable of influencing the orientation of particles suspended in a fluid. Ongoing research in our group shows that cell orientation in DLD devices under the influence of DEP is possible and the combination of these methods has the potential to open up for high throughput morphology-based sorting. When applying the electric field, RBCs switch their behaviour from being preferentially aligned against the post to being aligned in the plane of the device, Figure 40.

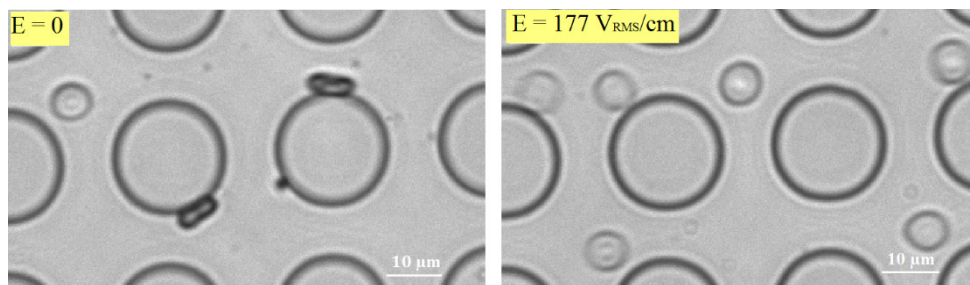


**Figure 40**

Changing the preferred orientation of RBCs in a DLD by applying an AC field. In a normal DLD, the orientation depend on the shear field of the fluid and the interaction with the posts, acting to align RBCs against the posts. However, under the influence of an AC field RBCs are seen to almost exclusively orient themselves in the plane of the device, considerably altering their effective size. Image from reference [227], used with kind permission from B. D. Ho.

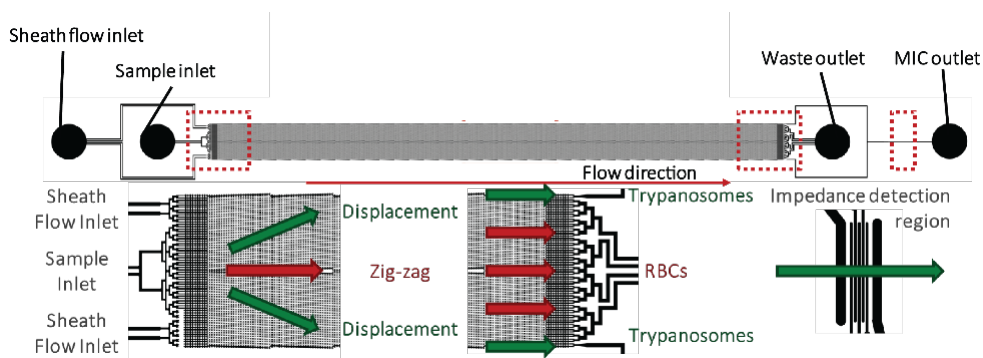


**Figure 41**  
 Combining DLD with MIC in order to get a sample-to-answer instrument for field diagnosis. By integrating electrodes to the trypanosome outlet we are able to get an electrical reading of the particles electrical properties, allowing for the discrimination between the trypanosomes and any RBCs which otherwise would end up as false-positives.

## Sample-to-answer

In order to achieve a complete device able to perform sample-to-answer diagnosis of HAT a method to read out the answer of the DLD separation is required. One approach, which was partially investigated in Paper II, is to integrate microsieve structures in the parasite outlet which, if present, captures these cells and focuses them to a small area making microscopic confirmation, *e.g.* by cell-phone based microscopes [228, 249], trivial. Pore sizes of this sieving structure down to  $1.5\ \mu\text{m}$  was possible to achieve with the current fabrication methods, however still a significant fraction of parasites was able to permeate this filter.

Other fabrication methods could achieve higher aspect ratios and consequently smaller pore sizes. Another approach would be to selectively treat the surface to promote the sticking of particles in the trypanosome outlet [91].

An elegant alternative to these optical read-out methods would be to implement electrical readout based on micro impedance cytometry (MIC) [229], which is a direction we are currently pursuing. A new device, Figure 41, fabricated by injection-moulding of cyclic-olefin-copolymer (COC) for mass pass production, with integrated electrodes has been shown capable of replicating the sorting results of Paper I and II while at the same time, with minimal user input, being able to give an answer to if parasites are present or not in the sample.

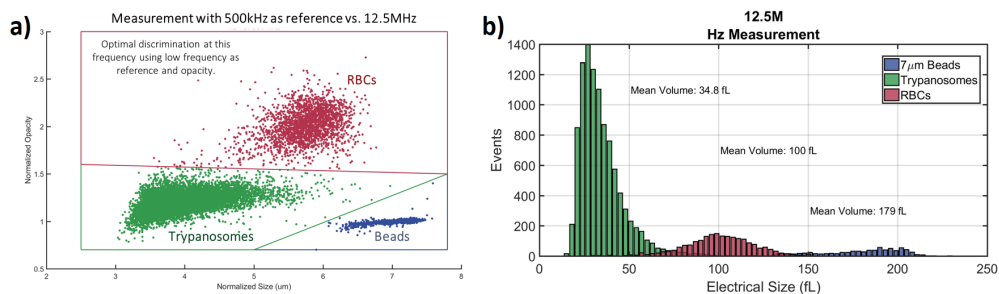


**Figure 42**

Preliminary results showing how MIC is able to, with high precision, discriminate different types of particles based on their electrical properties at specific frequencies. The combination of MIC and DLD is ideal as while MIC can discriminate between particles with high precision its limited throughput requires presorting of RBCs by DLD.

While MIC can discriminate between particles with high precision, Figure 42, the throughput is relatively limited. Particles need to be diluted in order to avoid overlapping events registered at the electrodes. By combining this technique, which has significant potential, with DLD we are able to remove a significant amount of the background particles. The small fraction of RBCs which remain after sorting in DLD, together with *e.g.* platelets can easily be discriminated by the MIC which is able to accurately capture the specific signal of a trypanosome which is based on its size and membrane polarizability. Resulting in a handheld, portable diagnostic tool which is able to go from sample-to-answer in field setting.

## Sorting of colloidal molecules

The colloidal particles where were fabricated in Paper VII have been show to have highly interesting properties. The temperature tunability of the precursor microgel particles which are retained in the finalized clusters allow for the precise control over the cluster-cluster interaction which can be very interesting for new materials and photonic crystals.

While the method proposed allows for the creation of a large library of clusters in a single step, governed by the Poisson distribution, the heterogeneity may limit the use of the final product. Consequently, in order to acquire a homogenous product, we need to sort the clusters based on its number of microgel particles. Initial studies have been carried out where the sample consists of the same precursor microgel particles, PNIPAM and PNIPMAM. The fabrication approach have been modified, which is reflected

in that the final sample has a significant number of single and tetramer microgels, with the diameter of the single microgels being  $\sim 1.0 \mu\text{m}$ . For the sorting a high throughput DLD with a critical diameter of  $D_c = 1.6 \mu\text{m}$  was fabricated. The results show high sorting performance with pure fractions both in outlet 1 (single microgels) and outlet 2 (tetramer clusters), Figure 43. Ongoing work include the quantification of the sorting performance together with characterization of the final cluster properties and their interactions.

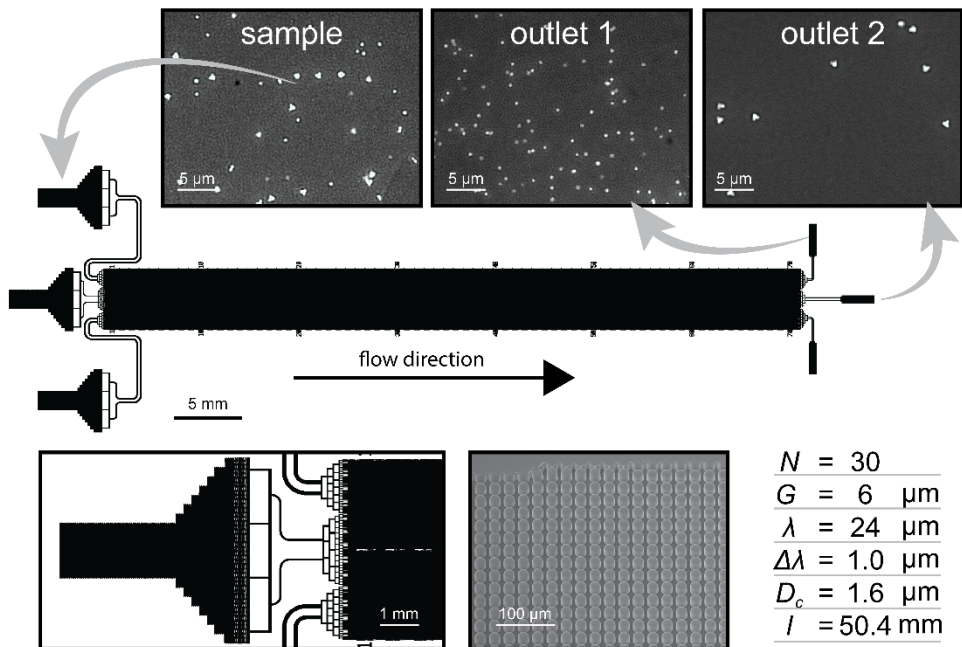


**Figure 43**

The sorting of microgel cluster particles in a DLD. Due to the fabrication method used a large number of single and tetramers clusters are present. The precursor microgel particles, same as in Paper VII, PNIPAM and PNIPMAM have a diameter of  $\sim 1.0 \mu\text{m}$  and by employing a DLD with a critical diameter of  $D_c = 1.6 \mu\text{m}$  we are able to, with high precision, separate clusters from the background of single microgel particles.





## 12. Populärvetenskaplig sammanfattning

**På många platser i världen råder svåra medicinska förhållanden. Sjukvården vi är vana vid i den industrialiserade delen av världen är långt ifrån vardagen för dessa människor. Den moderna utrustning i våra sjukhus bestående av avancerade, och dyra, instrument för en stor mängd av analyser finns inte tillgänglig. Dels på grund av dess kostnad och dels på grund av att många platser saknar tillgång till en stabil strömförsörjning som krävs för att driva dessa apparater. För att råda bot på detta och kunna utföra medicinska analyser under dessa förhållanden har vi arbetat med att utveckla så kallade lab-on-a-chip apparater med vilka vi hoppas kunna göra avancerad diagnostisk teknik tillgänglig även under svåra förhållanden i resurssvaga områden.**

Ett enkelt myggbett. En vanlig svensk sommardag är det mer regel än undantag och inget som lämnar några större efterverkningar. På andra platser i världen kan ett insektsbett vara ödesdigert om man har otur. Ett exempel på detta är tsetseflugan, som finns i stora delar av Afrika. En del av dessa flugor bär på små parasiter, som kan överföras från fluga till människa i samband med att flugan sticker. Parasiterna lever vidare i blodbanan på den smittade människan och orsakar en vad som kallas för sömnsjukan, en sjukdom som fått sitt namn på grund av att den smittade människan går in i ett koma-liknande tillstånd. Då sjukdomen drabbar några av de fattigaste länderna i Afrika där man i brist på infrastruktur och modern sjukvårdsapparat idag är tvungen att använda enkla metoder för att diagnosticera personer som man misstänker är smittade. Oftast tar man en droppe blod från personen och undersöker denna med hjälp av mikroskop för att hitta parasiten.

## Typiskt antal celler i en milliliter blod hos person infekterad av sömnsjukan

<b>Röda blodceller</b>	5 000 000 000
<b>Vita blodceller</b>	300 000
<b>Blodplättar</b>	70 000
<b>parasiter</b>	50

Tabellen visar de stora skillnaderna i koncentration mellan parasiter och normala blodceller (röda blodceller, vita blodceller och blodplättar).

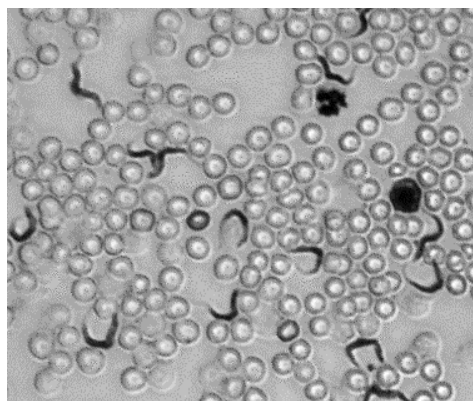
Detta är en väldigt svår uppgift då en liten droppe blod innehåller cirka

100 miljoner normala blodceller och en enda liten parasit. Att försöka hitta denna parasit och kunna ge patienten korrekt diagnos är som att hitta en nål i en höstack. Detta gör att tusentals människor dör varje år i brist på bättre diagnostiska instrument. Med hjälp av små så kallade lab-on-a-chip har vi utvecklat små, billiga och portable apparater vilka kan användas för att förbättra diagnosticeringen av denna sjukdom.

### Sömnsjukan

Sömnsjukan orsakas av en liten encellig maskliknande parasit. Dess längd är ungefär en tiondel av tjockleken av ett hårstrå. Trots att den är så liten så orsakar den svårt lidande. Om inte rätt behandling sätts in så leder en infektion till slut till döden. Parasiten överförs från en infekterad tsetsefluga till en människa medan den sticker efter blod. Parasiten förökar sig därefter i

blodsystemet och invaderar efter en tid det centrala nervsystemet. I detta stadie av sjukdomen orsakar parasiten stora neurologiska skador vilka gör att man går in i ett koma-liknande tillstånd vilket är vad som har gett sjukdomen namnet sömnsjukan. Det finns fortfarande en möjlighet att rädda patienten i detta stadie, om än med kraftigare medicinsk behandling med större biverkningar som följd. Hade man istället kunnat diagnosticera sjukdomen tidigare hade en mildare behandling kunnat användas och patienten hade haft större chans att klara sig. En tidig, och korrekt, diagnos är därför oerhört viktigt för att patienten ska få så stor chans som möjligt att överleva samt få så få biverkningar som möjligt av behandlingen.



Ett blodprov innehållandes parasiten som orsakar sömnsjukan. Observera att i detta prov har man blandat friskt blod med parasiter. I ett riktigt prov från en sjuk människa hade man istället haft cirka 1 parasit och 100 miljoner röda blodceller, vilket är anledningen till att det är så svårt att hitta parasiten i ett blodprov. Trots att den är så sällsynt i blodet och att den är så liten, så orsakar den stora skador, till och med dödliga, på den smittade personen. Därför är det viktigt att man lyckas hitta den fort så att rätt behandling kan sättas in i tid.

Då man inte har tillgång till de stora, dyra maskiner som finns på moderna sjukhus i västvärlden utförs diagnos genom att man undersöker ett blodprov i mikroskop och ser om man kan hitta en parasit. Detta är mycket problematiskt då antalet parasiter i blodet är oerhört mycket lägre än antalet blodceller, se tabellen på denna sida. Att finna en parasit bland alla dessa blodceller är som att leta efter en nål i en höstack. Som en följd av detta är det en stor del av smittade personer som inte kan få rätt diagnos i tid.

Detta är vad denna avhandling fokuserar på. Att utveckla enkla medicinska analysystem vilka kan användas under svåra förhållanden, exempelvis i fält i Afrika. För att hitta parasiten tar man en droppe blod från individen vilken vårt chip analyserar genom att sortera bort alla celler som naturligt finns i blodet. Efter detta kan man enkelt utläsa om personen har parasiter i sitt blod. Forskningen har hittills fokuserat på parasiten som orsakar sömnsjukan, men andra närbesläktade sjukdomar såsom malaria skulle potentiellt också kunna detekteras med en liknande metod.

### Lab on a chip

En lab-on-a-chip är en apparat som integrerar en eller flera laboratoriefunktioner på ett litet chip, typiskt några kvadratcentimeter stort.

Forskningsfältet är tvärvetenskapligt och spänner över fysik, biologi, kemi och elektronik. Tekniken härstammar från 1960-talet då man utvecklade metoder för att tillverka elektriska halvledarkomponenter såsom transistorer och dioder. Med i princip samma verktyg har man på senare år lyckats producera mikrometersmå kanalsystem på små ytor. Beroende på hur dessa



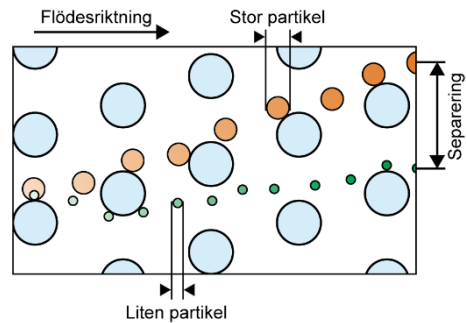
En revolution inom datorer har gjort att beräkningar som tidigare krävde datorer stora som hus nu kan utföras mycket snabbare med dagens mobiltelefoner. Många förväntar sig en liknande, medicinsk, revolution där man istället för att använda sig av ett stort analytiskt laboratorium med personal som manuellt till exempel blandar reagenter och analyserar prover så kan detta göras automatiskt i ett litet chip. Ett så kallat lab-on-a-chip. Figurer från Wikimedia commons.

kanalsystem utformas kan man få dem att utföra en mängd olika uppgifter, ofta avancerade operationer vilket tidigare krävt många steg i ett laboratorium. Exempel på applikationer som har presenterats inom detta fält inkluderar kraftfulla verktyg för analys och manipulering av enstaka celler och molekyler och verktyg för studier av nuklei nsyror.

Utvecklingen av forskningsfältet brukar ofta liknas vid datorernas utveckling, där datorer har gått från att vara stora som hus när de först introducerades till att idag finnas i var mans hand i form av en mobiltelefon. På samma sätt försöker man i detta fält ta stor, dyr och otillgänglig sjukvårdsutrustning och göra den tillgängliga för den breda massan i form av lab-on-a-chips.

### Deterministic Lateral Displacement

För att separera blodceller och parasiter med dessa chips använder vi oss av en metod som kallas för Deterministic Lateral Displacement (DLD), som kan liknas vid ett avancerat filter. Denna fungerar genom att man skapar ett stort fält av pelare som blodet får flöde förbi, se figur på denna sida. Beroende på hur man placerar dessa pelare kan man tvinga stora partiklar i en annan riktning än små partiklar, vilket ger upphov till en separation. Metoden har på senare tid använts flitigt för att separera partiklar och



Principskiss visandes ett litet område av en DLD sett uppifrån med flödet åt höger. Två partiklar flödas genom fältet av hinder och blir uppdelade på grund av deras storlekar.

celler med mycket hög noggrannhet. Det som gör den speciell är att den inte kräver någon yttre kraft, exempelvis ett elektriskt fält, vilket ofta krävs för andra typer av partikelseparation. Detta gör DLD-tekniken utomordentligt väl lämpad till att användas i små, enkla LOC-apparater avsedda att användas ute i fält.

När DLD först presenterades i 2004 av forskare på Princeton University i USA hade den stort inflytande på forskningsfältet. Det var en partikelsorteringsmetod av ej tidigare uppvisad känslighet. Metoden har därefter visat sig kapabel till att sortera en stor mängd biologiska och icke-biologiska prover, men det finns tillfällen då den konventionella DLD separationen inte fungerar. Problem uppstår när man sorterar partiklar som inte är runda. Något som i allra högsta grad gäller för diagnos av slemhinnan då man här vill sortera

bort de diskformade röda blodcellerna från den maskformade parasiten.

I en vanlig DLD separeras partiklar med avseende på deras minsta dimension. För en rund cell eller partikel är detta identiskt med dess diameter, men för en diskformad röd blodcell är det inte diametern över disken utan istället dess tjocklek. Just för röda blodceller och sömnsjukan-parasiten så är den minsta dimensionen identisk,  $\sim 2.5 \mu\text{m}$  vilket omöjliggör separation i en konventionell DLD. För att kringgå detta utvecklade vi i Lund separation baserad på form. Forskarna visade att man genom att optimera kanalhöjden kunde förstärka skillnader i form även om deras minsta dimension var identisk. Resultatet blev en nästan total separation av röda blodceller och parasiter, något som var mycket lovande för diagnosticering av sömnsjukan.

Nästa steg i detta projekt är att ta denna första prototyp till en färdig apparat som kan användas ute i fält för detektion av sömnsjukan. Frågor som måste lösas innan dess är hur man på enklast sätt kan minska analystiden och hur billiga man kan tillverka själva anordningarna.

#### **Möjligheterna med DLD**

Det vi arbetar med är att fortsätta utvecklingen av DLD. Vanligtvis brukar man sortera på storleken av en partikel, men vi arbetar med att

sortera partiklar baserat på faktorer som form och mjukhet, vilket vi utnyttjade för att kunna erhålla en noggrann separation mellan blodceller och parasiten som orsakar sömnsjukan. Vidare så gäller att ju fler faktorer av en cell man analyserar desto mer information erhåller man, något som kan vara viktigt då man vill kunna ge så säkra medicinska diagnoser som möjligt. Sortering och analysering av partiklar baserat på dessa egenskaper kan få stort genomslag för exempelvis cancerforskning och malaria. Så kallade cirkulerande tumörceller är cancerceller som finns i blodet och bidrar till att en cancer sprids i kroppen. Dessa är ofta mjukare än andra celler vilket gör att man skulle kunna hitta dem i blodet vilket skulle kunna vara viktigt för diagnosticering. En annan sjukdom man kan hoppas kunna detektera är malaria, som orsakas av en liten parasit som invaderar röda blodceller. Detta gör att de blir styvare och större än andra röda blodceller.

Den medicinska revolutionen har bara börjat. DLD tillsammans med andra tekniker kommer i framtiden bidra med instrument som tillgängliggör avancerad medicinsk diagnostik för alla. Tekniken kommer även revolutionera noggrannheten, kostnaden och tiden för ett test i dagens analytiska och medicinska laboratorium.



# 13. References

1. Le, H.P., *Progress and Trends in Ink-Jet Printing Technology*. Journal of Imaging Science and Technology, 1998. **42**(1): p. 49-62.
2. Herzenberg, L.A., D. Parks, B. Sahaf, O. Perez, M. Roederer, and L.A. Herzenberg, *The History and Future of the Fluorescence Activated Cell Sorter and Flow Cytometry: A View from Stanford*. Clinical Chemistry, 2002. **48**(10): p. 1819-1827.
3. Terry, S.C., J.H. Jerman, and J.B. Angell, *A gas chromatographic air analyzer fabricated on a silicon wafer*. IEEE Transactions on Electron Devices, 1979. **26**(12): p. 1880-1886.
4. Manz, A., Y. Miyahara, J. Miura, Y. Watanabe, H. Miyagi, and K. Sato, *Design of an open-tubular column liquid chromatograph using silicon chip technology*. Sensors and Actuators B: Chemical, 1990. **1**(1): p. 249-255.
5. Widmer, H.M., *Trends in industrial analytical chemistry*. Trends Anal. Chem., 1983. **2**: p. VIII-X.
6. Huang, L.R., E.C. Cox, R.H. Austin, and J.C. Sturm, *Continuous Particle Separation Through Deterministic Lateral Displacement*. Science, 2004. **304**(5673): p. 987-990.
7. Beech, J.P., S.H. Holm, K. Adolfsson, and J.O. Tegenfeldt, *Sorting cells by size, shape and deformability*. Lab on a Chip, 2012. **12**(6): p. 1048-1051.
8. Davis, J.A., D.W. Inglis, K.J. Morton, D.A. Lawrence, L.R. Huang, S.Y. Chou, J.C. Sturm, and R.H. Austin, *Deterministic hydrodynamics: Taking blood apart*. Proceedings of the National Academy of Sciences, 2006. **103**(40): p. 14779-14784.
9. Green, J.V., M. Radisic, and S.K. Murthy, *Deterministic lateral displacement as a means to enrich large cells for tissue engineering*. Anal Chem, 2009. **81**(21): p. 9178-82.
10. Holm, S.H., J.P. Beech, M.P. Barrett, and J.O. Tegenfeldt, *Separation of parasites from human blood using deterministic lateral displacement*. Lab on a Chip, 2011. **11**(7): p. 1326-1332.
11. Inglis, D.W., N. Herman, and G. Vesey, *Highly accurate deterministic lateral displacement device and its application to purification of fungal spores*. Biomicrofluidics, 2010. **4**(2): p. 024109.
12. Inglis, D.W., K.J. Morton, J.A. Davis, T.J. Zieziulewicz, D.A. Lawrence, R.H. Austin, and J.C. Sturm, *Microfluidic device for label-free measurement of platelet activation*. Lab on a Chip, 2008. **8**(6): p. 925-931.

13. Louterback, K., J. D'Silva, L. Liu, A. Wu, R.H. Austin, and J.C. Sturm, *Deterministic separation of cancer cells from blood at 10 mL/min*. AIP Advances, 2012. **2**(4): p. 042107.
14. Santana, S.M., M.A. Antonyak, R.A. Cerione, and B.J. Kirby, *Microfluidic isolation of cancer-cell-derived microvesicles from heterogeneous extracellular shed vesicle populations*. Biomedical microdevices, 2014. **16**(6): p. 869-877.
15. Wunsch, B.H., J.T. Smith, S.M. Gifford, C. Wang, M. Brink, R.L. Bruce, R.H. Austin, G. Stolovitzky, and Y. Astier, *Nanoscale lateral displacement arrays for the separation of exosomes and colloids down to 20 nm*. Nat Nanotechnol, 2016. **11**(11): p. 936-940.
16. Du, S. and G. Drazer, *Gravity driven deterministic lateral displacement for suspended particles in a 3D obstacle array*. Scientific Reports, 2016. **6**: p. 31428.
17. Giddings, J.C., *Unified Separation Science*. 1991: Wiley.
18. Martin, A.J.P. and R.L.M. Synge, *A new form of chromatogram employing two liquid phases: A theory of chromatography. 2. Application to the micro-determination of the higher monoamino-acids in proteins*. Biochemical Journal, 1941. **35**(12): p. 1358-1368.
19. Nguyen, N.T. and S.T. Wereley, *Fundamentals and Applications of Microfluidics*. 2002: Artech House.
20. Petersson, F., L. Åberg, A.-M. Sward-Nilsson, and T. Laurell, *Free Flow Acoustophoresis: Microfluidic-Based Mode of Particle and Cell Separation*. Analytical Chemistry, 2007. **79**(14): p. 5117-5123.
21. Akagi, T. and T. Ichiki, *Cell electrophoresis on a chip: what can we know from the changes in electrophoretic mobility?* Anal Bioanal Chem, 2008. **391**(7): p. 2433-41.
22. Hu, X., P.H. Bessette, J. Qian, C.D. Meinhart, P.S. Daugherty, and H.T. Soh, *Marker-specific sorting of rare cells using dielectrophoresis*. Proceedings of the National Academy of Sciences of the United States of America, 2005. **102**(44): p. 15757-15761.
23. Xia, N., T.P. Hunt, B.T. Mayers, E. Alsborg, G.M. Whitesides, R.M. Westervelt, and D.E. Ingber, *Combined microfluidic-micromagnetic separation of living cells in continuous flow*. Biomed Microdevices, 2006. **8**(4): p. 299-308.
24. MacDonald, M.P., G.C. Spalding, and K. Dholakia, *Microfluidic sorting in an optical lattice*. Nature, 2003. **426**: p. 421.
25. Yang, S., A. Undar, and J.D. Zahn, *A microfluidic device for continuous, real time blood plasma separation*. Lab Chip, 2006. **6**(7): p. 871-80.
26. Bow, H., I. Pivkin, M. Diez-Silva, S.J. Goldfless, M. Dao, J.C. Niles, S. Suresh, and J. Han, *A microfabricated deformability-based flow cytometer with application to malaria*. Lab on a Chip, 2011. **11**(6): p. 1065-1073.
27. Di Carlo, D., *Inertial microfluidics*. Lab Chip, 2009. **9**(21): p. 3038-46.
28. Yamada, M. and M. Seki, *Hydrodynamic filtration for on-chip particle concentration and classification utilizing microfluidics*. Lab on a Chip, 2005. **5**(11): p. 1233-1239.



29. Takagi, J., M. Yamada, M. Yasuda, and M. Seki, *Continuous particle separation in a microchannel having asymmetrically arranged multiple branches*. Lab Chip, 2005. **5**(7): p. 778-84.
30. Striegel, A.M. and A.K. Brewer, *Hydrodynamic chromatography*. Annu Rev Anal Chem (Palo Alto Calif), 2012. **5**: p. 15-34.
31. Inglis, D.W., J.A. Davis, R.H. Austin, and J.C. Sturm, *Critical particle size for fractionation by deterministic lateral displacement*. Lab Chip, 2006. **6**(5): p. 655-8.
32. Holm, S.H., J.P. Beech, M.P. Barrett, and J.O. Tegenfeldt, *Simplifying microfluidic separation devices towards field-detection of blood parasites*. Analytical Methods, 2016. **8**(16): p. 3291-3300.
33. Holm, S., J. Beech, and J.O. Tegenfeldt, *Combined density and size-based sorting in deterministic lateral displacement devices*, in *The 17th International Conference on Miniaturized Systems for Chemistry and Life Sciences ( $\mu$ TAS 2013)*. 2013: Freiburg, Germany.
34. Holm, S., J. Beech, and J. Tegenfeldt, *Density-based particle fractionation*, in *The Eighteenth International Conference on Miniaturized Systems for Chemistry and Life Sciences ( $\mu$ TAS 2014)*. 2014: San Antonio, Texas. p. 288-290.
35. Henry, E., S.H. Holm, Z. Zhang, J.P. Beech, J.O. Tegenfeldt, D.A. Fedosov, and G. Gompper, *Sorting cells by their dynamical properties*. Scientific Reports, 2016. **6**: p. 34375.
36. Barrett, M.P., J.M. Cooper, C. Regnault, S.H. Holm, J.P. Beech, J.O. Tegenfeldt, and A. Hochstetter, *Microfluidics-Based Approaches to the Isolation of African Trypanosomes*. Pathogens, 2017. **6**(4).
37. Bhagat, A.A., H. Bow, H.W. Hou, S.J. Tan, J. Han, and C.T. Lim, *Microfluidics for cell separation*. Med Biol Eng Comput, 2010. **48**(10): p. 999-1014.
38. Kersaudy-Kerhoas, M., R. Dhariwal, and M.P. Desmulliez, *Recent advances in microparticle continuous separation*. IET Nanobiotechnol, 2008. **2**(1): p. 1-13.
39. Gossett, D.R., W.M. Weaver, A.J. Mach, S.C. Hur, H.T.K. Tse, W. Lee, H. Amini, and D. Di Carlo, *Label-free cell separation and sorting in microfluidic systems*. Analytical and Bioanalytical Chemistry, 2010. **397**(8): p. 3249-3267.
40. Shields, C.W., C.D. Reyes, and G.P. Lopez, *Microfluidic cell sorting: a review of the advances in the separation of cells from debulking to rare cell isolation*. Lab on a Chip, 2015. **15**(5): p. 1230-1249.
41. Pamme, N., *Continuous flow separations in microfluidic devices*. Lab on a Chip, 2007. **7**(12): p. 1644-1659.
42. van Megen, W. and P.N. Pusey, *Dynamic light-scattering study of the glass transition in a colloidal suspension*. Physical Review A, 1991. **43**(10): p. 5429-5441.
43. Pusey, P.N., W. van Megen, P. Bartlett, B.J. Ackerson, J.G. Rarity, and S.M. Underwood, *Structure of crystals of hard colloidal spheres*. Physical Review Letters, 1989. **63**(25): p. 2753-2756.
44. Pusey, P.N. and W. van Megen, *Phase behaviour of concentrated suspensions of nearly hard colloidal spheres*. Nature, 1986. **320**: p. 340.

45. Ottewill, R.H. and N.S.J. Williams, *Study of particle motion in concentrated dispersions by tracer diffusion*. Nature, 1987. **325**: p. 232.
46. Reynolds, O., *XXIX. An experimental investigation of the circumstances which determine whether the motion of water shall be direct or sinuous, and of the law of resistance in parallel channels*. Philosophical Transactions of the Royal Society of London, 1884. **174**: p. 935-982.
47. Bruus, H., *Theoretical Microfluidics*. 2008: OUP Oxford.
48. Kamholz, A.E., B.H. Weigl, B.A. Finlayson, and P. Yager, *Quantitative Analysis of Molecular Interaction in a Microfluidic Channel: The T-Sensor*. Analytical Chemistry, 1999. **71**(23): p. 5340-5347.
49. Brody, J.P., T.D. Osborn, F.K. Forster, and P. Yager, *A planar microfabricated fluid filter*. Sensors and Actuators A: Physical, 1996. **54**(1): p. 704-708.
50. Martin, H. and B. Henrik, *A theoretical analysis of the resolution due to diffusion and size dispersion of particles in deterministic lateral displacement devices*. Journal of Micromechanics and Microengineering, 2008. **18**(7): p. 075030.
51. Lee, C.-Y., C.-L. Chang, Y.-N. Wang, and L.-M. Fu, *Microfluidic Mixing: A Review*. International Journal of Molecular Sciences, 2011. **12**(5): p. 3263-3287.
52. Beech, J.P., *Microfluidics Separation and Analysis of Biological Particles*. 2011, Lund University: Lund.
53. Davis, J.A., *Microfluidic Separation of Blood Components Through Deterministic Lateral Displacement*. 2008, Princeton University.
54. Wei, J., H. Song, Z. Shen, Y. He, X. Xu, Y. Zhang, and B.N. Li, *Numerical Study of Pillar Shapes in Deterministic Lateral Displacement Microfluidic Arrays for Spherical Particle Separation*. IEEE Trans Nanobioscience, 2015. **14**(6): p. 660-7.
55. Zeming, K.K., S. Ranjan, and Y. Zhang, *Rotational separation of non-spherical bioparticles using I-shaped pillar arrays in a microfluidic device*. Nature Communications, 2013. **4**: p. 1625.
56. Zhang, Z., E. Henry, G. Gompper, and D.A. Fedosov, *Behavior of rigid and deformable particles in deterministic lateral displacement devices with different post shapes*. J Chem Phys, 2015. **143**(24): p. 243145.
57. Beech, J.P., P. Jonsson, and J.O. Tegenfeldt, *Tipping the balance of deterministic lateral displacement devices using dielectrophoresis*. Lab on a Chip, 2009. **9**(18): p. 2698-2706.
58. Beech, J.P. and J.O. Tegenfeldt, *Tuneable separation in elastomeric microfluidics devices*. Lab on a Chip, 2008. **8**(5): p. 657-659.
59. D'Avino, G., *Non-Newtonian deterministic lateral displacement separator: theory and simulations*. Rheologica Acta, 2013. **52**(3): p. 221-236.
60. Zeming, K.K., N.V. Thakor, Y. Zhang, and C.-H. Chen, *Real-time modulated nanoparticle separation with an ultra-large dynamic range*. Lab on a Chip, 2016. **16**(1): p. 75-85.
61. Kulrattanarak, T., R.G.M. van der Sman, Y.S. Lubbersen, C.G.P.H. Schroën, H.T.M. Pham, P.M. Sarro, and R.M. Boom, *Mixed motion in deterministic ratchets due to*

- anisotropic permeability*. Journal of Colloid and Interface Science, 2011. **354**(1): p. 7-14.
62. Kulrattanak, T., R.G.M. van der Sman, C.G.P.H. Schroën, and R.M. Boom, *Analysis of mixed motion in deterministic ratchets via experiment and particle simulation*. Microfluidics and Nanofluidics, 2011. **10**(4): p. 843-853.
  63. Vernekar, R., T. Kruger, K. Loutharback, K. Morton, and D. W. Inglis, *Anisotropic permeability in deterministic lateral displacement arrays*. Lab on a Chip, 2017. **17**(19): p. 3318-3330.
  64. Inglis, D.W., *Efficient microfluidic particle separation arrays*. Applied Physics Letters, 2009. **94**(1): p. 013510.
  65. Feng, S., A.M. Skelley, A.G. Anwer, G. Liu, and D.W. Inglis, *Maximizing particle concentration in deterministic lateral displacement arrays*. Biomicrofluidics, 2017. **11**(2): p. 024121.
  66. Inglis, D.W., *A method for reducing pressure-induced deformation in silicone microfluidics*. Biomicrofluidics, 2010. **4**(2): p. 026504.
  67. Dincau, B., A. Aghilinejad, J.-H. Kim, and X. Chen, *Characterizing the High Reynolds Number Regime for Deterministic Lateral Displacement (DLD) Devices*. 2017(58455): p. V010T13A033.
  68. Vernekar, R. and T. Krüger, *Breakdown of deterministic lateral displacement efficiency for non-dilute suspensions: A numerical study*. Medical Engineering & Physics, 2015. **37**(9): p. 845-854.
  69. Hua, J., L.E. Erickson, T.Y. Yiin, and L.A. Glasgow, *A review of the effects of shear and interfacial phenomena on cell viability*. Crit Rev Biotechnol, 1993. **13**(4): p. 305-28.
  70. Leverett, L.B., J.D. Hellums, C.P. Alfrey, and E.C. Lynch, *Red Blood Cell Damage by Shear Stress*. Biophysical Journal, 1972. **12**(3): p. 257-273.
  71. Tsao, C.-W., *Polymer Microfluidics: Simple, Low-Cost Fabrication Process Bridging Academic Lab Research to Commercialized Production*. Micromachines, 2016. **7**(12): p. 225.
  72. Hyun, J.-c., J. Hyun, S. Wang, and S. Yang, *Improved pillar shape for deterministic lateral displacement separation method to maintain separation efficiency over a long period of time*. Separation and Purification Technology, 2017. **172**: p. 258-267.
  73. Loutharback, K., K.S. Chou, J. Newman, J. Puchalla, R.H. Austin, and J.C. Sturm, *Improved performance of deterministic lateral displacement arrays with triangular posts*. Microfluidics and Nanofluidics, 2010. **9**(6): p. 1143-1149.
  74. Xia, Y. and G.M. Whitesides, *SOFT LITHOGRAPHY*. Annual Review of Materials Science, 1998. **28**(1): p. 153-184.
  75. Qin, D., Y. Xia, and G.M. Whitesides, *Soft lithography for micro- and nanoscale patterning*. Nat Protoc, 2010. **5**(3): p. 491-502.
  76. Whitesides, G.M., E. Ostuni, S. Takayama, X. Jiang, and D.E. Ingber, *Soft lithography in biology and biochemistry*. Annu Rev Biomed Eng, 2001. **3**: p. 335-73.

77. Lee, J.N., C. Park, and G.M. Whitesides, *Solvent compatibility of poly(dimethylsiloxane)-based microfluidic devices*. *Analytical Chemistry*, 2003. **75**(23): p. 6544-6554.
78. Attia, U.M., S. Marson, and J.R. Alcock, *Micro-injection moulding of polymer microfluidic devices*. *Microfluidics and Nanofluidics*, 2009. **7**(1): p. 1.
79. Becker, H. and C. Gartner, *Polymer microfabrication technologies for microfluidic systems*. *Analytical and Bioanalytical Chemistry*, 2008. **390**(1): p. 89-111.
80. Becker, H. and L.E. Locascio, *Polymer microfluidic devices*. *Talanta*, 2002. **56**(2): p. 267-287.
81. Choudhury, D., J.R. Macdonald, and A.K. Kar, *Ultrafast laser inscription: perspectives on future integrated applications*. *Laser & Photonics Reviews*, 2014. **8**(6): p. 827-846.
82. Guckenberger, D.J., T.E. de Groot, A.M.D. Wan, D.J. Beebe, and E.W.K. Young, *Micromilling: a method for ultra-rapid prototyping of plastic microfluidic devices*. *Lab on a Chip*, 2015. **15**(11): p. 2364-2378.
83. Iliescu, C., H. Taylor, M. Avram, J. Miao, and S. Franssila, *A practical guide for the fabrication of microfluidic devices using glass and silicon*. *Biomicrofluidics*, 2012. **6**(1): p. 016505-016505-16.
84. Quake, S.R. and A. Scherer, *From micro- to nanofabrication with soft materials*. *Science*, 2000. **290**(5496): p. 1536-1540.
85. Sugioka, K. and Y. Cheng, *Femtosecond laser three-dimensional micro- and nanofabrication*. *Applied Physics Reviews*, 2014. **1**(4): p. 35.
86. Bhattacharjee, N., A. Urrios, S. Kang, and A. Folch, *The upcoming 3D-printing revolution in microfluidics*. *Lab on a chip*, 2016. **16**(10): p. 1720-1742.
87. Ho, C.M.B., S.H. Ng, K.H.H. Li, and Y.J. Yoon, *3D printed microfluidics for biological applications*. *Lab on a Chip*, 2015. **15**(18): p. 3627-3637.
88. Waheed, S., J.M. Cabot, N.P. Macdonald, T. Lewis, R.M. Guijt, B. Paull, and M.C. Breadmore, *3D printed microfluidic devices: enablers and barriers*. *Lab on a Chip*, 2016. **16**(11): p. 1993-2013.
89. Beck, M., M. Graczyk, I. Maximov, E.L. Sarwe, T.G.I. Ling, M. Keil, and L. Montelius, *Improving stamps for 10 nm level wafer scale nanoimprint lithography*. *Microelectronic Engineering*, 2002. **61-62**: p. 441-448.
90. Kovach, K.M., J.R. Capadona, A.S. Gupta, and J.A. Potkay, *The effects of PEG-based surface modification of PDMS microchannels on long-term hemocompatibility*. *J Biomed Mater Res A*, 2014. **102**(12): p. 4195-205.
91. Marie, R., J.P. Beech, J. Vörös, J.O. Tegenfeldt, and F. Höök, *Use of PLL-g-PEG in Micro-Fluidic Devices for Localizing Selective and Specific Protein Binding*. *Langmuir*, 2006. **22**(24): p. 10103-10108.
92. Wong, I. and C.-M. Ho, *Surface molecular property modifications for poly(dimethylsiloxane) (PDMS) based microfluidic devices*. *Microfluidics and Nanofluidics*, 2009. **7**(3): p. 291-306.

93. Crocker, J.C. and D.G. Grier, *Methods of Digital Video Microscopy for Colloidal Studies*. Journal of Colloid and Interface Science, 1996. **179**(1): p. 298-310.
94. Lichtman, M.A. and W.J. Williams, *Williams Hematology, Seventh Edition*. 2006: McGraw-Hill Companies, Incorporated.
95. Sender, R., S. Fuchs, and R. Milo, *Revised Estimates for the Number of Human and Bacteria Cells in the Body*. PLoS Biol, 2016. **14**(8): p. e1002533.
96. *Report on the Task Group on Reference Man. ICRP Publication 23.*, in *Ann ICRP*, W.S. Snyder, et al., Editors. 1975, The International Commission on Radiological Protection Oxford, England.
97. Canham, P.B., *The minimum energy of bending as a possible explanation of the biconcave shape of the human red blood cell*. Journal of Theoretical Biology, 1970. **26**(1): p. 61-81.
98. Yawata, Y., *Composition of Normal Red Cell Membranes*, in *Cell Membrane*. 2004, Wiley-VCH Verlag GmbH & Co. KGaA. p. 27-46.
99. Baskurt, O.K., M.R. Hardeman, and M.W. Rampling, *Handbook of Hemorheology and Hemodynamics*. 2007: IOS Press.
100. Kim, J., H. Lee, and S. Shin, *Advances in the measurement of red blood cell deformability: A brief review*. Journal of Cellular Biotechnology, 2015. **1**(1): p. 63-79.
101. Tomaiuolo, G., *Biomechanical properties of red blood cells in health and disease towards microfluidics*. Biomicrofluidics, 2014. **8**(5): p. 051501.
102. Kim, Y., K. Kim, and Y. Park, *Measurement Techniques for Red Blood Cell Deformability: Recent Advances*, in *Blood Cell - An Overview of Studies in Hematology*, T.E. Moschandreu, Editor. 2012, InTech: Rijeka. p. Ch. 10.
103. Walker, H.K., W.D. Hall, and J.W. Hurst, *Clinical Methods: The History, Physical, and Laboratory Examinations*. 1990, Butterworth Publishers: Boston.
104. Bessis, M., R.I. Weed, and P.F. Leblond, *Red Cell Shape: Physiology, Pathology, Ultrastructure*. 2012: Springer Berlin Heidelberg.
105. Bessis, M., *Corpuscles: Atlas of Red Blood Cell Shape*. 2012: Springer Berlin Heidelberg.
106. Hoffman, J.F., *Questions for Red Blood Cell Physiologists to Ponder in This Millenium*. Blood Cells, Molecules, and Diseases, 2001. **27**(1): p. 57-61.
107. Buttarello, M. and M. Plebani, *Automated blood cell counts: state of the art*. Am J Clin Pathol, 2008. **130**(1): p. 104-16.
108. Seo, J.Y., S.T. Lee, and S.H. Kim, *Performance evaluation of the new hematology analyzer Sysmex XN-series*. International Journal of Laboratory Hematology, 2015. **37**(2): p. 155-164.
109. Basiji, D.A., W.E. Ortyrn, L. Liang, V. Venkatachalam, and P. Morrissey, *Cellular Image Analysis and Imaging by Flow Cytometry*. Clinics in laboratory medicine, 2007. **27**(3): p. 653-viii.
110. Carpenter, A.E., T.R. Jones, M.R. Lamprecht, C. Clarke, I.H. Kang, O. Friman, D.A. Guertin, J.H. Chang, R.A. Lindquist, J. Moffat, P. Golland, and D.M. Sabatini,

- CellProfiler: image analysis software for identifying and quantifying cell phenotypes.* Genome Biology, 2006. **7**(10): p. R100.
111. Dintenfass, L., *Internal viscosity of the red cell and a blood viscosity equation.* Nature, 1968. **219**(5157): p. 956-8.
  112. Mohandas, N., M.R. Clark, M.S. Jacobs, and S.B. Shohet, *Analysis of factors regulating erythrocyte deformability.* J Clin Invest, 1980. **66**(3): p. 563-73.
  113. Jones, J.G., R. Adams, and S. Evans, *Bulk filtration through micropore membranes for analysing blood cell rheology in clinical research.* Clinical Hemorheology and Microcirculation, 1994. **14**(2): p. 149-169.
  114. Teitel, P., *Basic Principles of the 'Filterability Test' (FT) and Analysis of Erythrocyte Flow Behavior,* in *Red Cell Rheology,* M. Bessis, S.B. Shohet, and N. Mohandas, Editors. 1978, Springer Berlin Heidelberg: Berlin, Heidelberg. p. 55-70.
  115. Reid, H.L., A.J. Barnes, P.J. Lock, J.A. Dormandy, and T.L. Dormandy, *A simple method for measuring erythrocyte deformability.* Journal of Clinical Pathology, 1976. **29**(9): p. 855-858.
  116. Hochmuth, R.M., *Micropipette aspiration of living cells.* J Biomech, 2000. **33**(1): p. 15-22.
  117. Kuznetsova, T.G., M.N. Starodubtseva, N.I. Yegorenkov, S.A. Chizhik, and R.I. Zhdanov, *Atomic force microscopy probing of cell elasticity.* Micron, 2007. **38**(8): p. 824-33.
  118. Yoon, Y.Z., H. Hong, A. Brown, D.C. Kim, D.J. Kang, V.L. Lew, and P. Cicuta, *Flickering analysis of erythrocyte mechanical properties: dependence on oxygenation level, cell shape, and hydration level.* Biophys J, 2009. **97**(6): p. 1606-15.
  119. Zhang, H. and K.K. Liu, *Optical tweezers for single cells.* Journal of the Royal Society Interface, 2008. **5**(24): p. 671-690.
  120. Hou, H.W., A.A.S. Bhagat, W.C. Lee, S. Huang, J. Han, and C.T. Lim, *Microfluidic Devices for Blood Fractionation.* Micromachines, 2011. **2**(3): p. 319.
  121. Shelby, J.P., J. White, K. Ganesan, P.K. Rathod, and D.T. Chiu, *A microfluidic model for single-cell capillary obstruction by *Plasmodium falciparum*-infected erythrocytes.* Proceedings of the National Academy of Sciences, 2003. **100**(25): p. 14618-14622.
  122. Otto, O., P. Rosendahl, A. Mietke, S. Golfier, C. Herold, D. Klaue, S. Girardo, S. Pagliara, A. Ekpenyong, A. Jacobi, M. Wobus, N. Töpfer, U.F. Keyser, J. Mansfeld, E. Fischer-Friedrich, and J. Guck, *Real-time deformability cytometry: on-the-fly cell mechanical phenotyping.* Nature Methods, 2015. **12**: p. 199.
  123. Park, E.S., C. Jin, Q. Guo, R.R. Ang, S.P. Duffy, K. Matthews, A. Azad, H. Abdi, T. Todenhöfer, J. Bazov, K.N. Chi, P.C. Black, and H. Ma, *Continuous Flow Deformability-Based Separation of Circulating Tumor Cells Using Microfluidic Ratchets.* Small, 2016. **12**(14): p. 1909-1919.
  124. Shaw Bagnall, J., S. Byun, D.T. Miyamoto, J.H. Kang, S. Maheswaran, S.L. Stott, M. Toner, and S.R. Manalis, *Deformability-based cell selection with downstream*

- immunofluorescence analysis*. Integrative biology : quantitative biosciences from nano to macro, 2016. **8**(5): p. 654-664.
125. Zhang, J., S. Yan, D. Yuan, G. Alici, N.-T. Nguyen, M. Ebrahimi Warkiani, and W. Li, *Fundamentals and applications of inertial microfluidics: a review*. Lab on a Chip, 2016. **16**(1): p. 10-34.
  126. Hou, H.W., A.A.S. Bhagat, J. Han, and C.T. Lim, *Deformability Based Cell Margination – A Simple Microfluidic Design for Malarial Infected Red Blood Cell Filtration*. 2010: p. 1671-1674.
  127. Hur, S.C., N.K. Henderson-MacLennan, E.R. McCabe, and D. Di Carlo, *Deformability-based cell classification and enrichment using inertial microfluidics*. Lab Chip, 2011. **11**(5): p. 912-20.
  128. Fedosov, D.A., M. Peltomaki, and G. Gompper, *Deformation and dynamics of red blood cells in flow through cylindrical microchannels*. Soft Matter, 2014. **10**(24): p. 4258-4267.
  129. Sheetz, M.P. and S.J. Singer, *Biological membranes as bilayer couples. A molecular mechanism of drug-erythrocyte interactions*. Proc Natl Acad Sci U S A, 1974. **71**(11): p. 4457-61.
  130. Yawata, Y., *Acanthocytosis and Its Related Disorders*, in *Cell Membrane*. 2004, Wiley-VCH Verlag GmbH & Co. KGaA. p. 251-260.
  131. Li, A., H. Seipelt, C. Muller, Y. Shi, and M. Artmann, *Effects of salicylic acid derivatives on red blood cell membranes*. Pharmacol Toxicol, 1999. **85**(5): p. 206-11.
  132. Reinhart, W.H., N.Z. Piety, J.S. Goede, and S.S. Shevkopyas, *Effect of osmolality on erythrocyte rheology and perfusion of an artificial microvascular network*. Microvascular research, 2015. **98**: p. 102-107.
  133. Rasia, M. and A. Bollini, *Red blood cell shape as a function of medium's ionic strength and pH*. Biochimica et Biophysica Acta (BBA) - Biomembranes, 1998. **1372**(2): p. 198-204.
  134. Gedde, M.M., E. Yang, and W.H. Huestis, *Resolution of the paradox of red cell shape changes in low and high pH*. Biochim Biophys Acta, 1999. **1417**(2): p. 246-53.
  135. Barrett, M.P., R.J.S. Burchmore, A. Stich, J.O. Lazzari, A.C. Frasch, J.J. Cazzulo, and S. Krishna, *The trypanosomiasis*. The Lancet, 2003. **362**(9394): p. 1469-1480.
  136. Gillespie, S.H., G.L. Smith, and A. Osbourn, *Microbe-vector Interactions in Vector-borne Diseases*. 2004: Cambridge University Press.
  137. Brun, R., J. Blum, F. Chappuis, and C. Burri, *Human African trypanosomiasis*. The Lancet. **375**(9709): p. 148-159.
  138. *Trypanosoma*. The Australian society for parasitology 2010 [cited 2017 2017-12-17]; Available from: <http://parasite.org.au/>.
  139. Mazutis, L., J. Gilbert, W.L. Ung, D.A. Weitz, A.D. Griffiths, and J.A. Heyman, *Single-cell analysis and sorting using droplet-based microfluidics*. Nature protocols, 2013. **8**(5): p. 870-891.
  140. Franco, J.R., P.P. Simarro, A. Diarra, and J.G. Jannin, *Epidemiology of human African trypanosomiasis*. Clinical Epidemiology, 2014. **6**: p. 257-275.

141. Majekodunmi, A.O., A. Fajinmi, C. Dongkum, K. Picozzi, M.V. Thrusfield, and S.C. Welburn, *A longitudinal survey of African animal trypanosomiasis in domestic cattle on the Jos Plateau, Nigeria: prevalence, distribution and risk factors*. *Parasites & Vectors*, 2013. **6**(1): p. 239.
142. Rassi, A., Jr., A. Rassi, and J. Marcondes de Rezende, *American trypanosomiasis (Chagas disease)*. *Infect Dis Clin North Am*, 2012. **26**(2): p. 275-91.
143. Alvar, J., I.D. Vélez, C. Bern, M. Herrero, P. Desjeux, J. Cano, J. Jannin, M.d. Boer, and W.H.O.L.C.T. the, *Leishmaniasis Worldwide and Global Estimates of Its Incidence*. *PLOS ONE*, 2012. **7**(5): p. e35671.
144. Duggan, A.J. and M.P. Hutchinson, *Sleeping sickness in Europeans: a review of 109 cases*. *J Trop Med Hyg*, 1966. **69**(6): p. 124-31.
145. Masocha, W. and K. Kristensson, *Passage of parasites across the blood-brain barrier*. *Virulence*, 2012. **3**(2): p. 202-212.
146. Odiit, M., F. Kansime, and J.C. Enyaru, *Duration of symptoms and case fatality of sleeping sickness caused by Trypanosoma brucei rhodesiense in Tororo, Uganda*. *East Afr Med J*, 1997. **74**(12): p. 792-5.
147. Stevens, J., H. Noyes, and W. Gibson, *The Evolution of Trypanosomes Infecting Humans and Primates*. *Memórias do Instituto Oswaldo Cruz*, 1998. **93**: p. 669-676.
148. Commons, C. *Attribution-NonCommercial 4.0 2017* [cited 2017 2017-12-13]; Available from: <https://creativecommons.org/licenses/by-nc/4.0/deed.en>.
149. CDC. *Parasites - African Trypanosomiasis*. 2018 [cited 2018; Available from: <https://www.cdc.gov/parasites/sleepingsickness/>].
150. Utzinger, J., S.L. Becker, S. Knopp, J. Blum, A.L. Neumayr, J. Keiser, and C.F. Hatz, *Neglected tropical diseases: diagnosis, clinical management, treatment and control*. *Swiss Med Wkly*, 2012. **142**: p. w13727.
151. *World Health Organization, Accelerating work to overcome the global impact of neglected tropical diseases: a roadmap for implementation*. 2012 October 2017]; Available from: [http://www.who.int/neglected\\_diseases/NTD\\_RoadMap\\_2012\\_Fullversion.pdf](http://www.who.int/neglected_diseases/NTD_RoadMap_2012_Fullversion.pdf).
152. Vickerman, K., L. Tetley, K.A. Hendry, and C.M. Turner, *Biology of African trypanosomes in the tsetse fly*. *Biol Cell*, 1988. **64**(2): p. 109-19.
153. Barry, J.D. and R. McCulloch, *Antigenic variation in trypanosomes: enhanced phenotypic variation in a eukaryotic parasite*. *Adv Parasitol*, 2001. **49**: p. 1-70.
154. Morrison, L.J., L. Marcello, and R. McCulloch, *Antigenic variation in the African trypanosome: molecular mechanisms and phenotypic complexity*. *Cellular Microbiology*, 2009. **11**(12): p. 1724-1734.
155. Eperon, G., M. Balasegaram, J. Potet, C. Mowbray, O. Valverde, and F. Chappuis, *Treatment options for second-stage gambiense human African trypanosomiasis*. *Expert Review of Anti-Infective Therapy*, 2014. **12**(11): p. 1407-1417.
156. Matovu, E., J.C.K. Enyaru, D. Legros, C. Schmid, T. Seebeck, and R. Kaminsky, *Melarsoprol refractory T. b. gambiense from Omugo, north-western Uganda*. *Tropical Medicine & International Health*, 2001. **6**(5): p. 407-411.



157. Delespaux, V. and H.P. de Koning, *Drugs and drug resistance in African trypanosomiasis*. Drug Resist Updat, 2007. **10**(1-2): p. 30-50.
158. Alirol, E., D. Schruppf, J. Amici Heradi, A. Riedel, C. de Patoul, M. Quere, and F. Chappuis, *Nifurtimox-Eflornithine Combination Therapy for Second-Stage Gambiense Human African Trypanosomiasis: Médecins Sans Frontières Experience in the Democratic Republic of the Congo*. Clinical Infectious Diseases, 2013. **56**(2): p. 195-203.
159. Robays, J., M.M.C. Bilengue, P.V.d. Stuyft, and M. Boelaert, *The effectiveness of active population screening and treatment for sleeping sickness control in the Democratic Republic of Congo*. Tropical Medicine & International Health, 2004. **9**(5): p. 542-550.
160. Chappuis, F., L. Loutan, P. Simarro, V. Lejon, and P. Büscher, *Options for Field Diagnosis of Human African Trypanosomiasis*. Clinical Microbiology Reviews, 2005. **18**(1): p. 133-146.
161. Woo, P.T., *The haematocrit centrifuge technique for the diagnosis of African trypanosomiasis*. Acta Trop, 1970. **27**(4): p. 384-6.
162. Lutumba, P., J. Robays, C. Miaka, V. Kande, D. Mumba, P. Büscher, B. Dujardin, and M. Boelaert, *Validité, coût et faisabilité de la mAECT et CTC comme tests de confirmation dans la détection de la Trypanosomiase Humaine Africaine*. Tropical Medicine & International Health, 2006. **11**(4): p. 470-478.
163. Lumsden, W.H.R., C.D. Kimber, P. Dukes, L. Haller, A. Stanghellini, and G. Duvallet, *Field diagnosis of sleeping sickness in the Ivory Coast. I. Comparison of the miniature anion-exchange/centrifugation technique with other protozoological methods*. Transactions of the Royal Society of Tropical Medicine and Hygiene, 1981. **75**(2): p. 242-250.
164. Ancelle, T., A. Paugam, F. Bourlioux, A. Merad, and J.P. Vigier, *[Detection of trypanosomes in blood by the Quantitative Buffy Coat (QBC) technique: experimental evaluation]*. Med Trop (Mars), 1997. **57**(3): p. 245-8.
165. Bailey, J.W. and D.H. Smith, *The quantitative buffy coat for the diagnosis of trypanosomes*. Trop Doct, 1994. **24**(2): p. 54-6.
166. Mattia, A.R., M.A. Waldron, and L.S. Sierra, *Use of the Quantitative Buffy Coat system for detection of parasitemia in patients with babesiosis*. J Clin Microbiol, 1993. **31**(10): p. 2816-8.
167. WHO, *Control and surveillance of human African trypanosomiasis: report of a WHO expert committee, in technical report series; no. 984*, WHO, Editor. 2013: Geneva.
168. Truc, P., V. Jamonneau, P. N'Guessan, P.B. Diallo, and A. Garcia, *Parasitological diagnosis of human African trypanosomiasis: a comparison of the QBC® and miniature anion-exchange centrifugation techniques*. Transactions of The Royal Society of Tropical Medicine and Hygiene, 1998. **92**(3): p. 288-289.
169. Lumsden, W.H., C.D. Kimber, D.A. Evans, and S.J. Doig, *Trypanosoma brucei: Miniature anion-exchange centrifugation technique for detection of low*

- parasitaemias: Adaptation for field use*. Trans R Soc Trop Med Hyg, 1979. **73**(3): p. 312-7.
170. FIND. *Diagnosis of human African trypanosomiasis by acridine orange fluorescence microscopy*. LABORATORY PROTOCOL 2010 2010 [cited 2017 2017-12-30]; 1.1:[Available from: [https://www.finddx.org/wp-content/uploads/2016/03/protocol\\_for\\_hat\\_diagnosis\\_by\\_AO\\_FM\\_FIND\\_15JUN10.pdf](https://www.finddx.org/wp-content/uploads/2016/03/protocol_for_hat_diagnosis_by_AO_FM_FIND_15JUN10.pdf)].
  171. Njogu, R.M. and J.K. Kiaira, *Trypanosoma brucei: A quick method for separating blood-stream trypomastigotes from infected blood by differential osmotic lysis*. Comparative Biochemistry and Physiology Part A: Physiology, 1982. **71**(2): p. 265-269.
  172. Matovu, E., A. Kazibwe, A. Boobo, S. Biéler, and J. Ndung'u, *Revisiting Red Blood Cell Lysis as a Critical Step in Demonstrating Trypanosomes in Patient Blood*. 2010. **2017**(2017-10-16).
  173. Biéler, S., E. Matovu, P. Mitashi, E. Ssewanyana, S.K. Bi Shamamba, P.R. Bessell, and J.M. Ndung'u, *Improved detection of Trypanosoma brucei by lysis of red blood cells, concentration and LED fluorescence microscopy*. Acta Tropica, 2012. **121**(2): p. 135-140.
  174. Truc, P., V. Lejon, E. Magnus, V. Jamonneau, A. Nangouma, D. Verloo, L. Penchenier, and P. Buscher, *Evaluation of the micro-CATT, CATT/Trypanosoma brucei gambiense, and LATEX/T b gambiense methods for serodiagnosis and surveillance of human African trypanosomiasis in West and Central Africa*. Bull World Health Organ, 2002. **80**(11): p. 882-6.
  175. Jamonneau, V., P. Truc, A. Garcia, E. Magnus, and P. Büscher, *Preliminary evaluation of LATEX/T. b. gambiense and alternative versions of CATT/T. b. gambiense for the serodiagnosis of Human African Trypanosomiasis of a population at risk in Côte d'Ivoire: considerations for mass-screening*. Acta Tropica, 2000. **76**(2): p. 175-183.
  176. WHO, *Report on African trypanosomiasis*, TDR/SWG/01, Editor. 2001: Geneva, Switzerland.
  177. Lutumba, P., F. Meheus, J. Robays, C. Miaka, V. Kande, P. Büscher, B. Dujardin, and M. Boelaert, *Cost-effectiveness of Algorithms for Confirmation Test of Human African Trypanosomiasis*. Emerging Infectious Diseases, 2007. **13**(10): p. 1484-1490.
  178. Murray, M., P.K. Murray, and W.I.M. McIntyre, *An improved parasitological technique for the diagnosis of African trypanosomiasis*. Transactions of the Royal Society of Tropical Medicine and Hygiene, 1977. **71**(4): p. 325-326.
  179. Gunther, A. and K.F. Jensen, *Multiphase microfluidics: from flow characteristics to chemical and materials synthesis*. Lab on a Chip, 2006. **6**(12): p. 1487-1503.
  180. Song, H., D.L. Chen, and R.F. Ismagilov, *Reactions in Droplets in Microfluidic Channels*. Angewandte Chemie (International ed. in English), 2006. **45**(44): p. 7336-7356.

181. Ajaev, V.S. and G.M. Homsy, *Modeling shapes and dynamics of confined bubbles*. Annual Review of Fluid Mechanics, 2006. **38**: p. 277-307.
182. Umbanhowar, P.B., V. Prasad, and D.A. Weitz, *Monodisperse Emulsion Generation via Drop Break Off in a Coflowing Stream*. Langmuir, 2000. **16**(2): p. 347-351.
183. Teh, S.-Y., R. Lin, L.-H. Hung, and A.P. Lee, *Droplet microfluidics*. Lab on a Chip, 2008. **8**(2): p. 198-220.
184. Simon, M. and A. Lee, *Microfluidic Droplet Manipulations and Their Applications*, ed. P. Day, A. Manz, and Y. Zhang. 2012: Springer-Verlag. 23-50.
185. Kim, J.H., T.Y. Jeon, T.M. Choi, T.S. Shim, S.H. Kim, and S.M. Yang, *Droplet microfluidics for producing functional microparticles*. Langmuir, 2014. **30**(6): p. 1473-88.
186. Clausell-Tormos, J., D. Lieber, J.C. Baret, A. El-Harrak, O.J. Miller, L. Frenz, J. Blouwolff, K.J. Humphry, S. Koster, H. Duan, C. Holtze, D.A. Weitz, A.D. Griffiths, and C.A. Merten, *Droplet-based microfluidic platforms for the encapsulation and screening of Mammalian cells and multicellular organisms*. Chem Biol, 2008. **15**(5): p. 427-37.
187. Tan, Y.-C., K. Hettiarachchi, M. Siu, Y.-R. Pan, and A.P. Lee, *Controlled Microfluidic Encapsulation of Cells, Proteins, and Microbeads in Lipid Vesicles*. Journal of the American Chemical Society, 2006. **128**(17): p. 5656-5658.
188. Hindson, B.J., K.D. Ness, D.A. Masquelier, P. Belgrader, N.J. Heredia, A.J. Makarewicz, I.J. Bright, M.Y. Lucero, A.L. Hiddessen, T.C. Legler, T.K. Kitano, M.R. Hodel, J.F. Petersen, P.W. Wyatt, E.R. Steenblock, P.H. Shah, L.J. Bousse, C.B. Troup, J.C. Mellen, D.K. Wittmann, N.G. Erndt, T.H. Cauley, R.T. Koehler, A.P. So, S. Dube, K.A. Rose, L. Montesclaros, S. Wang, D.P. Stumbo, S.P. Hodges, S. Romine, F.P. Milanovich, H.E. White, J.F. Regan, G.A. Karlin-Neumann, C.M. Hindson, S. Saxonov, and B.W. Colston, *High-Throughput Droplet Digital PCR System for Absolute Quantitation of DNA Copy Number*. Analytical Chemistry, 2011. **83**(22): p. 8604-8610.
189. Xu, S., Z. Nie, M. Seo, P. Lewis, E. Kumacheva, H.A. Stone, P. Garstecki, D.B. Weibel, I. Gitlin, and G.M. Whitesides, *Generation of Monodisperse Particles by Using Microfluidics: Control over Size, Shape, and Composition*. Angewandte Chemie, 2005. **117**(5): p. 734-738.
190. Song, Y.J., J. Hormes, and C. Kumar, *Microfluidic synthesis of nanomaterials*. Small, 2008. **4**(6): p. 698-711.
191. Dendukuri, D. and P.S. Doyle, *The Synthesis and Assembly of Polymeric Microparticles Using Microfluidics*. Advanced Materials, 2009. **21**(41): p. 4071-4086.
192. Bhattacharya, S., A. Datta, J.M. Berg, and S. Gangopadhyay, *Studies on surface wettability of poly(dimethyl) siloxane (PDMS) and glass under oxygen-plasma treatment and correlation with bond strength*. Journal of Microelectromechanical Systems, 2005. **14**(3): p. 590-597.
193. Rosen, M.J., *Frontmatter*, in *Surfactants and Interfacial Phenomena*. 2004, John Wiley & Sons, Inc. p. i-xiii.

194. Baret, J.C., *Surfactants in droplet-based microfluidics*. Lab Chip, 2012. **12**(3): p. 422-33.
195. Roach, L.S., H. Song, and R.F. Ismagilov, *Controlling Nonspecific Protein Adsorption in a Plug-Based Microfluidic System by Controlling Interfacial Chemistry Using Fluorous-Phase Surfactants*. Analytical Chemistry, 2005. **77**(3): p. 785-796.
196. Zhu, P. and L. Wang, *Passive and active droplet generation with microfluidics: a review*. Lab on a Chip, 2017. **17**(1): p. 34-75.
197. Chong, Z.Z., S.H. Tan, A.M. Ganan-Calvo, S.B. Tor, N.H. Loh, and N.T. Nguyen, *Active droplet generation in microfluidics*. Lab on a Chip, 2016. **16**(1): p. 35-58.
198. Collins, D.J., A. Neild, A. deMello, A.Q. Liu, and Y. Ai, *The Poisson distribution and beyond: methods for microfluidic droplet production and single cell encapsulation*. Lab Chip, 2015. **15**(17): p. 3439-59.
199. Baroud, C.N., F. Gallaire, and R. Dangla, *Dynamics of microfluidic droplets*. Lab Chip, 2010. **10**(16): p. 2032-45.
200. Anna, S.L., *Droplets and Bubbles in Microfluidic Devices*. Annual Review of Fluid Mechanics, 2016. **48**(1): p. 285-309.
201. Christopher, G.F. and S.L. Anna, *Microfluidic methods for generating continuous droplet streams*. Journal of Physics D: Applied Physics, 2007. **40**(19): p. R319.
202. Seemann, R., M. Brinkmann, T. Pfohl, and S. Herminghaus, *Droplet based microfluidics*. Rep Prog Phys, 2012. **75**(1): p. 016601.
203. Zhao, C.-X. and A.P.J. Middelberg, *Two-phase microfluidic flows*. Chemical Engineering Science, 2011. **66**(7): p. 1394-1411.
204. Thorsen, T., R.W. Roberts, F.H. Arnold, and S.R. Quake, *Dynamic pattern formation in a vesicle-generating microfluidic device*. Phys Rev Lett, 2001. **86**(18): p. 4163-6.
205. Xu, J.H., S.W. Li, J. Tan, Y.J. Wang, and G.S. Luo, *Preparation of highly monodisperse droplet in a T-junction microfluidic device*. AIChE Journal, 2006. **52**(9): p. 3005-3010.
206. Anna, S.L., N. Bontoux, and H.A. Stone, *Formation of dispersions using "flow focusing" in microchannels*. Applied Physics Letters, 2003. **82**(3): p. 364-366.
207. Dreyfus, R., P. Tabeling, and H. Willaime, *Ordered and Disordered Patterns in Two-Phase Flows in Microchannels*. Physical Review Letters, 2003. **90**(14): p. 144505.
208. Ganan-Calvo, A.M. and J.M. Gordillo, *Perfectly monodisperse microbubbling by capillary flow focusing*. Phys Rev Lett, 2001. **87**(27 Pt 1): p. 274501.
209. Garstecki, P., I. Gitlin, W. DiLuzio, G.M. Whitesides, E. Kumacheva, and H.A. Stone, *Formation of monodisperse bubbles in a microfluidic flow-focusing device*. Applied Physics Letters, 2004. **85**(13): p. 2649-2651.
210. Malloggi, F., N. Pannacci, R. Attia, F. Monti, P. Mary, H. Willaime, P. Tabeling, B. Cabane, and P. Poncet, *Monodisperse colloids synthesized with nanofluidic technology*. Langmuir, 2010. **26**(4): p. 2369-73.

211. Priest, C., S. Herminghaus, and R. Seemann, *Generation of monodisperse gel emulsions in a microfluidic device*. Applied Physics Letters, 2006. **88**(2): p. 024106.
212. Dangla, R., S.C. Kayi, and C.N. Baroud, *Droplet microfluidics driven by gradients of confinement*. Proceedings of the National Academy of Sciences, 2013. **110**(3): p. 853-858.
213. Rémi, D., F. Etienne, L. Yonatan, and N.B. Charles, *The physical mechanisms of step emulsification*. Journal of Physics D: Applied Physics, 2013. **46**(11): p. 114003.
214. van Dijke, K., G. Veldhuis, K. Schroen, and R. Boom, *Parallelized edge-based droplet generation (EDGE) devices*. Lab Chip, 2009. **9**(19): p. 2824-30.
215. Garstecki, P., H.A. Stone, and G.M. Whitesides, *Mechanism for Flow-Rate Controlled Breakup in Confined Geometries: A Route to Monodisperse Emulsions*. Physical Review Letters, 2005. **94**(16): p. 164501.
216. Utada, A.S., A. Fernandez-Nieves, H.A. Stone, and D.A. Weitz, *Dripping to jetting transitions in coflowing liquid streams*. Phys Rev Lett, 2007. **99**(9): p. 094502.
217. Suryo, R. and O.A. Basaran, *Tip streaming from a liquid drop forming from a tube in a co-flowing outer fluid*. Physics of Fluids, 2006. **18**(8): p. 082102.
218. Zhu, P., T. Kong, Z. Kang, X. Tian, and L. Wang, *Tip-multi-breaking in Capillary Microfluidic Devices*. Sci Rep, 2015. **5**: p. 11102.
219. Rayleigh, L., *On The Instability Of Jets*. Proceedings of the London Mathematical Society, 1878. **s1-10**(1): p. 4-13.
220. Gau, H., S. Herminghaus, P. Lenz, and R. Lipowsky, *Liquid Morphologies on Structured Surfaces: From Microchannels to Microchips*. Science, 1999. **283**(5398): p. 46.
221. Zhu, P., T. Kong, L. Lei, X. Tian, Z. Kang, and L. Wang, *Droplet Breakup in Expansion-contraction Microchannels*. Scientific Reports, 2016. **6**: p. 21527.
222. Kreutz, J.E., T. Munson, T. Huynh, F. Shen, W. Du, and R.F. Ismagilov, *Theoretical Design and Analysis of Multivolume Digital Assays with Wide Dynamic Range Validated Experimentally with Microfluidic Digital PCR*. Analytical Chemistry, 2011. **83**(21): p. 8158-8168.
223. Ward, T., M. Faivre, M. Abkarian, and H.A. Stone, *Microfluidic flow focusing: Drop size and scaling in pressure versus flow-rate-driven pumping*. ELECTROPHORESIS, 2005. **26**(19): p. 3716-3724.
224. Xu, Q., M. Hashimoto, T.T. Dang, T. Hoare, D.S. Kohane, G.M. Whitesides, R. Langer, and D.G. Anderson, *Preparation of Monodisperse Biodegradable Polymer Microparticles Using a Microfluidic Flow-Focusing Device for Controlled Drug Delivery*. Small, 2009. **5**(13): p. 1575-1581.
225. Wang, J.-T., J. Wang, and J.-J. Han, *Fabrication of Advanced Particles and Particle-Based Materials Assisted by Droplet-Based Microfluidics*. Small, 2011. **7**(13): p. 1728-1754.
226. Zhao, Y., L. Shang, Y. Cheng, and Z. Gu, *Spherical Colloidal Photonic Crystals*. Accounts of Chemical Research, 2014. **47**(12): p. 3632-3642.

227. Ho, B.D., *Deterministic Sorting by Electrical Properties and Morphology*, in *Physics*. 2017, Lund University: Lund.
228. Gorocs, Z. and A. Ozcan, *On-chip biomedical imaging*. IEEE Rev Biomed Eng, 2013. **6**: p. 29-46.
229. McGrath, J.S., C. Honrado, D. Spencer, B. Horton, H.L. Bridle, and H. Morgan, *Analysis of Parasitic Protozoa at the Single-cell Level using Microfluidic Impedance Cytometry*. Scientific Reports, 2017. **7**: p. 2601.
230. Beech, J., T. Mäkelä, P. Majander, and J. Tegenfeldt, *Throughput through thin-film fluidics*, in *Twelfth International Conference on Miniaturized Systems for Chemistry and Life Sciences ( $\mu$ TAS)*. 2008: San Diego, California, USA.
231. Barteneva, N.S., E. Fasler-Kan, and I.A. Vorobjev, *Imaging Flow Cytometry: Coping with Heterogeneity in Biological Systems*. Journal of Histochemistry and Cytochemistry, 2012. **60**(10): p. 723-733.
232. Hardeman, M.R., J.G. Dobbe, and C. Ince, *The Laser-assisted Optical Rotational Cell Analyzer (LORCA) as red blood cell aggregometer*. Clin Hemorheol Microcirc, 2001. **25**(1): p. 1-11.
233. Guck, J., R. Ananthakrishnan, H. Mahmood, T.J. Moon, C.C. Cunningham, and J. Käs, *The optical stretcher: a novel laser tool to micromanipulate cells*. Biophysical Journal, 2001. **81**(2): p. 767-784.
234. Bow, H., I.V. Pivkin, M. Diez-Silva, S.J. Goldfless, M. Dao, J.C. Niles, S. Suresh, and J. Han, *A microfabricated deformability-based flow cytometer with application to malaria*. Lab Chip, 2011. **11**(6): p. 1065-73.
235. Yazdani, A.Z. and P. Bagchi, *Phase diagram and breathing dynamics of a single red blood cell and a biconcave capsule in dilute shear flow*. Phys Rev E Stat Nonlin Soft Matter Phys, 2011. **84**(2 Pt 2): p. 026314.
236. Tran-Son-Tay, R., S.P. Sutera, and P.R. Rao, *Determination of red blood cell membrane viscosity from rheoscopic observations of tank-treading motion*. Biophysical Journal, 1984. **46**(1): p. 65-72.
237. Grover, W.H., A.K. Bryan, M. Diez-Silva, S. Suresh, J.M. Higgins, and S.R. Manalis, *Measuring single-cell density*. Proceedings of the National Academy of Sciences, 2011. **108**(27): p. 10992.
238. Augustsson, P., J.T. Karlsen, H.W. Su, H. Bruus, and J. Voldman, *Iso-acoustic focusing of cells for size-insensitive acousto-mechanical phenotyping*. Nature Communications, 2016. **7**: p. 9.
239. Laloo, D.G., D. Shingadia, G. Pasvol, P.L. Chiodini, C.J. Whitty, N.J. Beeching, D.R. Hill, D.A. Warrell, and B.A. Bannister, *UK malaria treatment guidelines*. Journal of Infection, 2007. **54**(2): p. 111-121.
240. Croft, S.L., M.P. Barrett, and J.A. Urbina, *Chemotherapy of trypanosomiasis and leishmaniasis*. Trends in Parasitology, 2005. **21**(11): p. 508-512.
241. He, Z., F. Guo, C. Feng, B. Cai, J.P. Lata, R. He, Q. Huang, X. Yu, L. Rao, H. Liu, S. Guo, W. Liu, Y. Zhang, T.J. Huang, and X. Zhao, *Fetal nucleated red blood cell*

- analysis for non-invasive prenatal diagnostics using a nanostructure microchip.* Journal of Materials Chemistry B, 2017. **5**(2): p. 226-235.
242. Allard, W.J., J. Matera, M.C. Miller, M. Repollet, M.C. Connelly, C. Rao, A.G.J. Tibbe, J.W. Uhr, and L.W.M.M. Terstappen, *Tumor Cells Circulate in the Peripheral Blood of All Major Carcinomas but not in Healthy Subjects or Patients With Nonmalignant Diseases.* Clinical Cancer Research, 2004. **10**(20): p. 6897-6904.
243. Massagué, J. and A.C. Obenauf, *Metastatic colonization by circulating tumour cells.* Nature, 2016. **529**: p. 298.
244. Anasetti , C., B.R. Logan , S.J. Lee , E.K. Waller , D.J. Weisdorf , J.R. Wingard , C.S. Cutler , P. Westervelt , A. Woolfrey , S. Couban , G. Ehninger , L. Johnston , R.T. Maziarz , M.A. Pulsipher , D.L. Porter , S. Mineishi , J.M. McCarty , S.P. Khan , P. Anderlini , W.I. Bensinger , S.F. Leitman , S.D. Rowley , C. Bredeson , S.L. Carter , M.M. Horowitz , and D.L. Confer *Peripheral-Blood Stem Cells versus Bone Marrow from Unrelated Donors.* New England Journal of Medicine, 2012. **367**(16): p. 1487-1496.
245. Chong, P.P., L. Selvaratnam, A.A. Abbas, and T. Kamarul, *Human peripheral blood derived mesenchymal stem cells demonstrate similar characteristics and chondrogenic differentiation potential to bone marrow derived mesenchymal stem cells.* J Orthop Res, 2012. **30**(4): p. 634-42.
246. Beech, J.P., B.D. Ho, G. Garriss, V. Oliveira, B. Henriques-Normark, and J.O. Tegenfeldt, *Separation of pathogenic bacteria by chain length.* Analytica Chimica Acta, 2018. **1000**: p. 223-231.
247. Jakobsson, O., M. Antfolk, and T. Laurell, *Continuous flow two-dimensional acoustic orientation of nonspherical cells.* Anal Chem, 2014. **86**(12): p. 6111-4.
248. Gimsa, J., *A comprehensive approach to electro-orientation, electrodeformation, dielectrophoresis, and electrorotation of ellipsoidal particles and biological cells.* Bioelectrochemistry, 2001. **54**(1): p. 23-31.
249. Breslauer, D.N., R.N. Maamari, N.A. Switz, W.A. Lam, and D.A. Fletcher, *Mobile Phone Based Clinical Microscopy for Global Health Applications.* PLOS ONE, 2009. **4**(7): p. e6320.









Cite this: *Lab Chip*, 2011, 11, 1326

www.rsc.org/loc

PAPER

## Separation of parasites from human blood using deterministic lateral displacement†

Stefan H. Holm,‡<sup>a</sup> Jason P. Beech,‡<sup>a</sup> Michael P. Barrett<sup>b</sup> and Jonas O. Tegenfeldt<sup>\*ac</sup>

Received 3rd November 2010, Accepted 20th January 2011

DOI: 10.1039/c0lc00560f

We present the use of a simple microfluidic technique to separate living parasites from human blood. Parasitic trypanosomatids cause a range of human and animal diseases. African trypanosomes, responsible for human African trypanosomiasis (sleeping sickness), live free in the blood and other tissue fluids. Diagnosis relies on detection and due to their often low numbers against an overwhelming background of predominantly red blood cells it is crucial to separate the parasites from the blood. By modifying the method of deterministic lateral displacement, confining parasites and red blood cells in channels of optimized depth which accentuates morphological differences, we were able to achieve separation thus offering a potential route to diagnostics.

### 1. Introduction

Human African trypanosomiasis is caused by parasitic protozoa of the *Trypanosoma brucei* subgroup.<sup>1</sup> The parasites, transmitted by tsetse flies, proliferate in the haemolymphatic system of infected patients in stage 1 of the disease. In stage 2 they invade the central nervous system where they cause increasing neurological dysfunction, including the changes to sleep–wake patterns that lend the disease its common name of sleeping sickness. Two subspecies of *T. brucei* are responsible for human disease, both forms of which are fatal if left untreated. *T. brucei rhodesiense* causes an acute form where uncontrolled parasite proliferation leads to death within weeks of an infection. *T. brucei gambiense* causes a chronic infection where parasite proliferation is limited and several years elapse between infection and development of stage 2 disease, which can last for a year or more prior to death. Treatment of stage 1 disease is easier than for stage 2 and different drugs are used.<sup>2</sup> At stage 2, treatment depends either on melarsoprol, a highly toxic organic arsenical that kills 5% of those taking the drug, or eflornithine, which is given for two weeks by intravenous infusion. Eflornithine costs are high enough to limit use of the drug. Early stage treatment involves the use of either suramin or pentamidine depending on the type of parasite. Although both of these drugs have non-negligible

side effects, early diagnosis and treatment are very much preferred over late stage treatment. However, diagnosis of human African trypanosomiasis is challenging and the standard parasitological techniques currently used are estimated to give false negatives in 20–30% of cases.<sup>3</sup> Large scale screening for *gambiense* disease (which is responsible for >90% of all current cases) involves use of the serologically based Card Agglutination Test for Trypanosomiasis (CATT). The test, however, depends upon particular surface antigens found on most, but not all, *gambiense* parasites which limit its sensitivity and selectivity.<sup>4</sup> The gold standard in diagnosis depends upon microscopical detection of parasites in blood. This is very difficult in *gambiense* disease where the parasitaemia is frequently below 1000 cells per mL of blood.<sup>3</sup> Given the low abundance of parasites in blood, methods have been developed to concentrate the trypanosomes prior to microscopy, each with its limitations, as reviewed by Chappuis *et al.*<sup>3</sup> Microhematocrit Centrifugation Technique (MHCT) involves separating the buffy coat containing the white blood cells (WBC) and trypanosomes from the denser red blood cells (RBCs). Quantitative Buffy Coat (QBC) is a method derived from this approach that also uses high-speed centrifugation together with fluorescence detection. Both of these techniques have a detection limit of ~500 trypanosomes per mL of blood.

Currently the best trypanosome separation technique is the mini-Anion-Exchange Centrifugation Technique (mAECT) which has been reported of having a detection limit of 100 trypanosomes per mL of blood. This method exploits the negative surface charge of RBCs to remove them from a blood sample while neutrally charged trypanosomes pass through the column and can then be concentrated by centrifugation. A large field-study in 2004 concluded the sensitivity of mAECT to be 75.3%, cost per test almost €3 and time per test half an hour.<sup>5</sup>

An alternate method to these separation techniques is to selectively lyse the RBCs.<sup>6</sup> This method has been estimated to

<sup>a</sup>Division of Solid State Physics, nmC@LU, Lund University, PO Box 118, S-221 00 Lund, Sweden. E-mail: jonas.tegenfeldt@if.lth.se; Fax: +46 (0)46 222 3637; Tel: +46 (0)46 222 8063

<sup>b</sup>Welcome Trust Centre for Medical Parasitology, Institute of Infection, Immunity and Inflammation, College of Medical, Veterinary and Life Sciences, University of Glasgow, UK

<sup>c</sup>Department of Physics, University of Gothenburg, Gothenburg, Sweden

† Electronic supplementary information (ESI) available. See DOI: 10.1039/c0lc00560f

‡ Authors contributed equally.

also have a detection limit of  $\sim 500$  trypanosomes per mL of blood but has been difficult to implement and has yet to receive widespread use.

All of the above methods are focused on increasing the trypanosome concentration by removing the background cells, predominantly RBCs. Given that 1 mL of blood might contain fewer than 1000 parasites, but on the order of  $5 \times 10^9$  RBCs,  $0.35 \times 10^9$  platelets and  $7 \times 10^6$  WBCs the task is not trivial. However, advances in microfluidics, together with the fact that trypanosomes differ in multiple biophysical ways from blood cells including surface charge (as previously exploited in mAECT), size, shape and motility, offer the potential for new routes to separation of trypanosomes from blood cells. In the work reported here we are concerned with the problem of removing RBCs and present a proof of concept of a lab-on-a-chip microfluidic device that can readily separate trypanosomes from RBCs.

## 2. Deterministic lateral displacement

Deterministic Lateral Displacement (DLD) is a microfluidics-based particle separation technique, easy to implement in cheap disposable plastic chips, that we believe is well suited for the task of removing parasites from blood cells in order to aid detection. The method of separation by DLD was first developed by Huang *et al.*<sup>7</sup> and has been shown capable of separating RBCs, WBCs, platelets and plasma from whole blood<sup>8</sup> as well as separating different types of WBCs based on their size.<sup>9</sup> The mechanism of separation by DLD is based on the interaction of particles suspended in a fluid (in this case whole blood and parasites) with an ordered array of micrometre-sized posts that the fluid is forced to flow through under low Reynolds number conditions. The array of circular posts divides the fluid into many narrow streams, the widths of which correspond to the critical radii. Particles smaller than a critical size are able to follow one such stream through the array whereas larger particles are forced, through interactions with posts, to change streams many times, always in the same direction, becoming laterally displaced. For spherical particles the critical size,  $D_c$ , at which the transition between following the flow (zigzagging mode) and being displaced (displacement mode) occurs is given by eqn (1), which was empirically deduced by Davis.<sup>10</sup>

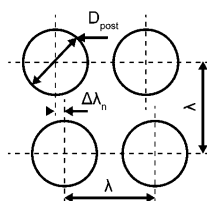


**Fig. 1** A rhombic unit cell within the array of posts. In each of the 13 sections in the device every row is shifted a specific distance,  $\Delta\lambda_n$ , with respect to the preceding row giving a range of critical diameters,  $D_{c,n}$ , as described by eqn (1). The gap (post–post separation) is given by  $d = \lambda - D_{\text{post}}$  and the periodicity is given by  $N_n = \lambda/\Delta\lambda_n$ .

$$D_{c,n} = 1.4dN_n^{-0.48} \quad (1)$$

The definitions of the array parameters are shown in Fig. 1. The amount of lateral displacement is a function of the array parameters and of the particles' effective sizes (and as we will show here, morphology).

A full description of the device, with all array parameters, can be found in the ESI, Section 1†. The device consists of 13 sections, each with a specific and increasing critical diameter,  $D_{c,n}$  ( $n = 1, 2, \dots, 13$ ), and where each section gives rise to a lateral displacement of  $\sim 160 \mu\text{m}$  for particles with diameters larger than  $D_{c,n}$ . The total displacement for a particle with diameter  $D_{\text{particle}}$  is given by  $x_{\text{particle}} \approx 160 \mu\text{m} \sum_{n=1}^{13} (D_{\text{particle}} > D_{c,n})$ . The boolean term within the brackets equals 1 if true, else 0. A spherical particle that has a smaller diameter than all of the critical diameters in the device should not be laterally displaced at all and is expected to emerge from the device at the position depicted by the first vertical grey line at  $x = 0 \mu\text{m}$  in Fig. 2a. At the same time a particle which, for example, is larger than the third critical diameter but smaller than the fourth should emerge on the fourth vertical line at  $x \approx 480 \mu\text{m}$ . Particles are separated into 14 fractions with thresholds ranging from 3 to 9  $\mu\text{m}$  in 0.5  $\mu\text{m}$  steps, see Fig. 2b.

Spherical, fluorescent polystyrene microspheres with diameters in the range 3–10  $\mu\text{m}$  were used to calibrate our device. Fig. 2a shows how the microspheres are displaced by well-defined

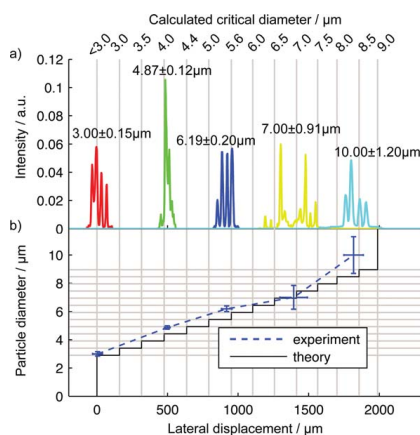


**Fig. 2** Calibration of a deep separation device (20  $\mu\text{m}$ ) using fluorescent polystyrene microspheres. (a) The distribution of particles at the end of the separation device. The greater the diameter of the particles the further they are laterally displaced. The grey vertical lines show theoretical displacements for each discrete 0.5  $\mu\text{m}$  step in critical diameter. The individual spikes correspond to the rows of posts in the actual device. (b) Comparison of the expected displacement of hard spheres according to theory (black line) with the experimentally measured displacements (blue dashed line). Vertical error bars show the standard deviation in the diameters of the microspheres according to the manufacturer, and horizontal error bars show the standard deviation in the lateral distribution measured at the end of the device.

amounts depending on their size, as described above. Fig. 2b shows a comparison of the measured displacement with the theory. Comparing microsphere sizes with their mean lateral displacements shows that the device parameters used result in a somewhat larger critical diameter than predicted by the theory. This applies to all of the microsphere sizes but is most notable for those of 10  $\mu\text{m}$  diameter. For 10  $\mu\text{m}$  microspheres the mean lateral displacement differs by almost 20% from the expected value. We believe this is due in part to the large diameter of the microspheres compared to the gap between posts (12  $\mu\text{m}$ ) and the large disturbance in the flow field this must cause, and in part due to a small imbalance in the exit flow in our present design. The volume flow through the channel that collects particles with maximum displacement (in this case 10  $\mu\text{m}$ ) was smaller than intended and particle trajectories tended to curve in toward the centre of the device where the volume flow was marginally larger leading to a decrease in total displacement for these particles.

In all work previously reported on DLD, devices have been fabricated much deeper than even the largest dimension of the particles, the aim being to attain high volume throughput. Particles are assumed to be either spherical or approximately spherical in these devices. We have previously shown that non-spherical particles can be oriented in DLD devices such that they present different dimensions to the device<sup>11</sup> thereby changing the effective size of the particle so that it approaches that of the selected dimension, for example the diameter of a disk shaped particle or the length of a long thin particle. The smallest dimensions of RBCs and parasites are very similar, the result, being that in a conventional deep DLD device their effective sizes are also very similar. This makes separation impossible or at best gives it very poor resolution. The method we present here, of tailoring device depth to the specific particle system, overcomes this problem and makes it possible to control the sensitivity of DLD to specific morphologies.

### 3. *Trypanosoma cyclops* as a model system

The African trypanosomes comprise a taxonomic group that includes those subspecies discussed above that are infectious to man, but also numerous other hemoflagellates infectious to other vertebrate species. Given the risks and regulatory constraints associated with working with *T. brucei* subspecies, we have confined our initial proof-of-concept studies to trypomastigotes (the flagellated parasite form found in the mammalian host) of the parasite *T. cyclops*, Fig. 3. This is a parasite of the macaque monkey, *Macaca*, found in Southeast Asia which also propagates as a trypomastigote in culture medium. The *T. cyclops* culture forms are similar but not identical to *T. brucei*. Cultured *T. cyclops* trypomastigotes are expected to be 33.5  $\mu\text{m}$  long and 2.5  $\mu\text{m}$  wide according to the literature,<sup>12</sup> while *T. brucei* trypomastigotes are described as 30  $\mu\text{m}$  long and 1.5–3.5  $\mu\text{m}$  wide.<sup>3</sup> Initial size characterisation of our cultured *T. cyclops* was carried out by microscopical examination of 160 parasites resulting in a measured length of  $30.6 \pm 4.7 \mu\text{m}$  and a broadest width of  $2.6 \pm 0.4 \mu\text{m}$ . No distinct subpopulations could be distinguished within the culture based on the size and there was very little correlation (correlation coefficient of 0.14) between the length and width of the parasites, see the ESI, Section 2†. The width of the *T. cyclops* is almost identical to the width of the RBCs which makes

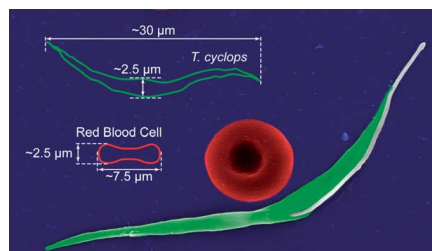


Fig. 3 A colour-enhanced scanning electron micrograph of an RBC (red) and a *T. cyclops* (green), both of which are representative of the most common size and shape. The dimensions of the two are also given.

separation in conventional DLD devices very difficult as described above.

It is possible that properties, such as surface charge and flagellum waveform, for example, differ between *T. cyclops* and *T. brucei*. However, the Deterministic Lateral Displacement technique that we employ depends primarily on cell shape and size. We thus believe that *T. cyclops* represent a legitimate surrogate for pathogenic *T. brucei* in demonstrating the separability of trypanosomes from RBCs in blood using DLD.

### 4. Materials and methods

To make a master for replica moulding SU-8 (MicroChem, Newton, MA, USA) was spin coated onto 3" silicon wafers at varying thicknesses and patterned using UV light in a contact mask aligner (Karl Suss MJB3 and MJB4, Munich, Germany). A chrome mask was fabricated by Delta Mask (Delta Mask, Enschede, The Netherlands) with a design drawn in L-Edit 11.02 (Tanner Research, Monrovia, CA USA). Before casting, the master was given an anti-adhesion layer of 1H,1H,2H,2H-perfluorooctyltrichlorosilane (ABCRC GmbH & Co. KG, Karlsruhe, Germany) to facilitate demoulding.<sup>13</sup> PDMS monomer and hardener (Sylgard 184, Dow Corning, Midland, MI, USA) were mixed to a ratio of 10 : 1, degassed, poured onto the master and baked for 1 hour at 80 °C. Connection tubes were cast directly into the PDMS to avoid the need for any additional adhesive. Our first generation of devices were sealed with glass slides as is commonly done. In these devices we observed a high proportion of echinocytes (deformed RBCs). We discovered later that this is due to the proximity to the glass surface consistent with the observations by Lim *et al.*<sup>14</sup> In order to avoid this problem we fabricated devices entirely in PDMS. The patterned PDMS slab was bonded to a blank PDMS slide following surface treatment with oxygen plasma (Plasma Preen II-862, Plasmatic Systems, Inc, North Brunswick, NJ, USA). A pressure gradient was used to drive flow through the DLD devices. Outlets were kept at atmospheric pressure and the overpressure at the three inlets was controlled individually using an MFCS-4C (Fluigent, Paris, France). This made it possible to hydrodynamically focus the sample into a stream of  $\sim 10 \mu\text{m}$  in width. A schematic overview of the device is shown in Fig. 4a.

All images were taken through an inverted Nikon Eclipse TE2000-U microscope (Nikon Corporation, Tokyo, Japan) using an Andor Luca EMCCD camera (Andor Technology,

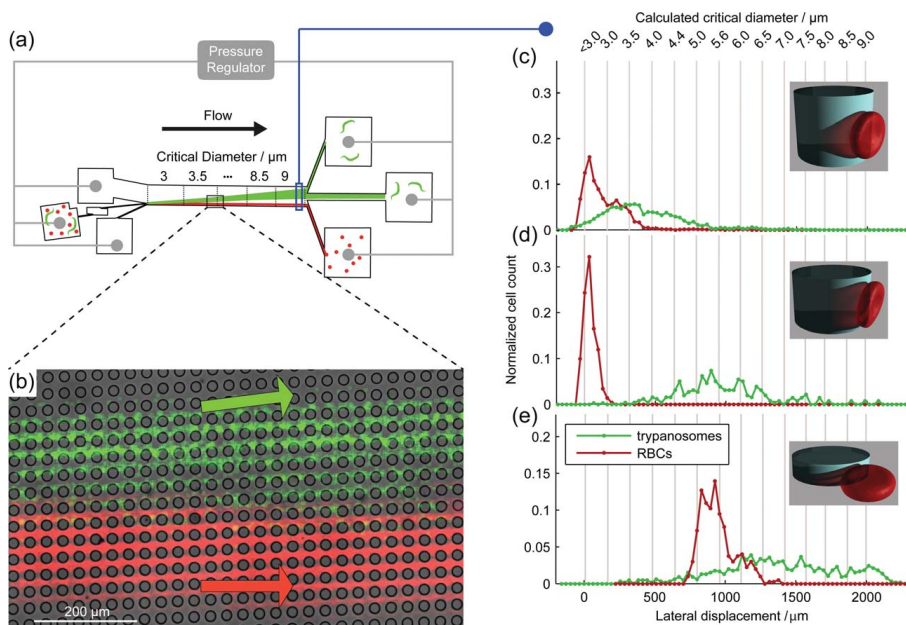


**Fig. 4** (a) Overview of our DLD device. A focused stream of particles enters from the left. Particles larger than the critical diameter are laterally displaced (upwards in the figure) by  $\sim 160 \mu\text{m}$  in each section and can be collected at the end of the device. The distributions of RBCs and *T. cyclops* are measured at the end of devices of three different depths. (b) A time-integrated micrograph showing a mixture of RBCs and parasites imaged in brightfield and coloured red. Overlaid on this image, in green, is an epifluorescence micrograph in which only the DAPI-stained trypanosomes can be seen having been displaced out of the stream of blood cells. (c) In a  $33 \mu\text{m}$  deep device the RBCs behave like spherical particles with diameters of  $3 \mu\text{m}$  or less with a lateral displacement of  $x_{\text{RBC}} = 9 \pm 23 \mu\text{m}$ . Trypanosomes, despite being much longer, are not displaced significantly more,  $x_{\text{Tryp}} = 66 \pm 105 \mu\text{m}$ , resulting in a large overlap. (d) In an  $11 \mu\text{m}$  deep device the spread in the displacement of the trypanosomes is still large,  $x_{\text{Tryp}} = 980 \pm 330 \mu\text{m}$ . The mean displacement however is sufficiently large that the trypanosomes are almost all separated from the RBCs, which at this depth still behave like small particles,  $x_{\text{RBC}} = 36 \pm 44 \mu\text{m}$ . (e) In a  $4 \mu\text{m}$  deep device the RBCs are confined such that they present their largest dimension, the diameter of the disc, to the array. Oriented thus they behave like particles with a diameter of around  $6 \mu\text{m}$ .  $x_{\text{RBC}} = 944 \pm 123 \mu\text{m}$ . Trypanosomes are also oriented such that their effective size increases,  $x_{\text{Tryp}} = 1386 \pm 424 \mu\text{m}$ . The variation in both the shape of trypanosomes and the manner by which they move through the array gives rise to the large spread in displacement, and a large overlap between the distributions.

Belfast, Northern Ireland). Differential Interference Contrast (DIC) was used to ensure adequate contrast of blood cells and trypanosomes.

Fluorescent polystyrene microspheres with diameters  $4.87 \pm 0.12 \mu\text{m}$ ,  $6.19 \pm 0.20 \mu\text{m}$  (Polysciences Inc., Warrington, PA; 18340, 19102),  $3.00 \pm 0.15 \mu\text{m}$ ,  $7.00 \pm 0.91 \mu\text{m}$  and  $10.00 \pm 1.20 \mu\text{m}$  (Duke Scientific Corp. Palo-Alto, CA; R0300, 35-2, 36-3) were used to evaluate the device.

Particle tracking software was written in MATLAB 2009b (The MathWorks, Natick, MA, USA). The tracking program was based on available MATLAB code and optimized for our specific setup. The software was able to track many particles in

a field of view when the signal-to-noise ratio was sufficiently high and when the concentration was low enough to avoid particle overlap. This made it possible to obtain readings of particle trajectories of several hundreds of cells per experiment. However, for the final simultaneous measurement of undiluted blood and trypanosomes ImageJ 1.43 was used instead to evaluate the separation. By removing the static background and generating binary images, a time-integrated micrograph could be constructed which closely matched the actual distributions. Despite being less accurate than the particle tracking software, this method does not need to be able to discriminate between separate particles making it more suitable for analysis of samples of high concentration. Still, particle overlap will lead to underestimation of the number of cells in regions of high concentration giving the appearance of broader distributions with less sharp peaks.

For work with blood and *T. cyclops*, surfaces were treated to minimize adhesion. Immediately after  $\text{O}_2$  plasma treatment and

§ The tracking program was built around a free MATLAB adaption of the IDL Particle Tracking software, and can be found at <http://www.physics.georgetown.edu/matlab/>. This intensity-based tracking core was optimised for reduced noise and correct path detection.

bonding, devices were filled with 0.2% PLL(20)-g[3.5]-PEG(2) (SuSoS AG, Dübendorf, Switzerland) in DI water and allowed to rest for at least 20 min before rinsing with DI water for another 20 min.

Long-time storage of *T. cyclops* was achieved at  $-80\text{ }^{\circ}\text{C}$  in 10% dimethyl sulfoxide (DMSO, Fluka, St Louis, MO: 41639). After thawing, trypanosomes were incubated in Cunningham's medium<sup>15</sup> with 20% Fetal Calf Serum (FCS, Sigma-Aldrich, St Louis, MO: F2442) at  $28\text{ }^{\circ}\text{C}$  under which conditions the parasites proliferated. A full description of freezing, reactivation and cell culturing can be found in the ESI, Section 3†.

Blood was extracted from the first authors, *via* finger pricking and diluted around 20 times to facilitate particle tracking in autoMACS™ running buffer (Miltenyi Biotec, Auburn, CA). Because blood serum is known to lyse *T. cyclops*,<sup>12</sup> in the experiments where blood and parasites were run simultaneously, serum was removed and blood cells resuspended in autoMACS™. Section 4 of the ESI† contains details.

The experiments were carried out in two stages. Firstly separations were performed at low concentration in order to enable automated particle tracking. The purpose of this first step was to find the device depth which maximizes separation of RBCs and parasites. Once the optimum depth was found a second series of measurements was performed in order to verify that the device would also function with whole blood.

## 5. Results and discussion

While the behaviour of spherical particles is reasonably well described by eqn (1), non-spherical particles behave in a much more complex fashion and a new approach to device design is warranted.

Device depth, we discovered, has a large effect on the displacement of both RBCs and parasites. In order to evaluate the sorting efficiency we defined the purified fraction,  $F_p$ , as the fraction of trypanosomes captured with a lateral displacement chosen such that 99% of the RBCs are rejected in the device.

This percentage is chosen to estimate the fraction of trypanosomes that can be collected with 100-fold enrichment. As the vast majority of blood cells are RBCs this is a valid estimation. Fig. 4c–e shows the distributions of *T. cyclops* and of RBCs at the end of three of our devices, almost identical except for depth. During fabrication we aimed for a gap size of  $12\text{ }\mu\text{m}$  in all three devices. Although the same photo-mask was used in all three cases, some variation in the gap size is inevitably introduced due to the variation in resist thickness and the processing parameters needed in each case. Fig. S1d, in the ESI†, shows micrographs of thin slices of the three PDMS devices in which the gap,  $d$ , between posts can be seen in the profile. The gap in the  $33\text{ }\mu\text{m}$  device is marginally narrower ( $\leq 10\%$ ) than in the other two devices. The smaller gap leads to a  $\leq 10\%$  reduction in critical size in the  $33\text{ }\mu\text{m}$  device compared to the values shown in the ESI, Table S1†. The result of this is that while RBCs are not displaced in the  $11\text{ }\mu\text{m}$  deep device, a fraction of them ( $\sim 1/3$ ) are displaced in section two of the  $33\text{ }\mu\text{m}$  device. This leads to a broadening of the distribution. One would also expect the parasites to be displaced marginally more in this device, but as we will discuss below, the effects of device depth dominate their behaviour.

In a  $33\text{ }\mu\text{m}$  deep device RBCs behave like particles around  $3\text{ }\mu\text{m}$  in diameter and parasites like particles in the range  $3\text{--}5\text{ }\mu\text{m}$  and almost no separation occurs,  $F_p = 14.0\%$ . In a  $11\text{ }\mu\text{m}$  deep device the RBCs behave like particles smaller than  $3\text{ }\mu\text{m}$  but *T. cyclops* are displaced to a much greater degree. At this depth RBCs and *T. cyclops* are well separated,  $F_p = 99.5\%$ . In a  $4.0\text{ }\mu\text{m}$  deep device the RBCs behave like particles with an effective diameter of  $\sim 6\text{ }\mu\text{m}$  while the mean displacement of *T. cyclops* also increases relative to the deeper devices. In a device as shallow as  $4.0\text{ }\mu\text{m}$ , due to the overlap in the distributions of both *T. cyclops* and RBCs, separation is very poor,  $F_p = 53\%$ .

The increased displacement comes about when particles, partially confined in shallow channels, are forced to adopt orientations that give them a greater effective size in the device. For RBCs that have a biconcave disc shape, see Fig. 3, the effect is, we believe, solely due to orientation constraints. In a  $33\text{ }\mu\text{m}$  deep device (Fig. 4c) RBCs have room to rotate and will be forced to do so by a combination of the shear field and the interactions with posts. Because of this rotation they present their smallest dimensions to the array. The inset shows the orientation of an RBC in a deep device. For an RBC the smallest dimension is around  $2.5\text{ }\mu\text{m}$  and indeed the RBCs are displaced by a similar amount as microspheres smaller than  $3\text{ }\mu\text{m}$  diameter. In the  $11\text{ }\mu\text{m}$  deep device, Fig. 4d, the orientation of RBCs is the same as that in the  $33\text{ }\mu\text{m}$  deep device and the displacement therefore the same. It is only when the depth of the device becomes smaller than the diameter of RBCs that an effect is observed. In a  $4.0\text{ }\mu\text{m}$  device (Fig. 4e) the rotation of RBCs is severely constrained and they present their largest dimension to the device (see inset) giving them an effective size of  $\sim 6\text{ }\mu\text{m}$ , close to their diameter.

The increase in the effective size of the trypanosomes is more complex and not as intuitive or as easily characterised as that of the RBCs. A series of videos can be found in Section 5 of the

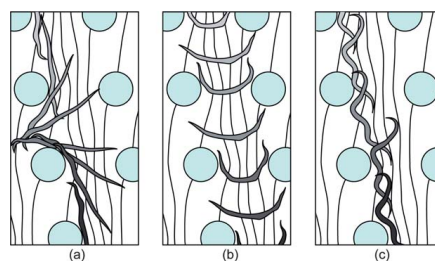


**Fig. 5** Mechanisms that give long particles a larger effective size (see ESI, Section 5† for corresponding movies). (a) Shear forces in conjunction with post-particle interactions can give rise to rotation. When a particle is perpendicular with the direction of flow it is influenced by many flow streams and the effective size is increased. (b) Long but flexible particles such as *T. cyclops* can be seen locked into a u-shape. In this case they are unable to rotate in the space between one row and the next and they behave like particles with a large effective size. (c) Even in the absence of the effects described in (a) and (b), when parasites are aligned with the flow direction, their bent shape gives rise to an effective size that is larger than their width. This effective size could fluctuate if the parasite is motile and constantly changing shape.

ESI† in which parasites can be seen moving through sections 2 and 6 of devices of different depths. Fig. 5 shows some sketches that summarize the most frequently observed modes of motion that lead to increased effective size.

Because the *T. cyclops* are around 30  $\mu\text{m}$  in length the orientation constraints should be minimal in the 33  $\mu\text{m}$  deep device. This can also be seen in Fig. 4c where they are not significantly displaced. In an 11  $\mu\text{m}$  deep device (Fig. 4d) *T. cyclops* are constrained to a degree that greatly changes their effective sizes leading to greater lateral displacement. Because the orientations of RBCs are not constrained at this depth the amount by which they can be separated from parasites is greatly increased. As can be seen in Fig. 4e, *T. cyclops* are displaced to an even greater extent in the 4.0  $\mu\text{m}$  deep device than in the 11  $\mu\text{m}$  device but because RBCs are also affected at this depth the overlap in displacement distributions results in a poor separation.

Rotation has a considerable effect on particles as long, thin and relatively rigid as trypanosomes. Fig. 5a illustrates how, when perpendicular to the flow direction, a long particle will be influenced by many flow streams that can force the particle to move in the displacement mode.

As long, flexible particles rotate they tend to become trapped in a U-shape configuration between rows of posts in the fashion illustrated in Fig. 5b. The shallower the device, the more frequently this trapping occurs. This mode of transport through the device appears to be stable and once parasites entered this mode they moved for long distances through the device without rotation and without becoming stuck. In this configuration the parasites have the largest possible effective size.

The fact that the parasites are not straight also influences their effective size as depicted in Fig. 5c. This together with the constant undulation due to the motion of their flagella contributes to an increase in their effective size (the flagella can be seen in white along the side of the parasite in Fig. 3 and a swimming parasite is shown in the ESI, Section 5†). The flagellar movement gives rise to a swimming speed of 20  $\mu\text{m s}^{-1}$  which is small compared to the velocity through the array (600  $\mu\text{m s}^{-1}$ ) and is therefore not expected to affect the displacement significantly.

In general the trend we observe is that the modes shown in Fig. 5 become more prevalent as devices become shallower and that this collectively leads to greater lateral displacement of the parasites in our devices.

In the second series of measurements we focused on the 11  $\mu\text{m}$  deep device which gave the highest separation efficiency in the previous measurements with a pure trypanosome fraction of  $F_p = 99.5\%$ . Because a future diagnostic device should be able to deal with whole blood it is important that the device can function both at those cell concentrations found in blood and also in the presence of serum. Because serum kills *T. cyclops* (as explained above) this was demonstrated in two separate experiments.

Firstly we injected the resuspended blood and parasites, at whole blood concentration, into the device with the results shown in Fig. 6. Despite a small broadening of the RBC peak, the separation efficiency was not degraded,  $F_p = 99.6\%$ . The RBCs still behave like spherical particles of 3  $\mu\text{m}$  or less with a small lateral displacement,  $x_{\text{RBC}} = 24 \pm 75 \mu\text{m}$ . The lateral displacement of the trypanosomes is also in agreement with the first series of measurements at this depth,  $x_{\text{tryp}} = 841 \pm 259 \mu\text{m}$ . While many WBCs are too large to enter the device the behaviour of

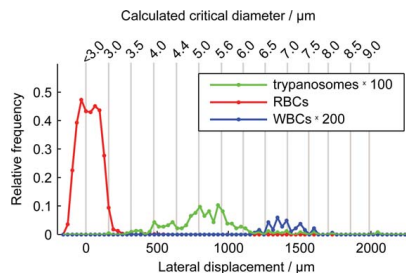


**Fig. 6** Evaluation of trypanosomes in resuspended whole blood. The lateral displacements of RBCs and trypanosomes are  $x_{\text{RBC}} = 24 \pm 75 \mu\text{m}$  and  $x_{\text{tryp}} = 841 \pm 259 \mu\text{m}$  respectively with a purified fraction of  $F_p = 99.6\%$ . This is in parallel with the preceding diluted separation experiment at this depth except for the broader distribution profile of the RBCs which in part is due to particle overlap as previously discussed. The behaviour of WBCs was also characterised and they were found to become separated from the major trypanosome fraction.  $x_{\text{WBC}} = 1400 \pm 111 \mu\text{m}$ . The number of counted cells are  $n_{\text{RBC}} = 19\,700$ ,  $n_{\text{WBC}} = 61$  and  $n_{\text{trypanosomes}} = 435$ . The sample concentrations are  $c_{\text{RBC}} = 4.9 \times 10^6 \mu\text{L}^{-1}$ ,  $c_{\text{WBC}} = 2600 \mu\text{L}^{-1}$ ,  $c_{\text{trypanosomes}} = 8400 \mu\text{L}^{-1}$ .

those small enough to do so ( $<11 \mu\text{m}$ ) was also characterized in these measurements and they were found to be laterally displaced by the same amount as  $\sim 7 \mu\text{m}$  sized spherical particles,  $x_{\text{WBC}} = 1400 \pm 111 \mu\text{m}$ , meaning that they are also separated from the parasites. The size and number concentration of these WBCs suggest that they are lymphocytes, which are between 7 and 8  $\mu\text{m}$  in diameter and are present in blood at concentrations around 2000  $\mu\text{L}^{-1}$ .

Secondly, using  $\text{Na}_2 \text{EDTA}$  at 1.75  $\text{mg mL}^{-1}$  as an anticoagulant we were able to flow whole blood through the device for 75 minutes with no visible clogging of cells and no change in the critical size in the devices. See ESI, Section 6† for more details.

While shallow devices separate a much higher fraction of parasites from blood there are some limitations. Large blood cells such as monocytes (14–17  $\mu\text{m}$ ) and neutrophils (10–12  $\mu\text{m}$ ) might clog the device. The experiment with whole blood shows that while some WBCs undoubtedly become stuck at the entrance to the channel, this has a large area and does not become blocked in the first 75 minutes at least. The filter in the sample inlet also removes any WBCs that would otherwise become stuck in the pillar array. Since we are only interested in finding parasites, provided clogging does not occur over the relevant timescales for the experiment (less than 1 hour) WBCs are not expected to constitute a problem. Clogging due to WBCs could further be decreased either by improving the entrance to the device and the prefilter or alternatively by implementing a two step separation in which the WBCs, which have larger effective sizes than both RBCs and parasites at any device depth, are first removed in an array that is deeper than the largest blood cells (e.g.  $>20 \mu\text{m}$ ).

The volume flow and therefore throughput of a shallow device are also less than for a deeper channel with otherwise equal dimensions. The device we present here was designed to study the behaviour of individual, non-spherical particles as device depth is



altered, which is best done with a narrow sample stream. There is therefore much room to improve the throughput in the next generation of devices. The following are a few examples of how this could be done.

In addition to working with whole blood to further increase the throughput the width of the sample stream could be increased from 10  $\mu\text{m}$  to 1 mm and still make the device no longer than a microscope slide. Making devices thin<sup>16</sup> would also make it possible to stack multiple devices and run them in parallel with a single inlet and a single outlet. These steps alone would increase the throughput from the 1  $\text{nL}\cdot\text{s}^{-1}$  in our current device to 1  $\mu\text{L}\cdot\text{s}^{-1}$ . With a goal of one million true positives per false negative on average we need to (assuming Poisson statistics) collect  $6 \ln 10 \approx 14$  parasites. With a lowest target concentration of 100 parasites per mL this translates into 140  $\mu\text{L}$  of blood which would take less than three minutes to sort.

The way we envision our method being of use is as a preparative step before either conventional smear examination or automated, on-chip detection of parasites. The latter would be more time and cost-effective and could be achieved by first capturing and concentrating the parasites after separation from RBCs using for example sieving structures or sticky surface modifications followed by subsequent detection with a cheap, field-portable camera such as the cell-phone cameras developed by the Ozcan group (see ref. 17 for an example). This one-step device would constitute a considerable improvement compared to the aforementioned more complicated and labor-intensive techniques such as mAECT and QBC.

In addition to possible utility in finding African trypanosomes in the blood of human or animal victims of trypanosomiasis, it is noteworthy that related parasites *e.g.* *Trypanosoma cruzi*, the causative agent of Chagas disease in Latin America and *Leishmania* species responsible for the leishmaniasis throughout the tropical and sub-tropical world, can also present as elongate, flagellated cells in mammalian blood. These could also be separated using the same basic principals outlined here. These latter parasites, however, spend much of their time within the mammalian host, as intracellular amastigote forms, hence the general utility for diagnosis of the diseases caused by the parasites would require further evaluation.

## 6. Conclusions

We have successfully shown how particle orientation, controlled *via* device depth, can be used to accentuate morphological differences making possible the sorting of otherwise indistinguishable particles in DLD devices. We have separated *T. cyclops*, a non-pathogenic relative of *T. brucei* from RBCs opening up for a cheap, simple to use, point-of-care, diagnostics

tool. The next generation of devices will be designed to achieve both a higher throughput and a lower detection limit along with features for the capture and concentration of the parasites.

## Acknowledgements

This work was carried out within nmC@LU (the Nanometer Structure Consortium at Lund University). The work was supported by the Swedish Foundation for Strategic Research (SSF), the Swedish Research Council (VR) grant nr. 2007 584, the Crafoord Foundation grant no. 2008 0841 and 2005 1123, and the Knut and Alice Wallenberg Foundation. We would also like to extend our gratitude to Dr Mathis Riehle for first introducing us to the problem of HAT diagnostics.

## References

- 1 M. P. Barrett, R. J. S. Burchmore, A. Stch, J. O. Lazzari, A. C. Frasch, J. J. Cazzulo and S. Krishna, *Lancet*, 2003, **362**, 1469–1480.
- 2 M. P. Barrett, D. W. Boykin, R. Brun and R. R. Tidwell, *Br. J. Pharmacol.*, 2007, **152**, 1155–1171.
- 3 F. Chappuis, L. Loutan, P. Simarro, V. Lejon and P. Buscher, *Clin. Microbiol. Rev.*, 2005, **18**, 133–146.
- 4 P. Dukes, W. C. Gibson, J. K. Gashumba, K. M. Hudson, T. J. Bromidge, A. Kaukus, T. Asonganyi and E. Magnus, *Acta Trop.*, 1992, **51**, 123–134.
- 5 P. Lutumba, J. Robays, C. Miaka, V. Kande, D. Mumba, P. Bscher, B. Dujardin and M. Boelaert, *Trop. Med. Int. Health*, 2006, **11**, 470–478.
- 6 E. Matovu, A. Kazibwe, A. Boobo, S. Biler and J. Ndung'u, *Revisiting Red Blood Cell Lysis as a Critical Step in Demonstrating Trypanosomes in Patient Blood*, FIND, Geneva, Switzerland, 2009.
- 7 L. R. Huang, E. C. Cox, R. H. Austin and J. C. Sturm, *Science*, 2004, **304**, 987–990.
- 8 J. A. Davis, D. W. Inglis, K. J. Morton, D. A. Lawrence, L. R. Huang, S. Y. Chou, J. C. Sturm and R. H. Austin, *Proc. Natl. Acad. Sci. U. S. A.*, 2006, **103**, 14779–14784.
- 9 D. W. Inglis, J. A. Davis, T. J. Zieziulewicz, D. A. Lawrence, R. H. Austin and J. C. Sturm, *J. Immunol. Methods*, 2008, **329**, 151–156.
- 10 J. A. Davis, PhD thesis, Princeton University, 2008.
- 11 J. Beech and J. Tegenfeldt, *The Thirteenth International Conference on Miniaturized Systems for Chemistry and Life Sciences*, Jeju, Korea, 2009, 800–802.
- 12 D. Weinman, *Trans. R. Soc. Trop. Med. Hyg.*, 1972, **66**, 628–633, IN621–IN622, 634–636.
- 13 M. Beck, M. Graczyk, I. Maximov, E. L. Sarwe, T. G. I. Ling, M. Keil and L. Montelius, *Microelectron. Eng.*, 2002, **61-2**, 441–448.
- 14 G. H. W. Lim, M. Wortis and R. Mukhopadhyay, *Proc. Natl. Acad. Sci. U. S. A.*, 2002, **99**, 16766–16769.
- 15 I. Cunningham, *J. Protozool.*, 1977, **24**, 325–329.
- 16 J. P. Beech, T. Mkel, P. Majander and J. O. Tegenfeldt, *The 12th International Conference on Miniaturized Systems for Chemistry and Life Sciences*, San Diego, USA, 2008, 1492–1494.
- 17 O. Mudanyali, C. Oztoprak, D. Tseng, A. Erlinger and A. Ozcan, *Lab Chip*, 2010, **10**, 2419–2423.



## Separation of Parasites from Human Blood using Deterministic Lateral Displacement

Stefan H. Holm, Jason P. Beech, Michael Barrett and Jonas O. Tegenfeldt

### -Electronic Supporting Information-

#### 1. Device parameters

Our device was designed to have 13 sections each consisting of one discrete critical diameter,  $D_c$ , according to Eq. 1, see Fig. E1a. Array parameters are defined in Fig. E1b. The diameter of the posts,  $D_{post}$ , is 20 $\mu\text{m}$  throughout the device. The gap between the posts,  $d = \lambda - D_{post}$ , is 12 $\mu\text{m}$  and is also constant throughout the device.  $\lambda$  is the centre-to-centre spacing of the posts. The critical diameter in the device is varied by varying  $\Delta\lambda$ , the amount each row is laterally shifted with regard to the previous row. Table E1. shows  $\Delta\lambda_n$  for each of the  $n=1, \dots, 13$  sections and the  $D_{c,n}$  that this gives rise to.  $N = \lambda / \Delta\lambda_n$  is the periodicity of the array. The small deviations from whole and half micrometer values for  $D_{c,n}$  are the result of technical constraints of the mask generating process, forcing us to fit our designs to a 0.2  $\mu\text{m}$  manufacturing grid.

$$D_{c,n} = 1.4 \cdot d \cdot N_n^{-0.49} \quad (1)$$

**Table E1.** The device was designed to have 13 sections containing discrete critical diameters. All sections have equal  $D_{post}$  and  $\lambda$  but  $\Delta\lambda$  is varied. Each different  $\Delta\lambda_n$  gives a specific  $N_n$  and therefore, according to Eq. 1, a specific  $D_{c,n}$ .

Section Number n	Row Shift $\Delta\lambda_n$ [ $\mu\text{m}$ ]	Period $N_n$	Critical Diameter $D_{c,n}$ [ $\mu\text{m}$ ]	Lateral displacement x [ $\mu\text{m}$ ]
1	0.80	40.00	2.86	160.0
2	1.20	26.67	3.47	156.0
3	1.60	20.00	3.99	160.0
4	2.00	16.00	4.44	160.0
5	2.60	12.28	5.04	156.0
6	3.20	10.00	5.56	160.0
7	3.80	8.42	6.04	152.0
8	4.40	7.27	6.48	154.0
9	5.20	6.15	7.02	156.0
10	6.00	5.33	7.52	150.0
11	6.80	4.71	7.99	136.0
12	7.80	4.10	8.53	156.0
13	8.80	3.64	9.04	132.0

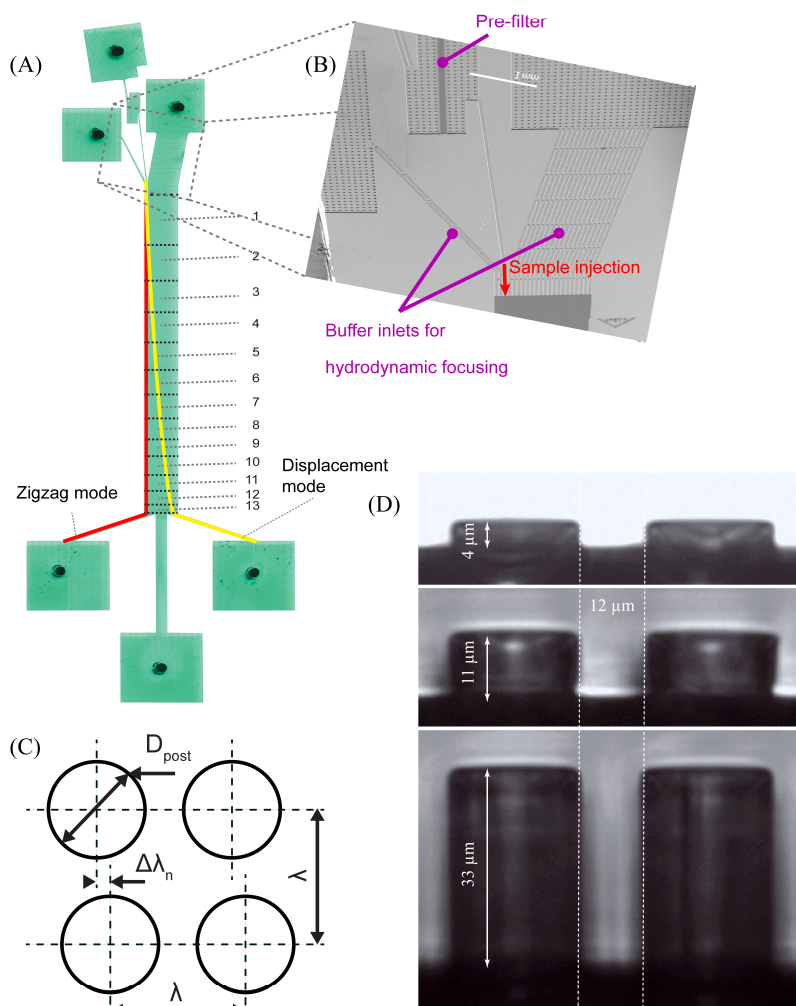


Fig. E1. Device parameters. (A) Our device contains 13 sections, each with one critical size. This image was taken by filling the device with food colouring and scanning on a flat bed scanner. Each section has a  $\Delta n$  chosen to give critical diameters from  $\sim 3\mu\text{m}$  to  $\sim 9\mu\text{m}$  in steps of  $\sim 0.5\mu\text{m}$ , see table E1. (B) Electron micrograph of the device. Sample is focused by a sheath flow of buffer. The pre-filter removes large particles (diameter  $> 12\mu\text{m}$ ) that would otherwise clog the separation array. (C) Definitions of device parameters. (D) Devices were fabricated at 3 different depths. These cross sections show the profiles of the pillars in each of the three devices.

## 2. Size measurement of *T. cyclops*

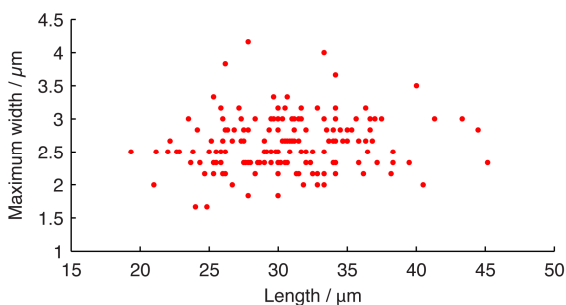


Figure E2. Scatter plot showing the size variation of the cultured *T. cyclops*. 160 trypanosomes were measured with a mean length of  $30.6 \pm 4.6 \mu\text{m}$  and a mean width of  $2.6 \pm 0.4 \mu\text{m}$ . This corresponds to values found in the literature and also shows its close relation to the pathogenic *T. brucei*.

## 3. Handling of *T. cyclops*

### Freezing

- Harvest cells by centrifuging log-phase culture (i.e. 5-7 days since last split) at 1000 g for 10 min
- Aspirate medium and resuspend cells in Cunningham's medium containing 20% Fetal Calf Serum (FCS) which has been preheated to 28°C. The final volume should be chosen to reach a concentration of  $\sim 7 \cdot 10^7$  cells/ml
- Slowly add 10% Dimethyl sulfoxide (DMSO) while stirring
- Transfer cells to autoclaved cryotube, wrap with parafilm
- Encapsulate tube with foam rubber to protect cells from freezing too rapidly, place package in a Styrofoam box in freezer at -80°C

### Reactivation

- Heat Cunningham's medium with 20% FCS to 28°C
- Take out the tube from freezer and immerse immediately in 28°C warm water, shake tube while still immersed in water
- Rinse outside of tube with tap water followed by rinsing with ethanol
- Transfer cell suspension to autoclaved 50 ml Falcon tube. Add 10 ml medium at a rate of 1 ml/minute drop by drop. The remaining 40ml can be added faster

### Culture splitting (every 14 days)

- Autoclave culture flasks
- Sterilize laminar flow hood and gloves with 70% EtOH, allow to air dry for 30s
- Add 20% FCS to the Cunningham's medium, heat to 28°C
- Fill each culture flask with 19ml
- Use sterile pipettes to transfer 1ml of trypanosome suspension to each culture flask

- Collect another 1ml of suspension to perform cell counting
- Store culture flasks in a sterile environment at 28°C

#### 4. Sample preparation

##### Drawing blood samples

- Prick finger with Haemedic Haemolance® low flow
- Fill a pipette tip with 190µl autoMACS™ running buffer
- Aspirate one large drop of blood (~10µl)
- Pipette down and up in an Eppendorf tube to homogenize the liquids
- Add around 20µl into the sample inlet reservoir of the device

##### *T. cyclops* samples

- Use log-phase growth trypanosomes, 5-7 days since last split
- Fill a 1.5ml eppendorf tube with 1ml of trypanosome culture
- Wash sample twice at 1000g for 1min to exchange medium to autoMACS™
- Pipette 20ul of trypanosomes into the sample inlet reservoir
- Use autoMACS™ in the other inlets

##### Simultaneous analysis of RBCs and *T. cyclops*

- Pool a 1ml trypanosome sample at 1000g for 1 min, wash twice and resuspend in 100ul autoMACS™
- Aspirate 160µl of autoMACS™ in a 200µl pipette tip
- Prick finger with Haemedic Haemolance® low flow
- Aspirate 40µl of blood with the filled pipette tip into the Eppendorf tube
- Wash blood sample three times with autoMACS™ at 1000g for 1 min, resuspend pellet with 20µl of the trypanosome sample
- Add the samples to the inlet reservoir

##### Staining of *T. cyclops*

- Dilute the DAPI stock solution to 50µg/ml
- Fill an eppendorf tube with 1ml trypanosome sample
- Add 10µl of the DAPI solution to the trypanosomes, pipett up and down to mix, cover with aluminium foil and let rest for 45 minutes
- Stop staining by washing three times in autoMACS™

## 5. Motion of parasites through the separation device

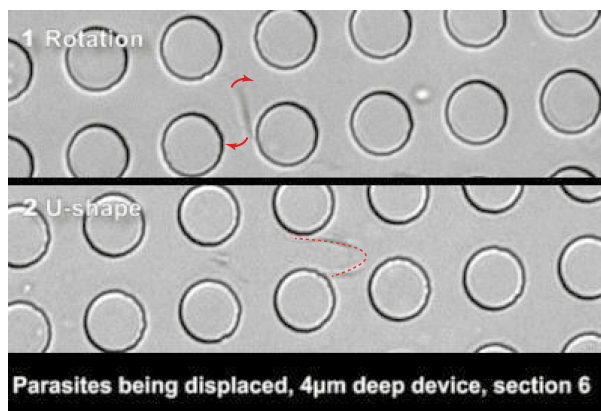
In this movie *T. cyclops* and RBCs can be seen. The RBCs are laying flat on a glass slide and are therefore seen disc side onwards. The diameter across the disc is  $\sim 7.5\mu\text{m}$ . The parasite can be seen swimming with the characteristic undulations of its flagella.



[Movie 1](#)

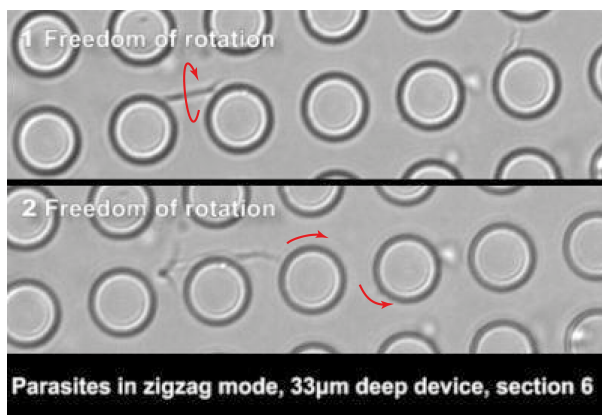
The following movies are representative of the behaviour of parasites in devices of different depths. All movies are at half actual speed.

Movie 2 shows how the parasites are being displaced in section 6 of the device, where the critical diameter is  $5.5\mu\text{m}$ . Rotation in the plane of the device (frame 1) and being trapped in a u-shape (frame 2) are two common modes, that we have observed, that greatly increase the effective size of the parasites.



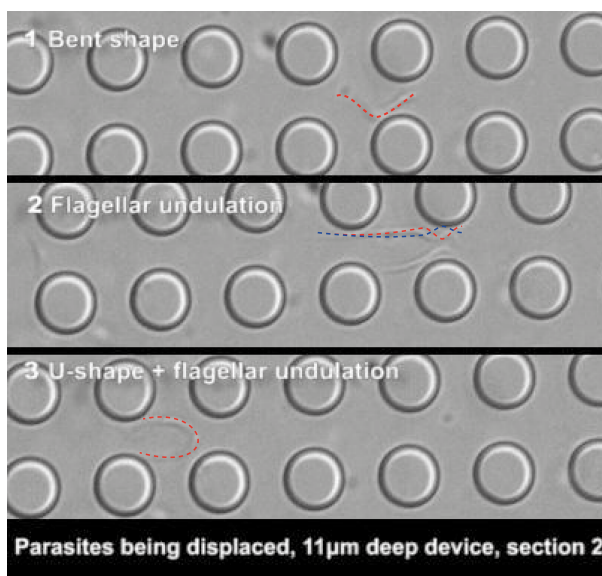
[Movie 2](#)

Movie 3 shows how freedom of rotation about their long axis in a deep device ( $33\mu\text{m}$ ) allows parasites to adopt an orientation that gives them a smaller effective size. In section 6 of the device at this depth all parasites are moving in the zigzag mode.



[Movie 3](#)

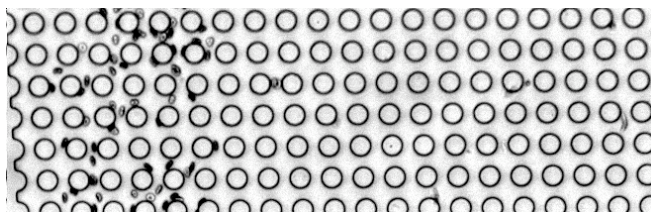
Movie 4 shows examples of parasite being displaced in section 2 of the  $11\mu\text{m}$  deep device. Frame 1 shows how the bent shape of a parasite gives it a large effective size if it is unable to rotate around its long axis. Frame 2 shows the larger effective size due to rapid flagellar motion and Frame 3 a combination of flagellar motion and the u-shape configuration.



[Movie 4](#)



In movie 5 RBCs can be seen following the flow in the zigzag mode straight down on the left of the field of view. As this device is 11 $\mu\text{m}$  deep the RBCs can be seen rotating freely as they pass the posts. A parasite can be seen moving in the displacement mode on the right of the field of view. This parasite has been separated from the RBCs. Before it leaves the field of view the parasite can be seen performing a characteristic flip, as seen above in movie 2, frame 1 and it remains in the displacement mode.

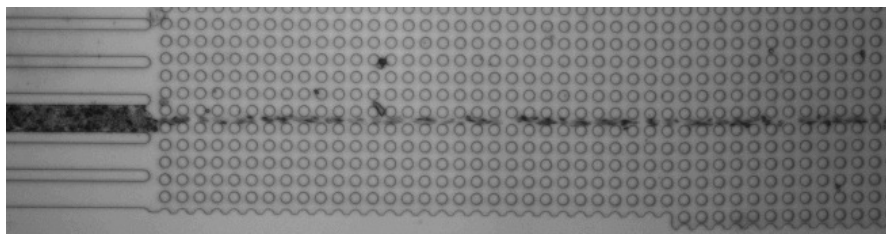


[Movie 5](#)

## 6. Do devices become clogged with blood cells or blood serum?

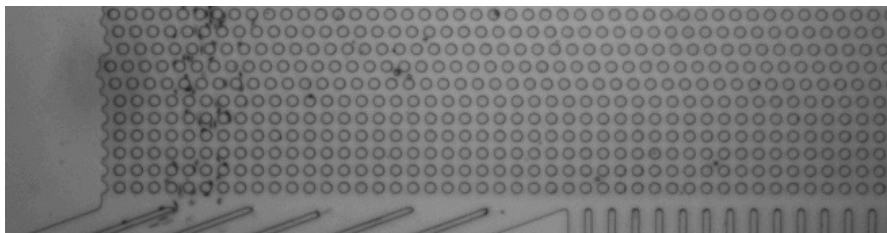
The PDMS surfaces in our devices are modified with PLL(20)-g[3.5]-PEG(2) (SuSoS AG, Dübendorf, Switzerland) as described in the materials and methods section of the paper and 1.75mg/ml  $\text{Na}_2\text{EDTA}$  is used as an anti coagulant. In order to test the effectiveness of these two treatments whole blood was injected into a device (11 $\mu\text{m}$  in depth) and the flow of blood through the device was monitored for 75 minutes. The following movies show whole blood at the entrance and exit of the separation array. Figure E3 shows the distribution of the RBCs at the end of the device over a 75-minute period.

Movie 6 shows whole blood + 1.75mg/ml  $\text{Na}_2\text{EDTA}$  30 minutes after first being injected into our device. The stream is being focused by sheath flow to approximately 10 $\mu\text{m}$  in width.



[Movie 6](#)

Movie 7 shows the same device under the same conditions as in movie 6 but taken at the outlet. The stream of blood cells has broadened to approximately  $100\mu\text{m}$  but the RBCs are not being displaced.



[Movie 7](#)

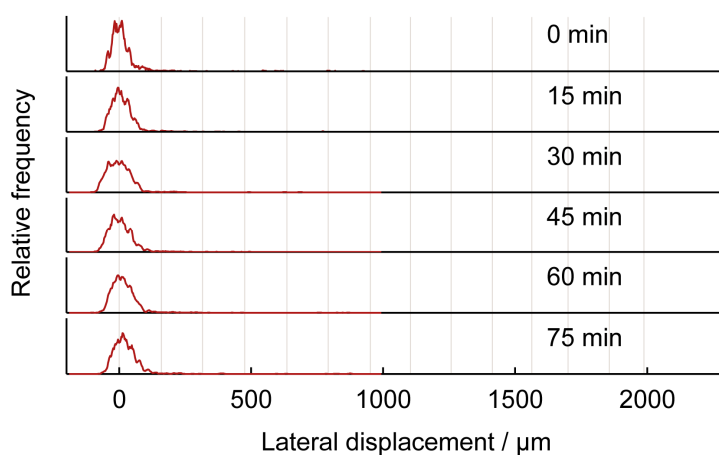


**Fig. E3.** The distribution of RBCs at the end of the device is shown as a function of time. Distributions are measured by tracking particles in films similar to movie 7. No change in the distribution can be seen after 75 minutes of running the device.

# Paper II





Cite this: *Anal. Methods*, 2016, 8, 3291

## Simplifying microfluidic separation devices towards field-detection of blood parasites†

S. H. Holm,<sup>a</sup> J. P. Beech,<sup>a</sup> M. P. Barrett<sup>b</sup> and J. O. Tegenfeldt<sup>\*a</sup>

With our sights set on a simple and inexpensive diagnostics device based on extraction and enrichment of parasites from human blood, we present a device design that relies on a combination of multiple different deterministic lateral displacement arrays. Our end goal is a microfluidic device that will be easy to use in the rural, resource-deprived areas where simple-to-use medical tools are crucially needed for rapid and accurate diagnosis. Here, we exemplify this in the application of blood parasite enrichment from a sample of blood. With trypanosomes as a model system we show a combination of functionalities designed into a single device based on several deterministic lateral displacement arrays of different depths arranged in series. With only one inlet and no expensive or complicated pumping mechanisms to run separations we ensure the level of simplicity necessary for field use.

Received 14th February 2016  
Accepted 20th February 2016

DOI: 10.1039/c6ay00443a

[www.rsc.org/methods](http://www.rsc.org/methods)

### Introduction

For many tropical diseases, identifying parasites or infected blood cells among a huge background of normal blood cells is the gold standard for diagnosis.<sup>1</sup> Particle separation techniques such as acoustophoresis,<sup>2</sup> margination<sup>3</sup> and inertial focusing<sup>4,5</sup> have been developed that show great promise as candidates for the field diagnosis of tropical diseases, however the gap between how microfluidics devices are run in labs and how they need to be run in the field is still considerable. In well-equipped labs there are pressure pumps, expensive pressure control units or syringe pumps plus advanced microscopes to monitor device function, giving information that is in turn used to make changes to flow rates and pressures. In the field however the lack of equipment, and in many cases maybe even access to a power grid, means that devices designed to work well in the lab, are doomed to failure. One approach would be to develop cheaper, less power consuming flow-control and optical systems. Another approach is to develop systems that require as little control as possible, which can perform complex operations with minimum requirements on external control. Paper-based microfluidics<sup>6</sup> is the epitome of the second approach, where all functions are designed into the device and the only external control required is the application of a droplet of sample followed by a simple visual readout. While these

systems are promising for many applications, they are not well-suited to high-resolution particle separations for which device structures often need to be much more well-defined on the microscopic scale than the random fibrous structure of paper. Here we describe a device that is designed to perform complex, high-resolution size and shape-based particle separation without expensive fluidic control equipment. The separation mechanism in our device is deterministic lateral displacement (DLD).<sup>7</sup> The basic concept is to use simple and cheap pressure generation (a disposable syringe where air is compressed to give an over-pressure), simple sample input (one inlet only for the entire device), and sequential particle sorting units based on DLD to decomplex a mixture of particles. While applicable to any system containing particles that differ in size and/or shape we focus here on the separation of parasites from the genus *Trypanosoma* from blood cells. We have previously shown how trypanosomes and erythrocytes exhibit different behaviours in DLD devices as the device depth is changed, a fact that we previously used to perform separations.<sup>8</sup> In the present work we use multiple array parameters, including depth, to realize complex functions in our device while simultaneously simplifying fluid control and use the decomplexing of a mixture of human blood and trypanosomes as a test system.

Endemic to sub-Saharan Africa, human African trypanosomiasis (HAT) is a fatal vector-borne parasitic disease caused by the protozoan parasite *Trypanosoma brucei*, transmitted by tsetse flies.<sup>9</sup> Its diagnosis relies to a great extent on tedious and laborious microscopic detection in blood smears or lymph node aspirates.<sup>10</sup> The key bottleneck with conventional microscopic diagnosis of HAT is the relatively low number of parasites against the overwhelming background of blood cells. Consequently the detection threshold for normal microscopic diagnosis is relatively high ( $\sim 10\,000\text{ ml}^{-1}$ )<sup>11</sup> in comparison to the

<sup>a</sup>Division of Solid State Physics, NanoLund, Lund University, PO Box 118, S-221 00 Lund, Sweden. E-mail: [jonas.tegenfeldt@ff.lth.se](mailto:jonas.tegenfeldt@ff.lth.se); Fax: +46 46 222 3637; Tel: +46 46 222 8063

<sup>b</sup>Welcome Trust Centre for Medical Parasitology, Institute of Infection, Immunity and Inflammation, College of Medical, Veterinary and Life Sciences, University of Glasgow, UK

† Electronic supplementary information (ESI) available. See DOI: 10.1039/c6ay00443a

parasitaemia (parasite number density in blood). This varies periodically during the course of the disease but can at times be as low as  $100 \text{ ml}^{-1}$ , and consequently, there could be more than 50 million blood cells (predominantly erythrocytes) per parasite.<sup>11</sup> Today, expensive and power-consuming technologies, such as ion exchange chromatography and centrifugation, are available at most modern facilities, and can be used for relatively efficient parasite detection (*via* enrichment relative to blood cell concentration). However, it is challenging to employ these tools in the geographical areas where the disease is prevalent, due to the lack of reliable power and storage facilities. Our aim is to use a microfluidic sorting scheme to extract the parasites for visual inspection, thus addressing the limitations of current technologies.

### Deterministic lateral displacement

Our device, Fig. 1, can be fabricated in cheap materials, has no moving parts or power requirements and being no larger than a microscope slide, is highly portable. It is based on Deterministic Lateral Displacement (DLD), a method first shown in 2004 by Huang *et al.* that in its simplest configuration separates particles based on size.<sup>7</sup> In brief, DLD uses an array of obstacles in a fluidic channel. Particles smaller than a critical size follow the overall flow direction, while larger particles are deflected at an angle relative to the flow, defined by the array. The critical size depends on the obstacle-obstacle distance (perpendicular to the flow direction, *Gap*) and the distance each row is shifted relative to the previous (*Row shift*), see Fig. 2A.<sup>12–16</sup>

The method has been shown capable of size-fractionating a wide range of samples including blood components,<sup>17,18</sup> cancer cells<sup>9</sup> and synthetic particles such as droplets in two-

phase flow.<sup>20</sup> A recent review<sup>21</sup> by Bridle *et al.* gives an expansive overview of this particle separation technique.

By controlling and exploiting shear forces our group recently added deformability<sup>22</sup> to the list of parameters by which particles can be separated using DLD devices. Also, by controlling the orientation of particles as they pass through the device, we have been able to separate particles based on shape. As a proof of principle we showed that channel depth could be used to control the orientation of particles, and used this effect to accentuate the differences in shape of parasites and human blood cells<sup>8</sup> making otherwise very difficult separations possible.

The work presented herein builds on these findings and involves a complete redesign of the device. The outcome is a more robust, easier to use device, with a significantly increased throughput. Our method provides a dramatically simpler and cheaper alternative to existing methods with the potential of enabling a fast and cheap point-of-care device that will have significant impact on field diagnosis.

### Device design

In designing our device we prioritized simplicity and ease of use. We require the device to handle blood with low concentrations of parasites, with as little dilution as possible, and output close to all parasites in a sample stream free of blood cells. We designed a device with one inlet only, so that flow can be driven simply using a disposable syringe. To avoid pressure control systems that are both expensive and demanding with regards to user input, all functionality must be designed into the device: (1) Removal of leukocytes in order to avoid clogging in subsequent steps, (2) creation of cell-free plasma, and (3) transfer of parasites into the cell-free plasma. The functionality in each section of the device comes from a combination of the array spacing parameters and the depth of the channel (height of the posts). The final device consists of three DLD arrays in series, each with its own depth, optimized to carry out these three tasks, Fig. 3A–B.

Section (1) is designed to function like a traditional size-based DLD with a depth larger than the diameter of all blood cells. As we have previously shown,<sup>8</sup> in deep devices particles rotate due to shear forces and are consequently sorted according to their smallest dimension. Here, the spherical leukocytes, being in the range 8–15  $\mu\text{m}$ , are displaced and removed from the sample *via* a side channel. Erythrocytes and trypanosomes, on the other hand, have a smallest dimension of  $\sim 2.5 \mu\text{m}$  which is below the critical size in this section. As a consequence, they are not laterally displaced and mainly follow the flow to the subsequent section.

Section (2) is shallow (3.5  $\mu\text{m}$ ) to minimize the rotational freedom of the cells and consequently maximize their effective size. The array is designed so that all cells are laterally displaced towards the channel walls creating a cell-free stream in the centre. A mirrored design<sup>23</sup> is employed to minimize the migration distance of cells to the nearest wall which results in a higher throughput.

Section (3) has the same post size, post gap and row shift as section (2) but is deeper, (9  $\mu\text{m}$  from previous optimization<sup>8</sup>).

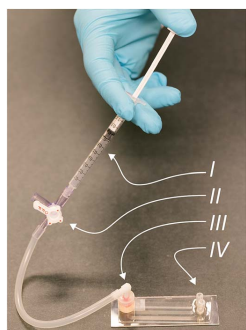
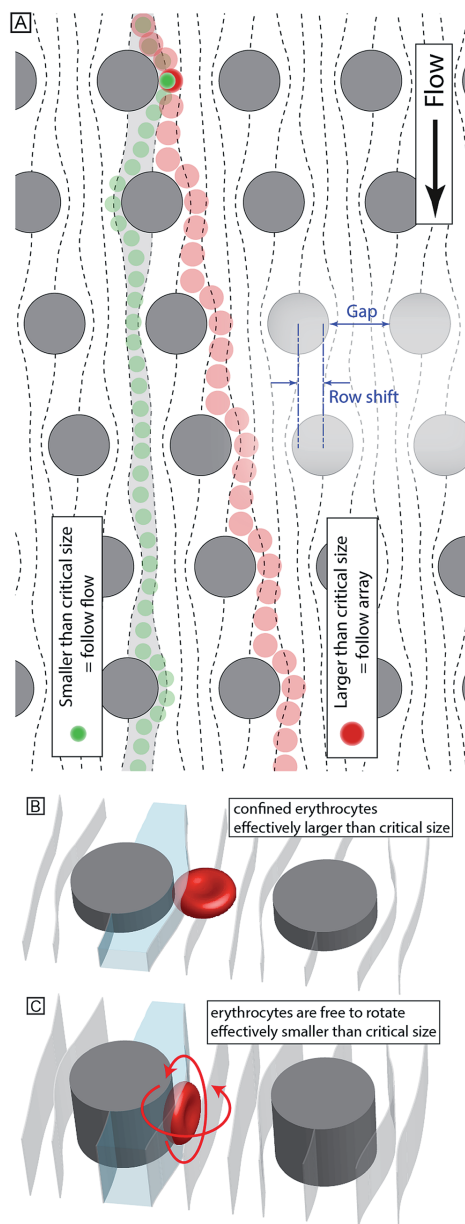


Fig. 1 Complete device consisting of a syringe (I), a pressure valve (II), sample inlet (III) and outlets for sorted particles (IV). Here, the fluid is actuated by compressing air with a simple syringe. When the desired pressure is reached, the valve is closed allowing for a stable pressure throughout the measurement. The sample is injected into the single inlet reservoir prior to attaching the pressure system. Following an analysis, the sorted particles (erythrocytes, leucocytes and *T. cyclops* parasites) can be visualized in, or collected from the outlets for further processing.



**Fig. 2** (A) Schematic illustration of size-based sorting in DLD devices. Particles smaller than the critical size follow the direction of fluid flow while particles larger than the critical size follow rows of posts. (B–C) Non-spherical particles (such as erythrocytes) behave very differently

The row shift direction is also mirrored such that displaced particles are focused into the centre of the channel. The key idea is that the depth of this section is sufficient for erythrocytes to rotate and behave like  $2.5\ \mu\text{m}$  particles, as decided by their thickness, and they consequently remain near the walls. At the same time the longer parasites are still partially confined and behave as effectively larger particles being displaced back into the cell-free plasma and into a separate outlet where a dense array of posts ( $8\ \mu\text{m}$  in diameter with a separation of  $2\ \mu\text{m}$  while keeping the array wide,  $4\ \text{mm}$ , in order to minimize the effect of clogged particles) serves as a sieving structure to capture and concentrate the cells of interest once they have been sorted. The parasites can thereafter be detected (future work will focus on detection schemes for the enriched parasites).

### Simple pump system

The single inlet design not only simplifies the sample handling and introduction to the device, but it also allows for a device which does not require advanced and expensive pressure controllers that would otherwise be necessary to fine-tune and balance the pressures applied to the different inlets. Instead, here a simple approach is employed where the air in a syringe is compressed in a controlled way, thereby resulting in a well-defined overpressure (see Fig. 4). The relatively large volume of air in the system compared to the small volume of fluid handled in the device, together with well-sealed connections ensures that the overpressure is maintained at a stable level over the course of the experiment.

## Method

### Device design and fabrication

L-Edit 11.02 (Tanner Research, Monrovia, CA USA) was used to draw the device design and photolithographic masks were manufactured by Delta Mask (Delta Mask, Enschede, The Netherlands). To fabricate a master consisting of a single continuous device three separate cycles of UV-lithography were performed which consisted of resist spinning, precisely aligned exposures (Karl Suss MJB4, Munich, Germany) and development using SU8 (SU8-2005, SU8-2007 and SU8-2015, Microchem Corp., MA, USA) on  $3''$  silicon wafers. After treatment of the master with an anti-adhesion layer of  $1H,1H,2H,2H$ -per-fluorooctyl-trichlorosilane (ABCR GmbH & Co. KG, Karlsruhe, Germany)<sup>24</sup> to facilitate demoulding, replicas were created in PDMS (Sylgard 184, Dow Corning, Midland, MI, USA) by standard replica moulding.<sup>25</sup> PDMS casts were oxygen plasma bonded to blank PDMS slides (Plasma Preen II-862, Plasmatic Systems Inc., North Brunswick, NJ, USA) to obtain devices entirely consisting of PDMS. To prevent sticking of cells in the devices, they were immediately filled with  $0.2\%$  (w/v) PLL(20)-g[3.5]-PEG(2) (SuSoS AG, Dubendorf, Switzerland) in deionized water and

when confined in shallow devices compared to in deep devices where they are able to rotate. In a shallow device (B) erythrocytes have an effective size corresponding to their diameter. In a deep device (C) they are instead sorted according to their much smaller thickness.

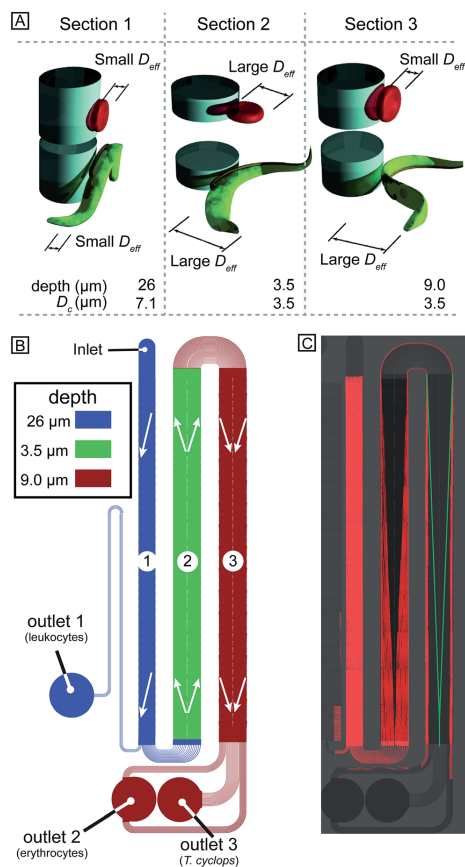


**Fig. 3** (A) Basic principle of how orientation changes the effective size of particles of different shape. (B) Schematic overview with the three different sections colour coded. Arrows represent the direction of displacement in each section. (C) False-coloured mosaic image consisting of 34 time-integrated micrographs showing the trajectories of erythrocytes and the parasites through the device.

allowed to rest for at least 20 min before flushing with deionized water for another 20 min. Silicon inlets and outlets 12 mm and 5 mm outer diameter silicon tubing (228-0725 and 228-0707, VWR International LLC, Radnor, PA, USA) were glued (Elastosil A07, Wacker Chemie AG, Munich, Germany) onto the device. The sample was applied to the inlet reservoir, which was subsequently connected to the syringe to drive the sample through the device.

To maximize the throughput, the device has been kept as wide as possible. This means however that, together with the relatively small angle of displacement, the device needs to be long. In fact, the final device is around 14 cm. To fit this onto

a standard glass slide the device is split up into its three different sections with multiple channels connecting the end of each array with the start of the proceeding array, see Fig. 5A–B. To ensure that the particles maintain their relative lateral position while moving between the different sections, careful calculations and CFD simulations (COMSOL Multiphysics 4.3, Comsol AB, Stockholm, Sweden) have been conducted, the key being to keep a constant resistance across the width of the device such that the flow and particle profiles are preserved around the 180° bends. More info on this optimization can be found in ESI section (3).†

### Experimental setup

All experiments were performed in compliance with the relevant laws and institutional guidelines. Blood was extracted *via* finger pricking (Haemolance, MedCore AB, Kista, Sweden) of healthy volunteers from which informed consent was obtained. Prior to each experiment, the devices were flushed with sterile filtered Cunningham's medium<sup>26</sup> with 20% fetal calf serum (Cat. No. F2442, Sigma-Aldrich, St. Louis, MO, USA), the medium used to culture the parasites, and 2 mM EDTA (Cat. No. E6758, Sigma-Aldrich) to inhibit coagulation of the blood. It is important to note that Cunningham's medium is only necessary to sustain our model system.

In order to obtain good statistics on the device performance, measurements were often conducted with the same device for several hours. Consequently, to counteract particle sedimentation and ensure a homogenous sample, a small magnetic stir bar (length 5 mm, diameter 2 mm) was placed in the inlet reservoir and controlled by a magnet connected to a small electric motor. With a stir rate of  $\sim 1$  Hz and the dimensions of the stir bar and inlet reservoir as given above, the shear rate is estimated to be on the order of  $10$  s<sup>-1</sup> to  $100$  s<sup>-1</sup>, which is less than the physiological shear rates of up to  $\sim 10^4$  s<sup>-1</sup>.<sup>27,28</sup> Further, microscopic examination confirmed that the stir bar did not induce any morphological changes in the sample. For actual field use of the final device, the short time of analysis would eliminate the need for any stirring.

### Measurements and analysis

The lateral distribution of cells was characterized at the end of each section in the device through an inverted Nikon Eclipse TE2000-U microscope (Nikon Corporation, Tokyo, Japan) using an EMCCD camera (iXon EM+ DU-897, Andor Technology Ltd, Belfast, UK) and various objective lenses (Nikon, 10/20x Plan Fluor and 60x Apo TIRF). Differential Interference Contrast (DIC) was used to ensure adequate contrast of blood cells and trypanosomes.

Particle tracking software, based on available MATLAB code, was written in MATLAB R2014b (The MathWorks Inc, Natick, MA, USA) and optimized for accurate and efficient particle recognition. Detailed information together with the code can be found in ESI section (4).†

Blood and trypanosomes were analysed at concentrations, which allowed for automated particle tracking while the addition of anticoagulants opened up for measurements over several



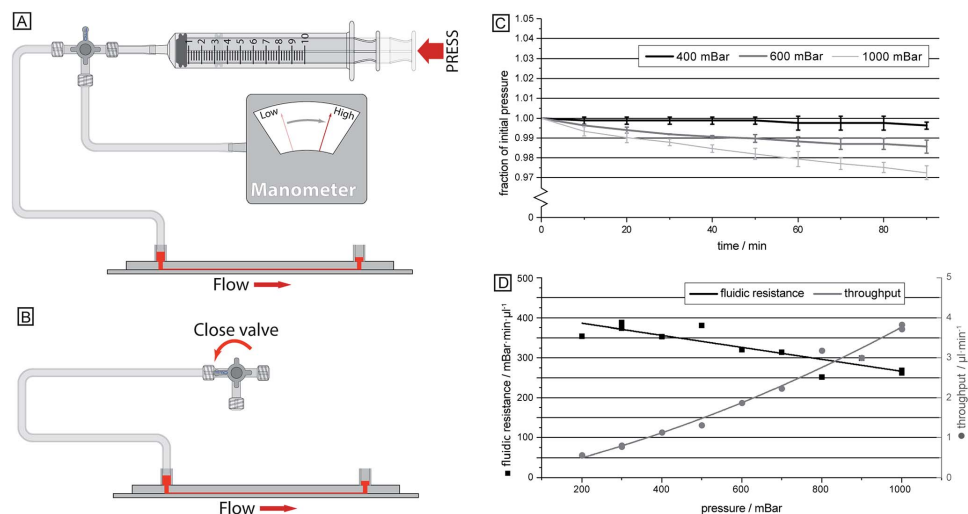


Fig. 4 (A–B) Schematic overview of the device connected with a simple syringe that was used in all measurements to induce fluid flow. A manometer was initially used to relate the syringe compression with the resulting overpressure, ensuring that the correct pressure was achieved. Thereafter a valve is closed resulting in a consistent pressure over longer times. (C) Applied pressure measured over 90 minutes given as fraction of the initial pressure. (D) Throughput in terms of sample fed into the system measured as a function of the pressure difference across the device.

hours per device without any blood clotting affecting the flow behaviour.

For all measurements, the morphologically similar but much less dangerous (and less restricted) parasite *T. cyclops* was used instead of the human parasites *T. brucei rhodesiense* or *T. brucei gambiense*.<sup>8</sup>

Blood and parasites were initially analysed separately in order to better characterize how the output of the device varied with flow rate. Subsequently, with the optimum flow rate determined, spiked samples were separated. For the initial samples where blood was run separately, it was diluted 10× in autoMACS Running Buffer (Miltenyi Biotec GmbH, Bergisch Gladbach, Germany). This is an isotonic PBS solution containing 2 mM EDTA, 0.5% BSA and 0.09% azide. In addition to preventing blood clotting, a lower concentration decreases the particle–particle interaction. For field-diagnostics we envision the collection of blood in pre-filled vials (e.g. BD Vacutainer® 366450, BD Biosciences, Franklin Lakes, NJ, USA). For the spiked blood samples, the blood was washed twice in Cunningham's buffer to remove the lytic factors causing natural lysis of *T. cyclops*, which is not adapted to human physiology (this step would not be necessary for the *T. brucei*). The 10× diluted blood sample was then spiked with trypanosomes at a concentration of approximately 1000 μl<sup>-1</sup>. This is in most cases a higher concentration than what occurs in normal rare cell detection. However, it allows us to accurately determine the device performance in terms of sorting efficiency. Detailed protocols are available in the ESI section (7).†

## Results and discussion

### Multi-layered device characterization

During UV-lithographic fabrication of the master, the different sections of varying depths could be precisely aligned to each other with an estimated positioning error less than 3 μm. This is small enough to have a negligible effect on the flow, and consequently, the relative lateral position of the particles in the device. Fig. 5A–E shows SEM micrographs of a finalized continuous device in PDMS consisting of multiple depths. Here, three of the main features of the device are shown. First, the channels of equal resistance connecting the subsequent arrays can be seen in Fig. 5A–B. Due to the complexity of the device with multiple arrays in series it will be longer than a normal DLD device. Consequently, to fit the entire device on a normal glass slide the device design is folded, forming a serpentine. In order to maintain the relative particle positions between sections, multiple channels with identical fluidic resistances are used to connect subsequent sections. To accomplish this, the shorter channels are designed to be narrower than the longer ones. Between section (1) and (2), there are in total 16 channels while 28 channels connect section (2) and (3). A detailed description of these channels can be found in ESI section (3).† In Fig. 5C–D the sieving structure in the outlet is shown. This feature has been implemented to capture sorted cells of interest and to focus them to a smaller area allowing for easier detection. In Fig. 5E–G the two step changes in height of the device are shown. The first of these two SEM micrographs

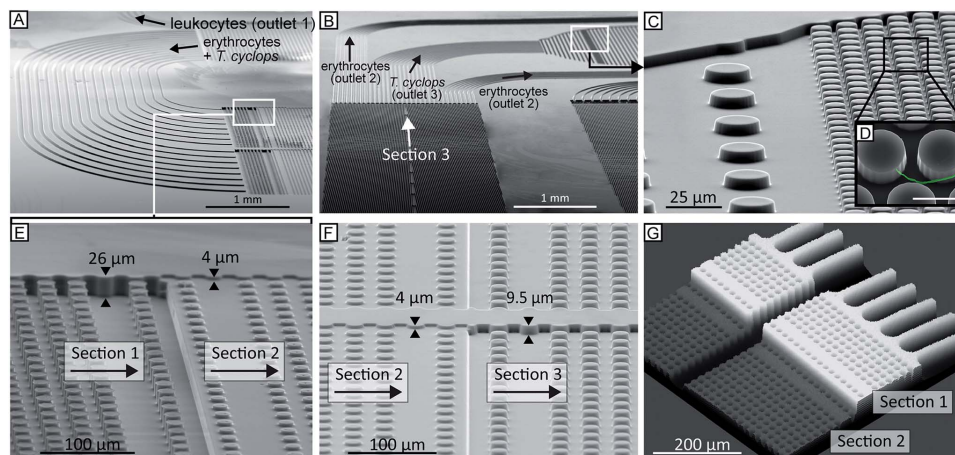


**Fig. 5** (A–F) SEM and (G) confocal images of the device. (A–B) The channels connecting the different sections of the device are designed to be of equal fluidic resistance, and therefore their individual widths are chosen to compensate for the varying lengths. Due to these channels, the flow symmetry is maintained and the relative positions of the particles are conserved between subsequent sections allowing for longer and more complex devices to be created. By precise alignment of the complementary photolithographic masks in three separate UV-lithographic cycles, sections of different channel depth could be fabricated into a single continuous device. (E–F). After the final section in the device, section (3), the trypanosomes have been focused to the centre and thus exit to the trypanosome outlet where a dense array of pillars (C–D) is defined with the purpose of capturing the parasites. Note the inset (D) where a parasite is highlighted (coloured green), scale bar is 10  $\mu\text{m}$ . (G) Confocal micrograph of a fluorescent solution (0.1% rhodamine B in  $\text{H}_2\text{O}$ ) passing through the step-change in depth between section (1) and (2), same as (E). The grey scale is mapped to the fluorescence signal.

shows how the deep channels in section (1) transition to the shallow channels in section (2). The other micrograph shows the end of the same section but here the transition is from the shallow section (2) to the intermediate section (3). Fig. 5G further shows the transition from deep to shallow channel depth, here visualized after being filled with 1  $\text{mg ml}^{-1}$  rhodamine B (#83689, Sigma) in  $\text{H}_2\text{O}$  and imaged using confocal microscopy.

#### Using a simple syringe to control flow rate

Compressing the syringe leads to a pressure drop across the device acting to drive the sample, which prior to this has been loaded into the sample inlet. Having a stable pressure is required as flow rate affects the sorting of deformable cells, as shown previously, allowing for sensitive measurements to take place over a longer time. Here we succeeded in achieving high pressure stability, Fig. 4C, by utilizing a large dead volume ( $\sim 12$  ml) together with sealed connections. At an initially applied overpressure of 1 bar across the device the resulting pressure decreased less than 3% over 90 minutes. The volumetric throughput is  $\sim 390$   $\mu\text{l}$  during this time, which according to Boyle's law explains the pressure decrease, indicating little to no leakages in the system.

The results from the calibration of the flow speed in relation to the syringe compression are given in Fig. 4D. Here, it can be seen that the hydrodynamic resistance of the device decreases

with increasing pressure, which is expected due to the elastic PDMS device becoming deformed, and inflated, at high pressures. Consequently, the flow rate is not linearly proportional to the applied driving pressure, instead it varies between 2.5 and 3.8  $\mu\text{l (min bar)}^{-1}$ . The volumetric flow rate here is given as the sample input rate. From this, approximately 20% of the total flow is separated out to outlet 1, enriched with leukocytes, while the sorting between erythrocytes and trypanosomes takes place in the remaining volume.

#### Erythrocytes and leukocytes at various flow rates

The behaviour of soft, deformable cells in a DLD device depends to a great extent on the flow rates. Increasing the flow rates leads to a larger force exerted on the cells by the fluid acting to deform them. Consequently their size and, as a result, the sorting in the device might change. Further, cells in channels deeper than their size can rotate freely under the influence of the shear field of the fluid, which as shown previously, acts to make the cells present their smallest dimension to the posts. An erythrocyte would due to this effect have an effective size the same as its thickness,  $\sim 2.5$   $\mu\text{m}$  instead of its diameter,  $\sim 7.5$   $\mu\text{m}$ . However, at low flow rates the shear stress exerted by the fluid becomes smaller, which acts to decrease the rotational effect. Another effect of higher flow rates is the increased pressure drop, which acts to inflate the deformable PDMS devices, something which in turn leads to an increase of the critical size.

The erythrocytes and parasites were initially measured separately at various flow rates to allow for automated particle tracking of a large number of cells. Thereafter, spiked blood samples were analysed at the most promising flow rates.

The results from the separate measurements of erythrocytes and *T. cyclops* are presented in Fig. 6, with the sorting efficiency further analysed in Fig. 7.

In Fig. 7 the output of each section is given for both erythrocytes and *T. cyclops* at several different flow rates as a fraction of the total number of that cell type in that specific section. It can be seen that in section (1), Fig. 6B, the fraction of cells separated out are larger at low flow rates but converges to ~20% with increasing flow rates (and consequently ~80% of the cells continue to section (2)). Section (1) is deeper than the largest dimensions of both cell types, the length of the *T. cyclops* and the diameter of the erythrocytes. As a result the cells can rotate freely as discussed previously, resulting in a decreased effective size. With the section designed with a critical size of 7.1  $\mu\text{m}$ , the cells are not expected to be laterally displaced. However, at low flow rates the shear stress exerted on the particles by the fluid is limited which leads to a decrease in both the orientation of the cells and also the cell deformation. As a consequence, the fraction of cells sorted out into outlet 1 can be higher than the expected 20%.

In section (2), Fig. 6C, the cells are steered towards the sides of the channel to open up a cell-free stream in the centre. Due to the low depth of this section, the cells are restricted from rotating which leads them to display a larger effective size and consequently they are more easily laterally displaced into the side streams along the channel walls. Here, the side streams are defined as the outermost 25% on both sides of the channel while the centre stream constitutes the remaining 50%. The size of these streams is defined by how the end of section (3) is divided into outlet 2 and 3, meaning that any cells residing in the centre stream at the end of section (2) are likely to also be sorted into outlet 3. In the same way, any cells residing in the side streams will end up in outlet 2 unless they are laterally displaced in section (3).

At lower flow rates, around 95% of cells entering section (2) will at the end reside in the side streams. However, at high flow rates the soft erythrocytes will, by deforming due to shear forces, avoid being laterally displaced and will end up as a contaminant among the parasites in outlet 3. At 3.8  $\mu\text{L min}^{-1}$  around 20% of the erythrocytes exiting this section do so in the centre stream and are expected to end up as a contamination in outlet 3, leading to poor separation sensitivity.

Section (3) is identical to section (2) except for the direction of displacement and the depth, Fig. 6D. By the increase in depth

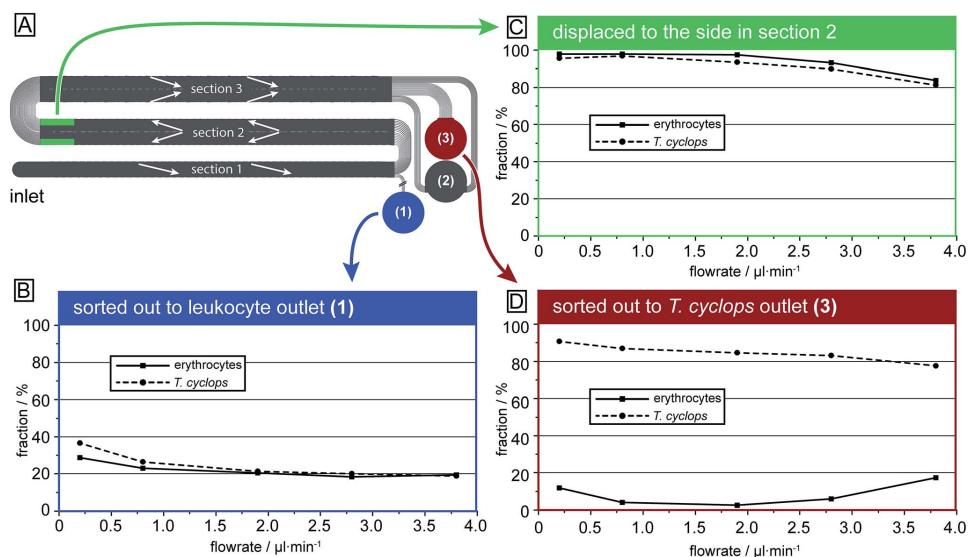


Fig. 6 Sorting efficiencies as a function of flowrate (i.e. the fraction of cells in section (1) that is sorted out into outlet 1, the fraction in section (2) which is focused along the channel walls and the fraction in section (3) which are sorted out into outlet 3). The numbers are given as the fraction of that cell type in that specific section. (A) Schematic overview of the device highlighting the origin of the data in the graphs. (B) After the first section the erythrocytes and parasites are sorted out in proportion to the fluid flow going into the outlet. (C) In section (2) most erythrocytes and parasites are focused to the side. (D) For the separation of *T. cyclops* and erythrocytes intermediate flow rates give the highest separation efficiency. Each data point represents a minimum of 1000 counts. For the highest flow rates the number of counts was around 7000 for both erythrocytes and *T. cyclops*.

## Analytical Methods

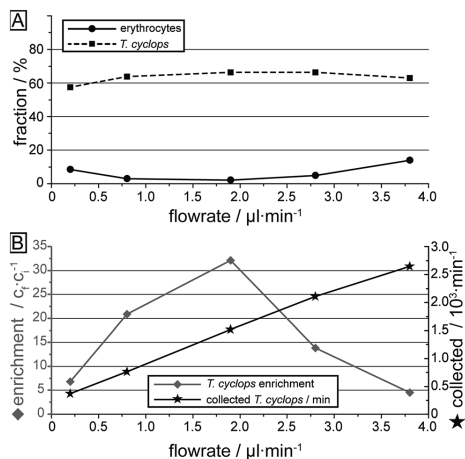


Fig. 7 Overall sorting performance versus applied pressure. (A) Fraction of erythrocytes and *T. cyclops* which are sorted into outlet 3. The numbers are given as the fraction of each cell type injected into the device. (B) Concentration enrichment of *T. cyclops* (ratio between the number of *T. cyclops* and the total number of particles) and the rate of trypanosomes arriving at the collection reservoir.

to 9.0  $\mu\text{m}$ , larger than the diameter of the erythrocytes, there is no steric hindrance to their orientation, leading to a decrease in their effective size as previously discussed. They are therefore not laterally displaced in this section and, if focused into the side streams in section (2), are sorted into outlet 2. Similar to the situation in section (1), it can be seen that if the flow rate is too low, the shear forces are not high enough to allow the cells to rotate and adopt the smaller effective size. Instead they have a maximum effective size equal to their diameter leading to a significant lateral displacement. At low flow rates (0.2  $\mu\text{l}\cdot\text{min}^{-1}$ ) 12% of the erythrocytes entering this section are sorted into outlet 3 even though they exit section (2) well-focused in the side streams. Consequently, the erythrocyte contamination in outlet 3 is here a result of unwanted lateral displacement in section (3). An increase of the flow rate leads to a decrease in the fraction of erythrocytes sorted out into outlet 3, however at too high pressure, the fraction once again increases. This is however believed to be an effect of erythrocytes not being well focused into the side streams when they exit section (2). This could potentially be avoided by increasing the width of section (2), leading to a decrease in the flow velocity (while maintaining the volumetric flow rate) and consequently the shear stress exerted on cells in this section.

For the *T. cyclops* the highest fraction of extracted cells is acquired at low pressures while the fraction decreases with increasing pressures. This shows how adjusting the depth of the channel can have a large impact on the behaviour of the cells, allowing for separation based on their differences in shape.

The measurements of *T. cyclops* and erythrocytes carried out separately at various flow rates are summarized in Fig. 7. Firstly,

the fraction of the two cells types which ends up in outlet 3 is shown, here calculated based on the input sample. This figure is similar to Fig. 6D, but the cells removed in section (1) have also been taken into account. The most notable difference is the decreased capture rate of *T. cyclops* at low flow rates which is due to the increase in fraction of *T. cyclops* being sorted out into outlet 1. As a result, the separation efficiency is decreased at these flow rates. The largest enrichment (32 times) is reached at 1.9  $\mu\text{l}\cdot\text{min}^{-1}$ . At this flow rate the fraction of erythrocytes entering outlet 3 is kept at a minimum (2.1%) while a large fraction of the trypanosomes are retained (66.5%). As a consequence, this was chosen as the flow rate for all the remaining measurements. However, it can be noted that even though the enrichment is the highest at this flow rate, the number of collected *T. cyclops* per minute increases with increasing flow rate. At a flow rate of 3.8  $\mu\text{l}\cdot\text{min}^{-1}$  the number of collected *T. cyclops* is almost twice that of 1.9  $\mu\text{l}\cdot\text{min}^{-1}$ . The optimum trade-off between throughput and purity will be determined by the choice of detection scheme in the specific application.

### Blood samples spiked with *T. cyclops*

As discussed, a flow rate of 1.9  $\mu\text{l}\cdot\text{min}^{-1}$  was chosen for the continued studies of spiked blood samples in order to receive the maximum enrichment of *T. cyclops*. In these measurements, the sorting of leukocytes was also considered in order to show the versatility of the device, and its potential for applications other than erythrocyte and *T. cyclops* separation.

On the whole, the outcome, given in Fig. 8, agrees with the previous measurements. For the erythrocytes 21.7% are diverted to outlet 1 (leukocyte outlet). For the remaining erythrocytes which continue into section (2) the fraction successfully focused into the side stream amounts to 97.6%.

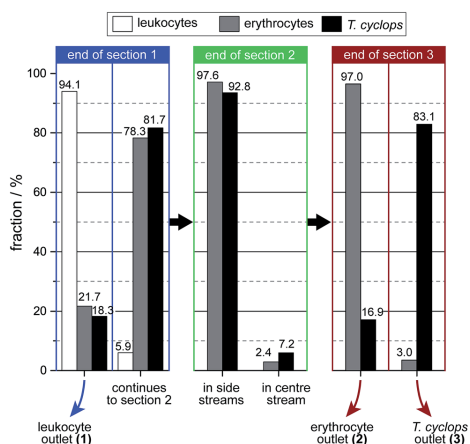


Fig. 8 Distribution of the three different cell types at the end of each section. The numbers are given as the fraction of that cell type in that section.

From this number, a small fraction (0.6%) is not retained along the sides of the channel in section (3) but instead end up in outlet 3 (*T. cyclops* outlet) as a contamination. The remaining 97.0% which still remain in the side streams exit into the correct outlet which is close to the result of the separate measurements.

For the trypanosomes 18.3% is laterally displaced into outlet 1 while 92.8% of the remaining parasites are successfully focused into the side streams. This is, in agreement with previous measurements a smaller fraction than for the erythrocytes. But as the *T. cyclops* should exit into outlet 3 from the centre of section (3), this would lead to an increased sorting efficiency. In the end, 83.1% of the remaining *T. cyclops* exit into outlet 3, equivalent to a 30-fold enrichment in the number concentration. The leukocytes are, contrary to the other cells, laterally displaced to a great extent in section (1). The majority of them, 94.1%, are sorted out into outlet 1 while the remaining fraction continues to the shallower section (2). A large fraction of these leukocytes are not able to enter this shallow section, however over the time scale of our experiments the number of leukocytes filtered out was too small to adversely affect the device performance. This is believed to be an effect of the device's robustness to pressure changes, with section (2) being aimed at focusing all cells towards the wall. The result of this is that any smaller pressure variations will not have an effect on the device performance.

The total output from the device is summarized in Fig. 9, here we can see that 100% of the extracted leukocytes are found in outlet 1 owing to the large size and shape difference between leukocytes and the other cell types. There is a relatively large number of background cells present, around 20% of each cell type, as expected due to the design of section (1). The addition of a focusing section, similar to section (2), positioned before the sorting-out of leukocytes takes place, the number of background cells in outlet 1 could be greatly reduced. In outlet 2 the

fraction of erythrocytes amounts to 76.0% (77.4%), while 67.9% (66.5%) of the *T. cyclops* are retained in outlet 3 (results of the earlier measurements on individual cell types are given in parenthesis). As can be seen, these fractions are in close agreement with the earlier measurements with a marginally smaller number of erythrocytes retained in outlet 2 while a slightly larger fraction of *T. cyclops* can be steered into outlet 3. It should however be noted that these numbers rely on the bifurcation of the flow into the outlets. The current device was designed to have, as described earlier, half the flow at the end of section (3) guided to outlet 2 and the other half to outlet 3. Changing these fractions would potentially lead to a better performance of the device. For example, decreasing the fraction of the flow in section (3) bifurcated into outlet 3 would remove more erythrocyte and would likely increase the specificity of the device.

## Conclusions

We have demonstrated a proof-of-principle of a device that, while simple-to-use, can perform complex separations such as the fractionation of parasites, leukocytes and erythrocytes. Our method utilizes several steps along the device where differences in morphology and size between the particles are given different weights by varying the depth of the DLD array. The principle of using multiple successive arrays to focus and then separate particles could be applied to any of the particle parameters (or combinations thereof) that have been shown to affect behaviour in DLD devices such as size, shape, deformability and dielectric properties. What is more, the device functions without expensive pressure controllers and can be run using pressurized air from a single disposable syringe.

We believe the approach that we have presented here shows great promise as a point-of-care test for a multitude of diseases. In addition to our test system with African trypanosomiasis other protozoan parasites could be considered such as, but not limited to, leishmaniasis, Chagas disease and malaria, where particle size, shape and deformability can be leveraged for the enrichment of hard to find objects. These diseases affect millions worldwide, not only *via* direct infection of human populations but also *via* the socioeconomic burden of livestock infection.<sup>29</sup>

While we believe the current device offers several advantages over current methods there is still work to be done towards a fully functioning field-ready diagnostic device. Most notably lacking is portable detection. One solution may be the devices developed by Ozcan *et al.*<sup>30</sup> that have shown great promise for field-detection of pathogens combined with telemedicine. Another would be integrated electronic cell counting based on impedance spectroscopy.<sup>31</sup>

Further, the current experiments were performed in devices made using soft lithography. This is a rapid prototyping technique that is suitable for research, but for field applications large numbers of devices would be needed at lower cost. Foil-based fluidics<sup>32,33</sup> and injection moulding approaches would provide the necessary basis for mass-produced devices and be fully compatible with our method.

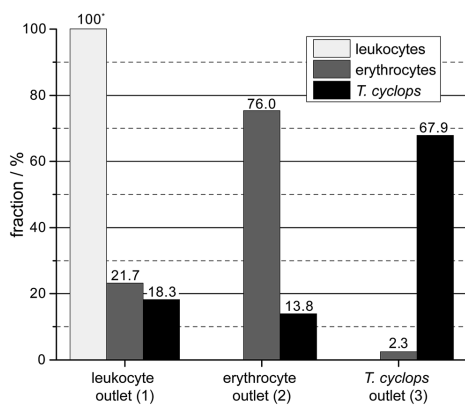


Fig. 9 The output of the device given as the fractional distribution of the three measured cell types.

## Acknowledgements

This work was carried out within NanoLund at Lund University as part of LAPASO (EU FP7 project 607350) and was supported by the Swedish Research Council (VR) grants no. 2007-584, 2011-6035 and 2015-05426, the Crafoord Foundation grants no. 2005-1123, 2008-0841 and 2015-0007 and the Knut and Alice Wallenberg Foundation. All device processing were conducted within Lund Nano Lab. We would like to thank Zhen Li (Lund University, Sweden) for her help in acquiring confocal images.

## Notes and references

- 1 P. Mitashi, E. Hasker, V. Lejon, V. Kande, J. J. Muyembe, P. Lutumba and M. Boelaert, *PLoS Neglected Trop. Dis.*, 2012, **6**, e1919.
- 2 A. Lenshof, C. Magnusson and T. Laurell, *Lab Chip*, 2012, **12**, 1210–1223.
- 3 H. Wei Hou, H. Y. Gan, A. A. Bhagat, L. D. Li, C. T. Lim and J. Han, *Biomicrofluidics*, 2012, **6**, 24115–2411513.
- 4 M. E. Warkiani, G. Guan, K. B. Luan, W. C. Lee, A. S. Bhagat, P. Kant Chaudhuri, D. S.-W. Tan, W. T. Lim, S. C. Lee, P. C. Y. Chen, C. T. Lim and J. Han, *Lab Chip*, 2014, **14**, 128–137.
- 5 D. Di Carlo, *Lab Chip*, 2009, **9**, 3038–3046.
- 6 D. M. Cate, J. A. Adkins, J. Mettakoonpitak and C. S. Henry, *Anal. Chem.*, 2015, **87**, 19–41.
- 7 L. R. Huang, E. C. Cox, R. H. Austin and J. C. Sturm, *Science*, 2004, **304**, 987–990.
- 8 S. H. Holm, J. P. Beech, M. P. Barrett and J. O. Tegenfeldt, *Lab Chip*, 2011, **11**, 1326–1332.
- 9 M. P. Barrett, R. J. S. Burchmore, A. Stich, J. O. Lazzari, A. C. Frasch, J. J. Cazzulo and S. Krishna, *Lancet*, 2003, **362**, 1469–1480.
- 10 J. E. Rosenblatt, L. B. Reller and M. P. Weinstein, *Clin. Infect. Dis.*, 2009, **49**, 1103–1108.
- 11 F. Chappuis, L. Loutan, P. Simarro, V. Lejon and P. Büscher, *Clin. Microbiol. Rev.*, 2005, **18**, 133–146.
- 12 D. W. Inglis, J. A. Davis, R. H. Austin and J. C. Sturm, *Lab Chip*, 2006, **6**, 655–658.
- 13 K. Lougherback, K. Chou, J. Newman, J. Puchalla, R. Austin and J. Sturm, *Microfluid. Nanofluid.*, 2010, **9**, 1143–1149.
- 14 S. Cerbelli, M. Giona and F. Garofalo, *Microfluid. Nanofluid.*, 2013, **15**, 431–449.
- 15 M. Jiang, K. Budzan and G. Drazer, *Microfluid. Nanofluid.*, 2015, **19**, 427–434.
- 16 R. Devendra and G. Drazer, *Microfluid. Nanofluid.*, 2014, **17**, 519–526.
- 17 J. A. Davis, D. W. Inglis, K. J. Morton, D. A. Lawrence, L. R. Huang, S. Y. Chou, J. C. Sturm and R. H. Austin, *Proc. Natl. Acad. Sci. U. S. A.*, 2006, **103**, 14779–14784.
- 18 D. W. Inglis, K. J. Morton, J. A. Davis, T. J. Zieziulewicz, D. A. Lawrence, R. H. Austin and J. C. Sturm, *Lab Chip*, 2008, **8**, 925–931.
- 19 K. Lougherback, J. D'Silva, L. Liu, A. Wu, R. H. Austin and J. C. Sturm, *AIP Adv.*, 2012, **2**, 042107.
- 20 H. N. Joensson, M. Uhlen and H. A. Svahn, *Lab Chip*, 2011, **11**, 1305–1310.
- 21 J. McGrath, M. Jimenez and H. Bridle, *Lab Chip*, 2014, **14**, 4139–4158.
- 22 J. P. Beech, S. H. Holm, K. Adolfsson and J. O. Tegenfeldt, *Lab Chip*, 2012, **12**, 1048–1051.
- 23 Y. S. Lubbersen, R. M. Boom and M. A. I. Schutyser, *Chem. Eng. Process.*, 2014, **77**, 42–49.
- 24 M. Beck, M. Graczyk, I. Maximov, E. L. Sarwe, T. G. I. Ling, M. Keil and L. Montelius, *Microelectron. Eng.*, 2002, **61–62**, 441–448.
- 25 Y. Xia and G. M. Whitesides, *Angew. Chem., Int. Ed.*, 1998, **37**, 550–575.
- 26 I. Cunningham, *J. Protozool.*, 1977, **24**, 325–329.
- 27 T. G. Papaioannou and C. Stefanadis, *Hellenic Journal of Cardiology*, 2005, **46**, 9–15.
- 28 O. Traub and B. C. Berk, *Arterioscler., Thromb., Vasc. Biol.*, 1998, **18**, 677–685.
- 29 P. M. Kristjanson, B. M. Swallow, G. J. Rowlands, R. L. Kruska and P. N. de Leeuw, *Agricultural Systems*, 1999, **59**, 79–98.
- 30 Z. Gorocs and A. Ozcan, *IEEE Reviews in Biomedical Engineering*, 2013, **6**, 29–46.
- 31 H. Morgan and D. Spencer, Chapter 10, *Microfluidic Impedance Cytometry for Blood Cell Analysis*, The Royal Society of Chemistry, 2015.
- 32 J. P. Beech, T. Mäkelä, P. Majander and J. O. Tegenfeldt, *Presented in part at the  $\mu$ TAS - the 12th international conference on miniaturized systems for chemistry and life sciences*, San Diego, CA, USA, 2008.
- 33 A. Laurberg Vig, T. Mäkelä, P. Majander, V. Lambertini, J. Ahopelto and A. Kristensen, *J. Micromech. Microeng.*, 2011, **21**, 035006.

# Simplifying Microfluidic Separation Devices towards Field-Detection of Blood Parasites

Stefan H. Holm, Jason P. Beech, Michael P. Barrett and Jonas O. Tegenfeldt

## - Electronic Supplementary Information -

### 1. Device Design

The device consists of three sections, each with parameters optimized to carry out that section's specific task. Section 1 is deep and has a large critical size in order to sort out WBCs. Section 2 has a lower critical size and is shallow, which maximizes the effective size of the particles making it easy to laterally displace them along the channel walls. Section 3 has the same array parameters as section 2 but the height has been decreased. The height has been optimized to take advantage of the shape difference between erythrocytes and the longer and slender parasites. At the specific height of section 3 (9.0  $\mu\text{m}$ ) the parasites will continue to be laterally displaced, this time however towards the centre. The erythrocytes, on the other hand, will appear with a smaller effective size and switch from displacement mode to zig-zag.

The parameters of each section can be found in ESI Table 1 below.

**ESI Table 1. Device Parameters**

	Section 1	Section 2	Section 3
gap, G ( $\mu\text{m}$ )	22	12	12
post diameter, P ( $\mu\text{m}$ )	20	20	20
post-to-post distance, $\lambda$ ( $\mu\text{m}$ )	42	32	32
row shift, $\Delta\lambda$ ( $\mu\text{m}$ )	2	1.2	1.2
period, N	21	26.67*	26.67*
repeats	45	48	48
length ( $\mu\text{m}$ )	39690	40960	40960
expected $D_c$ ( $\mu\text{m}$ )	7.14	3.47	3.47
depth ( $\mu\text{m}$ )	26	3.5	9.0
width ( $\mu\text{m}$ )	1890	3072	3072
resistance per unit cell ( $\text{Pa}\cdot\text{s}\cdot\text{m}^{-3}$ )	$7.5\cdot 10^{12}$	$16.6\cdot 10^{14}$	$2.2\cdot 10^{14}$
total resistance ( $\text{Pa}\cdot\text{s}\cdot\text{m}^{-3}$ )	$7.5\cdot 10^{12}$	$8.3\cdot 10^{14}$	$1.1\cdot 10^{14}$

\* Note that the periodicities in sections 2 and 3 vary within the section. They start with N=26 for one set of rows and then increase to N=27 for the remaining two sets of rows.

## 2. Pressure Response of Syringe Compression

The compression of the syringe gives rise to an overpressure driving the sample forward. The resulting overpressure is given by Boyle's law, i.e.  $P_0V_0 = P_1V_1$ . Here  $P_0$  is the ambient pressure (1 atm) and  $P_1$  is the resulting pressure of compressing the air from a volume of  $V_0$  to a volume of  $V_1$ .

The pressure difference across a channel with one end at ambient pressure is now simply given by:

$$\Delta P = P_0 \cdot \left( \frac{V_0}{V_1} - 1 \right)$$

Conversely, the required compression is easily obtained as a function of the desired pressure difference:

$$\frac{V_1}{V_0} = \frac{1}{\frac{\Delta P}{P_0} + 1}$$

To increase the pressure stability over time, an additional chamber of 10 mL was added as a dead volume in the system, acting as a pressure reserve to enable measurements over longer times with a consistent flow rate. In addition to this, tubings with a total volume of  $\sim 2.5$  mL was used, resulting in  $V_0 = 12.5$  mL.

Depending on the syringe used, different pressures can be achieved in one compression. In ESI Figure 1, the resulting overpressure  $\Delta P = (P_1 - P_0)$  is plotted as a function of the compression  $\Delta V = (V_0 - V_1)$ . Larger syringes are needed to achieve higher pressure in one compression.

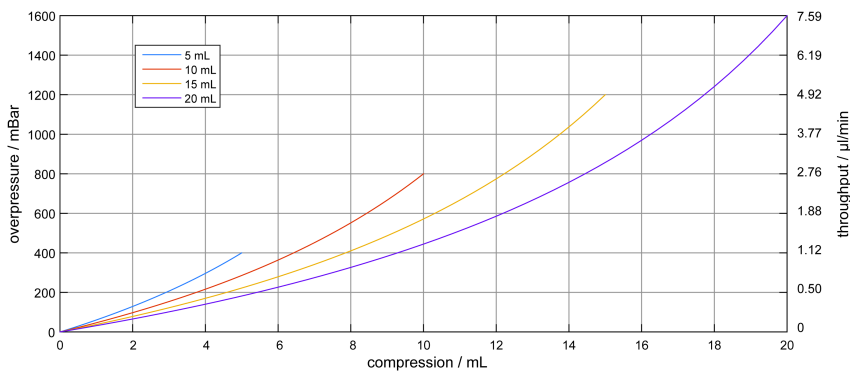


**Figure 1** Resulting overpressure (left) and throughput (right) by the compression of syringes of various sizes. Here the pressure system without the syringe is approximated to 12.5 mL. Consequently, to reach an overpressure of 1 bar, the syringe need to be of at least this volume



### 3. Channels of Identical Resistance Connecting Subsequent Sections

Due to the low angle of displacement and our device consisting of multiple sections, each with its dedicated task, the entire device will be relatively long (~15 cm). With a goal of fitting the device on a single glass slide (75 x 25 mm) the device was given a folded design, with channels connecting the different section. Here, it was crucial to ensure that the fluidic resistance of all the channels connecting two sections were equal. In order to accomplish this, the widths of the channels were adjusted to compensate for the length differences.

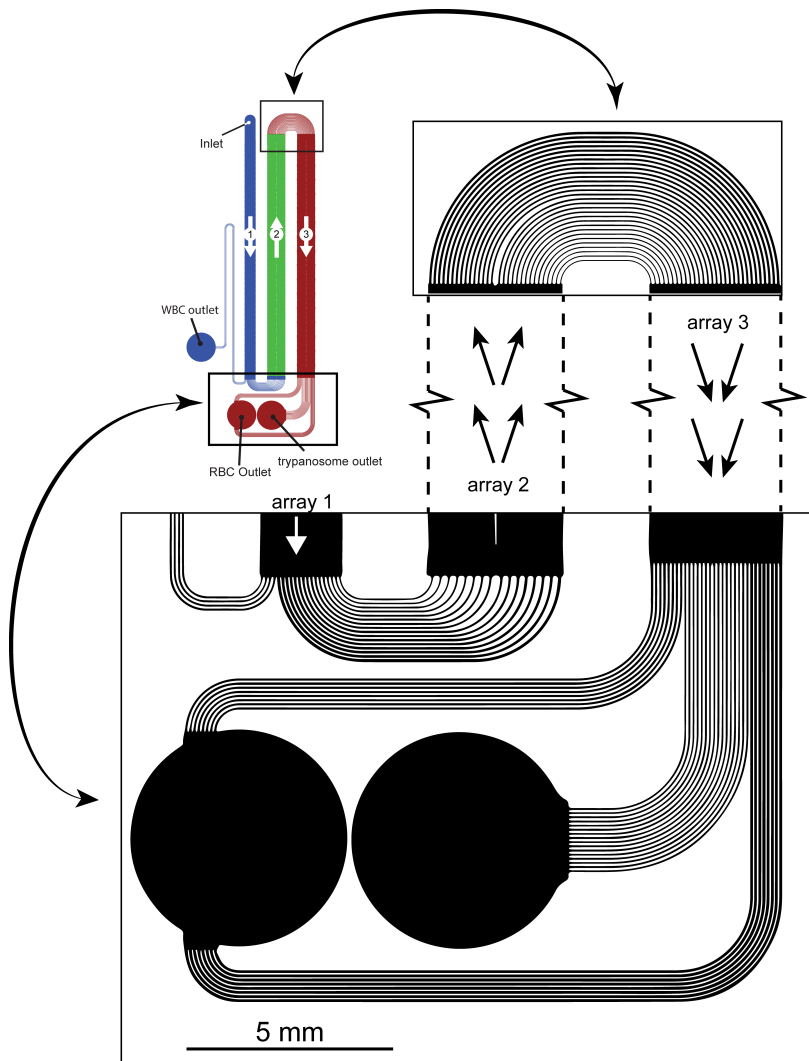


**Figure 2** Device overview showing the three different sections together with the connection channels of equal resistance ensuring that particles maintain their relative position in longer microfluidic devices

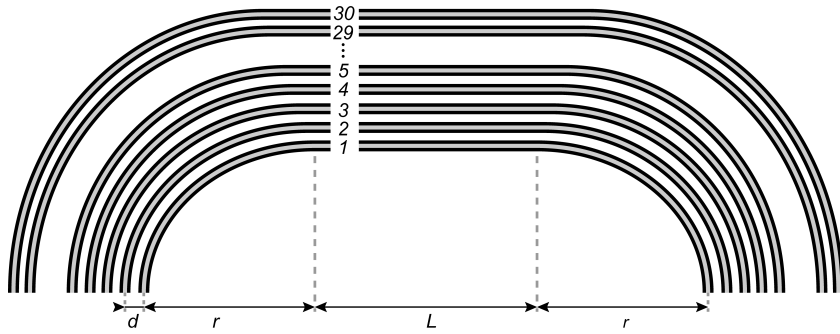


**Figure 3** Schematic illustration of the curved channels connecting section 2 and 3, showing how the lengths increases with increasing channel number.

For the channels connecting section 2 and 3, 30 channels were chosen. As can be seen in ESI Figure 3, the channels consist of two identical  $\frac{\pi}{2}$  rad annulus sectors connected via a straight channel. With a device width of 3072  $\mu\text{m}$ , the centres of the channels will be separated by a distance  $d = 102.4 \mu\text{m}$ . The radius of the innermost annulus sector is  $r = 550 \mu\text{m}$ . The straight channel is  $L_s = 1000 \mu\text{m}$  for the first 15 channel and 1064  $\mu\text{m}$  for the remaining 15.

With the hydraulic resistance given by<sup>1</sup>

$$R = \frac{12\eta L}{wh^3} \left[ 1 - \frac{h}{w} \left( \frac{192}{\pi^5} \sum_{n=1}^{\infty} \frac{1}{(2n-1)^5} \tanh\left(\frac{(2n-1)\pi w}{2h}\right) \right) \right]^{-1}$$

where  $w, h, L$  are the dimensions of the channel, and  $\eta$  the viscosity. By setting the width of channel 30 to 50  $\mu\text{m}$  the resistance can be calculated to  $4.024 \cdot 10^{16} \text{ Pa}\cdot\text{s}\cdot\text{m}^{-3}$ . Thereafter the widths corresponding to this resistance can be calculated for the remaining channels, the result can be found in ESI Table 2.

ESI Table 2. Parameters of channels between section 2 and 3					
Channel	$L_s / \mu\text{m}$	$r / \mu\text{m}$	$L_{\text{tot}} / \mu\text{m}$	$w / \mu\text{m}$	$R / 10^{16} \text{ Pa}\cdot\text{s}\cdot\text{m}^{-3}$
1	1064	11057.15	12121.15	50	4.0240
2	1064	10735.45	11799.45	48.83	4.0238
3	1064	10413.75	11477.75	47.65	4.0238
4	1064	10092.05	11156.05	46.47	4.0238
5	1064	9770.35	10834.35	45.3	4.0238
6	1064	9448.65	10512.65	44.12	4.0238
7	1064	9126.95	10190.95	42.94	4.0238
8	1064	8805.26	9869.26	41.77	4.0238
9	1064	8483.56	9547.56	40.59	4.0238
10	1064	8161.86	9225.86	39.41	4.0238
11	1064	7840.16	8904.16	38.24	4.0238
12	1064	7518.46	8582.46	37.06	4.0238
13	1064	7196.76	8260.76	35.88	4.0238
14	1064	6875.06	7939.06	34.71	4.0238
15	1064	6553.36	7617.36	33.53	4.0238
16	1000	6231.66	7231.66	32.12	4.0238

17	1000	5909.96	6909.96	30.94	4.0238
18	1000	5588.27	6588.27	29.77	4.0238
19	1000	5266.57	6266.57	28.59	4.0238
20	1000	4944.87	5944.87	27.41	4.0238
21	1000	4623.17	5623.17	26.24	4.0238
22	1000	4301.47	5301.47	25.06	4.0238
23	1000	3979.77	4979.77	23.88	4.0238
24	1000	3658.07	4658.07	22.7	4.0238
25	1000	3336.37	4336.37	21.53	4.0239
26	1000	3014.67	4014.67	20.35	4.0239
27	1000	2692.97	3692.97	19.16	4.0239
28	1000	2371.27	3371.27	17.98	4.0239
29	1000	2049.58	3049.58	16.79	4.0239
30	1000	1727.88	2727.88	15.6	4.0239

The connecting channels were validated by the use of COMSOL Multiphysics 5.0 (COMSOL AB, Stockholm, Sweden). ESI Figure 4 shows that there is no lateral flow prior to the particles enter the connecting channels. This ensures that they will retain their lateral position relative to each other between sections.

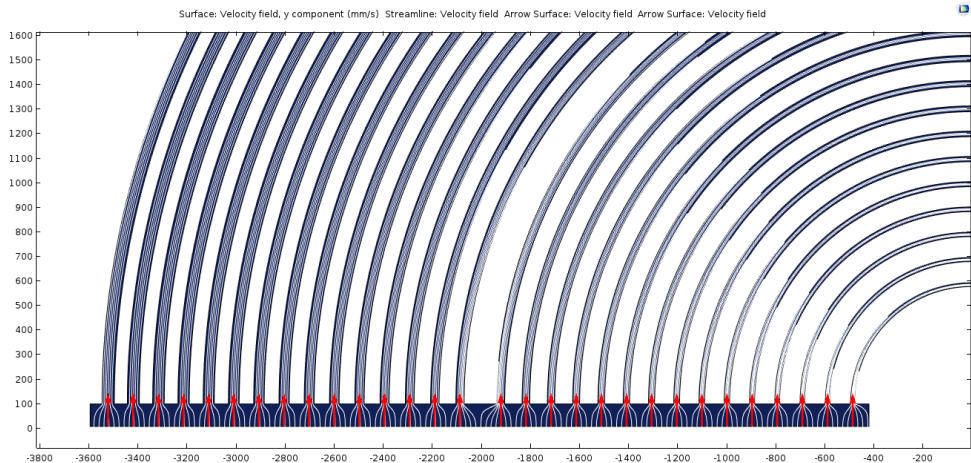


**Figure 4** 2D-plot of the curved channels connecting section 2 and 3, simulated by COMSOL. The fluid enters the model from the boundary at  $y=0$ . 30 flow streams have been positioned equidistant along the same border to illustrate that the flow is split up evenly before entering the channels. This ensures that particles will retain their relative lateral position between the different sections.

## 4. Automated Tracking Software

The tracking software was based around available MATLAB code but optimized for this specific task and a GUI was added to easily extract trajectories of several thousands of particles within minutes.

More information can be found at

<http://site.physics.georgetown.edu/matlab/>

<http://www.physics.emory.edu/faculty/weeks//idl/tracking.html>

See also ESI\_Movie1.mp4

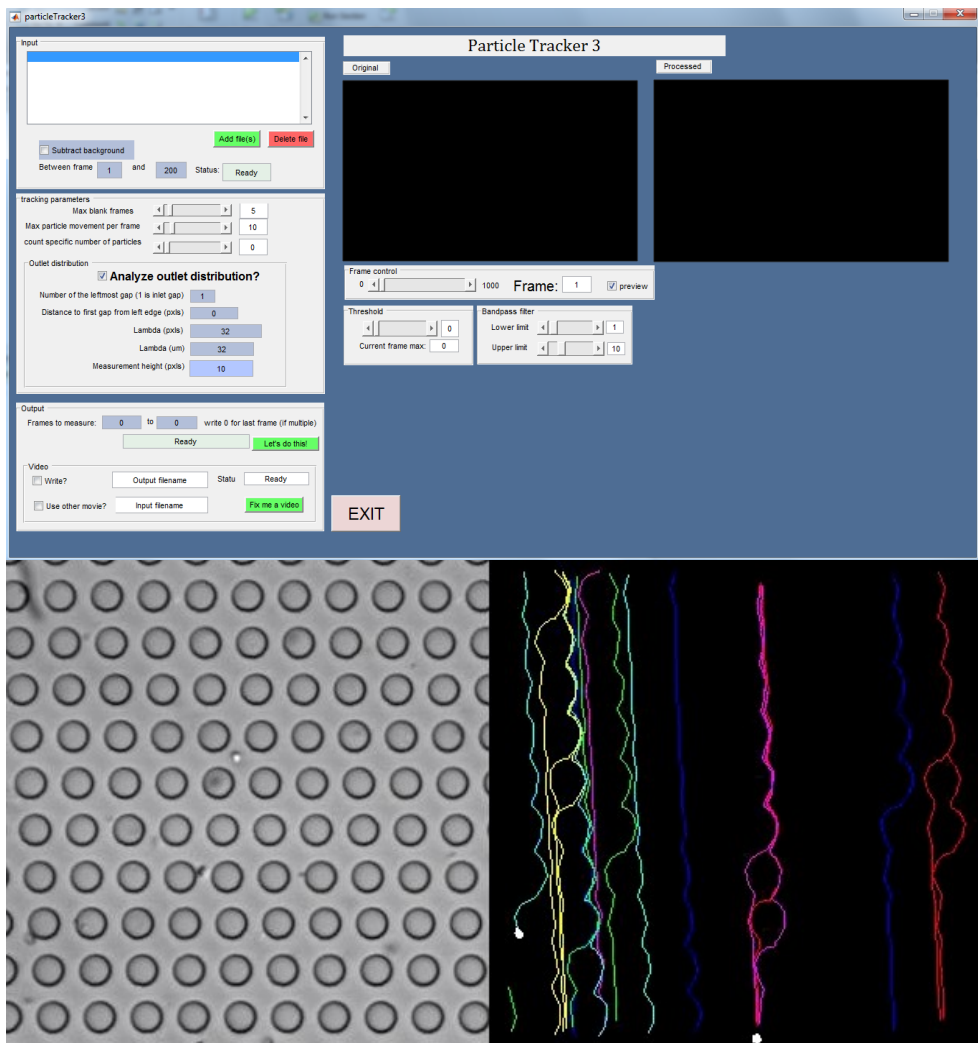


**Figure 5** Graphical user interface of the automated tracking software used to correctly determine the position of several thousands of particles in order to acquire good statistics

## Lateral Distribution of Trypanosomes at Various Pressures

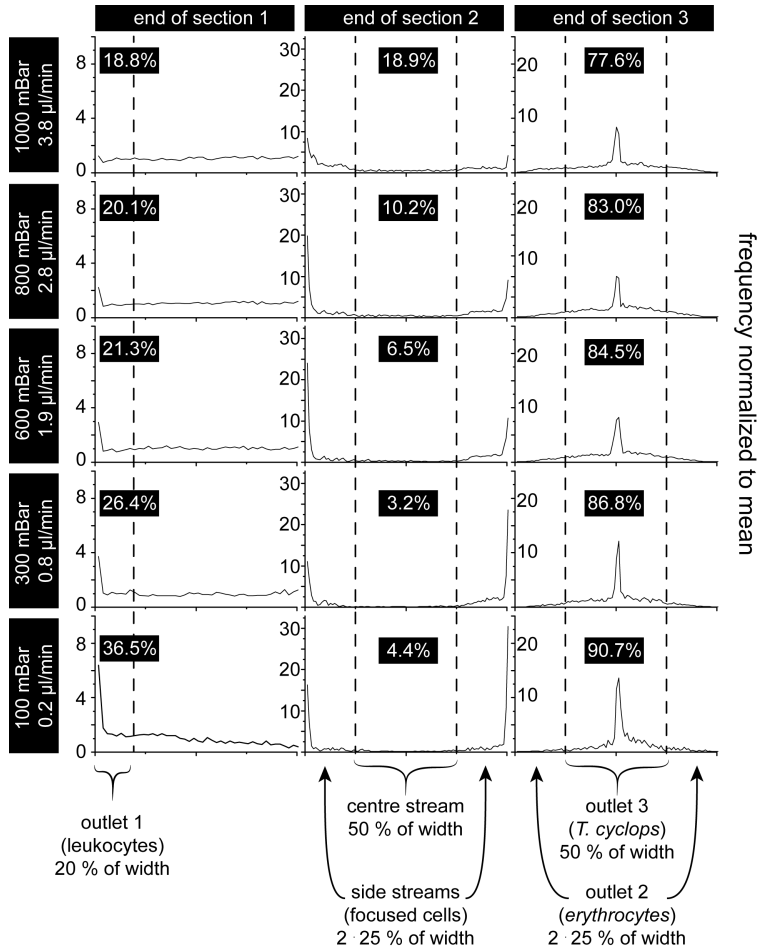


**Figure 6** Lateral distribution of trypanosomes at the end of the three different sections, measured at various pressures. The percentages refer to the fraction of the trypanosomes entering the section that are deviated to the indicated outlet. At the end of array 1, 20% of the total flow is diverted to the leukocyte outlet. As the leukocytes are spherical and larger, they are expected to become laterally displaced in this section, and consequently, enriched at this side of the device. However, at low flow velocities, and consequently low shear forces, the trypanosomes also behave as larger particles. Thus, they get enriched to some extent as well and more than the expected 20% are lost to the leukocyte outlet. As can be seen, at 100 mBar, 36.5% of the trypanosomes are sorted out to the leukocyte channel. In array 2, the cells are supposed to be laterally displaced towards the channel walls. At high flow velocities the soft cells will be squeezed by the shear stress and consequently behave as smaller particles. In this way they can avoid being displaced towards the side of the channels. At the end of section 3, the trypanosomes are expected to have been focused to the center of the channel while the RBCs should remain focused along the channel walls on the side. As can be seen here, increasing the flow rate will act to decrease the fraction of trypanosomes in the center outlet. This is believed to be a consequence of the increasing shear forces acting to, once again, deform the relatively soft parasites making them able to avoid being laterally displaced.

## 5. Lateral Distribution of Erythrocytes at Various Pressures

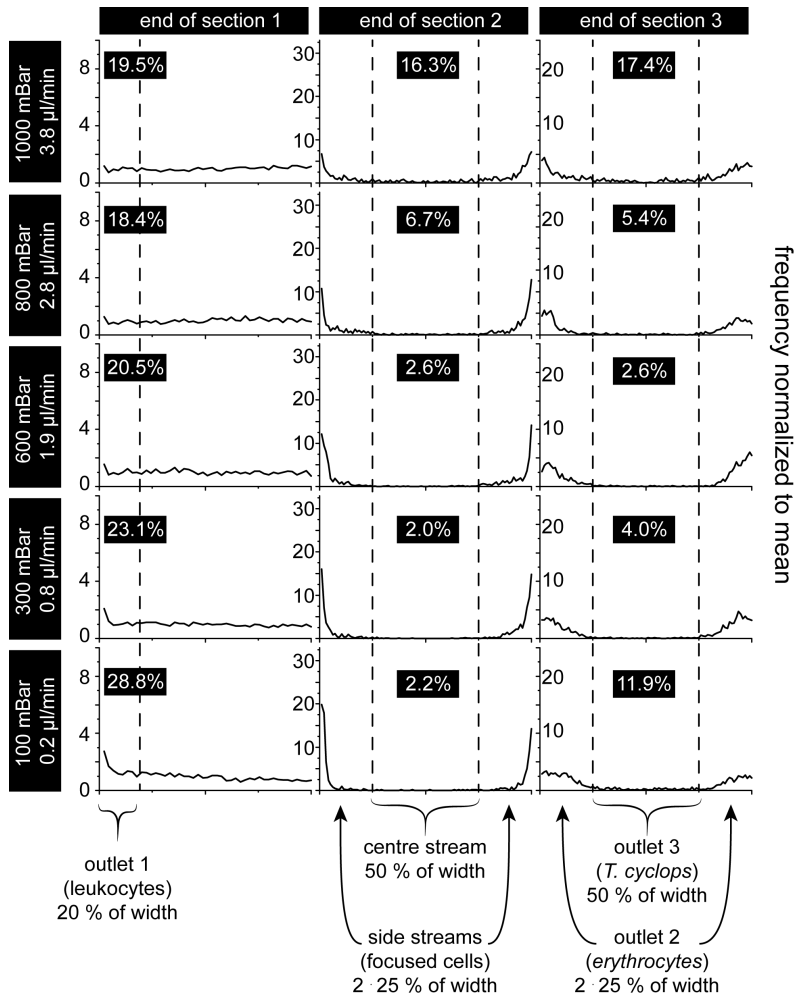


**Figure 7** Lateral distribution of erythrocytes at the end of the three different sections, measured at various pressures. The percentages refer to the fraction of the erythrocytes entering the section that are deviated to the indicated outlet. Similar to how the trypanosomes behave in Figure 2, the erythrocytes are not laterally displaced to a large extent in section 1. The low depth in section two, also here, act to maximize the effective size of the particles and consequently, with high accuracy, laterally displace the cells towards the channel walls. The most important numbers are given at the end of section 3 as this is the outlet distribution. Here we can see the same numbers as given in Figure 5A. At very low pressures the erythrocytes sediment and are sorted, in this section, according to their diameter,  $\sim 7.5 \mu\text{m}$ , instead of their width  $2.5 \mu\text{m}$ . As a consequence they are laterally displaced, to a larger extent, into the trypanosome outlet. At higher pressures the shear stress exerted on the erythrocytes act to decrease their effective size, making them avoid being laterally displaced. At even higher pressures, this will also happen in section 2 resulting in erythrocytes less focused along the channel walls. Consequently, at these high pressures, a larger amount of erythrocytes exit the trypanosome outlet. Further, the number of erythrocytes in the trypanosomes outlet are minimal at a pressure of 600 mBar.

## 6. Measurements of Spiked Samples

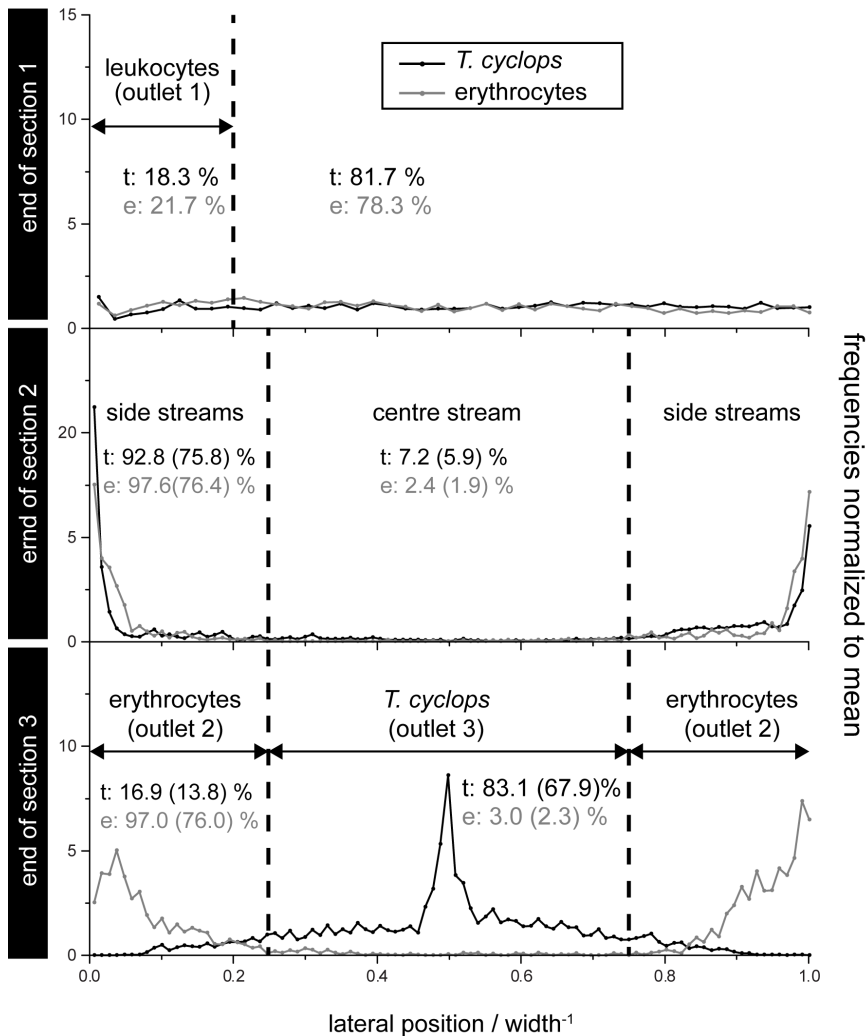


**Figure 8** Lateral distribution of spiked samples measured at  $1.9 \mu\text{l}/\text{min}$ . Overall the results are in close agreement with erythrocytes and *T. cyclops* analysed separately at this pressure (see Figure 6). At the end of section 1 the distribution of both cell types are uniform, as expected, due to the critical size being larger than the particle size. Consequently around 20 % of the cells are sorted out while the remaining fraction continues into section 2. In section 2 the majority of the cells are well-focused along the channel walls, opening up a cell-free stream in the centre. In section 3, which only differs from section 2 in terms of depth and displacement direction, the trypanosomes are displaced to a large degree with 83.1 % being sorted out into outlet 3, while the erythrocytes mainly zigzag into outlet 2.

## 7. Trypanosome Culturing

The parasite *T. cyclops* was kept in culture flask with Cunningham's medium supplemented with 20% FCS. The time between splits were kept at around 14 days.

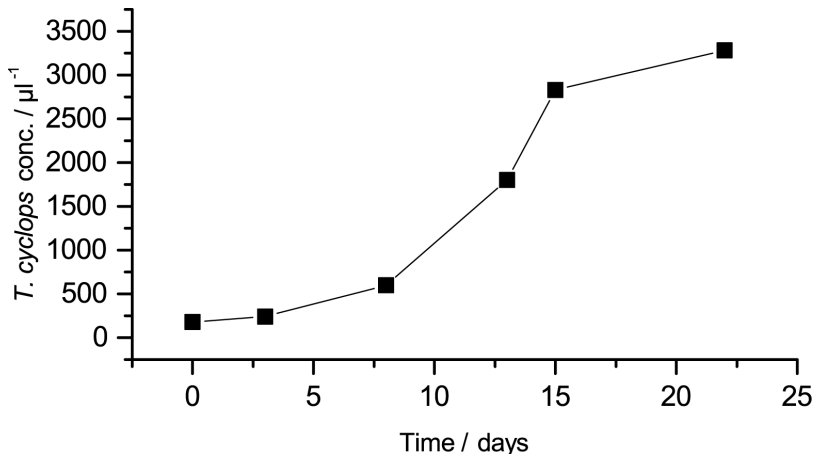


**Figure 9** Measured growth curve of *T. cyclops* using a haemocytometer. After around a week a burst in the density was noted as the population entered their exponential growth phase. After another week the culture entered the lag phase. Culture splitting was carried out around 14 days after last split in order to maintain the parasites healthy.

### Culture splitting (every 14 days)

- Sterilize two culture flasks by autoclaving
- Sterilize laminar flow hood and gloves with 70% EtOH
- Fill each culture flask with 15 ml of culture medium
- Add 4 ml (20%) FCS to the Cunningham's medium, heat suspension to 28°C
- Use sterile pipettes to transfer 1 ml of trypanosome suspension to the culture flask

### *T. cyclops* samples

- Use exponential-phase trypanosomes, around 7 days since last split. Take from upper half to avoid dead parasites and debris
- Count the density and dilute to desired concentration using culture medium
- Pipette 100  $\mu\text{l}$  of trypanosomes into inlet reservoir

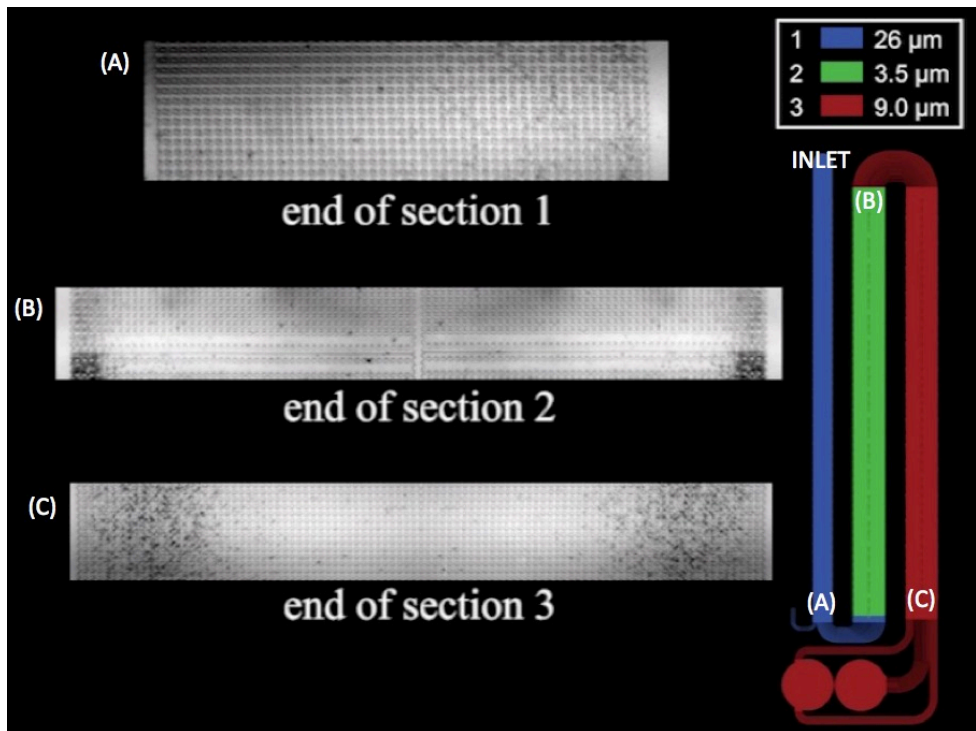
### Simultaneous Analysis of Erythrocytes and *T. cyclops*

- Count the *T. cyclops* density using a haemocytometer
- Create a running buffer containing culture medium with 3mM EDTA and 20% FCS to the desired density
- Dilute the *T. cyclops* to desired concentration using the running buffer



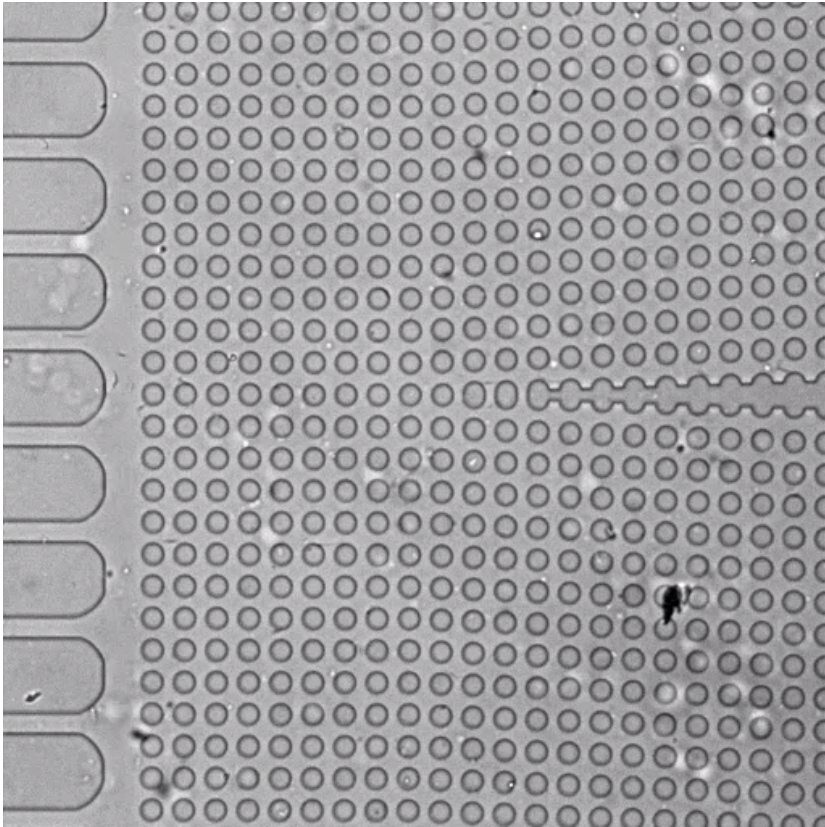
- Aspirate 150  $\mu\text{l}$  of the running buffer in a 200  $\mu\text{l}$  pipette tip
- Prick finger with Haemedic Haemolance® low flow
- Aspirate 50  $\mu\text{l}$  of blood with the filled pipette tip into the Eppendorf tube
- Wash blood sample three times with the running buffer at 1000 g for 1 min,
- Resuspend pellet with 475  $\mu\text{l}$  (for 10x dilution) of the *T. cyclops* solution in running buffer

## 8. Movies Showing Sorting of Erythrocytes and Trypanosomes



ESI\_Movie2.mp4

The lateral distribution of erythrocytes at the three different sections is presented. In the end of section 1, the erythrocytes are relatively evenly distributed. In section two, the cells are focused along the channel walls in order to open up the cell-free stream in the centre. In the final section 3 the erythrocytes are expected to be minimally displaced in order to achieve the best separation.



ESI\_Movie3.mp4

The end of section 3 is viewed at a high magnification, to see the individual *T. cyclops* parasites. At this flow rate (1.9  $\mu\text{l}/\text{min}$  - 600 mBar), the parasites are focused to a large extent to the centre of the device, exiting mainly to the parasite outlet. Some of the parasites can however be seen to avoid displacement, most likely due to their smaller size or different shape.

1. H. Bruus, *Theoretical Microfluidics*, OUP Oxford, 2008.



# Paper III





Cite this: *Lab Chip*, 2012, **12**, 1048

www.rsc.org/loc

## Sorting cells by size, shape and deformability†

Jason P. Beech,<sup>\*,a</sup> Stefan H. Holm,<sup>a</sup> Karl Adolffsson<sup>a</sup> and Jonas O. Tegenfeldt<sup>ab</sup>

Received 8th November 2011, Accepted 23rd January 2012

DOI: 10.1039/c2lc21083e

**While size has been widely used as a parameter in cellular separations, in this communication we show how shape and deformability, a mainly untapped source of specificity in preparative and analytical microfluidic devices can be measured and used to separate cells.**

Morphology has been used successfully for centuries for classification of species across all kingdoms of life ranging from bacteria to mammals and identification of disease through histological samples. During the past decades there has been an increasing fundamental interest in the connection between the shape of cells, their overall function and the underlying molecular networks. Yet a limited effort has been made to develop fast and efficient ways to sort based on shape. Imaging cytometry is one example; however it is limited by the resolution and speed of the sorting. A small number of microfluidic techniques have been developed recently to address these concerns.<sup>1,2</sup> Deformability of cells is an important clinical indicator of a wide range of medical conditions and is measured in bulk using, for example, ektacytometry.<sup>3</sup> Microfluidic approaches include the laser stretcher,<sup>4</sup> obstacle arrays,<sup>5,6</sup> margination<sup>7</sup> and inertial focussing.<sup>8</sup> None of the above-mentioned high-throughput approaches can be used for detailed high-resolution studies of the mechanical properties of large number of cells. Furthermore, although shape may influence the result in the above devices, with exception for direct imaging, the shape of the deformed particles and the anisotropy of the deformability cannot be discerned in the measurements.

Deterministic lateral displacement<sup>9</sup> (DLD) has been demonstrated to be a powerful mechanism for highly precise continuous sorting based on size. Devices consist of arrays of posts through which particles smaller than a critical radius,  $R_c$ , move with the flow and particles larger than the critical radius move along a direction defined by the device. For hard spherical particles, the operation of the device is straightforward, however, biological particles are often soft and non-spherical and their deformability and shape are known to influence the trajectories of the particles in DLD devices.<sup>10–12</sup> In this communication we explore the extent of these relative contributions and present an approach that opens up for sorting and

characterisation based on targeting them specifically as separation parameters.

We can define an effective size,  $R_{\text{eff}}$ , for a particle of arbitrary shape and deformability as the radius of a hard spherical particle that would follow an identical trajectory through a DLD device. In our simplified model we consider  $2R_{\text{eff}}$  as the projected width of a particle along a line, transverse to the overall flow direction, joining the centres of two posts (Fig. 1A). At this decision point the trajectory of the particle is determined by the relation between  $R_{\text{eff}}$  and  $R_c$ . The critical radius,  $R_c$ , in turn depends on the geometry of the array in a highly complex way but much of the behaviour can be captured surprisingly well by making the gross simplification of considering  $R_c$  also as the projected width of the first flow stream on this same line (Fig. 1A).

Because the effective size of a non-spherical particle depends on its orientation as it passes between two posts, the key to shape sensitive sorting is to control this orientation. One simple way to achieve this is through confinement of the particles: in deep devices non-spherical particles tend to become aligned in the flow between posts such that their smallest dimension defines  $R_{\text{eff}}$ . Conversely in a shallow device rotation is hindered, which for some particle shapes leads to a larger dimension defining  $R_{\text{eff}}$ . For example, by confining disc-shaped red blood cells, RBCs, in a device with depth less than the overall diameter, the trajectory of the particles is determined by a combination of their overall diameter and thickness. For sufficiently strong confinement, at a depth of approximately the thickness of the cell, the trajectory is entirely determined by the overall diameter, see Fig. 1D (and ESI† Section 2 for further details). This simple approach can now be used to measure different particle dimensions and to separate particles that would have identical  $R_{\text{eff}}$  in a deep device.<sup>1</sup>

Due to shear forces from the carrier fluid and normal forces from the stationary posts, a deformable particle will assume an increasingly elongated shape moving through a device as shear forces are increased, which in turn will change the effective radius,  $R_{\text{eff}}$ . Thus by gradually changing the shear rates and observing the effective sizes of the particles, we essentially perform a stress-strain measurement on the particles from which we can extract information about the mechanical properties of the cells.

All in all this gives us the ability to select the relative contributions of size, shape and deformability to the trajectories of the particles in applications including analysis, concentration, or separation.

We have evaluated our method using RBCs. Not only are the morphologies<sup>13</sup> and deformabilities<sup>14</sup> of RBCs of great clinical interest but because RBCs are both readily available and their shapes

<sup>a</sup>Division of Solid State Physics, nmC@LU, Lund University, PO Box 118, S-221 00 Lund, Sweden. E-mail: jason.beech@ftf.lth.se; Fax: +46 (0)46 222 3637; Tel: +46 (0)46 2222 4956

<sup>b</sup>Department of Physics, University of Gothenburg, Gothenburg, Sweden

† Electronic supplementary information (ESI) available. See DOI: 10.1039/c2lc21083e

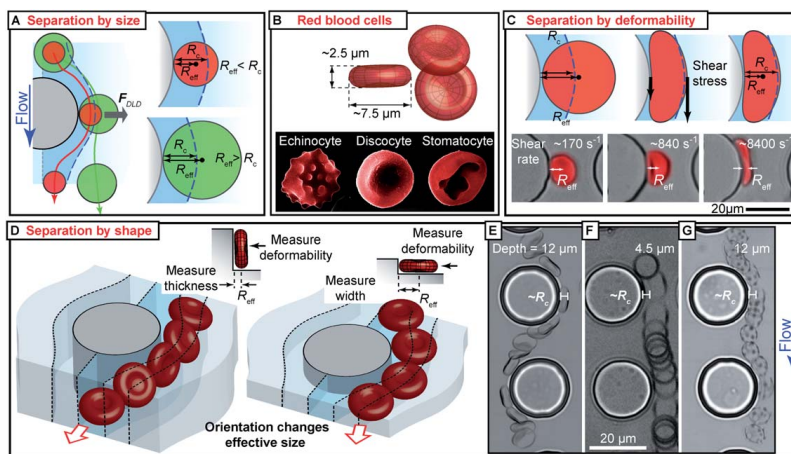


**Fig. 1** Mechanisms of separation by DLD. (A) Particles with  $R_{\text{eff}} < R_c$  follow the flow direction and those with  $R_{\text{eff}} > R_c$  are displaced at an angle to the flow direction. For hard spheres,  $R_{\text{eff}}$  is equal to the radius. (B) Red blood cells are normally disc-shaped but they can adopt other shapes when exposed to different chemicals. (C) Shear forces deform particles changing  $R_{\text{eff}}$ , and measuring the change in  $R_{\text{eff}}$  as a function of applied shear rate is equivalent to measuring the deformability of the particle. (D)  $R_{\text{eff}}$  depends on the orientation of the particle. Controlling orientation and measuring  $R_{\text{eff}}$  gives information about shape. It is also possible to measure deformability in different directions. (E) In a deep device RBCs rotate such that  $R_{\text{eff}} (< R_c)$  is equal to half the thickness. (F) Confinement in a shallow device means that the cell radius defines  $R_{\text{eff}} (> R_c)$ . (G) An echinocyte with  $R_{\text{eff}} > R_c$ .

and mechanical properties easily changed<sup>15</sup> they constitute an excellent model system for cells in general provided one keeps in mind that RBCs lack a nucleus and are therefore much simpler than most other cells.

Several models explain RBC shape, the most prominent being the bilayer-couple theory.<sup>15,16</sup> It relies on an asymmetry in composition between the two leaflets of the lipid bilayer forming the cell membrane, which means that the leaflets react differently to perturbations while remaining coupled to one another. If, for example, the area of one leaflet is altered, the resulting strain in the other leaflet will be relieved by bending the bilayer in analogy to the bending of a bimetallic strip upon heating. This bending can have a dramatic effect on both the shape of the cell and on its mechanical properties, and underlies many of the methods that are used to modify RBC morphologies.<sup>14</sup> Osmolarity provides another way to control the shape of a RBC but changes not only the shape of the cell but also the volume. In the current work we use sodium salicylate (SS) and Triton™ X-100 (TX) which modify the relative areas of the inner and outer leaflets, to form echinocytes and stomatocytes respectively without significantly altering cell volume. We used 16 mM SS<sup>17</sup> and 580 ppm TX,<sup>18</sup> which we found to give the most homogeneous and stable populations of RBCs with regard to morphologies, see Fig. 1B.

Experiments are performed in the following way. 1. Blood is drawn from healthy volunteers and prepared strictly adhering to a simple protocol as described in the ESI† Section 1.4 to minimize any variation in the morphology and/or deformability of the cells as a result of the handling of the blood. 2. The RBCs are injected into the device (ESI† Section 1.5) and a series of films are taken at low magnification of the outlet distribution of the cells as the driving pressure is changed across the range 5 to 800 mbar corresponding to wall shear rates (the maximum rate at the surface of the posts) in the range 40 to 6700  $\text{s}^{-1}$

and 100 to 16 400  $\text{s}^{-1}$  for the two device depths used ( $4.27 \pm 0.04 \mu\text{m}$  and  $10.84 \pm 0.12 \mu\text{m}$ ). To be able to map out the effective size with high resolution our devices are designed and fabricated with  $R_c$  ranging from 1.5 to 4.5  $\mu\text{m}$  in 13 steps (see the ESI† Section 1.1–3). Remember, the outlet distribution reflects the effective size of the cells and we can characterize this using polystyrene microspheres of known sizes. 3. Particle tracking software (described in the ESI† Section 1.6) is used to determine the distribution of RBCs at the end of the device. 4. In order to verify the deformation of the cells, high-speed films (100 to 10 000 frames  $\text{s}^{-1}$ ) at high magnification are also taken of cells moving through devices.

In Fig. 1E–G RBCs can be seen moving through a device at low shear rates such that they are not measurably deformed. The rotation of an RBC in a 12  $\mu\text{m}$  deep device results in the smallest possible  $R_{\text{eff}}$  as is clearly seen in Fig. 1E. In this array  $R_{\text{eff}}$  is defined by half of the thickness of the cell  $\sim 1.25 \mu\text{m} < R_c \sim 3 \mu\text{m}$  and the cell is therefore following the flow, which is evidenced by the fact that it crosses the column of posts. In a 4.5  $\mu\text{m}$  deep device†, shown in Fig. 1F, the RBC is forced to lay flat and  $R_{\text{eff}}$  is defined instead by the overall radius of the cell  $\sim 3.75 \mu\text{m}$  which is larger than  $R_c$  so that the cell moves in the displacement mode. See the ESI† (Section 2) for a graph summarizing the effect of device depth. Fig. 1G shows an echinocyte moving through the 12  $\mu\text{m}$  device†. Each echinocyte suffers a contraction in its width and a dilation in its thickness relative to the discocytes such that it is almost spherical while  $R_{\text{eff}}$  is still greater than  $R_c$  and the cell is displaced. This is interesting because what would be seen in a blood smear as a decrease in cell size actually leads to an increase in effective size in our device.

Fig. 1C shows images of deformation of RBCs moving through a 4.27  $\mu\text{m}$  deep device at different shear rates acquired with a high-speed camera. As before, at a device depth of 4.27  $\mu\text{m}$  the cells are



constrained to lie in the plane of the device. As the shear rate is increased, the deformation of the cells increases. It can clearly be seen how this deformation leads to a decrease in the width of the particle and therefore of  $R_{\text{eff}}$  (additional images and movies of RBCs with different morphologies in devices of 4.27 and 10.84  $\mu\text{m}$  depth can be found in Section 3 of the ESI†).

The overall behaviour of the different cell types can be conveniently summarized in a two-dimensional histogram based on the outlet distributions of cells in our devices, which directly reflects their effective size. Fig. 2 shows the distributions of cells at the ends of two devices as the shear rate is varied. It is immediately apparent that the different cell types show very distinct patterns, or 'fingerprints'.

The overall plots for the shallow devices (Fig. 2A, C and E) show that the discocytes and the echinocytes have similar mechanical properties. At low shear rates it can be seen that the unperturbed sizes are comparable. As the shear rate increases the similar slopes indicate similar deformabilities. The stomatocytes show a different behaviour. First of all they have a smaller unperturbed size and a flatter slope indicating less deformability. Secondly they show a distinct bistability, something that is even more evident in the deeper device.

In the deeper devices (Fig. 2B, D and F) the projected size of the echinocyte is clearly greater than that of the discocytes. The elasticity

of the discocytes is not accessible in our deep devices since the smallest critical size is greater than half the thickness of the discocytes. On the other hand it can clearly be seen that the echinocytes have a continuous elastic deformation. The stomatocytes seem to have a more complex mechanical structure. The data show a bistable situation with a quite resilient conformation up to a relatively high shear rate at an applied pressure of about 200 mbar that quickly snaps into a different conformation.

To exclude any other driving forces beyond deformation such as hydrodynamic lift or deformation of the device itself that may be involved in decreasing  $R_{\text{eff}}$  we repeated the experiments with hard polystyrene spheres (see the ESI† Section 5) and found no systematic change in the outlet distributions over the range of shear rates used for the cells. To demonstrate the capability of our method to detect changes in deformability we fixated echinocytes using glutaraldehyde without changing their morphology. The resulting data show a decreased slope (ESI† Section 4) clearly indicating a decrease in deformability.

In conclusion, we have demonstrated a scheme for size, morphology and deformability-based manipulations using DLD that we believe will be useful for preparative and analytical separations. Size-based manipulation is inherent to DLD and we add

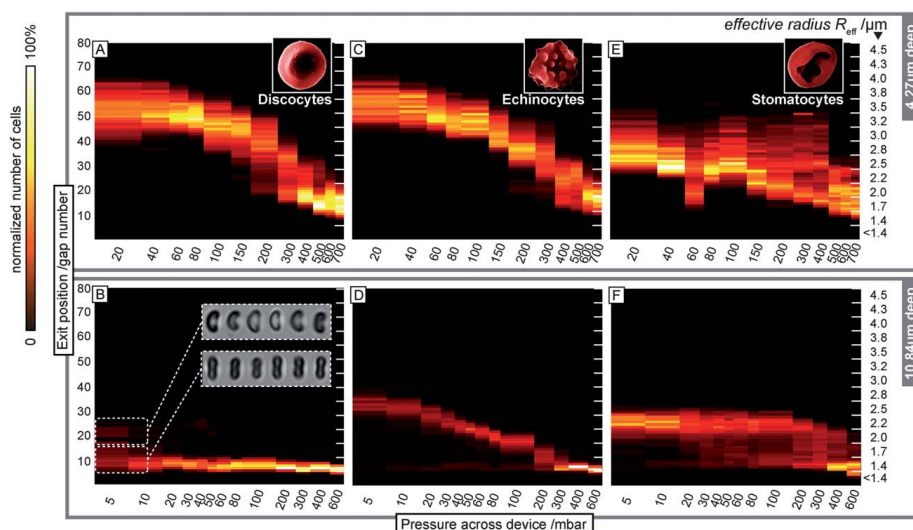


**Fig. 2** The exit position (reflecting the measured effective radius,  $R_{\text{eff}}$ ) as a function of applied pressure (and therefore shear rate and resulting shear stress) constitutes a cell type fingerprint. Here three red blood cell types are shown in devices of 4.27  $\mu\text{m}$  depth (A, C and E) and 10.84  $\mu\text{m}$  depth (B, D and F). Approximate values of the shear rates generated in our devices can be estimated by simulating fluid flow in the absence of particles. A change in driving pressure from 5 mbar to 800 mbar corresponds to average flow velocities in the range  $30 \mu\text{m s}^{-1}$  to  $4.6 \text{ cm s}^{-1}$  and  $110 \mu\text{m s}^{-1}$  to  $18 \text{ cm s}^{-1}$  and wall shear rates (the maximum rate at the surface of the posts) in the range  $40$  to  $6700 \text{ s}^{-1}$  and  $100$  to  $16\,400 \text{ s}^{-1}$  for the shallow and deep devices respectively. Cells are introduced through gap 5 and so exiting the device at gap 5 constitutes no lateral displacement of the cells as they traverse the device ( $R_{\text{eff}} \leq 1.4 \mu\text{m}$ ). Increasing gap number relates to increasing  $R_{\text{eff}}$  resulting in more lateral displacement. Lateral displacement is a measure of  $R_{\text{eff}}$  and as the shear rate is increased the resulting deformation leads to a decrease in  $R_{\text{eff}}$ . Note that the different populations are not completely pure. A subpopulation of weakly stomatocytic, bowl-shaped cells is present among the discocytes as can be seen in B (we are unsure as to the exact origin of these cells but they seem to constitute a subpopulation of cells that are more susceptible to the buffer than others) and can be distinguished at low shear rates. (D) SS and (F) TX do not transform all RBCs into echinocytes and stomatocytes. For both cell types a small fraction of cells remain disc-shaped and can easily be resolved from the morphologically altered majority in the deep devices.

morphology, *via* control of particle orientation, and deformability, *via* control of shear stresses, to this simple but powerful technique. Compared to imaging cytometry (see *e.g.* Amnis and CompuCyte), our method provides a simple means to passively sort particles based on morphological characteristics with high throughput and a resolution that is not fundamentally limited by diffraction. Although constrained to fairly simple shapes we expect our technique to open up for important applications in biomedicine involving, *e.g.*, length-sorting of bacteria or yeast thereby making it possible to fractionate with respect to phase in the cell-cycle of microorganisms without the addition of any deleterious additives or treatment of the cells. Compared to existing techniques for the measurement of deformability we can provide good throughput combined with good resolution together with some information on the anisotropy of the deformability. We envision our technique to be a good candidate for extraction of, *e.g.*, circulating tumour cells from blood.

To better understand the connection between the behaviour of the cells in our device and the mechanical properties of the cellular architecture, a more detailed picture of the shear stresses experienced by cells and of those mechanical properties that affect  $R_{\text{eff}}$  need to be elucidated with the aid of, *e.g.*, full 3D simulations and artificial cell analogues. The effect of the timescales involved for deformation and mechanical relaxation is another important topic that would open up for characterization of the viscous properties of the cells. By designing the post and array geometry appropriately we could change the variation in shear rates that the cells experience. This could be used in a device to independently measure elastic and viscous properties as well as overall deformation and shape.

### Acknowledgements

This work was carried out within the nmC@LU (the Nanometer Structure Consortium at Lund University) and was supported by the Swedish Foundation for Strategic Research (SSF), the Swedish Research Council (VR) grant no. 2007 584, the Crafoord Foundation grants no. 2008-0841 and 2005-1123 and the Knut and Alice Wallenberg Foundation. The authors would also like to thank Professor

Thomas Laurell and his students at the department of electrical measurements for kindly lending us the high-speed camera used.

### Notes and references

‡ These two devices are not the same as those used in the deformation measurements but have very similar dimensions.

- 1 S. H. Holm, J. P. Beech, M. P. Barrett and J. O. Tegenfeldt, *Lab Chip*, 2011, **11**, 1326–1332.
- 2 S. Sugaya, M. Yamada and M. Seki, *Biomicrofluidics*, 2011, **5**, 024103-1–024103-13.
- 3 M. R. Hardeman, P. T. Goedhart, J. G. G. Dobbe and K. P. Lettinga, *Clin. Hemorheol.*, 1994, **14**, 605–618.
- 4 J. Guck, R. Ananthakrishnan, H. Mahmood, T. J. Moon, C. C. Cunningham and J. Kas, *Biophys. J.*, 2001, **81**, 767–784.
- 5 J. P. Brody, Y. Q. Han, R. H. Austin and M. Bitensky, *Biophys. J.*, 1995, **68**, 2224–2232.
- 6 H. Bow, I. V. Pivkin, M. Diez-Silva, S. J. Goldfless, M. Dao, J. C. Niles, S. Suresh and J. Han, *Lab Chip*, 2011, **11**, 1065–1073.
- 7 H. W. Hou, A. A. S. Bhagat, A. G. L. Chong, P. Mao, K. S. W. Tan, J. Y. Han and C. T. Lim, *Lab Chip*, 2010, **10**, 2605–2613.
- 8 S. C. Hur, N. K. Henderson-MacLennan, E. R. B. McCabe and D. Di Carlo, *Lab Chip*, 2011, **11**, 912–920.
- 9 L. R. Huang, E. C. Cox, R. H. Austin and J. C. Sturm, *Science*, 2004, **304**, 987–990.
- 10 D. W. Inglis, PhD thesis: *Microfluidic Devices for Cell Separation*, Princeton University, 2007.
- 11 J. A. Davis, PhD Thesis: *Microfluidic Separation of Blood Components through Deterministic Lateral Displacement*, Princeton University, 2008.
- 12 J. A. Davis, D. W. Inglis, K. J. Morton, D. A. Lawrence, L. R. Huang, S. Y. Chou, J. C. Sturm and R. H. Austin, *Proc. Natl. Acad. Sci. U. S. A.*, 2006, **103**, 14779–14784.
- 13 V. Turchetti, C. De Matteis, F. Leoncini, L. Trabalzini, M. Guerrini and S. Forconi, *Clin. Hemorheol. Microcirc.*, 1997, **17**, 209–215.
- 14 F. C. Mokken, M. Kedaria, C. P. Henny, M. R. Hardeman and A. W. Gelb, *Ann. Hematol.*, 1992, **64**, 113–122.
- 15 M. P. Sheetz and S. J. Singer, *Proc. Natl. Acad. Sci. U. S. A.*, 1974, **71**, 4457–4461.
- 16 H. W. G. Lim, M. Wortis and R. Mukhopadhyay, *Proc. Natl. Acad. Sci. U. S. A.*, 2002, **99**, 16766–16769.
- 17 A. L. Li, H. Seipelt, C. Muller, Y. D. Shi and G. M. Artmann, *Pharmacol. Toxicol.*, 1999, **85**, 206–211.
- 18 Y. Yawata, *Cell Membrane: The Red Blood Cell as a Model*, Wiley-VCH, Weinheim, 2003.

# Sorting Cells by Size, Shape and Deformability

Jason P. Beech, Stefan H. Holm, Karl Adolffsson and Jonas O. Tegenfeldt

## Electronic Supporting Information

### 1 Materials and methods

#### 1.1 Device design

Our devices were designed with 13 sections, each with one  $R_c$  as shown in Fig. ESI 1 using the equation in Fig. ESI 11. The diameter of the posts,  $D_{\text{post}} = 20 \mu\text{m}$  and the gap between the posts,  $d = \lambda - D_{\text{post}} = 12 \mu\text{m}$  throughout the device ( $\lambda$  is the centre-to-centre spacing of the posts).  $R_c$  is varied in the device by varying  $\Delta\lambda$ , the amount each row is laterally shifted with regard to the previous row as shown in Figure ESI 1F. The small deviations from whole and half micrometer values for  $R_c$  are the result of having to fit to the  $0.2 \mu\text{m}$  manufacturing grid used in the mask generating process.

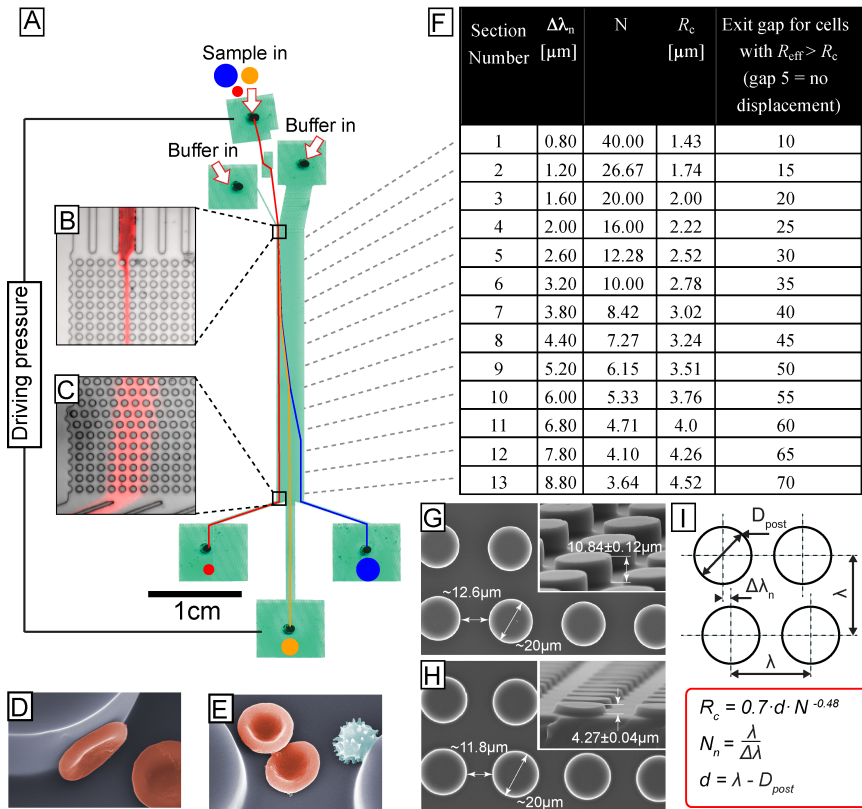


Fig. ESI 1 Overview of our device design. (A) To make an overview image of the device it is filled with green food colour and imaged by scanning in a flat-bed scanner. Sample is injected in the central channel and focused with a flow of buffer from the sides by controlling the over-pressure in the three inlets (outlets are kept at ambient pressure). The larger the particles are, the more they are displaced to the right as illustrated by the coloured lines. (B) A colour enhanced micrograph showing red blood cells being injected into the device. (C) In this device ( $10.8 \mu\text{m}$  deep) normal, disc-shaped red blood cells are not displaced. (D) and (E) False-coloured SEM images illustrating the dimensions of RBCs in relation to the dimensions of the two devices used, which are shown in (G) and (H) The red cells are normal discocytes and the blue cell is an echinocyte. (F) The devices contain posts with a diameter of  $20 \mu\text{m}$  and gaps of  $12 \mu\text{m}$  throughout. 13 sections with different critical radii  $R_c$  are achieved by varying the period  $N$  as shown in the table.  $R_c$  is calculated using the equation shown in 1).

Cells are injected into the device between posts 5 and 6 (counted from the left wall, see Fig. ESI 1 B below) which we denote gap 5. For each section, where the effective size of the cell is larger than the critical size the total displacement from the wall is increased by 5 gaps. Cells with an effective radius between  $2.0 \mu\text{m}$  and  $2.22 \mu\text{m}$  for example will be displaced in sections 1, 2 and 3 but not in section 4. The resulting displacement will be  $5 + 5 + 5 = 15$  gaps. Being injected at gap 5 and then displaced by 15 gaps means that these cells are “binned” together and will leave the device through gap 20. In reality though, imperfections in the device and the fluid flow, the random nature of diffusion, rotation and cell-cells interactions together with a finite dispersion in the size of a given cell type smooth out the outlet distributions, as can be seen in Fig. 2 in the main body of the paper.

## 1.2 Device fabrication

To make masters for replica moulding SU-8 (MicroChem, Newton, MA, USA) was spin coated onto 3" silicon wafers at thicknesses of  $4.27 \pm 0.04 \mu\text{m}$  and  $10.84 \pm 0.12 \mu\text{m}$  and patterned using UV light in a contact mask aligner (Karl Suss MJB3 and MJB4, Munich, Germany). A chrome mask was fabricated by Delta Mask (Delta Mask, Enschede, The Netherlands) with a design drawn in L-Edit 11.02 (Tanner Research, Monrovia, CA USA). An anti-adhesion layer of 1H,1H,2H,2H-perfluorooctyltrichlorosilane (ABC R GmbH & Co. KG, Karlsruhe, Germany) was applied before casting to facilitate demoulding. PDMS monomer and hardener (Sylgard 184, Dow Corning, Midland, MI, USA) were mixed to a ratio of 10:1, degassed, poured onto the master and baked for 1 hour at  $80 \text{ }^\circ\text{C}$ . Holes were punched in the patterned PDMS slab for fluidic connections and the slab was then bonded to a blank, PDMS-covered microscope slide following surface treatment with oxygen plasma (Plasma Preen II-862, Plasmatic Systems, Inc, North Brunswick, NJ, USA) to achieve a sealed device. Connection tubes were attached using a silicone adhesive (A07, Wacker Chemie AG, München, Germany).

## 1.3 Surface treatment

As a compliment to autoMACS™ buffer, which contains EDTA as an anticoagulant and BSA to prevent the adhesion of proteins to surfaces, the adhesion of blood cells to the inner surfaces of our devices was further decreased by formation on the PDMS of a polymer brush. Immediately after  $\text{O}_2$  plasma treatment and bonding, devices were filled with 0.2% PLL(20)-g[3.5]-PEG(2) (SuSoS AG, Dübendorf, Switzerland) in DI water and allowed to rest for at least 20 min before rinsing with autoMACS™ running buffer prior to running an experiment.

## 1.4 Red blood cell morphology and deformability changing protocols

Blood was extracted from healthy volunteers via finger pricking and diluted around 5 times in autoMACS™ running buffer (Miltenyi Biotech, Auburn, CA). Blood cell morphologies were altered by the addition of sodium salicylate to 2 mM (to form echinocytes) or Triton X-100 to 0.06% (to form stomatocytes) to the autoMACS™ prior to the addition of blood. Deformability of echinocytes was altered by fixation with 0.003% glutaraldehyde.

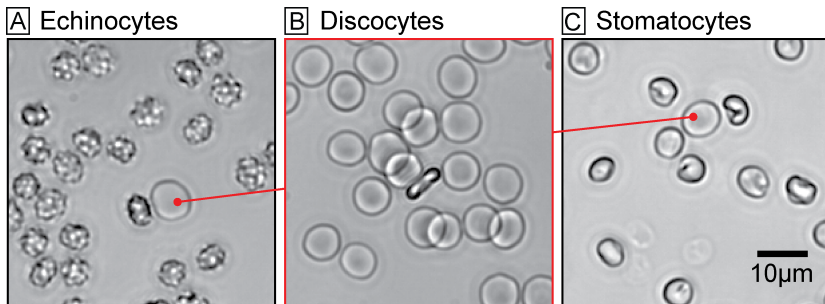


Fig. ESI 2 Transmission microscopy images of red blood cells with different morphologies. (A) Echinocytes formed using 16mM Sodium Salicylate. (B) Normal discocytes in autoMACS™ buffer. (C) Stomatocytes formed using 577 ppm Triton X-100. With both the Sodium Salicylate and Triton X-100 ~1% of RBCs retain a discocytic shape.

#### 1.4.1 Sodium salicylate to form echinocytes

To 100  $\mu$ l of autoMACS<sup>TM</sup> buffer is added 7  $\mu$ l of 0.3 M Sodium Salicylate and this in turn is added to 20  $\mu$ l of freshly drawn blood. The running buffer is 200  $\mu$ l of autoMACS<sup>TM</sup> buffer with 14  $\mu$ l 0.3 M Sodium Salicylate.

Final concentrations: autoMACS<sup>TM</sup> = 79% Sodium Salicylate = 16 mM, Blood = ~16% of whole blood

Sodium salicylate (SS) is an aspirin derivative. It is known to incorporate into the outer leaflet of the RBC membrane and is therefore an echinocytic agent. Concentrations of SS significantly less than 2 mM lead to the formation of a population of echinocytes with a broad distribution in shapes including stomatocytes, discocytes and echinocytes<sup>1</sup>. It is believed that this spread in morphologies stems from the distribution in cell age, cytoskeletal differences and/or metabolic rate. As the concentration of SS is increased the mean shape of the populations is driven towards the echinocytic. At 2 mM 98% of RBCs have been shown to adopt echinocytic forms, with the remaining 2% keeping their discocytic shape<sup>1</sup>. Using a simple analysis of optical microscopy images like those shown in Fig. ESI 2 A, we found that of 1846 RBCs treated with SS, 1.1% retained a discocytic shape. An increase in cell stiffness accompanies the shape changes caused by SS<sup>1</sup>.

#### 1.4.2 Triton X-100 to form stomatocytes

To 100  $\mu$ l of autoMACS<sup>TM</sup> buffer is added 1.4  $\mu$ l of 5% Triton X-100 and this in turn is added to 20  $\mu$ l of freshly drawn blood. The running buffer is 200  $\mu$ l of autoMACS<sup>TM</sup> buffer with 0.8  $\mu$ l of 5% Triton X-100.

Final concentrations: autoMACS<sup>TM</sup> = 82%, Triton X-100 = 577ppm, Blood = ~16% of whole blood

The non-ionic surfactant Triton X-100 is known to be a potent stomatocytic agent. However, care must be taken when using Triton X-100 to induce stomatocytes as the surfactant is also a haemolytic agent. The ability of RBCs to change shape without being lysed depends on the buffer. We found that when using autoMACS<sup>TM</sup> (BSA and EDTA) as a buffer, a concentration of 0.06% Triton X-100 gave sufficiently well-formed stomatocytes that were stable over the time scales, ~1 hour, of our experiments. As with echinocytes, the population of stomatocytes formed is not completely homogeneous. Of 1372 RBCs treated with Triton X-100, 1.0% retained a discocytic shape, see Fig. ESI 2 C.

#### 1.4.3 Fixation of echinocytes in 0.003% glutaraldehyde

10  $\mu$ l of freshly drawn blood was added to 200  $\mu$ l cold PBS, the cells spun down at 600 g for 30 seconds and the supernatant replaced with 200  $\mu$ l of fresh PBS. This was repeated 3 times. On the fourth time the supernatant was exchanged for 200  $\mu$ l new PBS with 0.003% glutaraldehyde and the cells incubated at room temperature for 30 minutes. Finally the cells were spun down and the supernatant replaced with 100  $\mu$ l of cold autoMACS<sup>TM</sup> buffer.

*Note: The glutaraldehyde stock solution was 20% in methanol. While methanol might affect the morphology of the cells this was not apparent during either light or electron microscopy. The change in deformability due to the fixation with glutaraldehyde is also assumed to dominate any effects from the small amounts of methanol present.*

#### 1.4.4 SEM preparation

SEM images were taken on LEO 1560 (Carl Zeiss SMT GmbH, Oberkochen, Germany) after fixation with glutaraldehyde and metalisation with 10nm of platinum.

### 1.5 Running experiments

A pressure gradient was used to drive flow through the DLD devices. Outlets were kept at atmospheric pressure and the overpressure at the three inlets was controlled individually in the range 5-800 mbar using an MFCS-4C pressure controller (Fluigent, Paris, France). Pressure control at each of the three inlets made it possible to hydrodynamically focus the sample into a stream of ~10  $\mu$ m in width as can be seen in Fig. ESI 1B. The concentration of RBCs in the device is also controlled by flow focusing such that the distance between cells is kept larger than the distance the cells move between movie frames, a condition that facilitates particle tracking. When particle tracking is not required much higher concentrations can be used.

All images were taken through an inverted Nikon Eclipse TE2000-U microscope (Nikon Corporation, Tokyo, Japan). High speed images were taken using an EoSens mini MC-1370 camera (Mikrotron GmbH, Unterschleissheim, Germany). In all other cases an Andor Luca or Andor Ixon EMCCD camera (Andor Technology, Belfast, Northern Ireland) were used.

Fluorescent polystyrene microspheres with diameters of  $3.00 \pm 0.15 \mu$ m, (Duke Scientific Corp. Palo-Alto, CA; R0300) and  $4.87 \pm 0.12 \mu$ m (Polysciences Inc., Warrington, PA 18340), that are much less deformable than RBCs were used to evaluate the effects of particle deformation in our devices.

## 1.6 Analysis

Particle tracking software was written in MATLAB 2009b (The MathWorks, Natick, MA, USA). The tracking program was based on IDL Particle Tracking software, available at <http://www.physics.georgetown.edu/matlab/>. The tracking core was optimized for our specific setup. The software was able to track many particles in a field of view when the signal-to-noise ratio was sufficiently high and when the concentration was low enough to avoid particle overlap allowing measurement of the total displacement of hundreds of particles at the end of the device for each set of experimental conditions. White blood cells are either trapped at the inlets of our devices or are displaced to a greater extent than the RBCs allowing us to easily identify them. They do not interfere with our measurements and are not included in the particle counting.

## 2 Effects of device depth

Fig. ESI 3 shows discocytes in devices of different depths. Shear rates have been chosen such that deformation is kept to a minimum. As can also be seen in ESI Movies 1-7, in devices deeper than the diameter of the discocyte, the cells are able to rotate and it is half of the cell thickness ( $\sim 1.25 \mu\text{m}$ ) that defines  $R_{\text{eff}}$ . In devices shallower than the cell diameter, cells are unable to fully rotate and  $R_{\text{eff}}$  increases. In a device of  $3 \mu\text{m}$  depth the radius of the cell ( $\sim 3.75 \mu\text{m}$ ) defines  $R_{\text{eff}}$ . It is interesting that the discocytes do not fully rotate in the  $8 \mu\text{m}$  deep device. We believe that this is due to some coupling between the cell and the walls of the device although more investigations are required. It is also interesting to note that in devices of depths between the radius and half of the thickness of the discocyte the cell becomes tilted at an angle between  $0^\circ$  (lying in the plane of the device) and  $90^\circ$  (standing up against the post). This means that as shear rate is increased the strain, which is toward the surface of the post, will not only compress but also bend the cell. This could provide a means of measuring the bending modulus of cells or other particles.

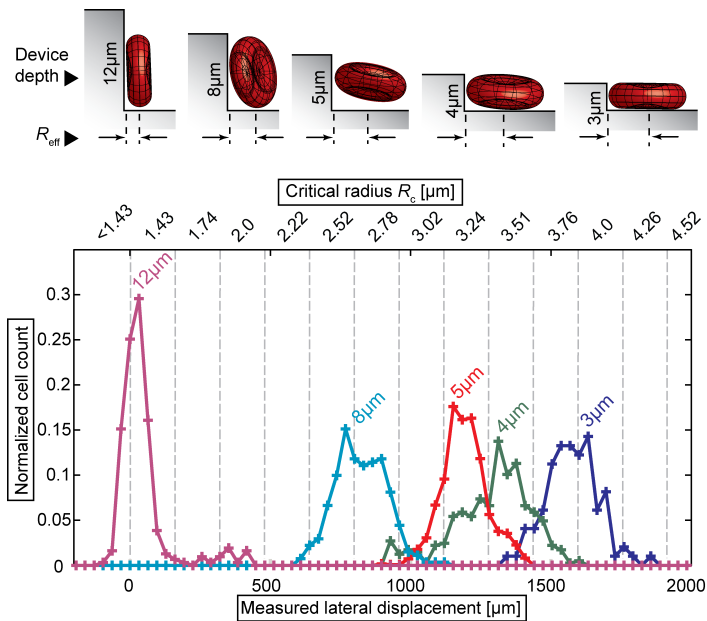


Fig. ESI 3 The effective size,  $R_{\text{eff}}$ , of non-spherical particles (discocytes) increases as device depth decreases. The device depth is shown next to each curve.

### 3 High-speed movies of RBC deformation

Movies of discocytes, echinocytes and stomatocytes in devices of 4.27  $\mu\text{m}$  and 10.84  $\mu\text{m}$  in depth representative of the typical behaviour of the cells. Colour enhanced still images from the movies are compiled in Fig. ESI 4.

ESI Movie1 – Discocyte in 4.3  $\mu\text{m}$  deep device + overview of inlet and outlet

ESI Movie2 – Discocyte in 10.8  $\mu\text{m}$  deep device

ESI Movie3 – Echinocyte in 4.3  $\mu\text{m}$  deep device

ESI Movie4 – Echinocyte in 10.8  $\mu\text{m}$  deep device

ESI Movie5 – Stomatocyte in 4.3  $\mu\text{m}$  deep device

ESI Movie6 – Stomatocyte in 10.8  $\mu\text{m}$  deep device

ESI Movie7 – Discocyte in 10.8  $\mu\text{m}$  deep device – cell rotates and thickness defines effective size

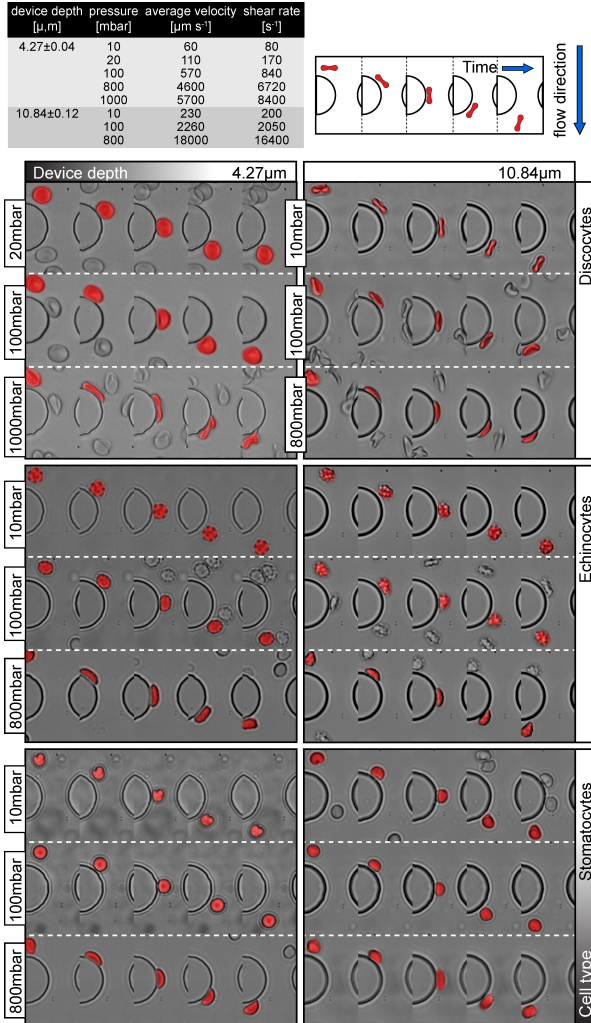


Fig. ESI 4 Colour-enhanced compilations of high-speed camera images, taken from movies 1-6, of cells moving through our devices. Each box shows one type of cell morphology in one of two devices (4.27 and 10.84  $\mu\text{m}$  deep) at three driving pressures. The insets at the top show, to the left, the average fluid flow velocity and wall shear rates at the pressures used, and on the right, how time evolves from left to right in the images. The effect of device depth on the orientation of discocytes can clearly be seen. Because echinocytes and stomatocytes are more spherical, their orientation due to device depth has less effect on their behaviour. At 10 mbar all cell types keep their morphologies but at higher pressures, in both devices, the cells are deformed and  $R_{\text{eff}}$  decreases.

#### 4 Decreasing deformability of echinocytes by fixation

Echinocytes were formed and subsequently fixated to decrease deformability using the protocols describes above. Fixation does not change the shape of the cells and, as can be seen in Fig. ESI 5, at shear rates below  $\sim 2050 \text{ s}^{-1}$  ( $\sim 10 \text{ mbar}$ ) the fixated echinocytes (right) and unfixated echinocytes (left) are not separated. However, the increased stiffness of the fixated cells gives them a considerably larger  $R_{\text{eff}}$  as shear rates are increased and at  $\sim 12300 \text{ s}^{-1}$  ( $\sim 300 \text{ mbar}$ ) separation is complete.

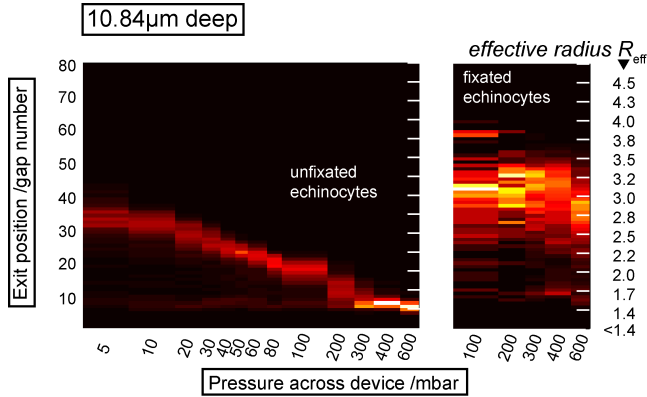


Fig. ESI 5 The stiffness of particles has a large effect on their trajectories through our devices. The effective size of echinocytes (left) decreases as they become deformed at high shear rates. Fixated echinocytes (right) are stiffer and are not deformed as readily, i.e. their effective size decreases less as the shear rate is increased. (At pressures below 100 mbar the fixated cells stick to the surface of the device and become trapped. This appears to be due to the fixation and is not a problem for normal, unfixated cells.)

#### 5 Is deformation responsible for the change in $R_{\text{eff}}$ ?

To exclude any other effects beyond deformation such as hydrodynamic lift that may be involved in decreasing  $R_{\text{eff}}$  we repeated the experiments with hard polystyrene spheres. Also, because PDMS is an elastomer, one would expect microfluidics channels fabricated in PDMS to deform to some degree under the pressures used to drive fluid flow. Hardy et al showed how the height of channels, initially  $500 \mu\text{m}$  wide and  $\sim 40 \mu\text{m}$  deep change due to this effect<sup>2</sup>. While Hardy's channels experienced changes in depth of as much as 20-30% in the pressure range we are using, our channels are filled with posts at  $\sim 26 \mu\text{m}$  centres which considerably stabilize the cross section of the channel. However, because any small changes in the gap size between posts will affect the critical diameter in the device it is important to separate these effects, if any,

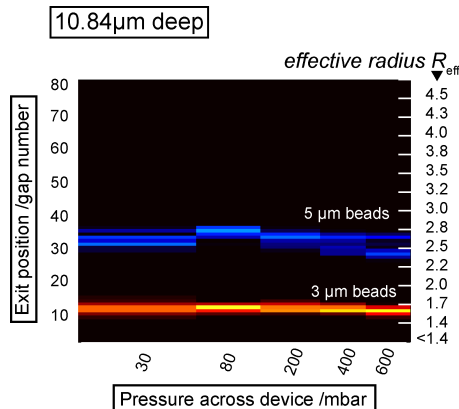


Fig. ESI 6 There is very little systematic change in the outlet distributions of hard polystyrene microspheres as the driving pressure, and consequently the shear-induced stress, is increased.



from the effects of particle deformation. In order to test the effects of device deformation polystyrene microspheres of 3  $\mu\text{m}$  and 5  $\mu\text{m}$  diameters were separated in the device over the pressure range used for the RBC experiments. As can be seen in Fig. ESI 6 there was no systematic change in the effective size of the microspheres and we can neglect both PDMS deformation and hydrodynamic lift in this pressure range in these devices.

1. A. L. Li, H. Seipelt, C. Muller, Y. D. Shi and G. M. Artmann, *Pharmacology & Toxicology*, 1999, **85**, 206-211.
2. B. S. Hardy, K. Uechi, J. Zhen and H. P. Kavehpour, *Lab Chip*, 2009, **9**, 935-938.



Paper IV





# SCIENTIFIC REPORTS

## OPEN Sorting cells by their dynamical properties

Ewan Henry<sup>1</sup>, Stefan H. Holm<sup>2</sup>, Zunmin Zhang<sup>1</sup>, Jason P. Beech<sup>2</sup>, Jonas O. Tegenfeldt<sup>2</sup>, Dmitry A. Fedosov<sup>1</sup> & Gerhard Gompper<sup>1</sup>

Received: 15 April 2016  
Accepted: 13 September 2016  
Published: 06 October 2016

Recent advances in cell sorting aim at the development of novel methods that are sensitive to various mechanical properties of cells. Microfluidic technologies have a great potential for cell sorting; however, the design of many micro-devices is based on theories developed for rigid spherical particles with size as a separation parameter. Clearly, most bioparticles are non-spherical and deformable and therefore exhibit a much more intricate behavior in fluid flow than rigid spheres. Here, we demonstrate the use of cells' mechanical and dynamical properties as biomarkers for separation by employing a combination of mesoscale hydrodynamic simulations and microfluidic experiments. The dynamic behavior of red blood cells (RBCs) within deterministic lateral displacement (DLD) devices is investigated for different device geometries and viscosity contrasts between the intra-cellular fluid and suspending medium. We find that the viscosity contrast and associated cell dynamics clearly determine the RBC trajectory through a DLD device. Simulation results compare well to experiments and provide new insights into the physical mechanisms which govern the sorting of non-spherical and deformable cells in DLD devices. Finally, we discuss the implications of cell dynamics for sorting schemes based on properties other than cell size, such as mechanics and morphology.

The ability to sort specific cells from heterogeneous populations of bioparticles is highly coveted in biomedical fields such as diagnostics and cell biology. Many of the standard cell sorting techniques, such as fluorescence- and magnetic-activated cell sorting devices<sup>1,2</sup>, are labor intensive, use cumbersome and expensive equipment, and require preliminary cell-labeling stages. In contrast, lab-on-a-chip technologies operate at a micrometer scale and provide a promising alternative to the current cell-sorting approaches. Microfluidic devices have multiple advantages over conventional approaches including reduced manufacturing costs, a smaller sample volume requirement, and the ability to sort cells based on their intrinsic properties, leading to an increased automation of the sorting process.

One increasingly popular microfluidic technique, pioneered by Huang *et al.*<sup>3</sup>, is called deterministic lateral displacement (DLD) and utilizes micropost arrays to continuously sort particles according to their size<sup>4-7</sup>. Various geometries of DLD arrays can be characterized by a critical separation radius  $R_c$ <sup>8</sup>, yielding a highly reliable method for separating rigid spherical particles of different sizes. Thus, sorting in DLDs arises as particles smaller than  $R_c$  are able to travel with the flow and swap between pillar lanes (i.e., lane swapping, where a lane is defined as a straight path running parallel alongside a row of pillars) in a zig-zag motion with nearly zero lateral displacement (neutral zig-zag mode, Fig. 1(a)), while particles larger than  $R_c$  are displaced laterally with respect to a driving fluid flow (displacement mode, particles remain in one lane without swapping, Fig. 1(a))<sup>3</sup>. The critical radius can be inferred from the streamlines of the fluid flow without the presence of particles (as illustrated in Fig. 1(b)) and has also been determined empirically<sup>9</sup>. Furthermore, different DLD devices have already been used successfully to separate biological particles and cells. For example, separation of red blood cells (RBCs), white blood cells and platelets from whole blood has been demonstrated<sup>4</sup>, and parasitic trypanosomatids have been extracted from blood samples<sup>5</sup>.

In the above examples, the considered sorting parameter is effective size. However, many bioparticles are non-spherical and deformable, and the idea of a single effective particle radius depends on the particle's orientation and the degree of deformation experienced in flow<sup>9-11</sup>. Furthermore, biological particles may undergo some type of periodic dynamical motion in shear flow (e.g., tumbling) with a constantly changing effective radius, which makes the prediction of sorting on the basis of a particle-free flow not possible. The potential variability of

<sup>1</sup>Theoretical Soft Matter and Biophysics, Institute of Complex Systems and Institute for Advanced Simulation, Forschungszentrum Jülich, 52425 Jülich, Germany. <sup>2</sup>Division of Solid State Physics, NanoLund, Lund University, PO Box 118, S-221 00 Lund, Sweden. Correspondence and requests for materials should be addressed to D.A.F. (email: d.fedosov@fz-juelich.de)

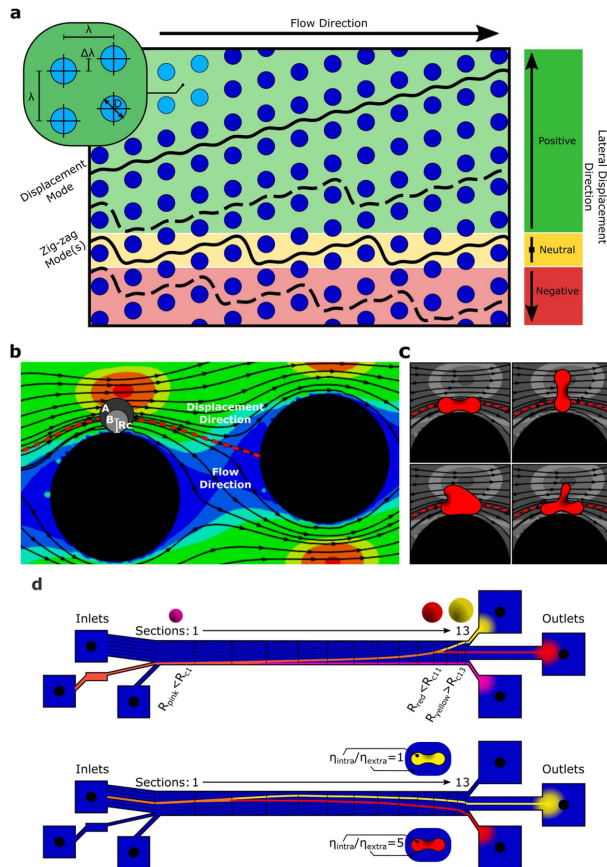


**Figure 1.** DLD sorting of rigid spheres vs RBCs. **(a)** The possible trajectories of particles traversing an obstacle array defined by the central post-to-post distance  $\lambda$ , row shift  $\Delta\lambda$ , and post diameter  $D$ . Solid lines represent the displacement (no lane swapping) and neutral zig-zag (swapping between lanes, where a lane is defined as a straight path running parallel alongside a row of pillars) modes available to rigid spherical particles. Anisotropic deformable particles have access to many additional zig-zag modes which allow for positive or negative lateral displacement, two of which are shown as dashed lines. **(b)** The flow field of a fluid driven from left to right, past two pillars of a DLD device obstacle array. The contour colors from blue to red correspond to the strength of fluid velocity in the flow direction. The red dotted line shows the separatrix between flow traveling over or under the second pillar. Rigid spherical particle A, with  $R_A > R_c$ , is carried over the pillar, in a displacement mode. Particle B, with  $R_B < R_c$ , is carried under the pillar assuming a neutral zig-zag mode<sup>3,8</sup>. **(c)** Deformable and anisotropic RBCs can flow above or under the separatrix depending on their orientation and deformation; dynamic characteristics which change as they interact with the flow. **(d)** Schematic behavior of particles in a DLD device with 13 successive sections, each with larger  $R_c$ : when the device is used to sort 3 sizes of rigid spherical beads, each size undergoes a transition from the displacement mode to a neutral zig-zag mode in a different section. The orange color corresponds to an initially polydisperse suspension of different spheres, while the other colors depict separated monodisperse fractions at the end of the device. The same device sees very different separation trajectories when sorting RBCs undergoing different types of dynamic behavior. Dynamic behavior can be controlled by changing the viscosity contrast between interior and extracellular fluids. Note that due to the presence of negative zig-zag modes for RBCs it is necessary to use the large central inlet to accommodate separation in both directions.

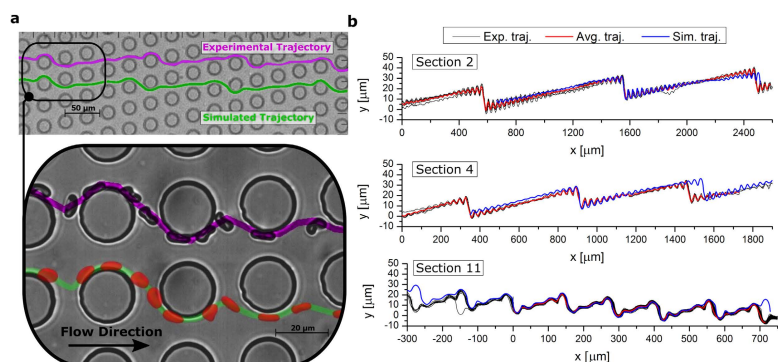


**Figure 2.** Experimental and simulated trajectories for RBCs at viscosity contrast  $C = 5$ . (a) The trajectories of the experimental and simulated RBCs are obtained by following their center of mass through the pillar array. (b) Experimental and simulated RBC trajectories for several sections of the thick device. Black lines show multiple aligned experimental RBC trajectories and red lines correspond to average experimental trajectories. The blue lines show the RBC trajectories found in simulations. Section 2 shows an approximately neutral zig-zag mode, section 4 illustrates a positive zig-zag mode, and section 11 leads to a negative zig-zag mode.

the effective size is illustrated in Fig. 1(c) for RBCs which have a rich dynamic behavior and deformability in a pillar array, and it is clear that the sorting of other such bioparticles will be similarly complex. Therefore, the effects of cell dynamics must be carefully considered in microfluidic devices and can even be used for novel sorting schemes which are sensitive to the mechanical properties of cells. Investigations on white blood cells in DLD devices have already indicated that deformations have an impact on their transit behavior<sup>12</sup>. Furthermore, RBC deformability has been suggested as a sorting parameter<sup>13</sup> and recent numerical simulations<sup>14–16</sup> of elasticity-based sorting have considered this possibility. Targeting these elastic, structural, and dynamical characteristics for sorting adds a new level of complexity to designing DLD devices and testing the myriad of combinations between cell types and device configurations experimentally would be expensive and impractical. Consequently, there is a compelling need for theoretical methods and simulations to understand the essential physical mechanisms and to make quantitative predictions of how cell dynamics will affect transit behavior of bioparticles in DLD devices.

In this work, we perform a combined numerical and experimental investigation of RBC sorting in DLD devices. Instead of analyzing the location of RBCs after they exit the pillar array, as is customary with DLD devices, we focus on quantitatively describing the entire trajectory of RBC transit through devices. We find that a description of trajectories through the two modes (i.e., displacement and neutral zig-zag, shown in Fig. 1(a)) is far too simple to adequately describe sorting of deformable and anisotropic particles. Even though the displacement mode defined by device geometry remains similar to previous experiments with rigid spherical particles, we observe a range of zig-zag modes in experiments and simulations, which can lead to positive, neutral and negative displacements of a RBC within different configurations of the device. Furthermore, the examination of RBC dynamic behavior immediately before and after lane-swapping events in DLDs allows us to identify a relationship between RBC trajectory, its dynamic behavior and hydrodynamic interactions. This relationship is further investigated by varying the ratio between intracellular and extracellular viscosities, as viscosity contrast is known to dramatically affect RBC dynamics<sup>17</sup>. Indeed, by invoking a different dynamic behavior such as tumbling or tank-treading, we show that it is possible to rationalize and control RBC trajectories in DLD devices. Thereby, we can propose a novel sorting strategy and show how a reliable simulation method for deformable and anisotropic particles through DLD devices becomes a powerful tool for designing sorting-schemes which depend on particles' dynamic behavior and hence, their intrinsic mechanical characteristics, such as rigidity and internal viscosity.

## Results

The experimental and simulation results are presented in unison to facilitate a detailed comparison. Initially the possible transit modes available to RBCs in two different DLD devices are considered, as these modes are different from the displacement and neutral zig-zag modes available to rigid spheres. The first device is thick enough to allow RBCs to explore a full range of dynamic behavior, while the second is sufficiently thin to force horizontal orientation of RBCs, suppressing reorientation dynamics due to confinement. A schematic of the device structure and pillar array geometry can be seen in Fig. 1 and Supplementary Figure S1. Both devices have 13 sequential sections, each housing a pillar array defined by the post diameter  $D = 20 \mu\text{m}$ , central post-to-post distance  $\lambda = 32 \mu\text{m}$ , and row shift  $\Delta\lambda$ , which increases from a value of  $0.8 \mu\text{m}$  to  $8.8 \mu\text{m}$  incrementally between subsequent sections (see Supplementary Table S1). We explore how the transition between different transit modes occurs at different sections in the device depending on RBC dynamic behavior, which is controlled directly using the different confinements of the thin and thick devices, and by changing the ratio  $C = \eta_i/\eta_o$  between intra-cellular viscosity of the

RBCs and extra-cellular medium. Finally, we discuss qualitatively why the different dynamic behavior arises and how it results in different transit behavior.

The transit of deformable anisotropic particles through the 13-section device is considerably different from that of rigid spheres, as depicted schematically in Fig. 1(d). This is not only due to transitions from the displacement to zig-zag modes occurring in different sections but also due to the availability of additional zig-zag modes. Ultimately, there is no reason why a particle should prefer the neutral, zero lateral-displacement, zig-zag mode; depending on the frequency of lane swapping, negative, neutral, and positive net lateral displacement can be induced.

**DLD transit modes in the thick device.** In order to understand the nature of the transit modes available to RBCs, we follow the trajectory of a RBC's center of mass through the obstacle array, by recording the  $x$  and  $y$  coordinates, along and perpendicular to the flow direction, respectively. Figure 2 depicts a selection of different zig-zag modes of RBCs in different sections of the thick DLD device at a physiological viscosity contrast of  $C = 5$ . Figure 2(a) shows a side by side comparison of simulated and experimental RBC snapshots and a zig-zag trajectory in section 11, which is defined by a row-shift of  $\Delta\lambda = 6.8\mu\text{m}$ . The high frequency of lane-swapping in the RBC trajectory makes it a good introductory example of a zig-zag mode because it is possible to view it with isometric scaling. This type of data representation will form the basis for comparisons between experimental and simulated results. In other sections of the devices, trajectories might have periodicity at length scales too large for isometric visualization. Consequently, the trajectories seen in Fig. 2(b) are displayed with different  $x$  and  $y$  scaling. This allows us to present a complete, albeit distorted, depiction of the trajectories. Furthermore, the experimental trajectories in Fig. 2(b) have been selected from a population of recorded trajectories in accordance with pre-screening criteria, which were used to remove trajectories of insufficient length as well as trajectories where inter-RBC interactions were detected. Further details about the data sample and the pre-screening criteria can be found in the Supplementary Information.

Figure 2(b) compares experimental and simulated RBC trajectories in various sections of the thick DLD device and nicely presents the range of different zig-zag modes which we observe. In order to quantitatively describe and differentiate these zig-zag modes, we define their average lateral displacement,  $l$ , per post encounter. The value of  $l$  can be calculated by considering the competing effects of lane-swapping events and lateral displacement induced by the geometry of the pillar array. The positive lateral displacement per post is simply  $\Delta\lambda$  and the average displacement per post encounter due to lane-swapping is given by the frequency of lane-swapping events multiplied by the distance between rows,  $-\lambda f$ . The additive effect of these two motions yields

$$l_i = \Delta\lambda_i - \lambda f_i, \quad (1)$$

the average lateral displacement per post encounter in the  $i^{\text{th}}$  section of the device. The frequency  $f_i$  of lane-swapping is determined by the inverse of the average number  $m$  of post encounters per lane-swapping event. Theoretically,  $m$  could have any positive value, where the special cases  $m = \infty$  and  $m = \lambda/\Delta\lambda$  yield the ideal displacement and neutral zig-zag modes discussed previously.

Using the calculation for  $l_i$  shown in Eq. (1), we return to Fig. 2 and quantitatively describe the observed zig-zag modes; in section 2 and 4 with  $\Delta\lambda_2 = 1.2\mu\text{m}$  and  $\Delta\lambda_4 = 2.0\mu\text{m}$ , we find nearly neutral zig-zag modes with values of  $l_2 = 1.2 - 32/30 = 0.13\mu\text{m}$  and  $l_4 = 0.22\mu\text{m}$ , close to the ideal case; finally section 11 induces a negative zig-zag mode, where lateral displacement is offset by the lane-swapping events and the average displacement per post is  $l_{11} = 6.8 - 32/4.4 = -0.47\mu\text{m}$ . Note that  $m$  takes a non-integer value in this case, because the periodicity between lane-swapping events is irregular. The irregular periodicity supports the idea that changes in RBC orientation and deformation cause it to explore more than one flow stream and exhibit more complex behavior than simple hard spheres. However, it is important to emphasize that the non-integer  $m$  values we find are not the result of random RBC behavior in the device. The behavior of RBCs is governed by local fluid flow and their elastic and viscous properties, which is supported by RBC dynamics in shear<sup>18,19</sup> and tube<sup>17</sup> flows, and therefore, there is no reason to expect random RBC dynamics in DLDs. The only randomness arises from the initial orientation and position of the RBCs as they enter the device, and the thermal fluctuations which result in cell diffusion and membrane flickering; however, RBC diffusion can practically be neglected in the current simulations in comparison to RBC transport induced by the flow due to flow rates being sufficiently large, resulting in a high Péclet number. Consequently, even the trajectories with a non-integer lane-swapping frequency are expected to be deterministic for the fixed simulation conditions. In experiments, there also exist a number of uncertainties (e.g., cell properties, flow control, device fabrication limits) which may affect the trajectory of a cell in the device. The inherent variability in RBC properties can perhaps be least controlled. However, the example of experimental results for section 11 of the thick device in Fig. 2(b), which consists of 69 well-aligned RBC trajectories (see Supplementary Figure S4), shows a consistent pattern of traversing 4 or 5 obstacles before performing a lane-swap. This indicates that the trajectories are not random, as otherwise a much broader variety of lane-swapping patterns would be observed, and that the geometry of section 11 and the corresponding flow are not very sensitive to 'moderate' variations in RBC properties. This complex yet deterministic nature of trajectories can be explained by an interplay between RBC dynamics (e.g., flow-rotation, deformation) and local flow mainly determined by the periodic geometry of the DLD device. Thus, a mismatch between RBC motion and periodic geometry may result in several different cell states (e.g., position, orientation) after a lane-swap, which will in turn decide the number of pillars traversed before the next swap and indeed the lane-swapping pattern thereafter.

By plotting the change in  $l_i$  as RBCs travel through the entire device, we are able to see the transitions between different sorting modes. The average lateral displacement  $l_i$  per post encounter for each individual section of the thick device is shown in Fig. 3(a) and the number of RBC trajectories used to calculate each  $l$  value can be found in the Supplementary Tables S2–S6. These data allow us to draw several important conclusions. Firstly, we find



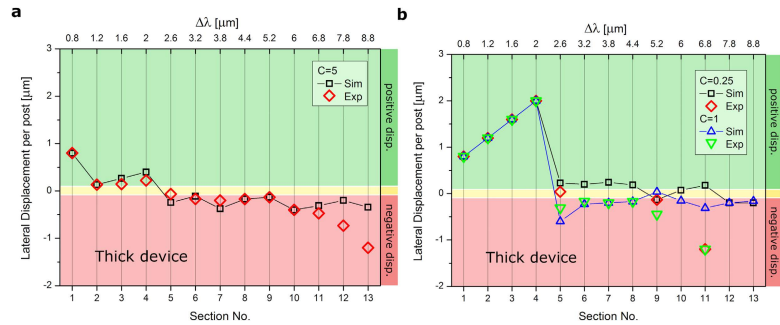


**Figure 3.** The average lateral displacement per post encounter  $l$  of RBCs in each individual section of the thick device at various viscosity contrasts  $C = \eta_p/\eta_s$ . (a) Data for the thick device at  $C = 5$ . Experimental values agree well with the simulated values and the transition to zig-zag modes occurs between sections 1 and 2. (b) Data for the thick device at  $C = 1$  and  $C = 0.25$ . Experimental and simulation trajectories at both viscosity contrasts undergo a transition from displacement to zig-zag modes between sections 4 and 5, which is later than found at a physiological value of  $C = 5$ .

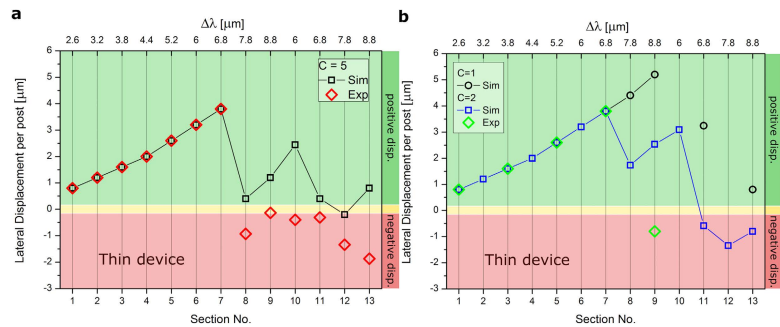


**Figure 4.** The average lateral displacement per post encounter  $l$  of RBCs in each individual section of thin device at various viscosity contrasts  $C = \eta_p/\eta_s$ . (a) Data for the thin device at physiological viscosity contrast  $C = 5$ . Transition to zig-zag modes is the same in experiments and simulations, occurring between sections 7 and 8. However, evolution of zig-zag modes with section number shows discrepancies due to inherent variability in RBC size. (b) Data for the thin device at viscosity contrasts  $C = 1$  and  $C = 2$ . Transition to zig-zag modes at contrast  $C = 2$  occurs between sections 7 and 8 for simulations and experiments, whereas the transition at  $C = 1$  occurs in section 10 for the simulations. Again, variability between experimental and simulation results can be attributed to the inherent variability in RBC diameter.

very good agreement between simulated and experimental trajectories for a viscosity contrast of  $C = 5$ . The only real deviations occur in the final few sections of the device, where the experimental trajectories are observed to undergo a more negative lateral displacement due to disturbances of the flow field when in the vicinity of the outlet; an effect we see consistently throughout the course of this work. The close agreement suggests that the simulation techniques adequately capture the hydrodynamic effects and RBC deformation and dynamics. Secondly, the transition from displacement to zig-zag mode occurs at the beginning of the device, between sections 1 and 2. After this transition the RBC transit modes become gradually negative as the lateral row shift  $\Delta\lambda$  increases with section number. The increase in  $\Delta\lambda$  promotes positive displacement due to geometry, however there is also a higher likelihood of lane-swapping events due to the increase of critical radius. These zig-zag modes with negative lateral displacement per post are not very far from the neutral mode, however they present a key manifestation of the transit behavior of deformable particles unavailable to hard spheres, and are due to the dynamic properties of RBCs with the responsible mechanisms postulated later in the discussion section. Finally, we note that the additive effect of some sections may cancel each other out, making their serial use in one device inefficient for separation.

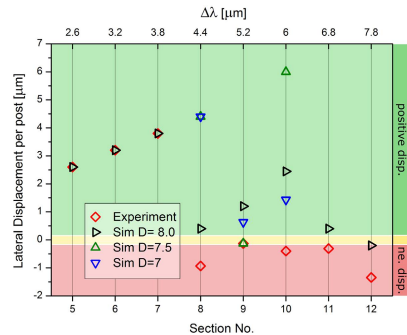


**Figure 5. Sensitivity of the thin device to RBC size.** The average lateral displacement per post encounter  $l$  for individual sections of the thin device. Several RBC diameters were considered to confirm that the later sections of the thin device are quite sensitive to moderate changes in the RBC size. Several simulations for the RBCs with diameters 7, 7.5 and 8  $\mu\text{m}$  have been performed.

**DLD transit modes in the thin device.** The thin device inhibits RBC orientation in flow, forcing the cell to align with the device plane. The highly constrained environment limits the range of dynamics available to the RBCs and therefore, the results should be closer to those predicted for hard spheres. Figure 4(a) shows the average lateral displacement of a RBC per post encounter for each section of the thin device. For a viscosity contrast  $C = 5$  in sections 1–7 an excellent agreement between the experimental and simulated values is observed, showing strong positive lateral displacement. Only in section 6 does lane-swapping begin to occur. However, these events are infrequent and the video frame is too narrow to capture two successive lane-swapping events for the same trajectory, making it difficult to obtain a period for a zig-zag mode. Similarly, it is difficult to run simulations long enough to accurately capture several lane-swapping events in section 6. Ultimately, we see a strong positive displacement in sections 1–7 of the thin device at  $C = 5$ . In the following sections, lane-swapping events occur frequently and RBCs travel in well-established zig-zag modes in the simulated and experimental trajectories. This transition from displacement dominated trajectories to lane-swapping dominated trajectories in section 8 agrees relatively well with the empirically predicted critical radius of  $R_c = 3.02 \mu\text{m}$  for hard spheres<sup>8</sup>, considering that the maximum RBC radius is about  $4.00 \mu\text{m}$  and it will often be less than this due to deformation in the flow. It is also important to notice the discrepancy between experimental and simulated trajectories after the transition to zig-zag modes in Fig. 4(a), which will be discussed below.

A sharp transition from pure positive displacement modes to zig-zag modes occurs in section 8 of the device for  $C = 5$  (Fig. 4(a)). It is in this section and subsequent ones that we begin to see less agreement between simulations and experiments. Specifically, simulated trajectories undergo less negative lateral displacement due to a smaller frequency of lane-swapping events. Furthermore, we see increasingly positive zig-zag modes in sections 8–10 in simulations, which is due to the increasing value of  $\Delta\lambda$  in subsequent sections causing an increased positive lateral displacement but a relatively low increase in the frequency of lane-swapping events. Larger deviations between experimental and simulation results are not unexpected when the confinement of the RBC is increased in a device, because the forced orientation of the RBC in the thin device amplifies the effects of size differences between simulated and sample RBCs. The diameter of real RBCs varies in the range between  $6 \mu\text{m}$  and  $9 \mu\text{m}$ , which is approximately a 10–15% deviation from the simulation value of  $8 \mu\text{m}$ . The possible differences in size are on the same order of magnitude as the change in critical radius for successive sections of the thin device.

To investigate the effect of RBC size in more detail, we performed several simulations for RBCs shown in Fig. 5 with different diameters at  $C = 5$ . The simulation results for different RBC sizes indicate that the discrepancies between experimental and simulated trajectories are likely to come from the variations in size of real RBCs. These results also confirm that the later sections of the thin device are very sensitive to moderate changes in the RBC size. Furthermore, a close quantitative agreement between experiments and simulations in Fig. 5 is difficult to obtain, because the experimental data points correspond to the averages of several trajectories of RBCs with potentially different sizes. In fact, a number of experimental trajectories were not taken into account, because they could not be aligned following our alignment criteria. The number of disregarded trajectories for the thin device was considerably larger than that for the thick device, as can be seen in Supplementary Tables S3 and S5, showing a decrease in the fraction of accepted trajectories from the videos in these sections. The thick device appears less sensitive to RBC size differences, since the effective RBC size corresponds to the cell thickness rather than to the RBC diameter due to its orientation in flow. The simulation results also illustrate that we are able to confidently check device sensitivity to values which are hard to measure and consistently manipulate in a lab setting, such as a variable cell size.

**Viscosity-contrast-based sorting.** The viscosity contrast between the intra- and extra-cellular fluids in simulation and experiment discussed so far is close to the value of  $C = \eta_i/\eta_o = 5$  for physiological conditions in real blood. However, it is well established that the viscosity contrast is an important factor in RBC dynamics in

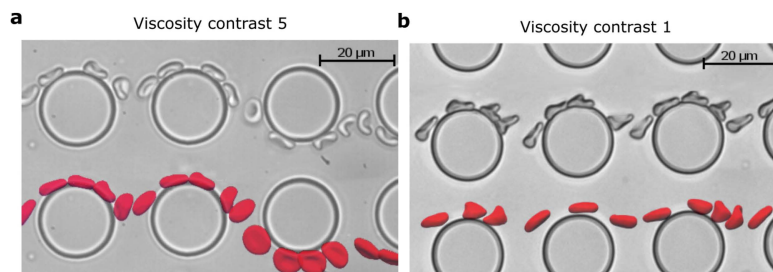


**Figure 6.** Stroboscopic images of RBCs in section 2, taken from simulations and experiments. (a) RBC lane swapping is promoted by tumbling when  $C = \eta_i/\eta_o = 5$ . (b) Tank-treading type dynamics occurs at  $C = 1$  and the RBC favors the displacement mode.

shear flow, as it leads to a transition from tank-treading to tumbling with increasing viscosity<sup>20,21</sup>. By altering the viscosity contrast, we demonstrate the importance of RBC dynamics within the device when attempting to use DLD as a technique for RBC separation. In addition to viscosity contrast  $C = 5$  between the intra- and extra-cellular fluids, simulations and experiments were carried out at  $C = 1$  and  $C = 0.25$  for the thick device, and  $C = 2$  for the thin device. In the experiments, the viscosity of the outer fluid is increased by adding dextran at various concentrations. Note that the different choice of  $C = 1$  and  $C = 2$  for the thick and thin devices, respectively, is due to pronounced adsorption (or sticking) of RBCs to the upper and lower walls, which occurs in the confined environment of the thin device for the higher dextran concentrations required to reach a viscosity contrast less than  $C = 2$ .

The lateral displacement per post  $l$  of the trajectories under these additional viscosity contrast conditions are shown in Figs 3(b) and 4(b). Simulations were first used to predict which sections display interesting behavior, and these sections were then investigated experimentally in order to validate results. For both  $C = 1$  and  $C = 0.25$  in sections 1–4 of the thick device, the change in viscosity contrast completely inhibits lane-swapping events. This substantial shift away from behavior in the physiological case of  $C = 5$  may be attributed to a change in RBC dynamics which will be discussed later. In subsequent sections, there is a transition to almost neutral zig-zag modes, with a gradually increasing tendency to adopt an average negative lateral displacement towards the later sections of the device. In the sections following the transition, the zig-zag modes at  $C = 0.25$  are slightly more positive than those for the  $C = 1$ , but the  $l$  values for both cases converge in the last two sections of the device. This suggests a small difference in dynamic behavior which is only relevant in deciding the lane swapping frequency in the middle sections of the device. Generally, we see good agreement between experimental and simulated results, the main differences occur in the later sections of the device which we attribute to a distortion of the flow field when in close proximity to the device outlet. The difference between the trajectories in the early sections at viscosity contrast  $C = 5$  compared with those at  $C = 1$  and  $C = 0.25$  demonstrates the importance of viscosity contrast for RBC sorting since it may dramatically alter the transit modes.

Figure 4(b) shows that the viscosity contrast also plays an important role in the transit of RBCs through the thin device. For a viscosity contrast of  $C = 1$ , the simulated RBC trajectories undergo a transition from the displacement mode to zig-zag mode only at section 10, while for  $C = 5$  the transition occurs earlier, at section 8. Additionally, for the intermediate viscosity contrast of  $C = 2$ , the transition to zig-zag modes occurs in the same section as for  $C = 5$ . Well-defined zig-zag modes follow the transition, with a region of positive zig-zag modes in sections 8–10. The  $l$  values in sections 8–10 are more positive than for the physiological contrast  $C = 5$ , and represent a behavior intermediate between the  $C = 5$  and simulated  $C = 1$  values. Generally, we see good agreement between simulated and experimental results, as again we have to consider the potential effects of RBC-size variations which we already presented in Fig. 5.

There are also differences in the average lateral displacement per post encounter for the viscosity contrasts  $C = 1$  and  $C = 2$ –5 in later sections of the device, which are especially pronounced in section 11. These results suggest that changes in RBC dynamics and deformation are still relevant in the thin device and that their effects are most pronounced on well-established zig-zag modes. As a conclusion, our results suggest that the viscosity contrast could be used as a targeted separation parameter by itself without other changes in RBC properties.

**RBC dynamics in DLDs.** The dependence of the transit modes of RBCs traveling through DLD obstacle arrays on viscosity contrast has revealed the importance of RBC dynamics. Single RBCs in shear flow have been shown experimentally to tumble at low shear rates and tank-tread at high shear rates<sup>18,19,22,23</sup>. Note that all these experiments have been performed under the conditions where the viscosity of suspending media was larger than that of the RBC cytosol. However, recent experiments<sup>20</sup> and simulations<sup>21</sup> indicate that the physiological viscosity contrast of  $C = \eta_i/\eta_o = 5$  suppresses the tank-treading motion of RBCs, leading to the preference for RBC tumbling. In case of  $C \lesssim 2$ –3, RBC membrane tank-treading is possible and the transition between tumbling and tank-treading for an increasing shear rate is attributed to the existence of a RBC minimum energy state, related to the weakly anisotropic shape of the spectrin network, such that the RBC has to exceed a certain energy barrier in

order to transit to the tank-treading motion<sup>23</sup>. Moreover, recent shear-flow experiments<sup>19</sup> have identified another dynamic state, RBC rolling, which occurs within the range of shear rates between RBC tumbling and tank-treading states.

The main difference in RBC dynamics for the cases of  $C = 0.25$ – $1$  and  $C = 5$  is the preference of tank-treading motion and tumbling dynamics, respectively. Figure 6 shows snapshots of simulated and experimentally observed RBCs in section 2 of the thick device at viscosity contrasts  $C = 1$  and  $C = 5$ . In addition to demonstrating the accuracy of the simulated RBC dynamics in comparison to the corresponding experimental data, Fig. 6 demonstrates the preferred transit modes of RBCs exhibiting different dynamic behavior. The tumbling and rolling motion, which occurs at the physiological viscosity contrast, favor a zig-zag transit mode. Conversely, the tank-treading dynamics at viscosity contrast  $C = 1$  noticeably inhibits lane swapping and the membrane deforms considerably (see trilobe RBC shapes in Fig. 6(b)) due to the shear forces experienced in the local vicinity of obstacles. Also, we observe in Fig. 6(a) that RBC tumbling motion directly precedes and follows lane-swapping events, indicating that tumbling dynamics plays an important role in determining the lane-swapping frequency of zig-zag modes. In comparison to tumbling motion, the tank-treading RBC seen in Fig. 6(b) is subject to local shear-flow alignment, which suppresses cell tumbling and therefore, swapping of lanes. This fact is consistent with the simulation data in Fig. 3, where the transition to zig-zag modes occurs at a later section for  $C = 1$  and  $C = 0.25$  in comparison with  $C = 5$ . The results for  $C = 0.25$  and  $C = 1$  are very similar, and this can be attributed to the fact that the only difference in RBC dynamics will be an increase in the frequency of tank-treading at  $C = 0.25$  due to the reduced internal viscosity. This minor change in dynamics is reflected in the small changes in  $l$  values between the two cases.

Another important aspect which influences the transit of RBCs through a DLD is related to hydrodynamic interactions of deformable particles with walls and obstacles. It is well known that deformable particles (including RBCs) in flow near a wall are subject to a lift force driving them away from the wall<sup>24–26</sup>. Even though the lift force would depend on particle properties (e.g., rigidity, viscosity contrast) and its dynamics (e.g., tank-treading or tumbling, inclination angle), it is well established that the lift force is stronger on a tank-treading RBC in comparison to a tumbling cell. Thus, the lift force on a RBC from the pillars in the thick device may inhibit the transition to zig-zag modes in early sections for  $C = 1$  and  $C = 0.25$  in comparison with  $C = 5$ .

## Discussion and Conclusions

We have presented a detailed comparison of experimental and simulated results for RBC transit through chirped DLD devices under various conditions. The behavior of RBCs in DLD sorting devices is different from that of rigid spheres in two key ways. The first distinction is that a RBC has many more transit modes available than a rigid particle due to the complex interplay between hydrodynamic interactions with obstacles (i.e., lift force), and RBC orientation and deformation. The second distinction follows directly from the first: given that a RBC's varying orientation and deformation depends on features such as viscosity contrast and deformability, changing these parameters will result in transitions to different transit modes. For instance, the preference for RBC tumbling at  $C = 5$  enables the transition from pure displacement to zig-zag mode in section 2 of the thick device, while the tank-treading motion of a RBC membrane at  $C = 1$  and  $C = 0.25$  delays this transition up to section 5. The main difference between these two cases arises from a well-documented hydrodynamic interaction of cells with a surface which is called the lift force and experienced by deformable particles in flow next to walls<sup>24–26</sup>. The lift force is stronger on a tank-treading cell in comparison to that performing tumbling dynamics, and pushes a RBC away from a pillar resulting in a delayed transition from the displacement to zigzag mode. Note that these hydrodynamic effects do not exist for rigid spheres when inertial effects can be neglected (i.e., nearly zero Reynolds number), which is the case for our experimental and simulation conditions.

Another effect, which can be important for deciding particle trajectory in DLDs, is related to direct particle-post collisions. Bowman *et al.*<sup>27</sup> presented a model based on the irreversibility of particle trajectory due to its collision with a post, which has rationalized well the traversal of drops in a gravity-driven DLD. In that study, the drops did not experience significant deformation since very low capillary numbers were employed, and therefore, the deformability effect can be excluded. However, it remains unclear whether the particle-post volume-exclusion effect is relevant for our DLD geometry and whether its contribution would be strong enough in comparison with the dynamics and deformability effects for RBCs described above.

For a thick device, which allows complete freedom in RBC orientation, an excellent quantitative agreement between experiments and simulations with a viscosity contrast  $C = 5$  between the intra- and extra-cellular fluids has been observed. As already mentioned for viscosity contrasts  $C = 0.25$ – $1$ , a change in RBC dynamics resulted in the inhibition of lane-swapping events in early sections of the device. Simulation results for the thin device at viscosity contrasts  $C = 2$ – $5$  show a good quantitative agreement for the displacement modes located in the first 7 sections of the device. Discrepancies between simulation and experiment following the transition to zig-zag modes in sections 8 and onwards are explained by the inherent experimental variability in RBC size, a characteristic which the thin device is especially sensitive to. Indeed, changing simulated RBC size within the range of real RBC sizes or varying the viscosity contrast dramatically alters the average lateral displacement per post of RBCs in sections 8–10, which immediately follow the transition from displacement to zig-zag modes. Furthermore, simulations with a viscosity contrast  $C = 1$  in the thin device display a similar inhibition of lane swapping seen in the thick device in comparison with the case of  $C = 5$  or  $C = 2$ , as the transition to zig-zag modes shifts from section 8 to section 10.

Based on our observations we can make several suggestions for device design and optimization, and possible future sorting schemes. Foremost, we see that neutral zig-zag modes and perfect displacement modes make only a small fraction of the possible cell transit modes. In order to design an optimal chirped device for sorting deformable particles, it will be necessary to consider the net displacement resulting from a range of negative, neutral and positive transit modes. Our results for different viscosity contrasts suggest that carefully selecting the viscosity of the suspending medium may allow sorting based on the viscosity of particles' intra-cellular fluid. A sorting

scheme of this kind would be performed best in a *thick* device which allows exploration of the full range of the particle dynamics induced by the viscosity contrast. For instance, two types of particles which differ only in their internal viscosity may be separated by tuning the viscosity of the suspending medium such that each particle's dynamics favors a different transit mode.

The other potential for such devices is elasticity-based sorting, which has been partially explored in recent experiments<sup>13</sup>. Based on the knowledge about RBC dynamics in shear flow<sup>18–20,23</sup>, it is plausible to expect DLD devices to be well suited for elasticity-based sorting of RBCs, which might be relevant in several blood diseases. Here, again the transitions between tumbling, rolling, and tank-treading motions<sup>19</sup> might be exploited; however, they appear to be suppressed by a high enough viscosity contrast<sup>20,21</sup> favoring tumbling motion. Therefore, we expect that elasticity-based sorting of cells in the thick device would be achieved best at a viscosity contrast smaller than about 2–3.

Elasticity-based sorting of RBCs should theoretically be also possible in the thin device. The simulation results in Fig. 4 for the thin device indicate that in the later sections there exist differences between the simulation results for viscosity contrasts  $C=2-5$  and  $C=1$ . These differences must come from RBC deformability in flow (here due to different fluid viscosities) and the later sections of the thin device are very sensitive to slight changes in effective RBC size which may occur due to cell deformation in flow. In practice however, as we have seen in Fig. 5, the trajectories in sections immediately following the zig-zag mode transition are somewhat unpredictable due to inherent variability in RBC sizes, so it is unlikely that the device would be able to distinguish between small changes in size and small changes in deformability. The deformation effect has been nicely illustrated in the recent simulation study<sup>16</sup>, where the effect of flow rate on the transit mode of a RBC in a similar thin device has been explored. An increase of flow rate in the device leads to stronger RBC deformations and change of the transition between the displacement and zig-zag modes. Thus, a proper tuning of the flow rate would be necessary for elasticity-based sorting of RBCs in the thin DLD. Returning to size-based sorting, we see that a thin device suppresses the variability in RBC dynamics and is consequently more sensitive to variations in cell size. As such, thin chirped devices look best suited for sorting RBCs based on their size.

For rigid spheres, there exist empirical relations between device geometry and the critical particle size where trajectories switch from the displacement to zig-zag mode<sup>28,29</sup>. This relation is possible due to the fact that there are only two available transit modes and a particle's preference for each depends solely on its size relative to the characteristic length scale of the device geometry. However, as demonstrated here for deformable particles, the transition between displacement and zig-zag modes and the presence of additional modes are much harder to predict, because the behavior depends on a complex combination of several additional variables such as particle elasticity, viscosity contrast, and flow speed. Consequently, a simple empirical relation for all these variables seems unlikely to be found. Also, any modeling simplification (e.g., omission of some cell properties) would not lead to predictive results for the transit in DLDs, and therefore it is necessary to use quantitatively reliable fluid simulation techniques which properly account for hydrodynamic effects, and particle models which can accurately capture the mechanical properties of deformable particles such as elasticity, the viscosity ratio between extracellular and intracellular fluids, and cell morphology.

In conclusion, we have demonstrated that the complex interplay between the dynamic behavior of deformable particles and the hydrodynamic interactions they experience near obstacles give rise to a much richer behavior in DLD devices than that found for rigid spheres. Still, the transit modes are not random but deterministic, and are determined by fluid flow and the mechanical properties of deformable particles. Thus, the combination of predictive simulations and experiments becomes a powerful tool for the design of novel sorting schemes which employ dynamic behavior and intrinsic mechanical characteristics of bioparticles as a quantitative separation parameter or biomarker. Such sorting schemes are not restricted only to blood related diseases and disorders (e.g., malaria, sickle-cell anemia), but can also be employed in many other areas including bacteriology, parasitology, and oncology. In addition, label-free microfluidic sorting of bioparticles by their dynamical properties offers significant improvements over conventional techniques, such as fluorescence- and magnetic-activated cell sorting<sup>1–2</sup>, by making sample handling easier and reducing costs. Finally, our work demonstrates the importance of reliable predictive simulation approaches for the development of purpose-specific microdevices, since simulations can provide a better understanding of dynamic behavior of bioparticles in microfluidics and lead to significant design optimizations.

## Methods

**Simulation techniques.** To represent the suspending fluid, we employ a mesoscale hydrodynamic simulation approach which is a variation of the smoothed dissipative particle dynamics (SDPD) method<sup>30</sup>, adapted to conserve angular momentum<sup>31</sup>. The RBC membrane is modeled as a triangulated network of springs<sup>32–34</sup>, whose vertices are coupled to the fluid via frictional forces.

The obstacle array is simulated using a 3D domain enclosing a single-column obstacle with its axis in the  $z$  direction, perpendicular to the roof and floor of the domain box. Efficient representation of an infinite bumper array environment is achieved with periodic boundary conditions in the  $x$  and  $y$  directions (along and perpendicular to the flow direction) and a shift in the  $y$  direction for each boundary-crossing event in the  $x$  direction, as depicted in Supplementary Figure S6. The flow was driven by a body force applied to each solvent particle in the  $x$  direction, which mimics the pressure drop used in experiments. No cross flow in  $y$  direction in this periodic configuration is enforced by applying an adaptive force in  $y$  direction to mimic side walls of a real DLD device. The floor, ceiling, and pillar walls of the DLD device are modeled by a layer of frozen particles which share the same equilibrium structure as the suspending fluid. In order to prevent particles from penetrating the walls and mixing of the intra-cellular fluid and suspending medium, RBC vertices and fluid particles are subject to bounce-back reflections at walls and RBC membrane. Finally, in order to ensure no-slip boundary conditions at solid walls, an

adaptive tangential force is applied to fluid particles next to impenetrable surfaces. For more simulation details see Supplementary Information.

**Experimental methods.** Devices were fabricated by replica molding, using the same method and equipment as in previous work by Beech *et al.*<sup>13</sup>, and the post-manufacture details are outlined in Supplementary Information. The experimental devices consist of 13 consecutive sections of obstacle arrays, which are differentiated by different lateral shifts  $\Delta\lambda$ . The geometry of a DLD device<sup>5,13</sup> is defined by the post diameter  $D = 20\ \mu\text{m}$ , lateral center-to-center spacing between posts  $\lambda = 32\ \mu\text{m}$ , lateral shift in successive pillar rows  $\Delta\lambda$ , and the height between the two enclosing plates  $H$ , as shown in Supplementary Figure S1. Two devices with this geometry are used and can be distinguished by the distance between the top and bottom plates covering the obstacle arrays. One device has a height of  $H = 11\ \mu\text{m}$ , which is larger than a RBC diameter of about  $8\ \mu\text{m}$ , while the other device had  $H = 4\ \mu\text{m}$ , which is smaller than the RBC diameter but larger than the RBC thickness of about  $2\text{--}3\ \mu\text{m}$ .

The study was approved by the Review Board of Lund University and performed in accordance with the applicable guidelines and regulations. Blood was taken from healthy volunteers (informed consent was obtained from all subjects) via finger pricking and diluted in an autoMACS™ buffer to achieve a viscosity contrast  $C = 5$  environment. A Dextran-500 (#700013-096, VWR International LLC, PA, USA) solute was added at concentrations of 11%, 4.5%, and 1% in order to perform experiments at viscosity contrasts of  $C = 0.25, 1, \text{ and } 2$ , respectively. The solutions were driven through the devices at a pressure drop of 22 mbar. Running the simulations at a comparable pressure drop, we calculate the average fluid velocity to be about  $0.5\ \text{mm/s}$  for the thick device and  $0.12\ \text{mm/s}$  in the thin device. These values correspond to the physiological values for blood flow in capillaries.

## References

- Shapiro, H. M. *Practical flow cytometry* (John Wiley & Sons, New York, 2003).
- Miltenyi, S., Müller, W., Weichel, W. & Radbruch, A. High gradient magnetic cell separation with MACS. *Cytometry* **11**, 231–238 (1990).
- Huang, L. R., Cox, E. C., Austin, R. H. & Sturm, J. C. Continuous particle separation through deterministic lateral displacement. *Science* **304**, 987–990 (2004).
- Davis, J. A. *et al.* Deterministic hydrodynamics: taking blood apart. *Proc. Nat. Acad. Sci. USA* **103**, 14779–14784 (2006).
- Holm, S. H., Beech, J. P., Barrett, M. P. & Tegenfeldt, J. O. Separation of parasites from human blood using deterministic lateral displacement. *Lab Chip* **11**, 1326–1332 (2011).
- Loutherback, K. *et al.* Deterministic separation of cancer cells from blood at 10 ml/min. *AIP Advances* **2**, 042107 (2012).
- Devendra, R. & Drazer, G. Gravity driven deterministic lateral displacement for particle separation in microfluidic devices. *Anal. Chem.* **84**, 10621–10627 (2012).
- Inglis, D. W., Davis, J. A., Austin, R. H. & Sturm, J. C. Critical particle size for fractionation by deterministic lateral displacement. *Lab Chip* **6**, 655–658 (2006).
- Zeming, K. K., Ranjan, S. & Zhang, Y. Rotational separation of non-spherical bioparticles using I-shaped pillar arrays in a microfluidic device. *Nat. Commun.* **4**, 1625 (2013).
- Ranjan, S., Zeming, K. K., Jureen, R., Fisher, D. & Zhang, Y. Dld pillar shape design for efficient separation of spherical and non-spherical bioparticles. *Lab Chip* **14**, 4250–4262 (2014).
- Fedosov, D. A., Noguchi, H. & Gompper, G. Multiscale modeling of blood flow: from single cells to blood rheology. *Biomech. Model. Mechanobiol.* **13**, 239–258 (2014).
- Inglis, D. W. *et al.* Determining blood cell size using microfluidic hydrodynamics. *J. Immun. Meth.* **329**, 151–156 (2008).
- Beech, J. P., Holm, S. H., Adolfsen, K. & Tegenfeldt, J. O. Sorting cells by size, shape and deformability. *Lab Chip* **12**, 1048–1051 (2012).
- Quek, R., Le, D. V. & Chiam, K.-H. Separation of deformable particles in deterministic lateral displacement devices. *Phys. Rev. E* **83**, 056301 (2011).
- Zhu, L., Rorai, C., Mitra, D. & Brandt, L. A microfluidic device to sort capsules by deformability: a numerical study. *Soft Matter* **10**, 7705–7711 (2014).
- Krüger, T., Holmes, D. & Coveney, P. V. Deformability-based red blood cell separation in deterministic lateral displacement devices - a simulation study. *Biomicrofluidics* **8**, 054114 (2014).
- Fedosov, D. A., Peltomäki, M. & Gompper, G. Deformation and dynamics of red blood cells in flow through cylindrical microchannels. *Soft Matter* **10**, 4258–4267 (2014).
- Abkarian, M., Faivre, M. & Viallat, A. Swinging of red blood cells under shear flow. *Phys. Rev. Lett.* **98**, 188302 (2007).
- Dupire, J., Socol, M. & Viallat, A. Full dynamics of a red blood cell in shear flow. *Proc. Natl. Acad. Sci. USA* **109**, 20808–20813 (2012).
- Vitkova, V., Mader, M.-A., Polack, B., Misbah, C. & Podgorski, T. Micro-macro link in rheology of erythrocyte and vesicle suspensions. *Biophys. J.* **95**, L33–L35 (2008).
- Yazdani, A. Z. K. & Bagchi, P. Phase diagram and breathing dynamics of a single red blood cell and a biconcave capsule in dilute shear flow. *Phys. Rev. E* **84**, 026314 (2011).
- Tran-Son-Tay, R., Sutura, S. P. & Rao, P. R. Determination of red blood cell membrane viscosity from rheoscopic observations of tank-treading motion. *Biophys. J.* **46**, 65–72 (1984).
- Fischer, T. M. Shape memory of human red blood cells. *Biophys. J.* **86**, 3304–3313 (2004).
- Cantat, I. & Misbah, C. Lift force and dynamical unbinding of adhering vesicles under shear flow. *Phys. Rev. Lett.* **83**, 880–883 (1999).
- Abkarian, M., Lartigue, C. & Viallat, A. Tank treading and unbinding of deformable vesicles in shear flow: determination of the lift force. *Phys. Rev. Lett.* **88**, 068103 (2002).
- Messlinger, S., Schmidt, B., Noguchi, H. & Gompper, G. Dynamical regimes and hydrodynamic lift of viscous vesicles under shear. *Phys. Rev. E* **80**, 011901 (2009).
- Bowman, T., Frechette, J. & Drazer, G. Force driven separation of drops by deterministic lateral displacement. *Lab Chip* **12**, 2903–2908 (2012).
- Davis, J. A. Microfluidic separation of blood components through deterministic lateral displacement. Ph.D. thesis, Princeton University, USA (2008).
- Zhang, Z., Henry, E., Gompper, G. & Fedosov, D. A. Behavior of rigid and deformable particles in deterministic lateral displacement devices with different post shapes. *J. Chem. Phys.* **143**, 243145 (2015).
- Español, P. & Revenga, M. Smoothed dissipative particle dynamics. *Phys. Rev. E* **67**, 026705 (2003).
- Müller, K., Fedosov, D. A. & Gompper, G. Smoothed dissipative particle dynamics with angular momentum conservation. *J. Comp. Phys.* **281**, 301–315 (2015).

32. Discher, D. E., Boal, D. H. & Boey, S. K. Simulations of the erythrocyte cytoskeleton at large deformation. II. Micropipette aspiration. *Biophys. J.* **75**, 1584–1597 (1998).
33. Noguchi, H. & Gompper, G. Shape transitions of fluid vesicles and red blood cells in capillary flows. *Proc. Natl. Acad. Sci. USA* **102**, 14159–14164 (2005).
34. Fedosov, D. A., Caswell, B. & Karniadakis, G. E. A multiscale red blood cell model with accurate mechanics, rheology, and dynamics. *Biophys. J.* **98**, 2215–2225 (2010).

### Acknowledgements

We acknowledge the FP7-PEOPLE-2013-ITN LAPASO “Label-free particle sorting” for financial support. Dmitry A. Fedosov acknowledges funding by the Alexander von Humboldt Foundation. We also gratefully acknowledge a CPU time grant by the Jülich Supercomputing Center.

### Author Contributions

D.A.F., G.G. and J.O.T. designed research; E.H., Z.Z. and D.A.F. designed and performed simulations; E.H., S.H.H., Z.Z. and J.P.B. performed experiments; E.H. and D.A.F. analyzed the data; all authors discussed and interpreted results; all authors wrote the manuscript.

### Additional Information

**Supplementary information** accompanies this paper at <http://www.nature.com/srep>

**Competing financial interests:** The authors declare no competing financial interests.

**How to cite this article:** Henry, E. *et al.* Sorting cells by their dynamical properties. *Sci. Rep.* **6**, 34375; doi: 10.1038/srep34375 (2016).



This work is licensed under a Creative Commons Attribution 4.0 International License. The images or other third party material in this article are included in the article's Creative Commons license, unless indicated otherwise in the credit line; if the material is not included under the Creative Commons license, users will need to obtain permission from the license holder to reproduce the material. To view a copy of this license, visit <http://creativecommons.org/licenses/by/4.0/>

© The Author(s) 2016





# SUPPLEMENTARY INFORMATION

## Sorting cells by their dynamical properties

Ewan Henry<sup>1</sup>, Stefan H. Holm<sup>2</sup>, Zunmin Zhang<sup>1</sup>, Jason P. Beech<sup>2</sup>, Jonas O. Tegenfeldt<sup>2</sup>, Dmitry A. Fedosov<sup>1</sup>, and Gerhard Gompper<sup>1</sup>

<sup>1</sup> *Theoretical Soft Matter and Biophysics, Institute of Complex Systems and Institute for Advanced Simulation, Forschungszentrum Jülich, 52425 Jülich, Germany; Email: d.fedosov@fz-juelich.de, g.gompper@fz-juelich.de*

<sup>2</sup> *Division of Solid State Physics, NanoLund, Lund University, PO Box 118, S-221 00 Lund, Sweden; Email: jonas.tegenfeldt@ftf.lth.se*

### Contents

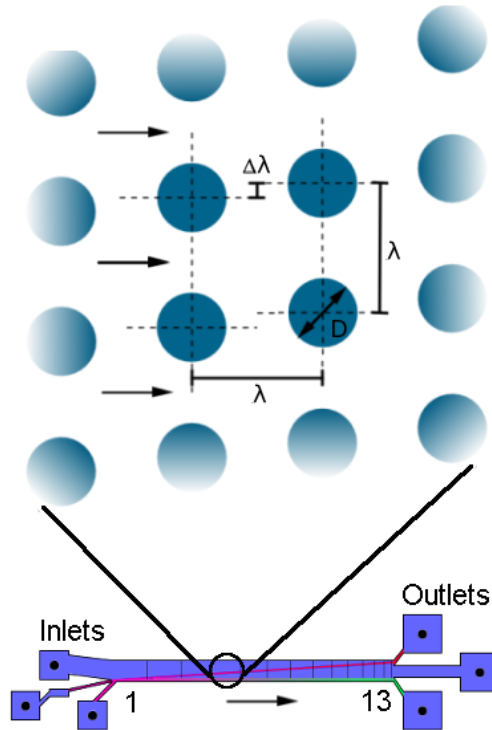
<b>1</b>	<b>Experimental materials and methods</b>	<b>1</b>
1.1	Device fabrication and design	1
1.2	Sample preparation	2
1.3	Data acquisition and analysis	3
<b>2</b>	<b>Numerical methods</b>	<b>5</b>
2.1	Fluid simulation - mesoscale hydrodynamics	5
2.2	Red blood cell model - triangulated surfaces	8
2.3	Simulation set-up and boundary conditions	9
<b>3</b>	<b>Supplementary videos</b>	<b>11</b>
3.1	Viscosity contrast $C = 5$	11
3.2	Viscosity contrast $C = 1$	11

## 1 Experimental materials and methods

### 1.1 Device fabrication and design

Devices were fabricated by replica molding, using the same method and equipment used in previous work by Beech *et al.* [1]. Adhesion of blood cells to the inner surface of our devices was reduced by formation of a polymer brush on the polydimethylsiloxane (PDMS). Immediately after O<sub>2</sub> plasma treatment and bonding, devices were filled with 0.2% PLL(20)-g[3.5]-PEG(2) (SuSoS AG, Dübendorf, Switzerland) and rinsed after 20 minutes with autoMACS™.

The experimental device has been designed to sort particles of different sizes, with successive sections within the device corresponding to different critical radii [2]. The device geometry [1,2] is defined by the post diameter  $D = 20 \mu\text{m}$ , lateral center-to-center spacing between posts  $\lambda = 32 \mu\text{m}$ , lateral shift in successive pillar rows  $\Delta\lambda$ , and the height between the two enclosing plates  $H$ , as shown in Supplementary Figure S1. The lateral shift can conveniently be defined as a fraction  $\epsilon$  of the post spacing  $\Delta\lambda = \epsilon\lambda$ . The experimental device consists of 13 consecutive sections of obstacle arrays, which are differentiated by the different lateral shifts  $\Delta\lambda$  between successive rows as summarized in Supplementary Table S1. We note that some of the sections have row-shift fractions  $\epsilon$  that are equivalent to  $M/N$ , where  $M$  and  $N$  are integers and  $M \neq 1$ , i.e. we have a "non-integer" row-shift fraction. This is due to limitations in the photomask fabricating process (a manufacturing grid of 200nm), which means that in many cases the desired integer row-shift fractions are not possible, in which case the nearest non-integer row-shift fraction is used. While non-integer row-shift fractions have been shown to give rise to two additional zig-zag modes with accompanying critical sizes [3, 4], in the present study these modes are not observed.



**Supplementary Figure S1: (top)** A close-up bird's eye view of the obstacle array. **(bottom)** Schematic of the sequential device with 13 sections, each with different  $\Delta\lambda$ . The flow direction is indicated by the arrows. Solution from the inlets on the left is carried by the flow within DLD to the right, where the particles of different sizes are collected at various outlets.

Two sequential devices have been used, distinguished by the distance between the top and bottom plates covering the obstacle arrays. One device had a height of  $H = 11 \mu\text{m}$ , which is larger than a RBC diameter of about  $8 \mu\text{m}$ , while the other device had  $H = 4 \mu\text{m}$ , which is smaller than the RBC diameter but larger than the RBC thickness of about  $2 - 3 \mu\text{m}$ . We will refer to these two devices as 'thick' and 'thin' DLDs, respectively.

Several inlets and outlets were employed to control flow and sample input/output, see Supplementary Figure S1. Both devices had one large fluid buffer inlet and one small buffer inlet to minimize the effects of walls and to create a well defined starting position to which total displacement can be compared. The sample inlet channel has been placed between the two buffer inlets and included a filter to remove any large particles which could cause clogging. A pressure gradient was used to drive the flow. Outlets were kept at atmospheric pressure and the overpressure at the inlets was maintained using a MFCS-4C pressure controller (Fluigent, Paris, France). Flow in the devices was driven by a pressure drop of 22 mbar between the buffer inlets and outlets.

## 1.2 Sample preparation

Blood was extracted from healthy volunteers via finger pricking. As mentioned in the paper, measurements were conducted both at a viscosity contrast of 5 and at a viscosity contrast of 1 between the cytosol and the surrounding

Section	$\Delta\lambda/\mu\text{m}$	$\epsilon$	$\frac{1}{\epsilon}$	Rows	$R_c/\mu\text{m}$
1	0.8	0.025	40	200	1.43
2	1.2	0.0375	80/3	130	1.74
3	1.6	0.05	20	100	2.0
4	2.0	0.0625	16	80	2.22
5	2.6	0.0813	160/13	60	2.52
6	3.2	0.1	10	50	2.78
7	3.8	0.1188	160/19	40	3.02
8	4.4	0.1375	80/11	35	3.24
9	5.2	0.1625	80/13	30	3.51
10	6.0	0.1875	16/3	25	3.76
11	6.8	0.2125	80/17	20	4.0
12	7.8	0.2438	160/39	20	4.27
13	8.8	0.275	40/11	15	4.52

**Supplementary Table S1:** Parameters defining the obstacle array geometry for each section of the DLD device.  $\Delta\lambda$  is the lateral shift between successive rows for each section,  $\epsilon = \Delta\lambda/\lambda$  is the section's shift fraction, and  $R_c$  is the critical particle size [5, 6]. The fourth column in the table specifies the number of rows in each section.

buffer. For high viscosity contrast measurements, the cells were suspended in autoMACS<sup>™</sup> running buffer (Miltenyi Biotec, Auburn, CA). This solution (pH 7.2) contains phosphate buffered saline (PBS) supplemented with 0.5% bovine serum albumin (BSA), 2 mM EDTA, and 0.09% azide. It acts to suppress blood clotting and is isotonic so it does not affect the cell shape due to a changed osmotic pressure. For low viscosity contrast measurements the autoMACS<sup>™</sup> running buffer was supplemented with Dextran-500 (# 700013-096, VWR International LLC, PA, USA). To measure the viscosity (see Supplementary Figure S2), Ubbelohde viscometers were used (UBBEL Visco, Paragon Scientific Ltd, UK.). The temperature ranged between 21.8-22.°C, which is similar to the measurements conducted with cells in the DLD device.

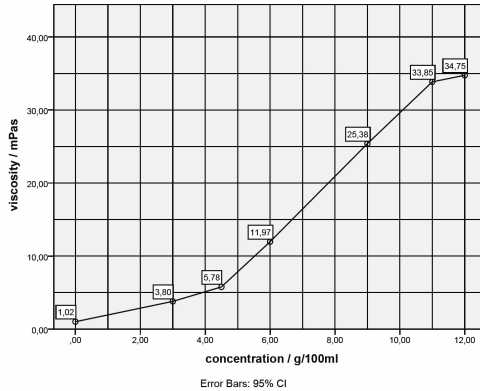
Dextran is widely used to change the viscosity of various samples. It is a neutral polysaccharide, i.e. the pH or salt concentration of the solution does not affect the resulting viscosity. In order to minimize the change to the osmotic pressure across the cell membrane, this larger Dextran molecule with an average molecular weight of 500 kDa was chosen. At a concentration of 11% the change in osmotic pressure is 0.22mM which is negligible compared to isotonic blood osmolarity of 300mM. Furthermore, microscopic examinations also confirmed that the low viscosity contrast samples did not visibly differ compared to the high viscosity contrast samples.

### 1.3 Data acquisition and analysis

All images were taken through an inverted Nikon Eclipse TE2000-U microscope (Nikon Corporation, Tokyo, Japan). High-speed images were taken using an EoSens mini MC-1370 camera (Mikrotron GmbH, Unterschleissheim, Germany). In all other cases an Andor iXon EMCCD camera (Andor Technology, Belfast, Northern Ireland) or Hamamatsu Orca Flash 4.0 (Hamamatsu, Shizuoka Pref., Japan) were used. Throughout the course of experiments, the dynamics and displacement of single RBCs in different device sections have been monitored.

The simultaneous transit of many RBCs through each section of the DLD device has been recorded to video using the microscope and camera set-ups previously described. Trajectories of individual RBCs were extracted from these recordings using the particle-tracking application MOSAIC in the image processing suite ImageJ [7]. Particle detection has been improved by subtracting a median average of all frames from the entire video and removing the background.

After extracting the sets of trajectories for different device sections from the video recordings, a pre-screening procedure has been performed. In the pre-screening process, trajectories which are too short or where direct interactions between RBCs have been detected, were discarded. As a rule of thumb, trajectories were considered to be too short if they were much shorter than the video domain, corresponding to RBC traversal over only a few pillars in the device. The short trajectories might be present at the beginning or the end of videos and also due to a detection failure if at some point video contrast becomes insufficient for tracking. The trajectories with direct interactions between RBCs



**Supplementary Figure S2:** Viscosity measurement of different dextran-500 concentrations in autoMACS. In order to achieve a viscosity contrasts of  $C = 2, 1$  and  $0.25$  between the medium and the cytosol, the suspending medium viscosity needed to be increased to two, five and twenty five times that of normal autoMACS buffer viscosity.

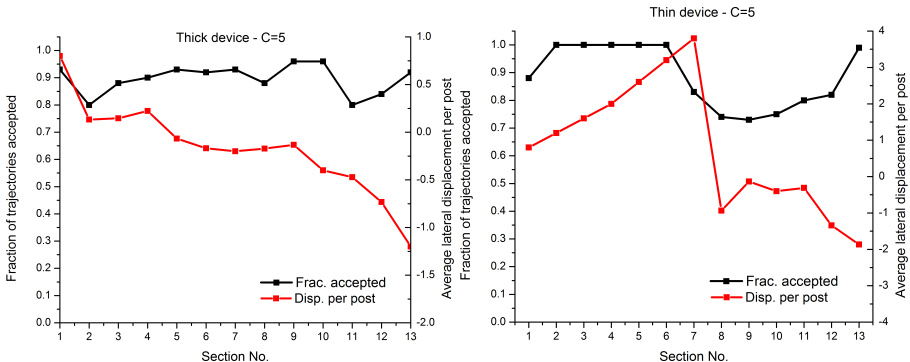
correspond to those where collisions between RBCs were detected. These trajectories were also excluded from further analysis, since such situation has not been considered in simulations.

In order to establish a common pattern followed by the RBCs in a given section of the device, all pre-screened trajectories were superimposed on top of one another and averaged into a single trajectory. Optimal positioning of trajectories for superposition has been found by the minimization of the Hausdorff distance between each member in the set of trajectories. The Hausdorff distance  $d_H(X, Y)$  between two sets  $(X, Y)$  of points in 2D Cartesian coordinates is defined as

$$d_H(X, Y) = \max\left\{ \sup_{x \in X} \inf_{y \in Y} d(x, y), \sup_{y \in Y} \inf_{x \in X} d(x, y) \right\}, \quad (1)$$

where *sup* denotes the supremum and *inf* the infimum.  $d_H(X, Y)$  can be thought of conceptually as the largest of all distances from a point in one set to the closest point in a second set. This method for the alignment of trajectories is very similar to techniques used in image-recognition algorithms [8]. In our algorithm, we have fixed a base trajectory in place, while a second trajectory traverses an overlaid grid to find the position with a minimum Hausdorff distance to the former trajectory. Additional refinement of the RBC trajectories has been done during this alignment stage, where some outliers were removed if computed  $d_H$  of a trajectory was larger than one standard deviation from the mean  $d_H$  value of all trajectories in the given section. These outliers can arise for multiple reasons, such as the presence of slightly different transit modes within one section (see Supplementary Figure S4), possible blockage between two posts (see Supplementary Figure S5), or even due to missing posts which might be due to some problems in device fabrication.

A summary of the RBC trajectory refinement for each device is shown in Supplementary Tables S2, S3, S4, and S5, where the numbers of total, accepted, and rejected trajectories are given for all experiments. Supplementary Figure S3 presents visually the fraction of accepted trajectories for the thick and thin devices at  $C = 5$ . Notice that the sections with lowest trajectory acceptance are those where the transition between displacement and zigzag modes is occurring, or where extremely negative zigzag modes with slight variations in row-swapping frequency result in large differences in lateral displacement per pillar. The possibility of different transit modes within a single section is illustrated in Supplementary Figure S4 for the section 11 of the thick device. 69 aligned trajectories yield a main average trajectory in this section with a displacement-zigzag pattern  $\{5, 4, 5, 4, 4, 5, 4\}$ , while 17 rejected trajectories seem to correspond to two other displacement-zigzag patterns  $\{5, 4, 4, 4, 5\}$  or  $\{5, 4, 5, 5, 4\}$ . The differences can arise from natural variations in RBC properties indicating that this section might be sensitive to them. However, it is also possible that the recorded trajectories are too short to properly capture the period of transit mode in section 11 and the displacement-zigzag



**Supplementary Figure S3:** (left) The fraction of trajectories accepted in each section of the thick device at  $C = 5$ . Note dips in the acceptance fraction which correspond to the transition from displacement to zig-zag and in later sections with relatively sensitive transit modes (see Supplementary Figure S4). (right) The fraction of trajectories accepted in each section of the thin device at  $C = 5$ . Note dip in the acceptance fraction corresponding to the transition from displacement to zigzag in sections 7-11 of the device. Note that the acceptance fractions for sections 2-5 are omitted as displacement-mode transit was evident from videos.

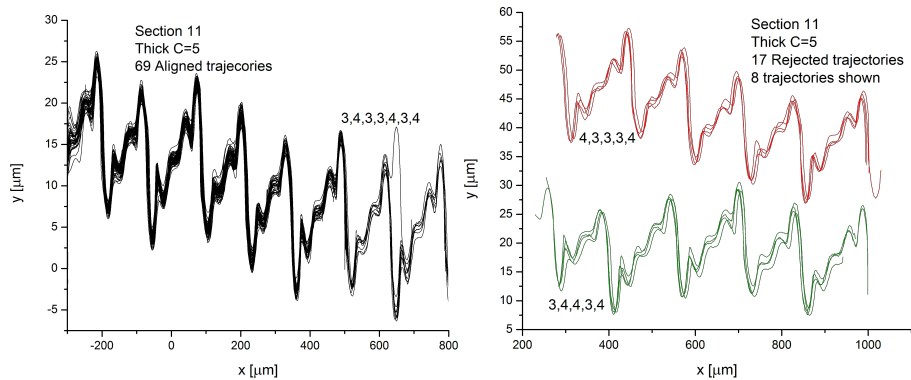
patterns above correspond to just portions of a full transit mode in this section. Currently, we cannot rule out one or another possibility. In addition, Supplementary Figure S5 illustrates a rejected trajectory, where a blockage between pillars has been detected. This example corresponds to a displacement mode and the sudden jump in the trajectory is due to the blockage of a single inter-pillar space identified visually from the video.

## 2 Numerical methods

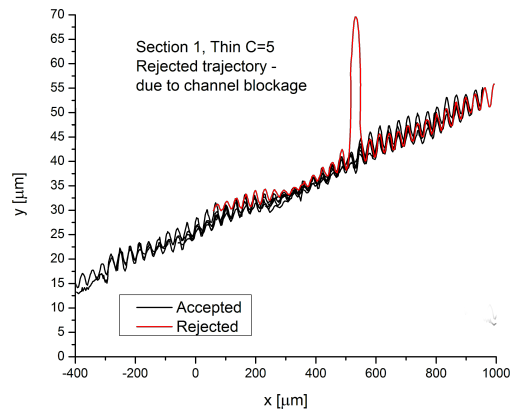
### 2.1 Fluid simulation - mesoscale hydrodynamics

To represent the suspending fluid, we employ a mesoscale hydrodynamic simulation approach which is a variation of the smoothed dissipative particle dynamics (SDPD) method [9], adapted to conserve angular momentum [10]. SDPD is a particle-based fluid-dynamics method [9] well suited to mesoscopic length scales. It improves upon the popular dissipative particle dynamic (DPD) method [11, 12], by incorporating the force scheme used in smoothed particle hydrodynamics [13, 14], which has been derived directly through the discretization of the Navier-Stokes (NS) equations. A caveat of the original SDPD method [9] is its violation of conservation of angular momentum caused by force components which act perpendicular to the inter-particle axis. Recent multi-particle collision dynamics simulations [15] and SDPD simulations [10] have demonstrated that conservation of angular momentum is necessary in order to properly describe the dynamics of two different fluid phases (e.g., extra- and intra-cellular fluids separated by a RBC membrane) in flow. Consequently, the original SDPD formulation has been extended to obtain a new SDPD+a method, which satisfies angular momentum conservation [10]. This method is necessary for accurate simulation of RBC dynamics in the DLD device.

A SDPD+a system contains  $N$  particles with mass  $m_i$ , moment of inertia  $I_i$ , position  $\mathbf{r}_i$ , translational velocity  $\mathbf{v}_i$ , and rotational velocity (or spin)  $\boldsymbol{\omega}_i$ . Discretization of the NS equation with spin [10] provides a set of pairwise forces



**Supplementary Figure S4:** (left) Example of the most prevalent trajectory in section 11 of the thick device at  $C = 5$ . 69 trajectories were aligned, showing the displacement-zigzag pattern  $\{5,4,5,4,4,5,4\}$ . (right) Illustration of the two minor populations of trajectories in section 11 of the thick device at  $C = 5$ . 17 rejected trajectories were aligned and found to either undergo the displacement-zigzag pattern  $\{5,4,4,4,5\}$  or  $\{5,4,5,5,4\}$ .



**Supplementary Figure S5:** A rejected trajectory due to a possible blockage between pillars.

Section	Total # of traj.	Rejected	Accepted	Accepted fraction	Average # of posts
1	27	2	25	0.93	46
2	25	5	20	0.8	67
3	17	2	15	0.88	37
4	10	1	9	0.9	30
5	15	1	14	0.93	27
6	12	1	11	0.92	26
7	28	2	26	0.93	25
8	25	3	22	0.88	32.2
9	23	1	22	0.96	28
10	50	2	48	0.96	22
11	86	17	69	0.80	22
12	134	21	113	0.84	19
13	97	8	89	0.92	14

**Supplementary Table S2:** The total number of RBC trajectories recorded in each section of the thick device at  $C = 5$  and the number of excluded and accepted trajectories. The average number of posts describes the average length of all accepted trajectories.

which include conservative (C), dissipative (D), rotational (R), and stochastic (S) terms as follows

$$\begin{aligned}
\mathbf{F}_{ij}^C &= \left( \frac{p_i}{\rho_i^2} + \frac{p_j}{\rho_j^2} \right) w_{ij} \mathbf{r}_{ij}, \\
\mathbf{F}_{ij}^D &= -\gamma_{ij} \left( \mathbf{v}_{ij} + \frac{(\mathbf{v}_{ij} \cdot \hat{\mathbf{r}}_{ij}) \hat{\mathbf{r}}_{ij}}{3} \right) + \frac{2\gamma_{ij}}{3} (\mathbf{v}_{ij} \cdot \hat{\mathbf{r}}_{ij}) \hat{\mathbf{r}}_{ij}, \\
\mathbf{F}_{ij}^R &= -\gamma_{ij} \frac{\mathbf{r}_{ij}}{2} \times (\boldsymbol{\omega}_i + \boldsymbol{\omega}_j), \\
\mathbf{F}_{ij}^S &= \sigma_{ij} \left( d\overline{\mathbf{W}}_{ij}^s + \frac{1}{3} \text{tr}[d\mathbf{W}_{ij}] \mathbb{1} \right) \cdot \frac{\hat{\mathbf{r}}_{ij}}{dt},
\end{aligned} \tag{2}$$

where  $p_i$  and  $p_j$  are local particle pressures given by the equation of state  $p = p_0 (\rho/\rho_0)^\alpha - b$ , with  $p_0$ ,  $\rho_0$ ,  $\alpha$ , and  $b$  being selected model parameters [10, 14]. Particle density  $\rho$  is calculated locally as  $\rho_i = \sum_j W_L(r_{ij})$ , where  $W_L(r) = \frac{105}{16\pi r_c^3} \left(1 + 3\frac{r}{r_c}\right) \left(1 - \frac{r}{r_c}\right)^3$  is the Lucy function [13] and  $r_c$  is the cut-off radius. The weight function  $w(r)$  is calculated by  $\nabla W_L(r) = -r w(r)$ , such that  $w_{ij} = w(r_{ij})$ . The coefficients  $\gamma_{ij}$  and  $\sigma_{ij}$  determine the strength of the dissipative and random forces, where the friction coefficient  $\gamma_{ij}$  is defined as

$$\gamma_{ij} = \frac{20\eta_0}{7} \frac{w_{ij}}{\rho_i \rho_j}, \tag{3}$$

with  $\eta_0$  being the desired dynamic viscosity. The random force coefficient is  $\sigma_{ij} = 2\sqrt{k_B T \gamma_{ij}}$ , while  $\text{tr}[d\mathbf{W}_{ij}]$  and  $d\overline{\mathbf{W}}_{ij}^s$  refer to the trace of a random matrix of independent Wiener increments  $d\mathbf{W}_{ij}$  and its traceless symmetric part, respectively. For a formal derivation of these equations, the reader is referred to Ref. [10].

Newton's second law of motion governs the time evolution of the  $i$ -th particle's position, translational velocity, and rotational velocity as follows

$$\dot{\mathbf{r}}_i = \mathbf{v}_i, \quad \dot{\mathbf{v}}_i = \frac{1}{m_i} \sum_j \mathbf{F}_{ij}, \quad \dot{\boldsymbol{\omega}}_i = \frac{1}{I_i} \sum_j \mathbf{N}_{ij}, \tag{4}$$

where  $\mathbf{N}_{ij} = \frac{1}{2} \mathbf{r}_{ij} \times \mathbf{F}_{ij}$  is the torque exerted on particle  $i$  by particle  $j$ . The equations of motion are integrated using the velocity-Verlet algorithm [16].

Section	Total # of traj.	Rejected	Accepted	Accepted fraction	Average # of posts
1	8	1	7	0.88	28
2	-	-	-	-	-
3	-	-	-	-	-
4	-	-	-	-	-
5	-	-	-	-	-
6	15	0	15	1.0	23
7	23	4	19	0.83	29
8	39	10	29	0.74	16
9	26	7	19	0.73	15
10	20	5	15	0.75	15
11	40	8	32	0.8	15
12	17	3	14	0.82	16
13	71	1	70	0.99	11

**Supplementary Table S3:** The total number of RBC trajectories recorded in each section of the thin device at  $C = 5$  and the number of excluded and accepted trajectories. The average number of posts corresponds to the average length of all accepted trajectories. Note that values for sections 2-5 are omitted as displacement-mode transit was evident from videos and there was no need for alignment.

## 2.2 Red blood cell model - triangulated surfaces

The RBC membrane is modeled as a triangulated network of springs [17–21], whose vertices are coupled to the fluid via frictional forces. A total of  $N_v$  particles constitute the mesh vertices and  $N_s = 3(N_v - 2)$  springs follow the edges of the mesh, reproducing the elasticity of the membrane ( $U_{sp}$ ). A total of  $N_t = 2N_v - 4$  triangles make up the entire membrane surface and incident triangles have an associated potential energy ( $U_{bend}$ ) given by the angle between them, associated with membrane bending rigidity. Furthermore, local and global area constraints ( $U_{area}$ ) are enforced along with a global volume constraint ( $U_{vol}$ ). Formally, the total energy of a RBC is given as

$$U_{tot} = U_{sp} + U_{bend} + U_{area} + U_{vol}. \quad (5)$$

The total contribution of springs is given by

$$U_{sp} = \sum_{j \in 1 \dots N_s} \left[ \frac{k_B T l_m (3x_j^2 - 2x_j^3)}{4\zeta(1 - x_j)} + \frac{k_p}{l_j} \right], \quad (6)$$

where  $l_j$  is the length of spring  $j$ ,  $l_m$  is the maximum permitted spring extension,  $x_j = l_j/l_m$  is the fractional extension towards maximum length,  $\zeta$  is the persistence length, and  $k_p$  is the spring constant. The equilibrium length of each spring  $l_{0j}$  is set in accordance with an initial triangulated mesh of a stress-free biconcave RBC shape [20, 21].

The membrane bending rigidity in absence of spontaneous curvature is described by a bending energy

$$U_{bend} = \sum_{j \in 1 \dots N_s} k_b [1 - \cos \theta_j], \quad (7)$$

where  $k_b$  is the bending constant and  $\theta_j$  is the instantaneous angle between the two triangles incident on edge  $j$ .

Finally, the area and volume constraints are accounted for by two potentials:

$$U_{area} = k_a \frac{(A - A_r)^2}{2A_r} + \sum_{j \in 1 \dots N_t} k_d \frac{(A_j - A_j^0)^2}{2A_j^0}, \quad U_{vol} = k_v \frac{(V - V_r)^2}{2V_r}, \quad (8)$$

where  $k_a$ ,  $k_d$ , and  $k_v$  are the global area, local area, and volume constraint coefficients, respectively.  $A$  is the instantaneous surface area of the membrane,  $A_j$  is the instantaneous area of the  $j$ -th triangle in the network, and  $V$  is the



Section	Total # of traj.	Rejected	Accepted	Accepted fraction	Average # of posts
1	14	0	14	1.0	31
3	12	2	10	0.83	37
4	29	5	24	0.83	25
5	13	2	11	0.85	41
6	13	27	0	1.0	27
7	37	1	36	0.97	37
8	31	7	25	0.78	23
9	96	0	96	1.0	28
11	38	6	32	0.84	21
13	97	8	89	0.92	31

**Supplementary Table S4:** The total number of RBC trajectories recorded in each section of the thick device at  $C = 1$  and the number of excluded and accepted trajectories. The average number of posts describes the average length of all accepted trajectories.

Section	Total # of traj.	Rejected	Accepted	Accepted fraction	Average # of posts
1	13	1	12	0.92	38
2	16	2	14	0.88	43
3	12	1	11	0.92	31
4	41	6	35	0.85	39
5	17	4	13	0.76	48
9	45	4	41	0.91	22
11	5	1	4	0.8	21

**Supplementary Table S5:** The total number of RBC trajectories recorded in each section of the thick device at  $C = 0.25$  and the number of excluded and accepted trajectories. The average number of posts describes the average length of all accepted trajectories.

instantaneous RBC volume. The desired total surface area  $A_r$ , individual triangle area  $A_j^0$ , and interior volume  $V_r$  are set in accordance with the initial triangulation [20, 21].

We relate the RBC model's variables to physical macroscopic properties of the RBC membrane by linear analysis for a regular hexagonal network [20, 21]. The membrane shear modulus is related to the spring variables by

$$\mu_0 = \frac{\sqrt{3}k_B T}{4\zeta l_m x_0} \left( \frac{x_0}{2(1-x_0)^3} - \frac{1}{4(1-x_0)^2} + \frac{1}{4} \right) + \frac{3\sqrt{3}k_p}{4l_0^3}, \quad (9)$$

with  $x_0 = l_0/l_m$ . The area-compression  $K$  and Young's  $Y$  moduli are found as  $K = 2\mu_0 + k_a + k_d$  and  $Y = \frac{4K\mu_0}{K+\mu_0}$ . The Helfrich model is employed to describe the bending coefficient  $k_b$  in terms of macroscopic bending rigidity  $\kappa$  [22], yielding  $k_b = 2\kappa/\sqrt{3}$ . The value of  $x_0$  is set to 2.2 for all springs [21].

### 2.3 Simulation set-up and boundary conditions

The floor, ceiling, and pillar walls of the DLD device are modeled by a layer of frozen particles with a thickness of  $r_c$  which share the same equilibrium structure as the suspending fluid. This ensures that all particle interactions occurring in the locality of boundaries do not display artifacts (e.g., particle density variations) which could arise in the absence of wall particles due to an improper distribution of conservative forces. Furthermore, the wall particles are included in calculation of fluid particle densities  $\rho$  near the wall.

Section	Total # of traj.	Rejected	Accepted	Accepted fraction	Average # of posts
1	14	2	12	0.86	27
3	6	0	6	1.0	45
5	13	0	13	1.0	28
7	11	0	11	1.0	12
9	23	2	21	0.91	9

**Supplementary Table S6:** The total number of RBC trajectories recorded in each section of the thin device at  $C = 2$  and the number of excluded and accepted trajectories. The average number of posts corresponds to the average length of all accepted trajectories.

In order to prevent particles from penetrating the walls, RBC vertices and fluid particles are subject to bounce-back reflections at walls. Bounce-back reflections are preferred over specular reflections as they achieve a better approximation of no-slip boundary conditions (BCs) at the wall. Finally, to fully guarantee no-slip BCs at the walls, an adaptive tangential force is applied to fluid particles within a distance  $r_c$  from the walls [23].

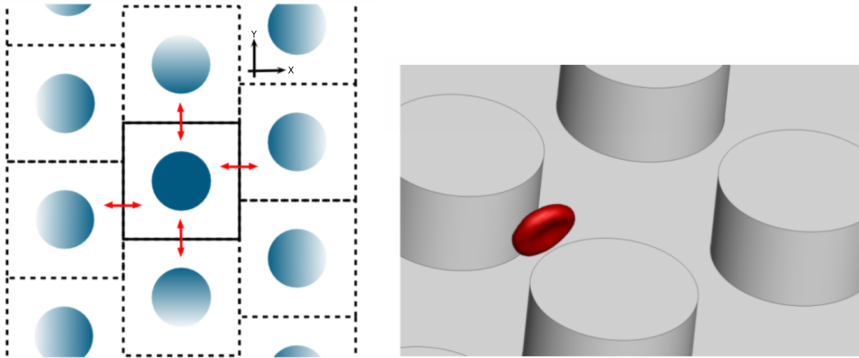
To prevent mixing between intra- and extra-cellular fluids, bounce-back reflections for the solvent particles are also introduced at a RBC membrane. Furthermore, the RBC is coupled to fluid flow via viscous friction between the  $N_v$  mesh vertices and local fluid particles. The dissipative and random force components of the DPD method are used to achieve these interactions [20]. No-slip BCs at membrane vertices are enforced by careful selection of the friction parameter  $\gamma$  in the dissipative force  $\mathbf{F}^D$ . A fluid sheared over the effective surface of a membrane vertex exerts a friction force on the membrane given as  $\mathbf{F}_v = \int_{V_h} n g(r) \mathbf{F}^D dV$ , where  $n$  is the fluid number density,  $g(r)$  is the radial distribution function of fluid particles about the membrane vertices, and  $V_h$  is the hemisphere volume of fluid situated above the vertex. Equating this integral to the total force required by a continuum hydrodynamical description leads to an expression for the calculation of  $\gamma$  [20].

The bumper array is simulated using a 3D domain enclosing a single-column obstacle with its axis in the  $z$  direction, perpendicular to the roof and floor of the domain box, as shown in Supplementary Figure. S6. Efficient representation of an infinite bumper array environment is achieved with periodic BCs in the  $x$  and  $y$  directions and a shift in the  $y$  direction for each boundary-crossing event in the  $x$  direction. The assumption of an infinite obstacle array neglects any effects induced by the walls at either edge of the device. The missing wall effects are revealed by solving the NS equation for a bumper array in 2D with explicit wall-edge boundaries. We find that the edge walls enforce a zero net flow in the  $y$  direction. This condition is recreated in the 3D infinite array using an adaptive force applied to solvent particles such that the net flow in the  $y$  direction vanishes.

Simulations are performed for every section of the device, altering the lateral shift  $\Delta\lambda$  induced at the periodic boundary to correspond with a specific section of the experimental device, as shown in Supplementary Table S1. This gives us a total of 13 trajectories for a single RBC transit through the 13 sections of each thin ( $H = 4\ \mu\text{m}$ ) and thick ( $H = 11\ \mu\text{m}$ ) device.

Establishing standard length and energy scales allows us to relate most simulation parameters to physical RBC properties. We use the RBC membrane area to define an effective RBC diameter  $D_r = \sqrt{A_r/\pi}$  and an average bond length for a given number of vertices  $l_0^2 = \frac{4\sqrt{3}A_r}{3N_t}$ . The experimental value for an average healthy RBC's surface area  $A_r = 133.5 \times 10^{-12}\ \text{m}^2$  [24] suggests a  $D_r = 6.5\ \mu\text{m}$ . For time scaling, we define a characteristic RBC relaxation time  $\tau = \eta_o D_r^3 / \kappa_r$ , where  $\eta_o$  is the suspending fluid viscosity and  $\kappa_r$  is the RBC membrane bending rigidity. The parameters used for the RBC model are summarized within Supplementary Table S6 in units of  $D_r$  and the thermal energy  $k_B T$ ; along side we present the corresponding average values for a healthy RBC in physical units.

The SDPD+a fluid parameters are given in Supplementary Table S7. The average distance between RBC vertices  $l_0$  is chosen as the length scale, which has a value of  $l_0 = 0.4$  in simulations. The exponent  $\alpha$  in the equation of state takes the value  $\alpha = 7$  and the SDPD equilibrium density  $\rho_0 = n$ , where  $n = 9$  is the fluid's number density. The speed of sound for the equation of state is given as  $c^2 = p_0 \alpha / \rho_0$  and the Mach number has been kept below 0.1 in all simulations, ensuring a good approximation for incompressible fluid flow.



**Supplementary Figure S6:** (left) Top-down schematic of the simulated domain. The solid lines enclose a square of the simulation domain and the dotted lines denote the periodic BCs with a shift in the  $y$  direction. (right) A snapshot of a simulated RBC in the obstacle array.

### 3 Supplementary videos

In order to best demonstrate the differences in RBC dynamics for cells with viscosity contrasts  $C = 5$  and  $C = 1$ , we present several videos of simulated and experimental RBC transit in sections 4 and 11 of the *thick* device.

#### 3.1 Viscosity contrast $C = 5$

The three videos “SIM\_Sec4Cont5.avi”, “EXP\_Sec4Cont5.avi”, and “SIM\_Sec11Cont5.avi” show the behavior of simulated and experimental RBCs traveling through sections 4 and 11 of the *thick* device in a suspending medium which is five times less viscous than the intracellular fluid. Notice that row-swapping events occur; the RBCs are in a zig-zag mode. The RBCs display tumbling dynamics, which is especially prevalent before and after row-swapping events.

#### 3.2 Viscosity contrast $C = 1$

The other two videos “SIM\_Sec4Cont1.avi” and “EXP\_Sec4Cont1.avi” also show the simulated and experimental RBCs traveling through section 4 of the thick device. However, the inner and outer fluids have the same viscosity and as a result, we see RBCs traveling in displacement modes without zig-zagging. The RBCs tumble to a lesser degree and there are clear local deformations as the cell membrane rearranges itself in a tank treading motion.

### References

- [1] J. P. Beech, S. H. Holm, K. Adolfsson, and J. O. Tegenfeldt. Sorting cells by size, shape and deformability. *Lab Chip*, 12:1048–1051, 2012.
- [2] S. H. Holm, J. P. Beech, M. P. Barrett, and J. O. Tegenfeldt. Separation of parasites from human blood using deterministic lateral displacement. *Lab Chip*, 11:1326–1332, 2011.
- [3] B. R. Long, M. Heller, J. P. Beech, H. Linke, H. Bruus, and J. O. Tegenfeldt. Multidirectional sorting modes in deterministic lateral displacement devices. *Phys. Rev. E*, 78:046304, 2008.
- [4] J. Frechette and G. Drazer. Directional locking and deterministic separation in periodic arrays. *J. Fluid Mech.*, 627:379–401, 2009.

RBC parameters	Scaled units	Physical units
$N_v$	1000	
$A_r$		$133.5 \times 10^{-12} \text{ m}^2$
$D_r$	$\sqrt{A_r/\pi}$	$6.5 \times 10^{-6} \text{ m}$
$l_0$	$0.061 D_r$	$3.91 \times 10^{-7} \text{ m}$
$V_r$	$0.34 D_r^3$	$93.1 \times 10^{-18} \text{ m}^3$
$T$		310 K
$Y_r$	$1.82 \times 10^5 \frac{k_B T}{D_r^2}$	$18.9 \times 10^{-6} \text{ N/m}$
$\kappa_r$	$70 k_B T$	$3 \times 10^{-19} \text{ J}$
$k_d$	$4.2 \times 10^4 \frac{k_B T}{D_r^2}$	$4.3 \times 10^{-6} \text{ N/m}$
$k_a$	$2.1 \times 10^6 \frac{k_B T}{D_r^2}$	$2.1 \times 10^{-4} \text{ N/m}$
$k_v$	$1.4 \times 10^7 \frac{k_B T}{D_r^3}$	$220 \text{ N/m}^2$

**Supplementary Table S7:** Parameters defining the model values used for the RBC properties and their physical equivalents.  $N_v$  is the number of membrane vertices,  $A_r$  is the RBC membrane area,  $l_0$  is the average bond length,  $V_r$  is the RBC volume,  $T$  is the temperature,  $Y_r$  is the membrane Young's modulus,  $\kappa_r$  is the membrane bending rigidity, and  $k_d$ ,  $k_a$ , and  $k_v$  are the local area, global area, and volume constraint coefficients, respectively. In all simulations, we have chosen  $A_r = 133.5$  and  $k_B T = 0.4$ , which implies that  $D_r = 6.5$  and  $l_0 = 0.4$ .

Fluid parameters	Scaled units	Physical units
$p_0$	$16 \frac{k_B T}{l_0^3}$	1.07 Pa
$b$	$12.8 \frac{k_B T}{l_0^3}$	0.86 Pa
$\eta_o$	$25.3 \frac{\sqrt{m k_B T}}{l_0^2}$	$1.2 \times 10^{-3} \text{ Pa} \cdot \text{s}$
$\eta_i$	$25.3, 126.6 \frac{\sqrt{m k_B T}}{l_0^2}$	$6 \times 10^{-3} \text{ Pa} \cdot \text{s}$
$k_B T$		$4.282 \times 10^{-21} \text{ J}$

**Supplementary Table S8:** Parameters defining the model values used for the fluid properties and their physical equivalents. Mass and length for SDPD+a fluid are measured in units of the fluid particle mass  $m$  and the membrane bond length  $l_0$ .  $p_0$  and  $b$  are parameters for the pressure equation, and  $\eta_o$  and  $\eta_i$  are the extra- and intra-cellular fluid dynamic viscosities, respectively. In all simulations, we have set  $m = 1$ ,  $l_0 = 0.4$ , and the thermal energy  $k_B T = 0.4$ .

- [5] L. R. Huang, E. C. Cox, R. H. Austin, and J. C. Sturm. Continuous particle separation through deterministic lateral displacement. *Science*, 304:987–990, 2004.
- [6] D. W. Inglis, J. A. Davis, R. H. Austin, and J. C. Sturm. Critical particle size for fractionation by deterministic lateral displacement. *Lab Chip*, 6:655–658, 2006.
- [7] C. A. Schneider, W. S. Rasband, and K. W. Eliceiri. Real-time deformability cytometry: on-the-fly cell mechanical phenotyping. *Nat. Methods*, 9:671–675, 2012.
- [8] D. P. Huttenlocher, G. A. Klanderman, and W. J. Rucklidge. Comparing images using the Hausdorff distance. *IEEE T. Pattern Anal.*, 15:850–863, 1993.
- [9] P. Español and M. Revenga. Smoothed dissipative particle dynamics. *Phys. Rev. E*, 67:026705, 2003.
- [10] K. Müller, D. A. Fedosov, and G. Gompper. Smoothed dissipative particle dynamics with angular momentum conservation. *J. Comp. Phys.*, 281:301–315, 2015.
- [11] P. J. Hoogerbrugge and J. M. V. A. Koelman. Simulating microscopic hydrodynamic phenomena with dissipative particle dynamics. *Europhys. Lett.*, 19:155–160, 1992.
- [12] P. Español and P. Warren. Statistical mechanics of dissipative particle dynamics. *Europhys. Lett.*, 30:191–196, 1995.

- [13] L. B. Lucy. A numerical approach to the testing the fission hypothesis. *Astronom. J.*, 82:1013–1024, 1977.
- [14] J. J. Monaghan. Smoothed particle hydrodynamics. *Annu. Rev. Astron. Astrophys.*, 30:543–574, 1992.
- [15] I. O. Götze, H. Noguchi, and G. Gompper. Relevance of angular momentum conservation in mesoscale hydrodynamics simulations. *Phys. Rev. E*, 76:046705, 2007.
- [16] M. P. Allen and D. J. Tildesley. *Computer simulation of liquids*. Clarendon Press, New York, 1991.
- [17] G. Gompper and D. M. Kroll. Network models of fluid, hexatic and polymerized membranes. *J. Phys.: Condens. Matter*, 9:8795–8834, 1997.
- [18] D. E. Discher, D. H. Boal, and S. K. Boey. Simulations of the erythrocyte cytoskeleton at large deformation. II. Micropipette aspiration. *Biophys. J.*, 75:1584–1597, 1998.
- [19] H. Noguchi and G. Gompper. Shape transitions of fluid vesicles and red blood cells in capillary flows. *Proc. Natl. Acad. Sci. USA*, 102:14159–14164, 2005.
- [20] D. A. Fedosov, B. Caswell, and G. E. Karniadakis. A multiscale red blood cell model with accurate mechanics, rheology, and dynamics. *Biophys. J.*, 98:2215–2225, 2010.
- [21] D. A. Fedosov, B. Caswell, and G. E. Karniadakis. Systematic coarse-graining of spectrin-level red blood cell models. *Comput. Meth. Appl. Mech. Eng.*, 199:1937–1948, 2010.
- [22] W. Helfrich. Elastic properties of lipid bilayers: theory and possible experiments. *Z. Naturforschung C*, 28:693–703, 1973.
- [23] D. A. Fedosov and G. E. Karniadakis. Triple-decker: Interfacing atomistic-mesoscopic-continuum flow regimes. *J. Comp. Phys.*, 228:1157–1171, 2009.
- [24] E. A. Evans and R. Skalak. *Mechanics and thermodynamics of biomembranes*. CRC Press, Inc., Boca Raton, Florida, 1980.



Paper V







# Concentration Effects in Deterministic Lateral Displacement Devices

Stefan H. Holm<sup>1</sup>, Zunmin Zhang<sup>2</sup>, Jason P. Beech<sup>1</sup>, Gerhard Gompper<sup>2</sup>, Dmitry A. Fedosov<sup>2</sup>  
and Jonas O. Tegenfeldt<sup>1</sup>

1. Department of Physics and NanoLund at Lund University, Lund, SWEDEN

2. Forschungszentrum Jülich, Jülich, GERMANY

## Abstract

An important step in diagnostics is the isolating of cells and microorganisms of interest from blood. Since these bioparticles are often present at very low concentrations, throughput needs to be as high as possible. In addition, to ensure simplicity, methods requiring a minimum of sample preparation are advantageous. Sorting schemes that function for whole blood are therefore highly interesting. Deterministic lateral displacement (DLD) has proven to be highly precise and versatile in terms of a wide range of sorting parameters. We have performed measurements and simulations on the trajectories of particles moving through DLD arrays in a background of blood at a range of flow velocities and concentrations ranging from pure buffer to whole blood. We find that the DLD in principle works as expected with particles following predictable trajectories. We find that increased flow rates can be used to alleviate the deleterious effects of the high concentration of blood cells. Our work opens up for sorting schemes combining the high precision and versatility afforded by DLD with whole blood sorting.

## Introduction

Blood separation is an important tool in biomedicine. Blood is relatively easy and painless to sample from a patient, and it contains a plethora of biological markers ranging from electrolytes, signaling molecules, proteins and nucleic acids to viruses, cells and microorganisms. To minimize confounding effects of irrelevant cells or to enrich the bioparticles of interest, the blood must be sorted. This is typically done using centrifugation. It is a simple and well-established technique, but it requires large sample volumes and it is not amenable to integration in lab-on-a-chip devices.

To simplify analysis and to decrease the amount of sample needed, several microfluidic approaches have been developed. Acoustophoresis and inertial focusing offer high throughput but require diluted samples. Margination is an interesting approach that mimics the leukocyte migration in small blood capillaries. It works best at whole blood concentrations and it has been demonstrated to separate out harder infected blood cells for malaria detection. However, it is quite limited in scope.

DLD on the other hand has been shown to be a highly versatile mechanism for particle sorting in microfluidics[1], with detailed understanding of underlying mechanisms and characterization of critical size[2]. While the first paper demonstrated highly precise sorting of microspheres as a function of size, and sorting of large DNA molecules, subsequent developments have demonstrated sorting with respect to *e.g.* shape, deformability and dielectric properties. The resolution is excellent and through parallelization and high applied pressures throughput has been extended to 10mL/min[3].

The first separations performed on blood [4] showed the relevance of DLD for diagnostics.

Subsequent work has demonstrated sorting of many biologically and diagnostically relevant separations [4-27].

The combined efforts of the field have given a greater understanding of the effects of device geometry [1, 2, 10, 12, 24, 26, 28-39] and particle properties [4, 10, 12, 16, 21, 22, 24, 27, 30, 31, 33, 40-45]. As stated by Davis and Huang [1, 4] increasing the Peclet number by increasing flow velocities tends to improve the resolution of separations because it decreases the influence of diffusion but, as first discussed by Davis [4] and later shown by Beech [12] sufficiently high shear forces at high flow rates deform soft particles, changing their effective size. Without prior knowledge of these effects it can be hard to design specific devices with the desired outcomes.

A question that remains largely unexplored is the effect of particle concentration on the performance of these devices. Feng *et al* developed modifications to devices that allowed for increased particle concentrations during enrichment [46]. Vernekar and Krüger performed 3D simulations of RBCs that showed that the trajectories of RBCs in DLD devices are affected by their concentration [47]. However, most commonly the challenge at hand is how to sort various cells and particles from the huge background of RBCs. To optimize sorting of particles in whole blood it is necessary to understand how the trajectories of particles moving through a DLD array are affected by the concentration of RBC in the surrounding medium, i.e. how are the trajectories of particles of interest in DLD affected by the hematocrit of the sample.

## Results and Discussion

### *Proof of principle*

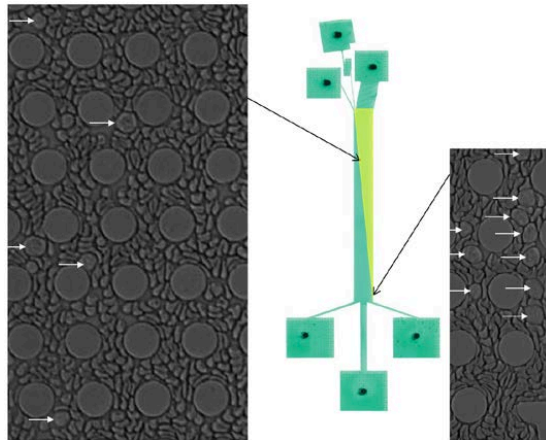


Figure 1. Enrichment of leukocytes in whole blood (45% hematocrit). Left image shows an elevated concentration of leukocytes in the middle of the device and the right image shows the larger concentration at the end. Leukocytes are highlighted by white arrows. For scale the posts are 20 $\mu$ m.

To demonstrate the usefulness of sorting of DLD at high hematocrit we first show that leukocytes are readily enriched using a standard DLD and whole blood, Figure 1. The DLD device consists of 13 separate sections with a critical size ranging from 3  $\mu$ m to 9  $\mu$ m in steps of 0.5  $\mu$ m. Posts are 20 $\mu$ m in diameter and the gaps are 12 $\mu$ m. Full details of this device can be found in [10]. A rough estimate based on counting WBCs and RBCs at the end of the device, gives us an approximate ratio of 1 WBC per 5 RBCs. Compared to the approximate ratio in whole blood, 1 WBC per 1000 RBCs, this equates to an enrichment factor of about 200.

Running polystyrene microspheres ( $4.87\pm 0.28\mu$ m, Polysciences Inc, USA, with concentration of 0.01% (v/v)) in the same device at hematocrits ranging from 0% to roughly 10%, it is clear

that the effective size of the particle decreases as the concentration is increased, i.e. we see a decrease in displacement index.

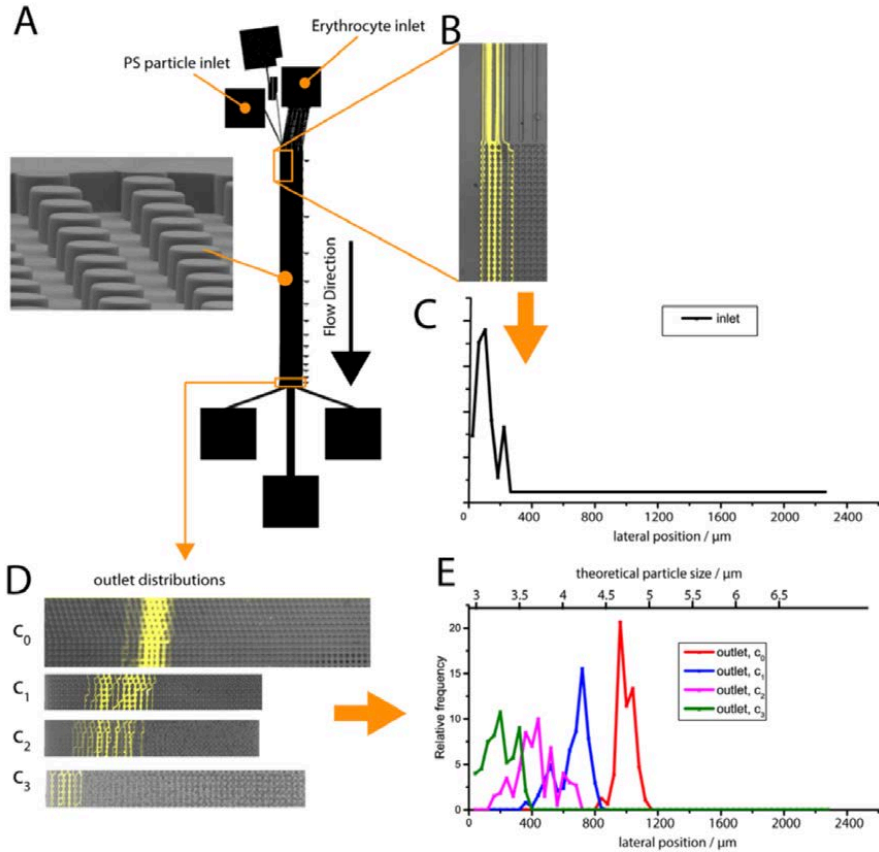


Figure 2. Overview of the DLD device, showing the overall design with three inlets and three outlets together with the SEM characterization of the posts in the separation array which reveals  $15\mu\text{m}$  high posts with near ideal vertical walls. (A) The polystyrene particles are injected from a single inlet while the erythrocytes, on the other hand, are injected both mixed with the particles and in the two other inlets. The inlet distributions (B-C) and outlet distributions (D-E) are given for various concentrations of erythrocytes,  $c_0 = 0$ ,  $c_1 = 10^5 \mu\text{L}^{-1}$ ,  $c_2 = 5 \cdot 10^5 \mu\text{L}^{-1}$ ,  $c_3 = 10^6 \mu\text{L}^{-1}$ , corresponding to whole blood diluted 50X, 10X and 5X respectively. The higher the concentration, the smaller the effective size of the polystyrene beads.

### Careful experimental characterization

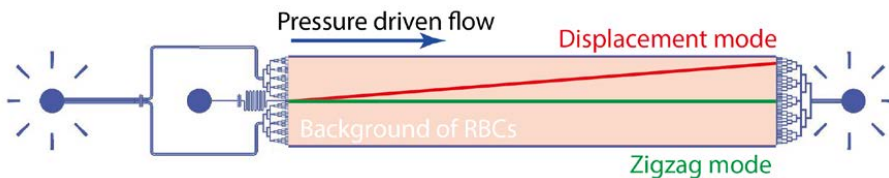


Figure 3 Our device and measurement concept.

More detailed measurements were conducted using a novel device (Figure 3) with just one section (post diameter  $20\mu\text{m}$ , gap size  $16\mu\text{m}$ , periodicity  $N = 15$  and a critical diameter of  $D_c = 6.11\mu\text{m}$ ). The device has two inlets: one central inlet for the microspheres and one inlet

for the blood. The latter is guided to two wide flow streams on either side of the particle flow stream.

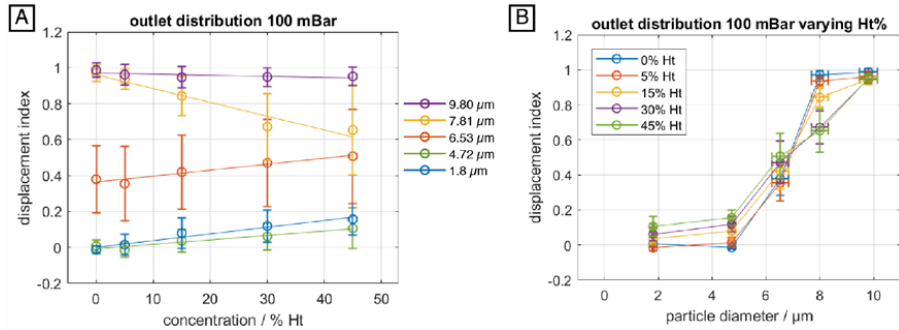


Figure 4 Effect of hematocrit on displacement of microspheres. (A) The displacement index as a function of hematocrit at 100mBar driving pressure for 5 microsphere sizes. (B) The displacement index at 100mBar as a function of microsphere diameter for 5 hematocrits.

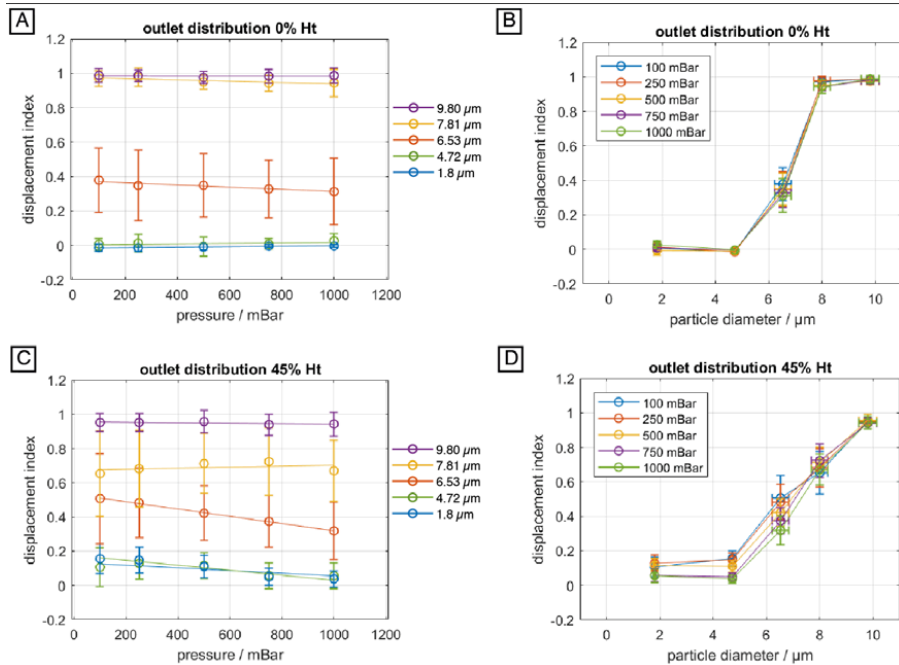


Figure 5 The effects of flow velocity (pressure) on outlet distributions at low and high hematocrit. (A) Displacement index as a function of pressure for 5 microsphere diameters at 0% hematocrit. (B) Displacement index as a function of microsphere diameter for 5 driving pressures at 0% hematocrit. (C) Displacement index as a function of pressure for 5 microsphere diameters at 45% hematocrit. (D) Displacement index as a function of microsphere diameter for 5 driving pressures at 45% hematocrit.

As a reference we performed standard DLD separation of microspheres in aqueous buffer solutions with no blood, *i.e.* 0% hematocrit, Figure 5A and B. The displacement index of the 1.8  $\mu\text{m}$  and 4.72  $\mu\text{m}$  spheres is 0. In other words, they follow the average fluid flow direction unperturbed by the effects of the DLD array. The 7.81  $\mu\text{m}$  and 9.80  $\mu\text{m}$  spheres however have a displacement index of 1, meaning that they are travelling through the entire device in displacement mode. Interestingly 6.53  $\mu\text{m}$  spheres have a mean displacement index of 0.4 and

a much broader distribution about this mean than the other spheres have about theirs. This behavior is believed to have two origins, both connected to the fact that the beads are close to the critical size. Firstly, the size distribution of the beads spans the range below and above the critical size, and secondly the effect of any defects in the DLD array is augmented.

For the experiments taking place with the microsphere particles mixed in blood, we identified three different regimes. For  $D_p \gg D_c$  no effect of the RBC background can be seen. For  $D_p > D_c$  and  $D_p < D_c$ , as the hematocrit is increased the overall trajectories tend to converge towards a displacement index of 0.5. This effect is greater the closer in size particles are to the critical size. We also find that the distributions tend to broaden as the hematocrit is increased, Figure 4. The magnitude of the effects due to the blood depends on the shear rate as can be seen in Figure 5. As the applied pressure is increased the effect of the blood tends to decrease.

#### *Underlying mechanisms*

First, we can rule out margination[48, 49]. Due to the low lateral speed in margination it is typically demonstrated in long channels. Hou *et al.* used 5mm long channels[50]. For particles moving between posts there is no net build-up of lateral translation and therefore no margination. We cannot observe any attractive force between the posts and the particles in the acquired movies. On the contrary, the particles are effectively repelled from the posts due to an increased concentration of RBC around the posts. For the upper and bottom walls we could however expect margination to be possible although the effect on the separation would be expected to be negligible. To detect this vertical margination more detailed imaging using e.g. confocal microscopy would be necessary together with 3D simulations.

The *capillary number* is often used to characterize systems where margination occurs. The capillary number is given by

$$Ca = \frac{\nabla p l r}{\kappa_s}$$

Here the  $\nabla p$  is the pressure gradient in the device, the length scale is given by  $l = \sqrt{G h}$  where  $G$  is the gap between posts and  $h$  is the depth of the device,  $r$  is the radius of the RBCs and  $\kappa_s$  is the shear modulus of the RBCs. With typical values for our experiments:  $\nabla p = \frac{100\text{mBar}}{19.44\text{mm}} = \frac{10^4\text{Pa}}{0.02\text{m}} = 500\text{kPa/m}$ ,  $l = \sqrt{G h} = \sqrt{16\mu\text{m} 15\mu\text{m}}$ ,  $r = 3.9\mu\text{m}$ ,  $\kappa_s = 5.3 \mu\text{N/m}$ , we obtain a capillary value of 5.7. This can be compared to  $Ca = 0.2-1$  in a recent theoretical study, where they observed a shift from displacement to zigzag within this range in DLD devices with a critical size  $D_c = 4.5-7.5 \mu\text{m}$ . This study was performed using a relatively shallow device depth,  $H = 4.8 \mu\text{m}$ , which consequently forces the RBCs to orient in such a way that they increase their effective size. Our measurements are conducted in a deep device together with an elevated Capillary number, consequently the RBCs are expected to be flowing in zigzag mode.

Another mechanism that we can rule out is that an increase of the RBC concentration would affect the velocity profile in the DLD and consequently change the critical sizes of the devices. In contradiction to this assumption, our simulations reveal that there is no significant change for the pattern of the flow profile in the circular post arrays when the concentration of RBCs is increased, as shown in Figure 6.

In addition, it is worthwhile to note that the concentration of RBCs could also affect the separation of the RBCs themselves. Our previous study for the RBC separation in DLD showed that the zigzag-to-displacement transition of the 2D RBCs was observed at  $\Delta\lambda = 1.51 \pm 0.05\mu\text{m}$ [51]. While by increasing the concentration to  $c_{RBCs} = 15.21\%$ , the transition is found to be shifted to the lower row shift ( $\Delta\lambda < 1.20\mu\text{m}$ ), corresponding to a lowering of the critical size.

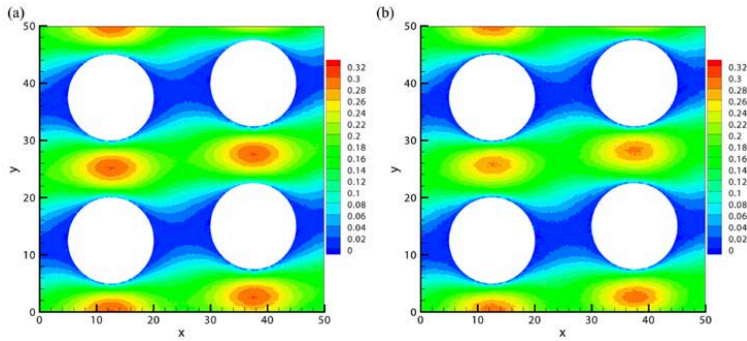


Figure 6. Comparison of flow velocity profiles ( $x$  component) in DLD arrays for the concentrations of RBCs at (a)  $c_{RBCs} = 0.0\%$  and (b)  $c_{RBCs} = 15.21\%$ .

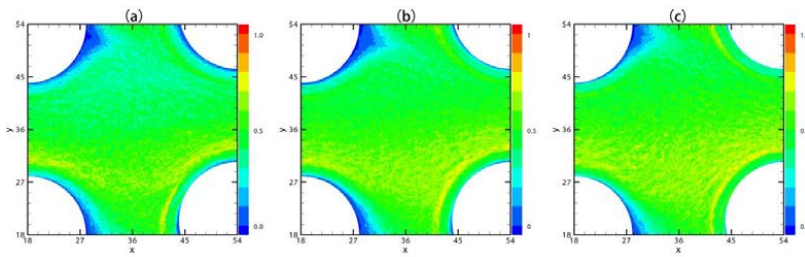


Figure 7 Distributions of the membrane particles of RBCs at (a) 11.31%, (b) 22.62% and (c) 33.93%. Averaging thousands of uncorrelated frames, from long trajectories, and then normalizing with the corresponding maximum value gives us each distribution.

As shown in Figure 7, the increase of the RBC concentration leads to an increase in the thickness of the RBC layer surrounding the pillars. This leads to steric effects that hinder the hard spheres from coming into contact with the pillars and has two main consequences. (1) The effective size of the pillars is larger and therefore the effective gap size and ultimately the effective critical size smaller. This leads to an increase in displacement index for those particles that are smaller than the critical size. The closer the diameter of the particles to the critical size, the larger this effect is. The trajectories of particles fully in the displacement mode (displacement index  $\sim 1$ ) are not changed by this effect. (2) The number of zigzagging RBCs at the down-stream gap increases the collision-induced zigzag motion of the harder spheres leading to a decrease in the displacement index (see Figure 8). For particles smaller than the critical size in the device, mechanism 1 seems to dominate. Also, for those particles that are larger than, but closer to the critical size this effect seems to dominate. For the largest particles effect 1 appears to dominate.

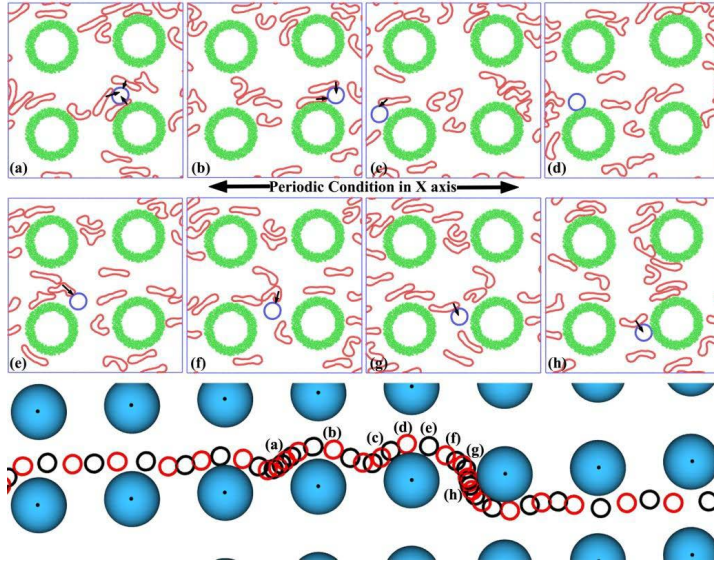


Figure 8. Flow structures in a typical collision-induced zig-zag motion extracted from the mixed mode trajectory of the particle ( $D_p \approx 5.12\mu\text{m} > D_c = 3.82\mu\text{m}$ ) at  $c_{\text{RBCs}} = 15.21\%$  and device parameters,  $\lambda = 25\mu\text{m}$ ,  $\Delta\lambda = 1.67\mu\text{m}$ ,  $\text{gap} = 10\mu\text{m}$ .

Higher concentration of RBCs is intuitively expected to induce more collisions between the RBCs and particles. In view of the observations in experiments and simulations, these collisions may increasingly disturb the lateral displacement of the particles and in turn affect the separation efficiency. In Figure 8, we illustrate a part of a typical collision-induced zigzag motion extracted from the mixed mode trajectory of the particle. It is apparent that the particle encounters numerous collisions with the crowding RBCs in the fluid, which could be roughly divided into two classes on the basis of the corresponding effect on the particle's movement. One could be denoted a "kick-up" collision, which hinders the particle from entering the lower neighboring streams and should be in favor of the displacement motion, as displayed in Figure 8(a-b). The other one could be denoted a "kick-down" collision, which forces the particle to flow into the lower neighboring streams and should be beneficial to the zigzag motion, as shown in Figure 8(c, e-h). Therefore, the ultimate separation motion of the particles in the concentrated flow would be determined by a consequence of the competition between these two collisions and the inherent separation mechanism of DLD. In this collision-induced zig-zag motion, although the "kick-up" collisions momentarily drive the particle away from the posts (in Figure 8a-b), the subsequent "kick-down" collisions could constantly provide sufficient forces to bring the particle back into the zig-zag stream (in Figure 8e-h) and consequently weaken the lateral displacement of the particle to the mixed mode. Further examinations show that the effective "kick-down" collisions for the induced zigzag motion usually means one or several RBCs accompany and drive the particle into the zigzag stream. In this way, it should be reasonable that the probability of the effective "kick-down" collisions is highly sensitive to the concentration and the zigzag frequency (relating to  $N$ ) of RBCs, which could be the underlying mechanism responsible for the observed concentration dependency.

Figure 9 shows some typical displacement trajectories of the particle  $D_p \approx 5.12\mu\text{m} > D_c = 3.82\mu\text{m}$  in the DLD with  $N=20$  at various concentrations of RBCs. Without RBCs, the displacement trajectory of the particle is perfectly along the post array gradient and close to the bottom posts, as shown in Figure 9(a). While increasing the concentration of RBCs in the fluid, the displacement trajectory becomes increasingly bumpy, wherein the particles irregularly move up and down in the flow channel due to the frequent collisions with the

RBCs (“kick-down” in Figure 9(d-2) and “kick-up” in Figure 9(d-3)). Compare also with experimentally observed trajectory that qualitatively corresponds this picture, Figure 10. Occasionally, there is an effective “kick-down” collision inducing an unexpected zigzag motion, as depicted in Figure 9(d-1). As a consequence, it is difficult to have a perfect displacement mode ( $I_S \approx 1$ ) for the particle in the fluid with high RBC concentration. Moreover, it seems that the probability of the effective “kick-down” collision decreases with reducing the row shift (increasing  $N$ ) in the DLD device, which may be associated with the reduced zigzag frequency of RBCs.

Figure 9. Snapshots of the displacement trajectories of the rigid spherical particle ( $D_P \approx 5.12\mu\text{m} > D_C = 3.3\mu\text{m}$ ). DLD device parameters,  $\lambda = 25\mu\text{m}$ ,  $\Delta\lambda = 1.25\mu\text{m}$ ,  $\text{gap} = 10\mu\text{m}$ .  $c_{\text{RBCs}} =$  (a) 0.0%, (b) 3.04%, (c) 9.13% and (d) 15.21%. Three detailed flow structures typically extracted from the trajectory (d) are displayed below.

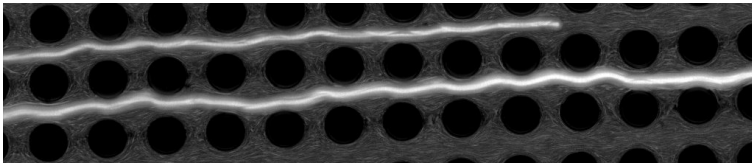


Figure 10. Experimental trajectories of fluorescent microspheres with diameter  $D_P = 9.8\mu\text{m} > D_C = 6.11\mu\text{m}$  in 30% blood. DLD device parameters,  $\lambda = 36\mu\text{m}$ ,  $\Delta\lambda = 2.4\mu\text{m}$ ,  $\text{gap} = 16\mu\text{m}$ .

For the particle with  $D_P \approx 6.06\mu\text{m} < D_C = 6.11\mu\text{m}$ , the simulation results show that the displacement index decreases with increasing hematocrit, indicating a contrary concentration dependency, Figure 11. Detailed examinations on the particle trajectories reveal that the existence of RBCs hinders the normal streamline alternation of the particles in the DLD devices, which therefore occasionally delays the regular zigzag motion and leads to a higher value of the displacement index at the higher RBC concentration, as clearly illustrated in Figure 12.

Extreme long simulations have been performed to examine how the concentration of RBCs affects the zigzagging period of the particles, wherein the particles flow past at least 500 posts in the devices and therefore around 30 zigzagging periods are counted. As shown in Figure 11,



in the absence of RBCs, the zigzagging period of the particles exhibits a narrow distribution around the device period ( $N = 15$ ), indicating a near-perfect zigzag motion. With increasing the concentration of RBCs to  $c_{RBC} = 11.31\%$  and  $22.62\%$ , the distribution expands to the higher value of the zigzagging period and becomes wider and wider, which may be mainly attributed to the delayed zigzag motion shown in Figure 12. At the highest concentration  $c_{RBC} = 33.93\%$ , it is interesting to observe several zigzag motions with extreme lower period (*e.g.*  $N = 5$ ), where the RBC-particle collisions accelerate the streamline alternation to the first stream and facilitate the zigzag motion. Here although the average value of the displacement index is very small, the more irregular period of the zigzag motion may lead to poor separation with very wide particle distribution in the outlets.

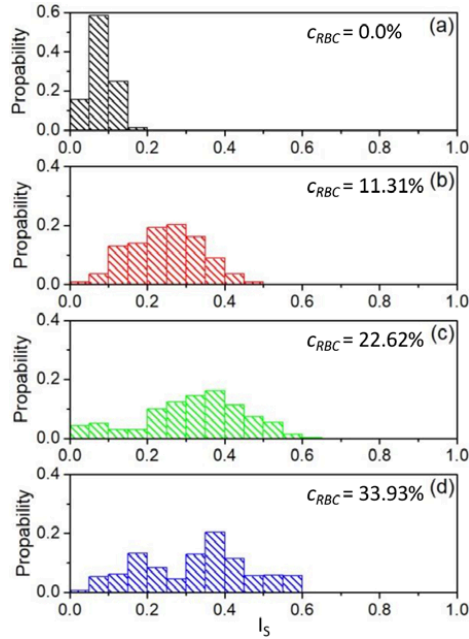


Figure 11. Simulation - shift of zigzag mode towards mixed mode as RBC concentration is increased. The outlet distribution of the hard spherical particles ( $D_p = 6.06\mu\text{m} < D_c = 6.11\mu\text{m}$ ) at different concentrations of RBCs. DLD device parameters,  $\lambda = 36\mu\text{m}$ ,  $\Delta\lambda = 2.4\mu\text{m}$ ,  $\text{gap} = 16\mu\text{m}$ .

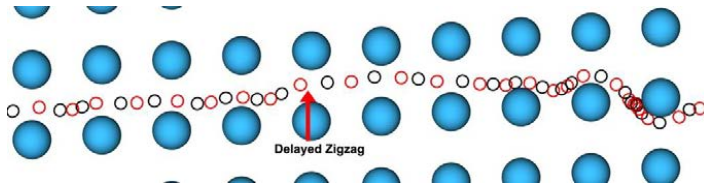


Figure 12 A snapshot of typical delayed zigzag trajectory of the rigid spherical particle with  $D \approx 6.06\mu\text{m} < D_c = 6.11\mu\text{m}$ . The regular alternation of black and red particles represents sequential frames with a constant time interval. DLD device parameters,  $\lambda = 36\mu\text{m}$ ,  $\Delta\lambda = 2.4\mu\text{m}$ ,  $\text{gap} = 16\mu\text{m}$ .

The overall effect of the increased hematocrit is summarized in Figure 13 and displays the same trends as we can see experimentally, Figure 4 and Figure 5.

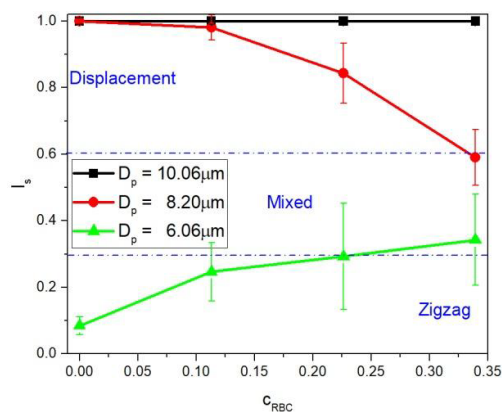


Figure 13. Simulated displacement indices as a function of hematocrit for 3 particle sizes.

## Materials and Methods

### Microfluidic devices

Devices were fabricated in PDMS (Sylgard 184, Dow Corning, Midland, MI, USA) using standard replica molding [52] of SU8 (SU8-2010, Microchem Corp., MA, USA) structures on a 3" silicon substrate. Designs were drawn in L-Edit 11.02 (Tanner Research, Monrovia, CA USA), the photomask printed by Delta Mask (Delta Mask, Enschede, The Netherlands) and the master fabricated using UV-lithography (Karl Suss MJB4, Munich, Germany). To facilitate demoulding from the master it was coated with an anti-sticking layer, 1H,1H,2H,2H-per-fluorooctyl-trichlorosilane (ABC R GmbH & Co. KG, Karlsruhe, Germany) [53]. PDMS casts were oxygen plasma bonded to microscope slides spun with a thin layer of PDMS (Plasma Preen II-862, Plasmatic Systems Inc., North Brunswick, NJ, USA) to obtain devices with all internal surfaces consisting of PDMS. Immediately after bonding, the devices were filled with solution of a 0.2 % (w/v) PLL(20)-g[3.5]-PEG(2) (SuSoS AG, Dubendorf, Switzerland) in deionized water and left for 20 minutes before subsequent flushing in order to minimize the adhesion of cells to the walls. Silicon tubing with 3mm inner and 5mm outer diameter (228-0725 and 228-0707, VWR International LLC, Radnor, PA, USA) were glued (Elastosil A07, Wacker Chemie AG, Munich, Germany) onto the device as reservoirs.

### Measurement setup

An MFCS-4C pressure controller (Fluigent, Paris, France) was used to control the overpressure at the inlets and the outlet reservoirs were kept at ambient pressure. Images were captured through an inverted Nikon Eclipse Ti microscope (Nikon Corporation, Tokyo, Japan) with an Andor NEO sCMOS camera (Andor Technology, Belfast, Northern Ireland) and Lumencor SOLA light engine™ (Lumencor Inc, OR, USA) with FITC, TRITC and DAPI filters, or brightfield and 4x, 10x and 60x water immersion objectives were used and all movies acquired at 10 frames per second.

The results of both experimental and simulated separations are plotted as the displacement index, which is defined as the ratio of the lateral displacement of particles per post to the row shift. For the ideal displacement mode, it tends to be one as the particles are displaced laterally from their original stream to flow along the gradient of post array. While for the ideal zigzag mode, it will be close to zero as the particles move in the direction of flow without net lateral displacement. In addition, previous simulation work and other experimental results have shown the existence of a mixed mode, which is an intermediate

state with alternating displacement and zigzag motion and corresponds roughly to a displacement index ranging from 0.3 to 0.6.

#### Reagents and blood samples

Experiments were performed by flowing suspensions of polystyrene microspheres (from...) of diameters 1.8, 4.72, 6.53, 7.81 and 9.80  $\mu\text{m}$  into the sample channel of our device while simultaneously flowing solutions of human blood into the background inlets at hematocrits of 0, 5, 15, 30 and 45% (whole blood). The lateral positions (degree of displacement) of the microspheres was measured at the end of the separation array and a displacement index (0 = zigzag mode and 1 = displacement mode) calculated.

An automated script was used to analyze the exit distribution of the sorted particles. The script is based on an analysis of intensity of the fluorescent particles after compensation for background. Each data point is derived from more than 100 particles. Due to the larger concentration in terms of number per unit volume, the smaller particles were sampled more than the larger particles.

#### Simulations

To model fluid flow within a microfluidic device, we employ the dissipative particle dynamics (DPD), which is a mesoscopic coarse-grained simulation technique for the study of various complex fluids. In this method, the simulated system consists of a collection of  $N$  particles with mass  $m_i$ , position  $r_i$  and velocity  $v_i$ , and each individual particle represents a cluster of atoms or molecules. The dynamics of the DPD particles is governed by Newton's second law of motion, and the total force acting between two particles within a selected cutoff ( $r_c$ ) region is a sum of three pairwise forces: conservative ( $F_{ij}^C$ ), dissipative ( $F_{ij}^D$ ) and random ( $F_{ij}^R$ ) forces.

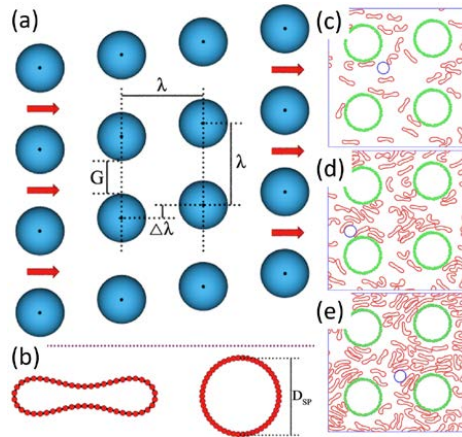


Figure 14. Schematic illustrations of the geometry and structures of the simulated DLD systems: (a) DLD array with circular posts. The geometry is defined by the post center-center distance  $\lambda$ , the post gap  $G$  and the row shift  $\Delta\lambda$ . (b) 2D models of RBCs and rigid spherical particles. (c-e) Instantaneous snapshots of typical fluid structures at different RBC concentrations (c) 11.31%, (d) 22.62% and (e) 33.93%. DLD device parameters,  $\lambda=36\mu\text{m}$ ,  $\Delta\lambda=2.4\mu\text{m}$ ,  $\text{gap}=16\mu\text{m}$ .

In this work, we apply the two-dimensional (2D) simulations to study the effect of the concentration of red blood cells (RBCs) on the separation of rigid spherical particles in DLD devices with circular post arrays, wherein both RBCs and rigid spherical particles are modelled as closed bead-spring chains with  $N_V$  particles (50 for RBCs and 30~60 for rigid spherical particles) connected by  $N_S = N_V$  springs, as illustrated in Figure 14. The bonding potential, bending energy and area constraint are applied to control the shape and rigidity of the cells and particles. It has been validated that these models and simulations are able to

capture the essential physical features required to correctly describe the motion of particles in conventional DLD devices with circular posts[51].

## Conclusion

We find that DLD is highly promising for separation of particles at high blood concentrations up to whole blood. The blood primarily influences trajectories of particles close to the critical size of the DLD array thereby decreasing the available resolution. We found that the effect of the blood can be minimized by increasing the flow rate in the device. This would be unproblematic for hard particles, but for soft cells the deformation of the cells must be taken into account.

## Acknowledgements

This work was carried out within NanoLund at Lund University with funding from FP7-PEOPLE-2013-ITN LAPASO “Label-free particle sorting” (project 607350) and the Swedish Research Council (VR) grant no. 2015-05426. All device processing was conducted within Lund Nano Lab. Dmitry A. Fedosov acknowledges funding by the Alexander von Humboldt Foundation. We also gratefully acknowledge a CPU time grant by the Jülich Supercomputing Center.

1. Huang, L.R., E.C. Cox, R.H. Austin, and J.C. Sturm, *Continuous Particle Separation Through Deterministic Lateral Displacement*. Science, 2004. **304**(5673): p. 987-990.
2. Inglis, D.W., J.A. Davis, R.H. Austin, and J.C. Sturm, *Critical particle size for fractionation by deterministic lateral displacement*. Lab on a chip, 2006. **6**(5): p. 655-658.
3. Louthback, K., J. D'Silva, L. Liu, A. Wu, R.H. Austin, and J.C. Sturm, *Deterministic separation of cancer cells from blood at 10 mL/min*. AIP Advances, 2012. **2**(4): p. 042107-7.
4. Davis, J.A., D.W. Inglis, K.J. Morton, D.A. Lawrence, L.R. Huang, S.Y. Chou, J.C. Sturm, and R.H. Austin, *Deterministic hydrodynamics: Taking blood apart*. Proceedings of the National Academy of Sciences of the United States of America, 2006. **103**(40): p. 14779-14784.
5. Zheng, S.Y., R. Yung, Y.C. Tai, and H. Kasdan, *Deterministic lateral displacement MEMS device for continuous blood cell separation*. Mems 2005 Miami: Technical Digest, 2005: p. 851-854.
6. Li, N., D.T. Kamei, and C.M. Ho, *On-chip continuous blood cell sub-type separation by deterministic lateral displacement*. 2007 2nd IEEE International Conference on Nano/Micro Engineered and Molecular Systems, Vols 1-3, 2007: p. 692-696.
7. Huang, R., T.A. Barber, M.A. Schmidt, R.G. Tompkins, M. Toner, D.W. Bianchi, R. Kapur, and W.L. Flejter, *A microfluidics approach for the isolation of nucleated red blood cells (NRBCs) from the peripheral blood of pregnant women*. Prenatal Diagnosis, 2008. **28**(10): p. 892-899.
8. Green, J.V., M. Radisic, and S.K. Murthy, *Deterministic Lateral Displacement as a Means to Enrich Large Cells for Tissue Engineering*. Analytical Chemistry, 2009. **81**(21): p. 9178-9182.

9. Inglis, D.W., N. Herman, and G. Vesey, *Highly accurate deterministic lateral displacement device and its application to purification of fungal spores*. *Biomicrofluidics*, 2010. **4**(2).
10. Holm, S.H., J.P. Beech, M.P. Barrett, and J.O. Tegenfeldt, *Separation of parasites from human blood using deterministic lateral displacement*. *Lab on a Chip*, 2011. **11**(7): p. 1326-1332.
11. Inglis, D.W., M. Lord, and R.E. Nordon, *Scaling deterministic lateral displacement arrays for high throughput and dilution-free enrichment of leukocytes*. *Journal of Micromechanics and Microengineering*, 2011. **21**(5).
12. Beech, J.P., S.H. Holm, K. Adolfsson, and J.O. Tegenfeldt, *Sorting cells by size, shape and deformability*. *Lab on a Chip*, 2012. **12**(6): p. 1048-1051.
13. Louterback, K., J. D'Silva, L.Y. Liu, A. Wu, R.H. Austin, and J.C. Sturm, *Deterministic separation of cancer cells from blood at 10 mL/min*. *Aip Advances*, 2012. **2**(4).
14. Zhang, B.Y., J.V. Green, S.K. Murthy, and M. Radisic, *Label-Free Enrichment of Functional Cardiomyocytes Using Microfluidic Deterministic Lateral Flow Displacement*. *Plos One*, 2012. **7**(5).
15. Liu, Z.B., F. Huang, J.H. Du, W.L. Shu, H.T. Feng, X.P. Xu, and Y. Chen, *Rapid isolation of cancer cells using microfluidic deterministic lateral displacement structure*. *Biomicrofluidics*, 2013. **7**(1).
16. Holmes, D., G. Whyte, J. Bailey, N. Vergara-Irigaray, A. Ekpenyong, J. Guck, and T. Duke, *Separation of blood cells with differing deformability using deterministic lateral displacement*. *Interface Focus*, 2014. **4**(6).
17. Laki, A.J., L. Botzheim, K. Ivan, V. Tamasi, and P. Civera, *Separation of Microvesicles from Serological Samples Using Deterministic Lateral Displacement Effect*. *Bionanoscience*, 2015. **5**(1): p. 48-54.
18. Liu, Z.B., Y. Lee, J.H. Jang, Y. Li, X. Han, K. Yokoi, M. Ferrari, L.D. Zhou, and L.D. Qin, *Microfluidic cytometric analysis of cancer cell transportability and invasiveness*. *Scientific Reports*, 2015. **5**.
19. Okano, H., T. Konishi, T. Suzuki, T. Suzuki, S. Ariyasu, S. Aoki, R. Abe, and M. Hayase, *Enrichment of circulating tumor cells in tumor-bearing mouse blood by a deterministic lateral displacement microfluidic device*. *Biomedical Microdevices*, 2015. **17**(3).
20. Civin, C.I., et al., *Automated Leukocyte Processing by Microfluidic Deterministic Lateral Displacement*. *Cytometry Part A*, 2016. **89A**(12): p. 1073-1083.
21. Holm, S.H., J.P. Beech, M.P. Barrett, and J.O. Tegenfeldt, *Simplifying microfluidic separation devices towards field-detection of blood parasites*. *Analytical Methods*, 2016. **8**(16): p. 3291-3300.
22. Tottori, N., T. Nisisako, J. Park, Y. Yanagida, and T. Hatsuzawa, *Separation of viable and nonviable mammalian cells using a deterministic lateral displacement microfluidic device*. *Biomicrofluidics*, 2016. **10**(1).
23. Wunsch, B.H., J.T. Smith, S.M. Gifford, C. Wang, M. Brink, R.L. Bruce, R.H.

- Austin, G. Stolovitzky, and Y. Astier, *Nanoscale lateral displacement arrays for the separation of exosomes and colloids down to 20 nm*. *Nature Nanotechnology*, 2016. **11**(11): p. 936-940.
24. Au, S.H., J. Edd, A.E. Stoddard, K.H.K. Wong, F. Fachin, S. Maheswaran, D.A. Haber, S.L. Stott, R. Kapur, and M. Toner, *Microfluidic Isolation of Circulating Tumor Cell Clusters by Size and Asymmetry*. *Sci Rep*, 2017. **7**(1): p. 2433.
  25. Kim, S.C., N. Dogra, B.H. Wunsch, J.T. Smith, S.M. Gifford, G. Stolovitzky, H. Hu, and P. Meyer, *On-Chip Liquid Biopsy: Progress in Isolation of Exosomes for Early Diagnosis of Cancer*. *Biophysical Journal*, 2017. **112**(3): p. 461A-461A.
  26. Tran, T.S.H., B.D. Ho, J.P. Beech, and J.O. Tegenfeldt, *Open channel deterministic lateral displacement for particle and cell sorting*. *Lab on a Chip*, 2017.
  27. Beech, J.P., B.D. Ho, G. Garriss, V. Oliveira, B. Henriques-Normark, and J.O. Tegenfeldt, *Separation of pathogenic bacteria by chain length*. *Analytica Chimica Acta*, 2018. **1000**: p. 223-231.
  28. Beech, J.P. and J.O. Tegenfeldt, *Tuneable separation in elastomeric microfluidics devices*. *Lab on a Chip*, 2008. **8**(5): p. 657-659.
  29. Louthierback, K., K.S. Chou, J. Newman, J. Puchalla, R.H. Austin, and J.C. Sturm, *Improved performance of deterministic lateral displacement arrays with triangular posts*. *Microfluidics and Nanofluidics*, 2010. **9**(6): p. 1143-1149.
  30. Zeming, K.K., S. Ranjan, and Y. Zhang, *Rotational separation of non-spherical bioparticles using I-shaped pillar arrays in a microfluidic device*. *Nature Communications*, 2013. **4**.
  31. Ranjan, S., K.K. Zeming, R. Jureen, D. Fisher, and Y. Zhang, *DLD pillar shape design for efficient separation of spherical and non-spherical bioparticles*. *Lab on a Chip*, 2014. **14**(21): p. 4250-4262.
  32. Wei, J.H., H. Song, Z.Y. Shen, Y. He, X.Z. Xu, Y. Zhang, and B.N. Li, *Numerical Study of Pillar Shapes in Deterministic Lateral Displacement Microfluidic Arrays for Spherical Particle Separation*. *Ieee Transactions on Nanobioscience*, 2015. **14**(6): p. 660-667.
  33. Zhang, Z.M., E. Henry, G. Gompper, and D.A. Fedosova, *Behavior of rigid and deformable particles in deterministic lateral displacement devices with different post shapes*. *Journal of Chemical Physics*, 2015. **143**(24).
  34. Holm, S.H., J.P. Beech, M.P. Barrett, and J.O. Tegenfeldt, *Simplifying microfluidic separation devices towards field-detection of blood parasites (vol 8, pg 3291, 2016)*. *Analytical Methods*, 2016. **8**(28): p. 5726-5726.
  35. Zeming, K.K., T. Salafi, C.H. Chen, and Y. Zhang, *Asymmetrical Deterministic Lateral Displacement Gaps for Dual Functions of Enhanced Separation and Throughput of Red Blood Cells*. *Scientific Reports*, 2016. **6**.
  36. Hyun, J.C., J. Hyun, S. Wang, and S. Yang, *Improved pillar shape for deterministic lateral displacement separation method to maintain*

- separation efficiency over a long period of time.* Separation and Purification Technology, 2017. **172**: p. 258-267.
37. Kim, S.C., B.H. Wunsch, H. Hu, J.T. Smith, R.H. Austin, and G. Stolovitzky, *Broken flow symmetry explains the dynamics of small particles in deterministic lateral displacement arrays.* Proceedings of the National Academy of Sciences of the United States of America, 2017. **114**(26): p. E5034-E5041.
  38. Pariset, E., C. Pudda, F. Boizot, N. Verplanck, J. Berthier, A. Thuaire, and V. Agache, *Anticipating Cutoff Diameters in Deterministic Lateral Displacement (DLD) Microfluidic Devices for an Optimized Particle Separation.* Small, 2017. **13**(37).
  39. Vernekar, R., T. Kruger, K. Loutherbach, K. Morton, and D.W. Inglis, *Anisotropic permeability in deterministic lateral displacement arrays.* Lab on a Chip, 2017. **17**(19): p. 3318-3330.
  40. Beech, J.P., P. Jonsson, and J.O. Tegenfeldt, *Tipping the balance of deterministic lateral displacement devices using dielectrophoresis.* Lab on a Chip, 2009. **9**(18): p. 2698-2706.
  41. Quek, R., D.V. Le, and K.H. Chiam, *Separation of deformable particles in deterministic lateral displacement devices.* Physical Review E, 2011. **83**(5).
  42. Kruger, T., D. Holmes, and P.V. Coveney, *Deformability-based red blood cell separation in deterministic lateral displacement devices-A simulation study.* Biomicrofluidics, 2014. **8**(5).
  43. Ye, S.J., X.M. Shao, Z.S. Yu, and W.G. Yu, *Effects of the particle deformability on the critical separation diameter in the deterministic lateral displacement device.* Journal of Fluid Mechanics, 2014. **743**: p. 60-74.
  44. Jiang, M.L., K. Budzan, and G. Drazer, *Fractionation by shape in deterministic lateral displacement microfluidic devices.* Microfluidics and Nanofluidics, 2015. **19**(2): p. 427-434.
  45. Henry, E., S.H. Holm, Z.M. Zhang, J.P. Beech, J.O. Tegenfeldt, D.A. Fedosov, and G. Gompper, *Sorting cells by their dynamical properties.* Scientific Reports, 2016. **6**.
  46. Feng, S.L., A.M. Skelley, A.G. Anwer, G.Z. Liu, and D.W. Inglis, *Maximizing particle concentration in deterministic lateral displacement arrays (vol 11, 024121, 2017).* Biomicrofluidics, 2017. **11**(3).
  47. Vernekar, R. and T. Kruger, *Breakdown of deterministic lateral displacement efficiency for non-dilute suspensions: A numerical study.* Medical Engineering & Physics, 2015. **37**(9): p. 845-854.
  48. Fedosov, D.A., J. Fornleitner, and G. Gompper, *Margination of White Blood Cells in Microcapillary Flow.* Physical Review Letters, 2012. **108**(2).
  49. Fedosov, D.A. and G. Gompper, *White blood cell margination in microcirculation.* Soft Matter, 2014. **10**(17): p. 2961-2970.
  50. Hou, H.W., H.Y. Gan, A.A.S. Bhagat, L.D. Li, C.T. Lim, and J. Han, *A microfluidics approach towards high-throughput pathogen removal from*

- blood using margination*. *Biomicrofluidics*, 2012. **6**(2).
51. Zhang, Z.M., E. Henry, G. Gompper, and D.A. Fedosov, *Behavior of rigid and deformable particles in deterministic lateral displacement devices with different post shapes*. *Journal of Chemical Physics*, 2015. **143**(24).
  52. Xia, Y.N., J.J. McClelland, R. Gupta, D. Qin, X.M. Zhao, L.L. Sohn, R.J. Celotta, and G.M. Whitesides, *Replica molding using polymeric materials: A practical step toward nanomanufacturing*. *Advanced Materials*, 1997. **9**(2): p. 147-149.
  53. Beck, M., M. Graczyk, I. Maximov, E.L. Sarwe, T.G.I. Ling, and L. Montelius, *Improving nanoimprint lithography stamps for the 10 nm features*. *Proceedings of the 2001 1st Ieee Conference on Nanotechnology*, 2001: p. 17-22.



Paper VI





# DENSITY-BASED SORTING IN DETERMINISTIC LATERAL DISPLACEMENT DEVICES\*

Stefan H. Holm, Jason P. Beech and Jonas O. Tegenfeldt  
Solid State Physics and NanoLund, Lund University, Sweden

## ABSTRACT

*We present a deterministic-lateral-displacement (DLD) device that extends the capabilities of this conventionally size-based particle separation technique to be sensitive to density using two different designs. By the use of T-shaped posts instead of the normally cylindrical posts the particle trajectories through the device will be a function of vertical position which in turn is determined by the buoyancy of the particles. In a more complex design, two DLD arrays are positioned on top of each other. This is combined with a lateral gradient in density. The particles will be focused to where they experience neutral buoyancy independent of size. The potential lies in fast sorting of complex biological samples together with diagnosis and treatment-monitoring of diseases affecting cell-density, e.g. cancer, sickle-cell anemia and malaria. We demonstrate proof-of-principle of combined size-and-density-based sorting, specifically particles of identical size but different density.*

**KEYWORDS:** Deterministic Lateral Displacement, Density, Fractionation

## INTRODUCTION

DLD is a powerful microfluidic technique first shown capable of separating particles based on size[1] and shown by our group to have the potential to discriminate cells based on shape [2-4], deformability[5], viscous properties[6], and dielectric properties[7]. A very common sorting parameter that is lacking is density. This is a highly specific biomarker with an intrinsic cell-to-cell variation a 100-fold lower than that of volume or mass variation[8]. Furthermore, the cell density is known to vary over the course of the cell-cycle [9], and diseases such as malaria, sickle cell anemia and cancer[10]. With these characteristics, cell density is a highly interesting biomarker which combined with the power of DLD has the potential to open up for new separation schemes.

Density based sorting is conventionally implemented using centrifugation, which sorts particles based on their sedimentation rate. This can be expanded to density gradient centrifugation, where the particles of interest are suspended in a layered fluid. Here the separation is independent of size as the particles move until they reach neutral buoyancy. The main limitation of centrifugation is the requirement for relative large amounts of sample and the requirement for bulky and expensive equipment.

To address these issues, a few examples of alternative schemes have been reported. One very simple approach is based on connecting a tube to a whisk[11]. This can be

---

\* Adapted from "Density-based particle fractionation", Stefan H. Holm, Jason P. Beech and Jonas O. Tegenfeldt, 18th International Conference on Miniaturized Systems for Chemistry and Life Sciences October 26-30, 2014, San Antonio, Texas, USA

used for crude centrifugation and can be made without any specialized tools. A slightly more sophisticated example is the hollow vibrating cantilever. As cells move through the cantilever, the overall mass of the cantilever changes, and this change can be monitored through the resonance frequency of the cantilever. In this way the density of individual cells can be measured[8], however at a rather low throughput. To address the limited throughput, an acoustophoretic device has been demonstrated based on a channel with a lateral density gradient[12]. As the acoustophoretic force is dependent on the density, using the density gradient the particles of interest can be focused to locations where the particle density matches the liquid medium density.

In our work we implement separation based on density in a DLD device through two different design principles. The first simplest approach is based on the use of T-shaped posts instead of standard cylindrical posts, (Figures 1 & 2). As the critical size above which particles are laterally displaced is a function of the distance between the posts (the gap,  $G$ ) we achieve a device with two separate critical sizes. As the vertical position of a particle depends on buoyancy, the trajectory through the device will be a function of both the particle size and density.

The second approach is based on the superposition of two DLD arrays pointing in two different directions. Here particles which are lighter than the medium will move upwards and thereby move in the direction of the top DLD array. Heavier particles will sediment down and thus move with the bottom DLD array in a different direction. Combining this geometry with a lateral density gradient allows us to sort particles independent of size with respect to density. Particles will be focused to lateral locations where they have neutral buoyancy.

## THEORY

In DLD the sample flows through a symmetric array of micrometer-sized posts under laminar flow conditions. Hydrodynamic and steric interactions between posts and particles give rise to a separation where larger particles are deflected at a specific angle with respect to the flow. However, small particles are not affected by these interactions and travel through the device without being laterally displaced, Figure 1 A, thus achieving a separation of the particles. The specific size above which particles are deflected is known as the critical size. This value,  $D_c$ , is a function of the periodicity of the array,  $N$ , and more important for this work the distance between two posts, the gap ( $G$ ), see the unit cell in Figure 1B.

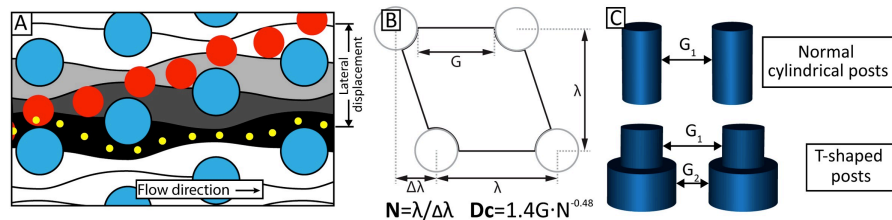


Figure 1. Schematic illustration showing a section of a DLD device, with posts colored blue. The hydrodynamic center of the small yellow particle is able to fit within the black flow stream while the larger red particle is laterally displaced to the adjacent flow stream for each row. (B) A unit cell in the DLD array together with definitions of the period and the critical size. (C) Illustration showing the normal cylindrical posts and the T-shaped posts used in this work. With T-shaped posts two different gaps, and consequently two separate critical diameters are present, where the particles' vertical positions determine their behavior in the device.

Traditionally the posts of a DLD device have been cylindrical with a single gap, and a single critical size as a result. However, by the use of T-shaped posts we obtain a device with two distinct gaps and consequently two separate critical sizes. The particles trajectory through the device will thus be a function of both their size and their lateral position.

## EXPERIMENTAL

Flow simulations of the device were carried out using COMSOL Multiphysics 4.3 (COMSOL AB, Sweden). The result for the flow through a unit cell is shown in Figure 2A together with horizontal slices of the unit cell showing the flow field for the small and the large gaps respectively. The graph displays the flow profiles along the shortest lines between the posts in the gaps.

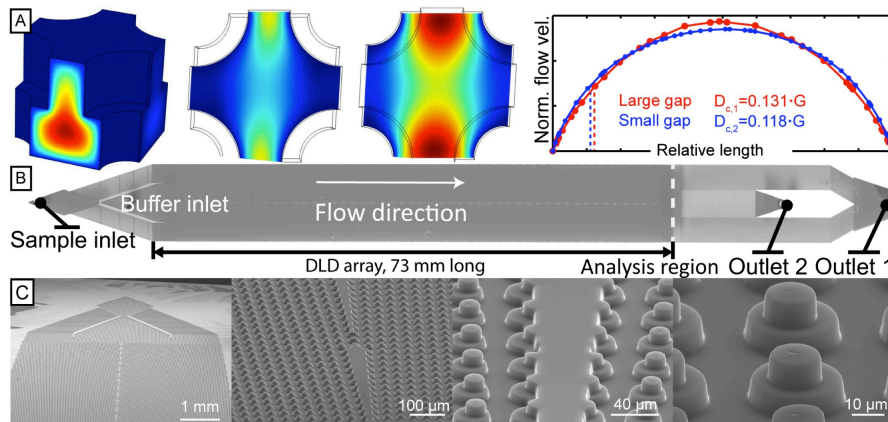


Figure 2. (A) FEM simulations performed in COMSOL Multiphysics 4.3a (Burlington, Ma, USA) to investigate how T-shaped posts affect the flow. First shown is a 3D model of a unit cell with the velocity field color coded (red - high speed and blue - low speed). The 2D-plots are horizontal slices of the unit cell showing the flow profiles at the center height of the small and large gap section respectively. The flow profile between two posts, which determines the critical diameter in the DLD device was then plotted (gap size normalized). From here the critical particle sizes,  $D_c$ , can readily be determined. (B) SEM-micrograph showing an overview of the device with the inlets and outlets and the separation array. (C) SEM-micrographs of the device inlet followed by higher magnified micrographs of the center section of the device showing the T-shaped posts.

The final device is  $\sim 10$  cm long and  $\sim 1$  cm in width, shown in Figure 2B-C. The particles enter through the sample inlet and if there is no interaction with the device they end up in outlet 1. However, if they are larger than the critical size at their lateral position they will be laterally displaced into outlet 2.

The unit cell width,  $\lambda$ , is  $36 \mu\text{m}$  and the T-shaped post radii are  $8$  and  $13 \mu\text{m}$ . Together with a periodicity,  $N$ , of  $18$  the resulting critical sizes in the device are expected to be  $3.50 \mu\text{m}$  and  $7.00 \mu\text{m}$ .

For the gradient device, we first combine two DLD devices ( $D_c = 2.86 \mu\text{m}$ ) pointing in two different directions, Figure 3. At the entrance, a gradient generator[13] is positioned, Figure 4.

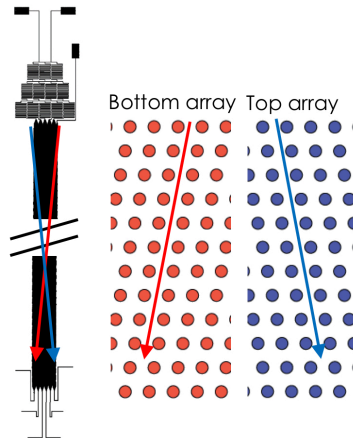


Figure 3. Overall design. Two DLD arrays are aligned on top of each other. The bottom array points towards the left and the top array towards right.

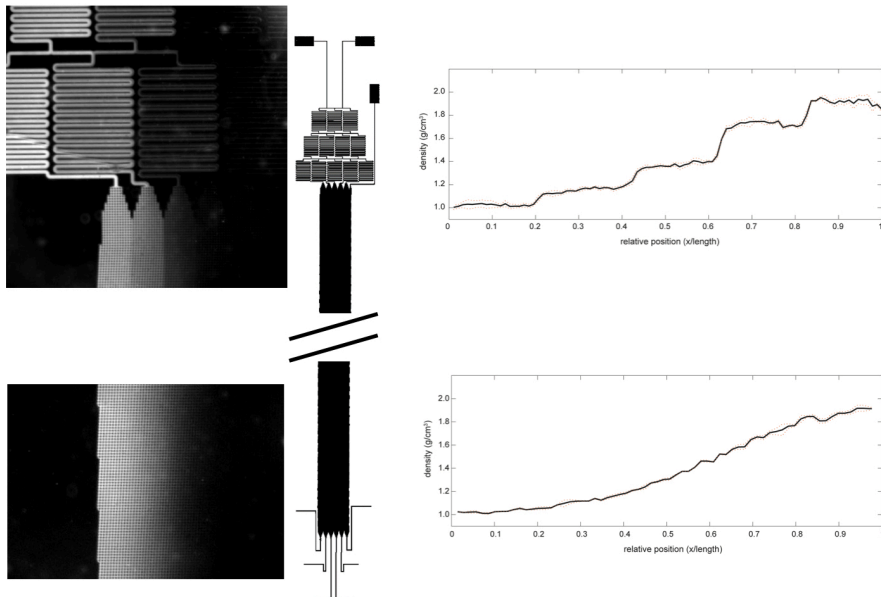


Figure 4. A gradient is created using a standard gradient generator. The resulting gradient is demonstrated using a fluorescent dye. At the beginning of the device (top in the graphics above), the gradient is stepwise and at the end of the device the gradient is smoothed out by diffusion (bottom in the graphics above).

## RESULT AND DISCUSSION

As expected the heavy silicon microspheres (negative buoyancy) sediment to the bottom and depending on the orientation of the device they experience the low or the high critical size (Figure 5A). In this case they are only separated for the small gap with an expected critical size of  $3.50\ \mu\text{m}$  and not in the large gap with an expected critical size of  $7.00\ \mu\text{m}$ .

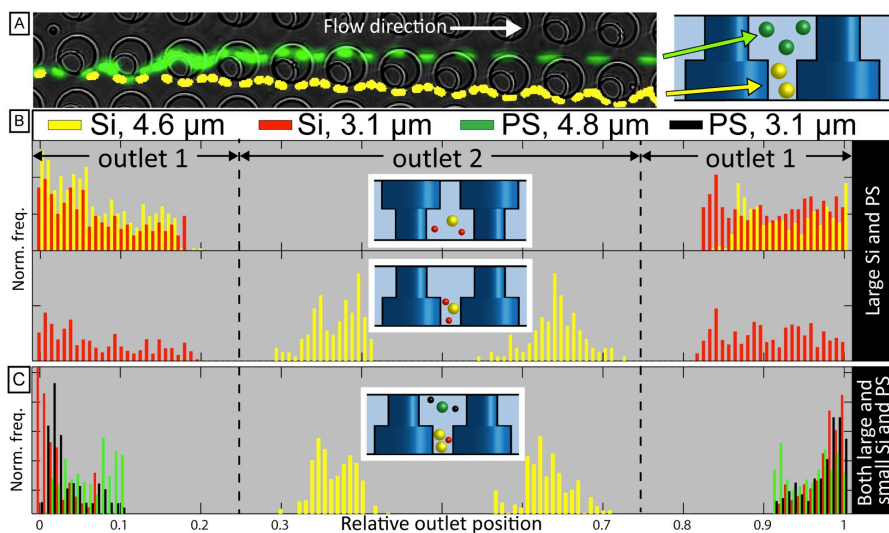


Figure 5 (A) False-colored time-integrated micrograph of a  $4.87 \mu\text{m}$  PS bead (green) and a  $4.63 \mu\text{m}$  Si sphere (yellow). The different lateral position can clearly be seen with the green particle above the small gaps. (B) Graph showing the distribution of silicon (Si) microspheres,  $3.13 \mu\text{m}$  (red) and  $4.63 \mu\text{m}$  (yellow), in DI water at the outlet of the device. The illustrations in the middle show how the device was oriented. When the device is flipped over the Si spheres sediment into the level with smaller gaps and the larger spheres are laterally displaced into outlet 2. (C) Outlet distribution of both large and small Si (yellow, red) and PS (green, black) microspheres in 25% sucrose solution. The buoyancy of the PS microspheres forces them into a vertical position with large gaps while the silicon microspheres sediment into a vertical position with small gaps. Combining of size and density-based separation allows for the sorting out a single specific particle type.

More interestingly, mixing particles of different density we demonstrate that we can separate particles that have similar size and that differ in density only (Figure 5C). Here, the buoyancy on the PS particles forces them to flow into the upper section of the device with a critical size above the particle sizes while, again the silicon particles sediment into lower level with a lower critical size which is between the size of the particles, and consequently only the large Si particles are displaced towards outlet 2.

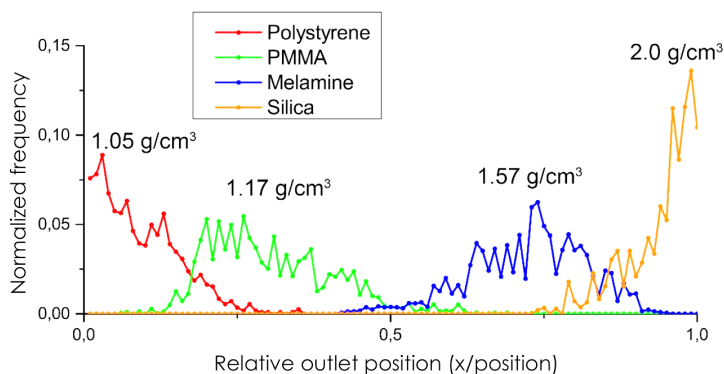


Figure 6. Separation of particles of similar sizes using a combination of two DLD arrays and a density gradient.

Using the gradient device, we separated particles of sizes within the narrow size range  $4.7 \pm 0.5 \mu\text{m}$  with densities ranging from  $1.05 \text{ g/cm}^3$  to  $2.0 \text{ g/cm}^3$ , Figure 6.

## CONCLUSION

We have successfully demonstrated a proof-of-principle device where separation is sensitive not only to size but also density of the particles. In contrast to other alternative single-cell techniques for density characterization[8], this approach is entirely passive.

## METHODS

### *For the T-shaped posts*

A master for replica molding was fabricated using two precisely aligned UV-lithography (MJB4, SUSS MicroTec, Germany) steps in 8 $\mu$ m thick SU8 (MicroChem, USA) on silicon wafers. Devices were then produced using standard soft lithography and bonded to a glass slide treated with oxygen plasma (Plasmatic Systems Inc, USA). Overpressure was used to induce flow in the device (MFCS-FLEX, Fluigent, France). Devices were flushed with 0.1% Tween for 5 minutes prior to the experiment to avoid non-specific sticking.

Microspheres of various sizes and materials were used: silicon (Si) microspheres, 2.0 g/cm<sup>3</sup>, 3.13 $\pm$ 0.42  $\mu$ m and 4.63 $\pm$ 0.46  $\mu$ m (Bangs laboratories Inc, USA) and fluorescent polystyrene (PS) microspheres, 1.05 g/cm<sup>3</sup>, 4.87 $\pm$ 0.28  $\mu$ m and 3.10 $\pm$ 0.15  $\mu$ m (Polysciences Inc, USA). Concentrations were  $\sim$ 10<sup>4</sup>/ $\mu$ L for samples with just one type of material and  $\sim$ 10<sup>3</sup>/ $\mu$ L for the sample containing particles of different materials. In our device the small spheres are expected to be below the smaller critical size while the larger spheres are between the smaller critical size and the larger critical size. The buffer used was 25 wt% sucrose (Sigma-Aldrich LLC, USA) in DI-water solution. The lateral positions of the particles at the end of the DLD array were determined using our own particle tracking software coded in MATLAB R2012b (MathWorks, MA, USA).

### *For the gradient DLD device*

Devices were fabricated in a similar fashion as for the T-shaped post devices. The opposing layers were precisely aligned following plasma activation using a microscope in combination with methanol as a lubricant to allow for a delayed bonding.

Samples consisted of particles of different densities: fluorescent polystyrene (1.05 g/cm<sup>3</sup>, 4.87 $\pm$ 0.28  $\mu$ m), PMMA (1.17 g/cm<sup>3</sup>, 4.9 $\pm$ 0.3  $\mu$ m), melamin (1.51g/cm<sup>3</sup>, 4.74 $\pm$ 0.14  $\mu$ m) and silica (2.0 g/cm<sup>3</sup>, 4.63 $\pm$ 0.46  $\mu$ m) in 0.1% Tween in milliQ and sonicated prior to use. The device was treated to minimize sticking with PLL-g-PEG for 20 minutes, followed by flushing with buffer for 10 minutes. Particles were injected in pairs to allow for discrimination. The low density buffer inlet consisted of 0.1% SDS in water while the high density buffer inlet consisted of 58% w/w sodium polytungstate ( $\rho = 1.9$  g/cm<sup>3</sup>).

## ACKNOWLEDGEMENTS

This work was carried out within and supported through NanoLund. In addition, the work was supported by the Swedish Foundation for Strategic Research (SSF), the Swedish Research Council (VR) grant nr. 2007 584, the Crafoord Foundation grant no. 2008 0841 and 2005 1123, and the Knut and Alice Wallenberg Foundation.



## REFERENCES

1. Huang, L.R., E.C. Cox, R.H. Austin, and J.C. Sturm, *Continuous Particle Separation Through Deterministic Lateral Displacement*. Science, 2004. **304**(5673): p. 987-990.
2. Holm, S.H., J.P. Beech, M.P. Barrett, and J.O. Tegenfeldt, *Separation of parasites from human blood using deterministic lateral displacement*. Lab on a Chip, 2011. **11**(7): p. 1326-1332.
3. Holm, S.H., J.P. Beech, M.P. Barrett, and J.O. Tegenfeldt, *Simplifying microfluidic separation devices towards field-detection of blood parasites*. Analytical Methods, 2016. **8**: p. 3291-3300.
4. Beech, J.P., B.D. Ho, G. Garriss, V. Oliveira, B. Henriques-Normark, and J.O. Tegenfeldt, *Separation of pathogenic bacteria by chain length*. Analytica Chimica Acta, 2018. **1000**: p. 223-231.
5. Beech, J.P., S.H. Holm, K. Adolfsson, and J.O. Tegenfeldt, *Sorting cells by size, shape and deformability*. Lab on a Chip, 2012. **12**(6): p. 1048-1051.
6. Henry, E., S.H. Holm, Z.M. Zhang, J.P. Beech, J.O. Tegenfeldt, D.A. Fedosov, and G. Gompper, *Sorting cells by their dynamical properties*. Scientific Reports, 2016. **6**.
7. Beech, J.P., P. Jonsson, and J.O. Tegenfeldt, *Tipping the balance of deterministic lateral displacement devices using dielectrophoresis*. Lab on a Chip, 2009. **9**(18): p. 2698-2706.
8. Grover, W.H., A.K. Bryan, M. Diez-Silva, S. Suresh, J.M. Higgins, and S.R. Manalis, *Measuring single-cell density*. Proceedings of the National Academy of Sciences, 2011. **108**(27): p. 10992.
9. Wolff, D.A. and H. Pertoft, *Separation of hela-cells by colloidal silica density gradient centrifugation .1. separation and partial synchrony of mitotic cells*. Journal of Cell Biology, 1972. **55**(3): p. 579-
10. Bosslet, K., R. Ruffmann, P. Altevogt, and V. Schirmmacher, *A rapid method for the isolation of metastasizing tumour cells from internal organs with the help of isopycnic density-gradient centrifugation in Percoll*. British Journal of Cancer, 1981. **44**(3): p. 356-362.
11. Wong, A.P., M. Gupta, S.S. Shevkoplyas, and G.M. Whitesides, *Egg beater as centrifuge: isolating human blood plasma from whole blood in resource-poor settings*. Lab on a Chip, 2008. **8**(12): p. 2032-2037.
12. Augustsson, P., J.T. Karlsen, H.W. Su, H. Bruus, and J. Voldman, *Iso-acoustic focusing of cells for size-insensitive acousto-mechanical phenotyping*. Nature Communications, 2016. **7**: p. 9.
13. Jeon, N.L., S.K.W. Dertinger, D.T. Chiu, I.S. Choi, A.D. Stroock, and G.M. Whitesides, *Generation of solution and surface gradients using microfluidic systems*. Langmuir, 2000. **16**(22): p. 8311-8316.



Paper VII





Cite this: DOI: 10.1039/xxxxxxxxxx

## Thermoresponsive colloidal molecules prepared using droplet-based microfluidics<sup>†</sup>

Feifei Peng,<sup>ac‡</sup> Stefan H. Holm,<sup>bc‡</sup> Linda K. Månsson,<sup>ac</sup> Somnath Ghosh,<sup>ac</sup> Jérôme J. Crassous,<sup>ac</sup> Peter Schurtenberger<sup>ac\*</sup> and Jonas O. Tegenfeldt<sup>bc\*</sup>Received Date  
Accepted Date

DOI: 10.1039/xxxxxxxxxx

www.rsc.org/journalname

A microfluidic droplet device has been used in the synthesis of colloidal molecules. Microgel particles based on the thermoresponsive polymers poly-*N*-isopropylacrylamide (PNIPAM) and poly-*N*-isopropylmethacrylamide (PNIPMAM), which exhibit different volume phase transition temperatures (VPTTs), were employed as building blocks. The microfluidic device was used to form microgel-containing water-in-oil droplets that were initially around 10  $\mu\text{m}$  in diameter. After allowing the water to evaporate through the oil and the device, compact colloidal molecule-like microgel clusters were formed. The clusters were crosslinked and redispersed in water in order to create stable colloidal molecules, where the interactions between individual particles could be selectively tuned via temperature, and varied from soft repulsive to attractive. This method offers good control over particle composition and high reproducibility in a simple way to fabricate a new type of multicomponent colloidal molecules with thermoresponsive interactions.

### 1 Introduction

For a long time, simple colloidal spheres have been used as a very popular model system to explore analogies between colloids, atoms and molecules and to investigate various phenomena in condensed matter physics and materials sciences.<sup>1–4</sup> However, in the past decade so-called colloidal molecules, clusters assembled from spherical colloids and that resemble space-filling molecular models, have emerged as more realistic model systems as they capture the anisotropic nature of atoms and molecules in terms of shape and interactions.<sup>5–7</sup> Further, colloidal molecules may also constitute important building blocks for the fabrication of more complex structures and phases than can be achieved using simple spheres, and has been a major driving theme in material science for the last decade.<sup>8–11</sup>

Colloidal molecules can be prepared through different approaches, each with its own advantages and disadvantages. Direct synthesis is a possible route,<sup>12–14</sup> whereas clustering of spherical colloids is the more common method. An example of the latter is the work of Wang *et al.* who reported an elegant approach where DNA hybridization was driving the assembly of

two types of patchy particles functionalised with complementary single-stranded DNA.<sup>15</sup> Other methods of cluster assembly build on coalescence of liquid protrusions,<sup>16,17</sup> electrostatic interactions between oppositely charged particles,<sup>18,19</sup> magnetostatic interactions between particles with embedded magnetic patches<sup>20</sup> and template-assisted geometrical confinement.<sup>21</sup>

The emulsion templating approach reported by Manoharan *et al.* is often considered the cradle of colloidal molecules.<sup>22</sup> Here, a polystyrene particle dispersion in toluene was sheared in a homogenizer together with deionized water to create an oil-in-water (O/W) emulsion, where the particles were bound to the O/W interface. By subsequent evaporative removal of the toluene the particles were compacted into dense clusters. This method has the possibility of rapidly fabricating a large number of clusters, but suffers from a wide cluster size distribution that (partially) reflects the polydispersity of the initial emulsion droplets and the lack of control in the emulsification step. In order to address these issues, Yi *et al.* developed a similar approach based on droplet microfluidics.<sup>23</sup> By using droplet microfluidics it is possible to create, with high reproducibility, emulsions consisting of uniform droplets and consequently decrease the variation in cluster size. Droplet microfluidics has recently gained widespread use for particle synthesis and has been shown capable of generating a wide range of particle types.<sup>24–26</sup> The advantage of droplet microfluidics over bulk methods stems from the dimensional scaling of microfluidics. The small systems allow for high generation frequencies, while the laminar flow results in excellent control, reproducibility and monodispersity of the emulsion droplets.

<sup>a</sup>Division of Physical Chemistry, Lund University, Lund, Sweden. E-mail: peter.schurtenberger@fchem1.lu.se

<sup>b</sup>Division of Solid State Physics, Lund University, Lund, Sweden. E-mail: jonas.tegenfeldt@fjflth.se

<sup>c</sup>NanoLund, Lund University, Lund, Sweden.

<sup>†</sup> Electronic Supplementary Information (ESI) available. See DOI: 10.1039/b000000x/

<sup>‡</sup> These authors contributed equally to this work.

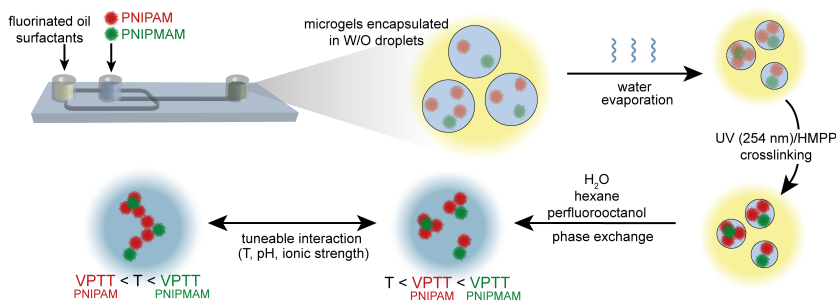


**Fig. 1** Schematic illustration showing the microfluidic generation of thermoresponsive colloidal molecules. A microfluidic flow focusing device is used to form monodisperse water droplets containing microgels. Through evaporation of the water content of the droplets, the microgel particles are forced into close contact. At this stage, the clusters can be made permanent through photocrosslinking. Following this, the clusters are washed and transferred from the oil into water where the interactions between different clusters can be studied. The interactions between microgels on different colloidal molecules can be tuned through changes in temperature, ionic strength and pH, and is dependent on the chemical nature of the building blocks.

These previously reported methods for fabricating colloidal molecules typically involve hard sphere-like colloids, such as polystyrene and poly(methyl methacrylate) (PMMA), as the basic building blocks. The resulting colloidal molecule-like clusters are expected to yield interesting assembled structures and dense phases, but the packing and interactions are governed by geometry alone.<sup>6,9</sup> In order to add an often-desired ability to tune the interactions in these systems, in this work we explore the use of thermoresponsive polymeric colloids, so-called microgels, to create colloidal molecules with a small number of directional binding sites with externally controllable and tuneable interactions. Microgels have already been widely used as versatile model systems to investigate the phase behaviour of colloidal suspensions as a function of the nature and range of the interaction potential.<sup>27–36</sup>

In the work reported here, we focus specifically on a droplet-based microfluidics approach for the assembly of thermoresponsive microgels into well-defined colloidal molecule-like clusters whose interactions can easily be tuned from soft repulsive to short-range attractive through an increase in temperature, as described schematically in Fig. 1. With this approach, “patchy” clusters were obtained from a mixture of fluorescently labelled poly-*N*-isopropylacrylamide (PNIPAM) and poly-*N*-isopropylmethacrylamide (PNIPMAM) microgels that differ with respect to the characteristic temperature, the so-called volume phase transition temperature (VPTT), at which a number of properties dramatically change, including size, volume fraction and charge density. We show that attractive interactions can be selectively induced between the colloidal molecules’ PNIPAM patches in the temperature regime in between the VPTTs for PNIPAM and PNIPMAM, much analogous to patch-patch interactions between proteins and other patchy bio-macromolecules. Not only may these colloidal molecules serve as important model systems for the study of patch-patch interactions, but might also find applications as building blocks for the construction of temperature-switchable materials in the material science area.

## 2 Materials and Methods

### 2.1 Microgel synthesis

#### 2.1.1 PNIPAM-co-AAc microgels

*N*-isopropylacrylamide monomer (NIPAM, 97%, Aldrich, 3.0 g), *N,N*-methylenebis(acrylamide) crosslinker (BIS, 99%, Sigma-Aldrich, 0.21 g, 5 mol% with respect to NIPAM), and methacryloxyethyl thiocarbonyl rhodamine B dye (MRB, Polysciences Inc., 3.0 mg) were stirred in Milli-Q water (150 mL) for 40 minutes at 60 °C and with nitrogen purging before increasing the temperature to 80 °C. At 80 °C, a solution of potassium persulphate initiator (KPS, >99%, Sigma-Aldrich, 51 mg in 20 mL of Milli-Q water) was added, followed by a solution of acrylic acid (AAc, 99.5%, Acros organics, 400 μL, 22 mol% with respect to NIPAM, in 10 mL of Milli-Q water). The reaction was allowed to proceed for 4 hours under stirring (500 rpm) before cooling down to room temperature. The microgel suspension was filtered through glass wool to remove traces of coagulum, and was thereafter purified by repeated cycles of centrifugation, decantation and redispersion.

#### 2.1.2 PNIPMAM-co-AAc microgels

*N*-isopropylmethacrylamide monomer (NIPMAM, 97%, Aldrich, 3.0 g), BIS crosslinker (0.18 g, 5 mol% with respect to NIPMAM), sodium dodecyl sulphate surfactant (SDS, >99%, Duchefa Biochemie, 13 mg) and a fluorescein isothiocyanate dye solution (prepared by reacting FITC (FITC, >90%, Sigma, 34 mg) and allylamine (AL, 98%, Aldrich, 35 μL) in a NaOH solution (10 mL, 10<sup>−4</sup> M) were stirred in Milli-Q water (132 mL) for 25 minutes at room temperature and with nitrogen purging before increasing the temperature to 80 °C. At 80 °C, a solution of KPS initiator (51 mg in 5 mL of Milli-Q water) was added, followed by a solution of AAc (355 μL, 22 mol% with respect to NIPMAM, in 10 mL of Milli-Q water). The reaction was allowed to proceed for 3 hours with stirring (500 rpm) before cooling down to room temperature. The microgel suspension was filtered through glass wool to

remove traces of coagulum, and was thereafter purified by dialysis for 2 weeks.

### 2.1.3 PNIP(M)AM-co-MA microgels

Polymerisable methacryloxy (MA) groups were attached to the carboxylic acid (CA) groups of the PNIP(M)AM-co-AAC microgels using a modified method of those reported by Liu *et al.*<sup>37</sup> and Reis *et al.*<sup>38</sup> In summary, HCl solution (2 M, 100  $\mu\text{L}/100$  g of microgel suspension) and glycidyl methacrylate (GMA, 97%, Aldrich, 1.2 mL/100 g of microgel suspension) were added to a 1 wt% PNIP(M)AM-co-AAC suspension under stirring (500 rpm). Stirring was continued for 30 minutes at room temperature, before increasing the temperature to 50 °C. Reactions were allowed to proceed for 24 hours before cooling down. The suspensions were filtered through glass wool and were then purified by means of repeated cycles of centrifugation, decantation and redispersion.

### 2.1.4 PNIP(M)AM-co-AL microgels

Using literature procedures,<sup>39,40</sup> NIP(M)AM, BIS (5 mol% with respect to NIP(M)AM) and AL (10 mol%) were co-polymerised to prepare PNIP(M)AM-co-AL microgels. KPS was used as initiator. Interparticle crosslinking of the obtained microgels was affected using glutaric dialdehyde (GDA, 50 wt%, Aldrich).

## 2.2 Droplet device design

A multitude of microfluidic methods have been shown capable of generating droplets, each with their own specific benefits and drawbacks. Much of the recent focus has been on devices which do not require any external actuation, *i.e.* passive droplet generation devices. These are often less versatile than their counterpart, active droplet generation devices, but provide on the other hand often better performance in terms of monodispersity and generation frequency. Passive droplet generation devices constitute five different modes of droplet formation (squeezing, dripping, jetting, tip-streaming and tip-multi-breaking). Each of these modes has its own specific route to how the dispersed phase liquid thread is broken up into individual droplets.<sup>41</sup> The specific mode of droplet formation depends on several parameters including device geometry, flow rates, interfacial tensions and fluid viscosities. In all modes except squeezing the droplet formation is caused by a competition between the interfacial tension and the viscous forces together with any inertial forces (if present). The interfacial tension acts to minimize the interfacial area and consequently suppresses the formation of new droplets. This is counteracted by the viscous and inertial forces, which act to deform the dispersed phase liquid thread. The competition between these forces is what determines the specific break up mode of the droplet formation. The final mode, squeezing, relies to a great extent on the confinement of the dispersed phase liquid. The liquid thread of this phase blocks the constriction for the continuous phase liquid, leading to a pressure build-up upstream, which results in the pinch off of a single droplet. In squeezing the ultimate droplet size is to a large extent coupled to the device geometry, resulting in a more stable droplet generation which is less affected by fluctuations in flow rate.<sup>42</sup> Consequently, this was the droplet formation mode which we envisioned for the current work.

Here, two different microfluidic droplet generation devices were used interchangeably, both with planar flow-focusing geometries.<sup>43–45</sup> A short device (Fig. 2A-C) was used for generating water-in-oil (W/O) droplets at a high frequency, while a longer device (Fig. 2D-F) was used to not only generate droplets, but also to monitor the shrinkage of the formed droplets that occurs as a result of solvent (water) evaporation. This longer device consisted of an identical droplet generation part but had a large section downstream consisting of six meandering channels positioned in parallel. The significantly decreased flow velocity, relative to the droplet generation part, combined with the channel length of  $\sim 40$  cm, results in long residence time for the generated droplets. The long residence time allows for observation of the droplet shrinking process that acts to compact the clusters. The residence time of droplets at a certain axial position is however expected to vary due to the parabolic flow profile, resulting in a Taylor dispersion of the sample, nonetheless this setup allows for easy visualisation of the shrinking of individual droplets before they are collected at the outlet.

In the squeezing and the dripping mode, the ratio between the droplet diameter  $d$  and the hydraulic diameter  $D_H$  of the constriction where droplets are formed is expected to scale as  $d/D_H \sim Ca^{1/3}$ ,<sup>42,46</sup> where  $D_H = 4A/P_w$ ,  $A$  is the cross sectional area of the constriction and  $P_w$  the perimeter of the cross section.  $Ca$  is the capillary number,  $Ca = U\mu/\gamma$ , which represents the ratio between viscous and interfacial stresses.  $U$  is the characteristic velocity,  $\mu$  the dynamic viscosity, and  $\gamma$  the interfacial tension. For our application, the clustering of microgel particles, the evaporation time is reduced with smaller droplets. With the constriction having a width and a height of around 10  $\mu\text{m}$ , we expect the device to form droplets with a diameter close to this size (corresponding to  $\frac{1}{2}$   $\mu\text{L}$  in volume). The other channels, apart from the constriction, were kept as wide as possible in order to focus the pressure drop to the constriction, acting to maximise the droplet generation frequency at a certain driving pressure. Fluidic simulation analysis were carried out by using MATLAB (MathWorks) in order to verify the pressure distribution in the devices. Further, it gave an indication of the relationship between residence time and driving pressure for the longer device. It should however be noted that this relationship is affected by the parabolic flow profile, resulting in a Taylor dispersion of the sample. Nonetheless, the longer channels allow for easy visualisation of the shrinking of individual droplets before they are collected at the outlet (Fig. S2†).

## 2.3 Droplet device fabrication

Microfluidic devices were fabricated using replica moulding of PDMS on SU8 patterned silicon wafers.<sup>47,48</sup> The device designs were drawn using the software L-Edit (Tanner Research). Thereafter 4'' chrome plated soda lime photomasks were fabricated by Delta Mask B.V. The silicon moulds were fabricated by depositing SU-8 2015 (MicroChem Corp.) at a thickness of 10  $\mu\text{m}$  using a spin coater (WS-400-6NPP-LITE, Laurell Technologies Corp.). This was patterned on 3'' silicon wafers using the mercury I-line in a contact mask aligner (MJB4, SÜSS MicroTec).

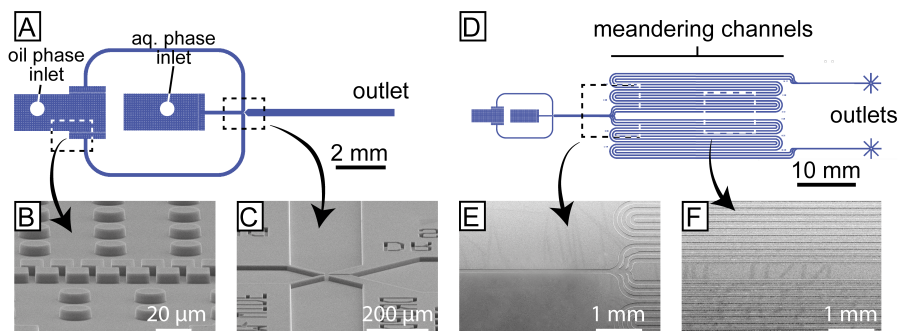


**Fig. 2** Overview of the two droplet devices used in the current study. **(A)** CAD drawing of the short, high generation frequency, flow focusing droplet device. This device contains an inlet for each phase and a single outlet. **(B)** Both inlets are equipped with a sieving structure with which unwanted particles which could potentially clog the device are removed. **(C)** The oil phase and the aqueous phase is combined at the constriction where droplets are formed. **(D)** CAD drawing of the longer meandering device. The first section is identical to that of the short device. **(E-F)** Downstream of where droplets are formed, six meandering channels have been added. By using six wide channels in parallel the flow velocity decreases significantly. Together with the lengths of the channels they provide a sufficiently long residence time of the droplets to allow for the study of droplets shrinkage.

Before casting, the master was silanised using 1H,1H,2H,2H-perfluoroctyltrichlorosilane (PFOTS, ABCR GmbH & Co. KG) to facilitate demoulding.<sup>49</sup> This was done by adding 70  $\mu\text{L}$  of PFOTS into a 5" petri dish heated to 175  $^{\circ}\text{C}$ . The procedure was carried out in the dehumidified atmosphere of a glove box. PDMS monomer mixed with 10 wt% curing agent (Sylgard 184, Dow Corning) degassed for at least half an hour, was poured onto the mould and allowed to cure for 1 hour at 80  $^{\circ}\text{C}$ . The PDMS slab was peeled off from the mould and inlet and outlet holes were punched using a 2 mm biopsy punch. To seal the device this patterned PDMS slab was bonded to a clean glass slide using oxygen plasma (Plasma Preen II-862, Plasmatic Systems). Finally, 5 mm silicon tubing (ID 3 mm, VWR) were glued (Elastosil A07, Wacker Chemie AG) to the device. The fluids were driven through the device by a pressure regulator (MFCS-4C Fluigent). Droplet formation and shrinkage were monitored by the use of an inverted microscope (Nikon Eclipse TE2000-U, Nikon Corporation), and a high-speed camera (MotionBLITZ EoSens mini, Mikrotрон) allowed for the extraction of detailed information about the droplet formation process.

## 2.4 Microfluidic cluster formation

The entire process for the successful microfluidic generation of colloidal molecules is schematically outlined in Fig. 1. To ensure integrity of the water droplets, the attractive interaction with the device walls is prevented by rendering the walls hydrophobic using PFOTS with an identical protocol as for the silanisation of the SU8 and the silicon oxide of the silicon master. The continuous phase consisted of a fluorinated oil allowing for droplet shrinkage and cluster formation by solvent evaporation as it is permeable to water vapour. In this work two different oils, HFE-7500 and FC-40 (3M), were evaluated as the continuous phase. They were

supplemented with 2 wt% surfactant Pico-Surf 1 (Dolomite). The dispersed phase consisted of a PNIPAM-co-MA or PNIPMAM-co-MA microgel suspension, or a mixture of the two. The evaporation of solvent, and consequently the clustering of microgels was monitored using the meandering device (Fig. 2D-F). A droplet's position along the channel is a measure of the time passed since its formation. The further along the channel, the smaller droplets are expected. Due to the large widths and the parallelisation of the outlet channels, the flow velocity is considerably lowered acting to evaporate the water content of the droplets before reaching the outlet. As described, the benefit of the longer meandering device is to study the cluster formation process. However, due to its length the droplet generation frequency at a specific pressure is expected to be lower than for the short device. Consequently, when a high number of clusters are needed for further characterisation and manipulation, the shorter droplet device is preferred. To acquire a large number of clusters, the generation was allowed to proceed for an extensive amount of time, up to 24 hours. At a generation frequency of around  $10\,000\text{ s}^{-1}$  this translates into around  $10^9$  droplets, which by parallelisation potentially could be increased 1-2 orders of magnitude. The droplets are initially collected in a 15 mL centrifuge tube (Falcon, Thermo Fisher Scientific), after completed droplet generation they are transferred into a glass vial. Here, a magnetic micro stir bar (VMR) is used to continuously mix the sample at room temperature. The evaporation is allowed to continue for 24 hours while oil without surfactant is sporadically added to compensate for loss of oil. Following this, CLSM is used to verify that the droplet size has decreased to an equilibrium size, which depends mainly on the Laplace pressure (acting to decrease the droplet size) and the limited ability of the microgels to interpenetrate, deform and compress (acting to maintain the droplet size).<sup>50</sup>

For crosslinking of the compact clusters, we used 2-hydroxy-



2-methylpropiophenone (HMPP, Sigma) as the photoinitiator for photocrosslinking. Due to the low solubility of HMPP in water, HMPP solutions were prepared by vortexing 500  $\mu\text{L}$  of HMPP in 49.5 mL of water (giving a nominal concentration of 1 wt%) containing the microgels for 10 minutes. After 5 minutes of rest to allow for sedimentation of excess HMPP, the top part of the mixture was extracted and used for droplet generation. After shrinking, the cluster suspension was extracted into a 10 mL glass vial which was depleted from air by purging with nitrogen. The cluster suspension was exposed to a handheld UV-lamp (UVP UVGL-15, 254 nm, 4 W) for 30 minutes to crosslink the microgel clusters.

The permanent clusters then need to be transferred from the oil phase into a continuous aqueous phase in order to enable subsequent studies. The transfer procedure builds on previous work by Abate *et al.*<sup>51</sup> and is carried out by adding 1 mL of 20 wt% perfluorooctanol (PFO) in oil to 500  $\mu\text{L}$  cluster suspension in a 15 mL centrifuge tube. The PFO acts as a demulsifier, breaking the emulsion by coalescing the dispersed aqueous phase while being vortexed for 1 minute. Four rounds of washing are subsequently needed in order to completely remove the oil and surfactants. First, 5 mL 1 wt% Span-80 in hexane is added and vortexed for 1 minute before centrifuging (Sigma 6K-15) at 3000 rpm (1830 g) for 15 min. Here, the top 6 mL is aspirated and discarded as the hexane has lowered the oil density below that of water. In the second round 1 mL of pure hexane is added, and the sample is vortexed 1 min then centrifuged (Biofuge pico) at 10 000 rpm (9500 g) for 5 min. The top 1 mL layer is aspirated and discarded. In the third washing round, 1 mL 0.1 wt% Triton X-100 in water is added, and the sample is again vortexed for 1 min and centrifuged for at 10 000 rpm (9500g) for 5 min. Also, 1 mL of the top layer is aspirated and discarded. The last round of washing is with 1 mL Milli-Q water, again vortexed for 1 min, centrifuged at 10 000 rpm (9500 g) for 5 min, and 1 mL of the top layer is discarded. The result is 500  $\mu\text{L}$  of dilute aqueous cluster suspension.

## 2.5 Dynamic light scattering (DLS)

DLS was performed using a goniometer-based light scattering instrument for static and dynamic light scattering that implements the so-called modulated 3D cross-correlation technique to suppress contributions from multiple scattering (3D LS Spectrometer, LS Instruments). Measurements were done at a wavelength  $\lambda = 660.0$  nm. The fluctuations in the intensity of the scattered light were measured at a scattering angle of  $45^\circ$  using two Avalanche photodiodes in a 3D cross-correlation configuration with a modulation unit.<sup>52</sup> 5 mm cylindrical NMR-tubes were used as sample cells. A single exponential fit of the obtained correlation functions yielded the diffusion coefficient, from which the hydrodynamic radius,  $R_H$ , was calculated using the Stokes-Einstein equation. Experimental values of  $R_H$  given correspond to the average of five consecutive measurements of 60 seconds each. Microgel swelling curves were obtained by measuring  $R_H$  as a function of temperature in the range 20 to 50  $^\circ\text{C}$ . Temperature control of the sample was ensured to  $\pm 0.1$   $^\circ\text{C}$  by regulating the vat temperature using an external water circulation thermostat.

## 2.6 Confocal laser scanning microscopy (CLSM)

Confocal micrographs were recorded on an inverted confocal laser scanning microscope (Leica DMI6000) with an SP5 tandem scanner operating in resonant mode and using a  $100\times/1.4\text{NA}$  oil immersion objective. The microscope is mounted in a thermostated enclosure that enables temperature control with an accuracy of  $\pm 0.2$   $^\circ\text{C}$ . The samples under study were kept between two cover glasses separated by a 0.12 mm spacer (Invitrogen Secure-Seal™ imaging spacer). Covalent incorporation of fluorescent rhodamine or fluorescein derivatives during microgel synthesis enabled fluorescence CLSM studies. A 543 nm HeNe and a 488 nm Ar laser were used to excite the red fluorescence of rhodamine (excitation max at 548 nm and emission max at 570 nm) and the green fluorescence of fluorescein (excitation max at 490 nm and emission max at 528 nm), respectively. Microgels and colloidal molecules were imaged at a minimum distance of 5  $\mu\text{m}$  from the bottom glass slide, unless otherwise stated.

## 2.7 Electrophoretic mobility

A Malvern Zetasizer Nano-Z (Malvern Instruments Ltd) equipped with a 633 nm 4 mW HeNe laser with automatic laser attenuator was used for electrophoretic mobility measurements. Disposable folded capillary cells (Malvern DTS1070) were used as sample cells. Measurements were performed at a fixed scattering angle of  $17^\circ$  using the M3-PALS laser interferometric technique. The electrophoretic mobility is given as the average of 5 consecutive measurements. Samples were equilibrated for 15 minutes prior to measurements.

# 3 Results and discussion

## 3.1 Microgel synthesis

The two types of colloidal building blocks used in this study, destined for assembly into colloidal molecules using a droplet-based microfluidic approach, are spherical microgel particles based on the thermoresponsive polymers PNIPAM and PNIPMAM, respectively, and dispersed in water. The two microgels were synthesised by free radical precipitation polymerisation as described in Materials and methods, yielding microgels with a dense-core fuzzy-shell morphology due to the faster reaction rate of the BIS crosslinker compared to the NIP(M)AM monomer.<sup>53,54</sup> Fluorescent rhodamine and fluorescein monomers were co-polymerised alongside NIP(M)AM and BIS to enable fluorescence CLSM studies of microgels and colloidal molecules. The size of the PNIPMAM microgels was controlled using SDS surfactant, whereas the PNIPAM microgels were synthesised under surfactant-free conditions.

In addition to NIP(M)AM, BIS and fluorophore, AAc was co-polymerised in order to incorporate CA groups. In a post-polymerisation step, the CA groups were then used as sites for attachment of polymerisable MA groups through reaction with GMA under acidic conditions and at elevated temperature (Fig. 3A). This modification step, which was adapted from Liu *et al.*<sup>37</sup> and Reis *et al.*,<sup>38</sup> thus converts PNIP(M)AM-co-AAc to PNIP(M)AM-co-MA. The attached MA groups serve as sites for further polymerisation and thereby offer the possibility to prepare crosslinked, stable

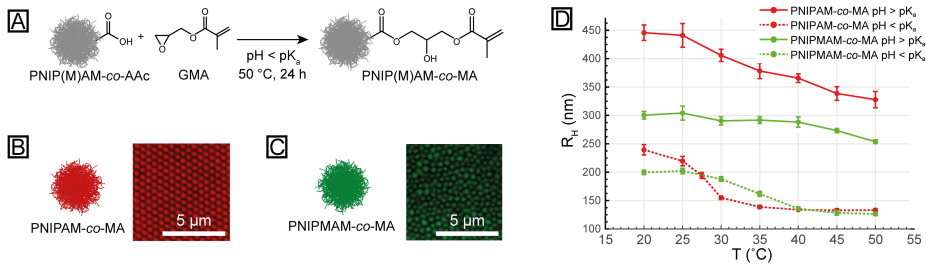


**Fig. 3** Preparation and characterisation of microgel particles. **(A)** Schematic description showing how PNIP(M)AM-co-MA microgels were obtained through attachment of GMA to CA groups on the PNIP(M)AM-co-AAc microgels under acidic conditions and 50 °C. **(B)** and **(C)** Schematic drawings of the two microgel particles used in this study together with CLSM micrographs recorded at 4.6 and 4.2 wt%, respectively, at 20 °C and under salt-free conditions. **(D)** Swelling curves illustrating the temperature dependence of the microgels' hydrodynamic radius  $R_H$  at  $\text{pH} > \text{pK}_a$  (Milli-Q water) (solid lines) and  $\text{pH} < \text{pK}_a$  (HCl aq. pH 3) (dashed lines).

colloidal molecules through photopolymerisation, where dissociation into the constituent microgel building blocks is prevented. In order to increase the crosslinking efficiency, we aimed for a high MA density in the loosely crosslinked microgel shell, at the point where neighbouring microgels can overlap. This was accomplished by introducing AAC to the reaction mixture only after initiation, and the distribution of MA groups naturally follows the same pattern. It is worth pointing out that the number of CA groups that were *de facto* incorporated during microgel synthesis was not determined in this study, and the efficiency of converting the CA groups to MA was also not quantified. Based on the study of Liu *et al.*,<sup>37</sup> we have reason to believe that the AAC-to-MA conversion is far from complete and that the majority of the CA groups remain. Still, as was also shown by Liu *et al.*, the conversion is sufficient for crosslinking to be effective. This is discussed in more detail in section 3.3.

### 3.2 Microgel characterisation

Schematic representations together with fluorescence CLSM micrographs of the two microgels used in this study, rhodamine-labelled PNIPAM-co-MA and fluorescein-labelled PNIPMAM-co-MA, are shown in Fig. 3B and C, respectively. The high degree of monodispersity of the PNIPAM-co-MA microgels was reflected in their ability to crystallise, here at 4.6 wt%. The crystalline regime for the PNIPMAM-co-MA system was never explored.

The thermoresponsive behaviour of the PNIP(M)AM-co-MA microgels was studied by DLS, by monitoring the temperature dependence of the hydrodynamic radius  $R_H$  (Fig. 3D). Linear PNIPAM and PNIPMAM both possess a lower critical solution temperature (LCST). For the corresponding microgels this is reflected in a volume phase transition when heated above a critical temperature referred to as the volume phase transition temperature (VPTT), 32 °C for PNIPAM and 45 °C for PNIPMAM, at which water is expelled as a response to poor solvent quality. In the present study, measurements were performed both in Milli-Q wa-

ter ( $\text{pH} > \text{pK}_a = 4.5$  of AAC) and in aqueous HCl solution ( $\text{pH} 3 < \text{pK}_a$ ) to illustrate the effect of pH. As is evident from Fig. 3D, pH has a strong effect on  $R_H$  throughout the probed temperature range. At  $\text{pH} > \text{pK}_a$ , the residual CA groups are deprotonated and charged, which contributes to strong osmotic swelling. The osmotic swelling is reduced as the pH is lowered to  $\text{pH} < \text{pK}_a$ , where the CA groups are protonated and uncharged, which is reflected in a decrease in  $R_H$ . The decrease in  $R_H$  is larger for the PNIPAM-co-MA than for the PNIPMAM-co-MA microgels, which suggests that the PNIPAM-co-MA microgels carry a larger number of CA groups.

Also the overall swelling behaviour is affected by pH: the gradual volume phase transitions observed at  $\text{pH} > \text{pK}_a$  become more narrow as the pH is reduced to  $\text{pH} < \text{pK}_a$  where the osmotic swelling is reduced. Worth noticing is also a shift of the VPTT to lower temperatures compared to what is traditionally reported for pure PNIPAM and PNIPMAM microgels, which could be explained by the MA modification. Furthermore, the VPTT of PNIPMAM has shifted more than that of PNIPAM, which might be an indication of a greater efficiency of incorporation of CA groups and/or of AAC-to-MA conversion. We consider the decrease in VPTT an interesting and potentially useful side effect, since a number of microgel and microgel suspension properties (size, charge density, volume fraction, interaction behaviour) can now be affected at lower temperatures. The VPTTs of the two microgels, each taken as the temperature corresponding to the point of steepest slope in the curves measured at pH 3, are given in Table 1 together with  $R_{H,\text{pH}3}^{20^\circ\text{C}}$  and the swelling ratio  $\alpha_{\text{pH}3}$ , which is defined as

$$\alpha_{\text{pH}3} = \frac{\left(R_{H,\text{pH}3}^{20^\circ\text{C}}\right)^3}{\left(R_{H,\text{pH}3}^{50^\circ\text{C}}\right)^3}$$

$\alpha_{\text{pH}3}$  differs somewhat between the two microgels, which might again be due to differences in incorporation of CA groups and/or in AAC-to-MA conversion.

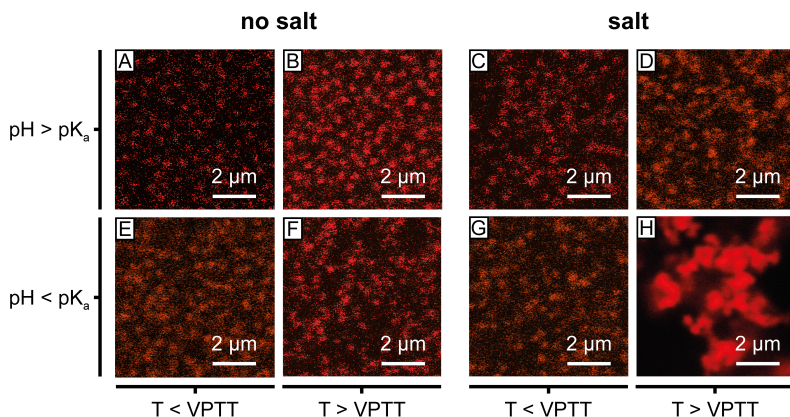


**Fig. 4** CLSM micrographs illustrating the effect of temperature (20 or 35 °C, *i.e.* below or above the VPTT), ionic strength (no salt added or 0.1 M KCl) and pH (in Milli-Q water or HCl aq. pH 3) on the interactions between the PNIPAM-co-MA microgels at 1.6 wt%. (H) At low pH and high ionic strength, an increase in temperature beyond the VPTT effectively induces attractive interactions resulting in the formation of a volume-spanning network structure. (A-G) With no added salt and/or at pH > pK<sub>a</sub> the suspensions remain liquid on increasing the temperature beyond the VPTT.

The volume phase transition observed by DLS is accompanied by an increase in charge density, as was reflected by an increase in the measured electrophoretic mobilities  $\mu$  (Table 1). At 20 °C the two microgels have nearly the same mobility, whereas at 55 °C, where the two are close to equal in size, the mobility of the PNIPAM-co-MA microgels is higher, indicating a larger number of charges. The measurements were performed at pH 3, where the majority of the CA groups are protonated and uncharged. The measured mobility thus stems from, to a smaller extent, deprotonated CA moieties, and, to a greater extent, from covalently bound charged initiator residuals. Since the extent of protonation of the CA groups depends on pH, the electrophoretic mobility does too. In the present study the pH dependence of  $\mu$  was never investigated, however.

Temperature not only influences microgel size and charge, but it affects microgel-microgel interactions as well. Under conditions where the electrostatic stabilisation is strongly screened, an increase in temperature across the VPTT causes reversible association of the microgels as the steric stabilisation is lost, the Hamaker constant is considerably increased and the attractive van der Waals as well as hydrophobic interactions become important. This behaviour is illustrated in Fig. 4 using the PNIPAM-co-

MA microgels, where CLSM micrographs recorded as a function of ionic strength, pH and temperature are displayed. At temperatures below the VPTT, all suspensions exhibit a liquid structure irrespective of ionic strength and pH (Fig. 4A, C, E and G). On increasing the temperature to above the VPTT, a volume-spanning network forms in the case of high ionic strength and pH < pK<sub>a</sub> (Fig. 4H), whereas high ionic strength or low pH alone is not sufficiently reduce the electrostatic stabilisation and these suspensions remain liquid (Fig. 4B, D and F). In summary, at high ionic strength both temperature and pH can be used to effectively tune the microgel-microgel interactions. From this follows that colloidal molecules constructed from these microgel building blocks would possess interaction sites that (under conditions of high salinity) respond to both temperature and pH, and that a combination of low pH and high temperature is required to induce attractions between the interaction sites.

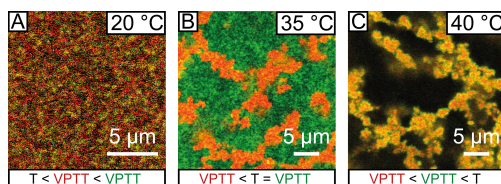


**Fig. 5** In a binary mixture of the PNIPAM-co-MA (red) and PNIPMAM-co-MA (green) microgels (0.8 wt% of each, 1.6 wt% in total) at high ionic strength (0.1 M KCl) and low pH (HCl aq. pH 3), temperature can be used to switch between (A) a repulsive-repulsive (20 °C), (B) an attractive-repulsive (35 °C) and (C) an attractive-attractive regime (40 °C).

**Table 1** Selected characteristics of the PNIPAM-co-MA and PNIPMAM-co-MA microgels

	PNIPAM-co-MA	PNIPMAM-co-MA
$R_{H,pH3}^{20^\circ C}$ (nm)	239±9	200±4
$\alpha_{pH3}$	5.8	3.9
$VPTT_{pH3}$ (°C)	29	35
$\mu_{pH3}^{20^\circ C}$ (m <sup>2</sup> /Vs)	$(-0.44±0.02) \times 10^{-8}$	$(-0.48±0.01) \times 10^{-8}$
$\mu_{pH3}^{25^\circ C}$ (m <sup>2</sup> /Vs)	$(-3.16±0.04) \times 10^{-8}$	$(-2.62±0.08) \times 10^{-8}$

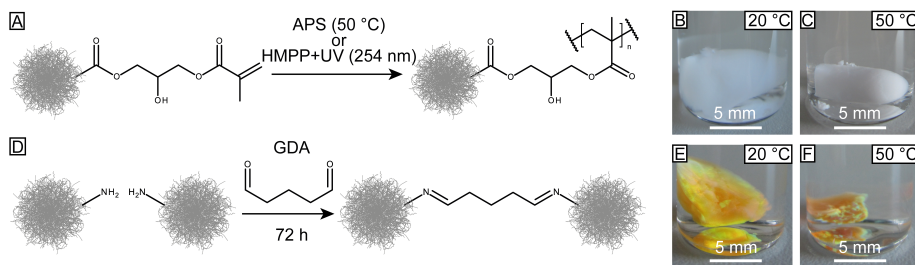


**Fig. 6** (A) Reaction scheme for the crosslinking of PNIP(M)AM-co-MA microgels, effected through photopolymerisation of the MA groups, initiated using HMPPP photoinitiator or APS thermal initiator. (B-C) Thermoresponsive macrogels based on PNIPAM-co-MA were obtained through addition of APS initiator at temperatures above the VPTT and at 0.1 M KCl. (D) Reaction scheme for the crosslinking of PNIP(M)AM-co-AL microgels using the bifunctional crosslinker GDA. (E-F) Thermoresponsive macrogels based on PNIP(M)AM-co-AL were obtained through addition of GDA to dense microgel suspensions at room temperature.

Moreover, in a binary mixture of the two microgels, at low pH and high ionic strength the two components are well-dispersed at 20 °C (Fig. 5A). An increase in temperature from 20 °C ( $T < VPTT_{\text{PNIPAM-co-MA}}, VPTT_{\text{PNIPMAM-co-MA}}$ ) to 35 °C ( $VPTT_{\text{PNIPAM-co-MA}} < T = VPTT_{\text{PNIPMAM-co-MA}}$ ) then allows for selective induction of attractive interactions among the PNIPAM-co-MA microgels, whereas the PNIPMAM-co-MA microgels remain repulsive (Fig. 5A and B). In the 35 °C micrograph (Fig. 5B), the individual PNIPMAM-co-MA microgels cannot be distinguished due to fast motion in combination with high line and frame averaging during imaging, but give rise to a smeared-out, green background. At 40 °C ( $VPTT_{\text{PNIPAM-co-MA}}, VPTT_{\text{PNIPMAM-co-MA}} < T$ ) also the PNIPMAM-co-MA microgels experience attractive interactions and decorate the already formed, red network (Fig. 5C). In summary, these results show that, in the binary mixture, temperature can be used to switch between three different interaction regimes: repulsive-repulsive, attractive-repulsive and attractive-attractive at low, intermediate and high temperature, respectively. This means that the preparation of patchy colloidal molecules from the binary mixture allows for induction of patch-patch attractions specific to the PNIPAM-co-MA constituents, much analogous to patch-patch interactions among proteins and other patchy bio-colloids.

### 3.3 Microgel-microgel crosslinking

To confirm that the PNIP(M)AM-co-MA microgels were able to form permanent microgel-microgel crosslinks, macrogels of several cubic centimetres in size were prepared (Fig. 6B). Here, microgel suspensions at high ionic strength (0.1 M KCl) were first heated to above the VPTT of the microgels to form gels. The gels could then be made permanent through the addition of ammonium persulphate (APS), a thermal free radical initiator capable of initiating polymerisation of the MA groups on neighbouring microgels (Fig. 6A). The formation of the macrogels thus confirms the feasibility of our crosslinking strategy, based on the presence of MA groups in combination with a free radical initiator. Furthermore, an important observation was that the macrogels retain the thermoresponsive behaviour of the individual microgels,

which was evidenced by shrinkage of the macrogels at temperatures above the VPTT (Fig. 6C). The observed deswelling was completely reversible, and the macrogels recovered their initial size and shape on cooling down to temperatures below the VPTT.

It is worth mentioning that another crosslinking strategy was also explored in this study. Here, microgel building blocks were prepared according to methods described by Shah *et al.*<sup>40</sup> and Hu *et al.*,<sup>55</sup> where NIP(M)AM and AL were co-polymerised to form amine-functionalised microgels (PNIP(M)AM-co-AL). The primary amine groups were then used as “handles” to effect microgel-microgel crosslinking through the use of the bifunctional crosslinker GDA (Fig. 6D). With this approach, thermoresponsive macrogels were successfully obtained (Fig. 6E and F) through the addition of GDA to dense microgel pellets obtained by centrifugation. However, extending this strategy to the microfluidics device did not yield permanently crosslinked colloidal molecule-like microgel clusters, as was evidenced by the redispersion of individual microgels after transfer of the clusters into water. We hypothesize that this is due to the GDA partitioning into the continuous oil phase (FC-40) instead of staying in the dispersed microgel-containing water droplets where the crosslinking should take place. Alternatively, it might be so that the amine groups are consumed in intraparticle crosslinking already before cluster formation and putative interparticle crosslinking; naturally only interparticle crosslinking contributes to the formation of stable colloidal molecule-like clusters.

### 3.4 Microfluidic formation of colloidal molecules

W/O droplets containing microgels (0.002 wt% PNIPAM-co-MA and 0.0021 wt% PNIPMAM-co-MA) were successfully generated with the flow focusing droplet device described in detail in section 2.2. Within the driving pressure range used in this study (700-1000 mBar) the device was consistently operating in the squeezing mode, as expected. This allows for a high generation frequency of relatively small droplets with high monodispersity. In order to quantify the droplet diameter 2835 droplets were measured by using a particle detection algorithm in the software ImageJ<sup>56</sup> (Fig. 7). The applied pressures were  $P_o = 922$  mBar

and  $P_w = 956$  mBar for the oil and water pressure, respectively. A Gaussian fit ( $R^2 = 0.992$ ) gives a droplet diameter of  $10.24 \pm 0.23 \mu\text{m}$ , which translates into a coefficient of variation,  $CV \equiv \sigma/\mu = 2.2\%$ , signifying a low polydispersity (Movie S1†).

Depending on the device used, the droplets were either directly extracted following generation or, in case of using the longer meandering device, allowed to reside in the device for an extended amount of time. This was done in order to enable visualisation of the droplet shrinking process, which takes place due to the evaporation of water. The advantage with the shorter droplet generation device was its much higher droplet generation frequency, which was a result of the lower fluidic resistance. Consequently, this device was used in order to acquire a large amount of clusters for further processing and characterisation. Droplets were generated for an extensive amount of time, often up to  $\sim 24$  hours. During these experiments it is essential that the droplet diameter is constant, as a change in the diameter may be reflected in the distribution of microgels per droplet, and consequently the final cluster size. A major cause of variations in droplet size over the course of a measurement is device clogging, which is especially critical if it occurs at the droplet generation constriction. This is due to several factors, including the significant change it would cause to the hydraulic resistance of the device, and consequently the flow rates. In addition, the droplet size is expected to change due to its high dependency on the constriction size. In order to maintain stable droplet generation through the measurements, the continuous phase was sterile filtered using a  $0.2 \mu\text{m}$  syringe filter (VWR). Even so, unwanted particles may also stem from the device fabrication, PDMS debris is for example generated when punching the holes for the inlets and outlet. To catch these the inlets were equipped with sieving structures with constrictions down to  $8 \mu\text{m}$ , smaller than the droplet generating constriction. By taking these precautions, the devices were able to generate droplets for extensive amounts of time with only minor deviations from the starting size (typically the droplet diameter increased by a few percent in 24 hours). The increase in size is believed to mainly be caused by debris which have been caught by the filter. The hydraulic resistance, the flow rate, and ultimately the droplet size, is affected much less by debris in the filter than in the droplet-generating constriction.

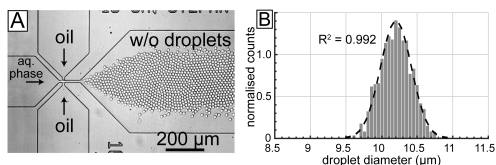


**Fig. 7** Characterization of droplet device performance. **(A)** Micrograph of droplet formation with a frequency of 17.3 kHz. The aqueous phase and the oil phase (HFE-7500) meet at the constriction. Here, the pressures applied across the device are 922 mBar and 956 mBar for the oil and aqueous phase respectively. **(B)** The droplet diameter is, for the flow rates used in this study, to a large extent determined by the size of the constriction ( $10 \mu\text{m}$ ). The variation in size is low with a measured coefficient of variation of 2.2%.

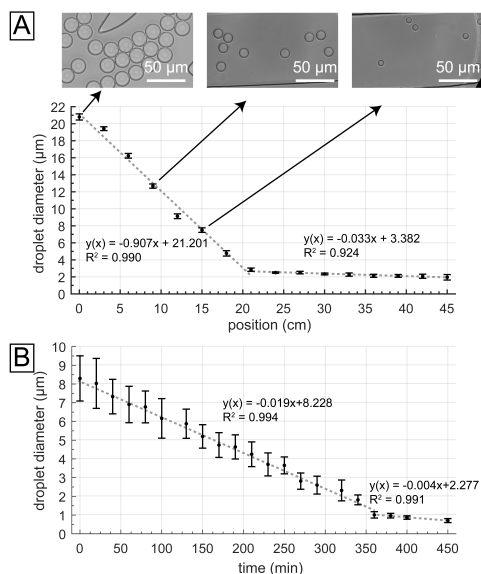


**Fig. 8** Evaporation of the water content of droplets in order to induce clustering of the microgels. **(A)** With the long meandering device, the shrinking of droplets could be measured *in-situ*. The mean droplet diameter decreases linearly with the axial position in the meandering channels. At around 20 cm, where the droplets have shrunk almost completely, the shrinking rate decreases considerably. This slow shrinking of droplets is believed to be enabled by rearrangement of the microgels inside the droplets. **(B)** For the short droplet generation device, the shrinking rate was measured off-chip. The variation in droplet diameters is in part caused by the droplets being generated over the course of 2 hours.  $t = 0$  denotes the time point at which droplets were transferred from the device to the petri dish. Although the variance is large, the droplet diameter seems to decrease linearly with time.

The droplet shrinking was carried out *in-situ* for the longer meandering device, and off-chip for the shorter droplet generation device, respectively. For the meandering device, Fig. 8A, the droplet diameter is presented as a function of the length travelled inside the meandering device, with  $x = 0$  being where the main channel is split up into the six parallel meandering channels. At around  $\sim 20$  cm into the meandering channels, the droplets are close to their minimum size. However, the shrinking seems to continue, only at a very limited rate. The position gives a rough idea of the time evolution of the shrinking, but since the velocity of the flow decreases along the channel, the relationship between the position and residence time of the droplets is not expected to be perfectly linear. A decrease in flow rate is expected as the water in the droplets evaporates and escapes through the PDMS. In addition, due to the parabolic flow profile, the droplets will exhibit different flow velocities depending on their position in the channel. Together with the Taylor dispersion, this makes it difficult to establish a precise relationship between droplet position

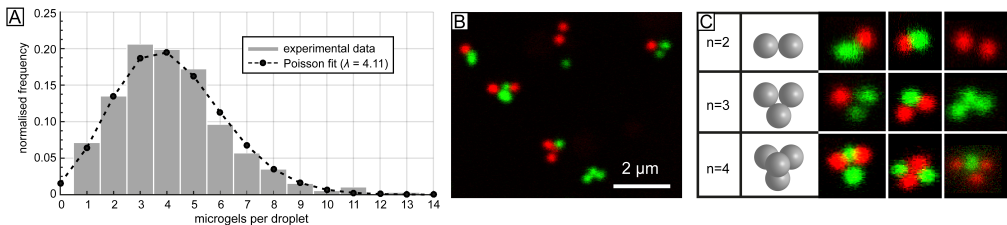


**Fig. 9** Distribution of microgels per cluster. **(A)** By approximating the encapsulation of microgels as independent events the number of microgels per droplet (and consequently per cluster) is expected to follow a Poisson distribution. The Poisson fit shows the expected number of microgels per droplet at formation, calculated from the zero-truncated Poisson distribution. The Poisson fit shows the expected number of microgels per droplet at formation, calculated from the zero-truncated Poisson distribution. **(B)** Chemically crosslinked clusters of PNIPAM (red) and PNIPMAM (green) in water. **(C)** At maximum shrinking of the droplets, clusters are forced to adopt certain conformations in order to maximise the packing efficiency, which are retained after crosslinking and transfer to water.

and residence time.

To monitor the shrinking as a function of time, particles generated with the shorter droplet generation device (Fig. 8B), are transferred off-chip into a glass vial for water evaporation. In the vial, evaporation was accelerated by stirring with a stir bar, meanwhile the pure HFE-7500 was added to prevent the emulsion from drying out. Due to the time taken to generate the droplets, they have already been able to shrink to a varying degree in the device before being transferred to the vial, which resulted in a broader droplet size distribution with larger standard deviations as compared to the situation in the long device (Fig. 8A and B).

Considering that the evaporation rate is proportional to the surface area of the droplets we would expect a linear decrease of droplet radius with time according to

$$\frac{dV}{dt} = -kA \Leftrightarrow \frac{dR}{dt} = -k$$

with  $V$ ,  $A$ ,  $R$  and  $k$  being the volume, area, radius and a positive constant respectively. For both cases, droplet shrinkage *in-situ* and off chip, an initial large decrease in droplet size can be observed (Fig. 8A and B). At some point the shrinking slows down to a very limited rate, due to steric hindrance by the microgels. At this point we believe that further solvent evaporation is enabled by the rearrangement of the microgels inside the droplets. Maximum droplet shrinkage or the minimal droplet radius is primarily given by the limited ability of microgels to interpenetrate, deform and compress as a result of their core-shell structure and the resulting swelling pressure.<sup>50,57,58</sup>

To ensure that the microgels were allowed to rearrange to a maximum extent, the droplets were given  $\sim 24$  hours to allow additional microgel rearrangements and subsequent droplet shrinkage to take place. With the droplets at their minimum size, the microgels are forced into close proximity (Fig. S4†). At this position the clusters were made permanent by crosslinking neighbouring microgels by activating HMPP with UV-light.

The relatively large droplet size ( $\sim 10 \mu\text{m}$ ) in comparison to the small size of the microgels ( $0.8 \mu\text{m}$ ) allows us to approximate the encapsulation of these particles as being independent events. This, together with the low variation in the droplet volume means

that the number of microgels per droplet can be assumed to follow a Poisson distribution. However, due to optical limitations the droplet content could only be correctly quantified for microgel-containing shrunken droplets, whereas empty droplets could not be measured. Consequently, the measured number of microgels per droplet is expected to instead follow a zero-truncated Poisson (ZTP) distribution with a probability mass function of

$$P(X = x) = \frac{\lambda^x}{(e^\lambda - 1)x!}$$

where  $k = 1, 2, 3, \dots$ , is the number of microgels per droplet and  $\lambda > 0$  is the average number of microgels per droplet before shrinking. After shrinking the expected value is instead given by

$$E[X] = \lambda \frac{1}{(1 - f(k=0; \lambda))} = \frac{\lambda}{1 - e^{-\lambda}}$$

with  $f(k; \lambda)$  denoting a standard Poisson distribution. A total of 408 shrunken droplets (PNIPAM-co-MA, 0.0027 wt%) in oil were measured (Fig. 9A), and the acquired mean number of microgels per droplets after shrinking was 4.18. By putting this value into the equation for the expected value of the ZTP distribution we can calculate the mean value of the initial encapsulation of microgels  $\lambda = 4.11$ . The discrepancy of the means is low due to the fact that the mean number of microgels per droplet is relatively high and the fraction of empty droplets is low,  $f(k=0; \lambda = 4.11) = 1.6\%$ . In order to verify that our data follows the ZTP distribution we used the chi-square goodness of fit test with a null hypothesis ( $H_0$ ) that the data follows this distribution. The chi square test is then

$$\chi^2_{k-2} = \sum_k \frac{(f_o - f_e)^2}{f_e} = 2.38$$

where  $f_o$  is the observed frequency,  $f_e$  the expected frequency under ZTP,  $k$  the number of possible outcomes (microgels per droplets) with an expected frequency larger than 1 (in our measurements the value is  $k = 10$ ). With a 0.05 level of significance and a  $k - 2 = 8$  degrees of freedom we get a percentage point of 15.51 for the chi-square distribution. Since  $\chi^2 = 2.38 < 15.51$  the decision is to not reject  $H_0$ . Our measured data is thus in

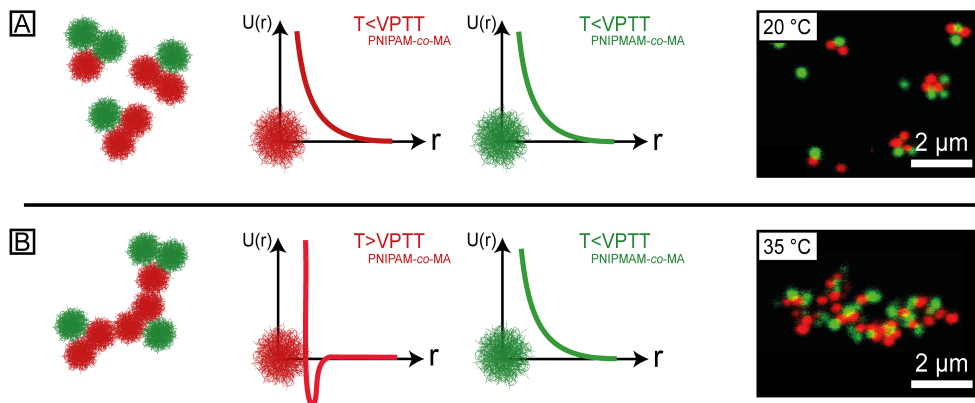


**Fig. 10** Interactions between microgel clusters or colloidal molecules with temperature. (A) At temperatures below the VPTT of both microgels, both types of interaction sites possess a soft repulsive potential and the clusters are non-attractive. (B) When the temperature is raised above the VPTT of the PNIPAM-co-MA microgels (red), their interactions become attractive and the clusters become effectively patchy. The two micrographs were recorded at 20 and 35 °C, respectively, at  $\text{pH} < \text{pK}_a$  (HCl aq. pH 3) and high salinity (0.1 M KCl).

agreement with a cluster distribution given by the ZPT distribution.

The washing and the subsequent transfer of the crosslinked clusters from the oil phase into a continuous aqueous phase initially proved difficult, with a relatively large fraction of the clusters being retained in the oil phase. After initial tries with the perfluorinated oil FC-40 we switched to the semifluorinated oil HFE-7500 due to a higher solubility in organic solvents that would increase the efficiency of oil removal and phase transfer of the clusters. Furthermore, the HFE-7500 exhibits a larger water solubility compared to FC-40, which lead to shorter droplet shrinking time.

Fig. 9B and C shows CLSM micrographs of crosslinked microgel clusters in water consisting of various numbers of microgel particles. Depending on the final application of the thermoresponsive clusters, the number of microgels per cluster can be altered by adjusting the droplet size (encapsulated volume) (Fig. S3†) or the initial concentration of the microgel suspension. In order to circumvent the Poisson distribution, other strategies such as pre-focusing of the microgels<sup>59</sup> or sorting of the finalised clusters can be employed.

### 3.5 Interactions between colloidal molecules with temperature, pH and ionic strength

The thermoresponsive behaviour of the mixed, or “patchy”, colloidal molecule-like clusters consisting of PNIPAM-co-MA and PNIAM-co-MA microgels was studied by CLSM (Fig. 10). The colloidal molecules were imaged at high ionic strength (0.1 M KCl) and  $\text{pH} < \text{pK}_a$  (HCl aq. pH 3), at 20 ( $T < \text{VPTT}_{\text{PNIPAM-co-MA}}$ ,  $\text{VPTT}_{\text{PNIAM-co-MA}}$ ) and 35 °C ( $\text{VPTT}_{\text{PNIPAM-co-MA}} < T = \text{VPTT}_{\text{PNIAM-co-MA}}$ ). At 20 °C, both types of microgel interac-

tion sites possess a repulsive interaction behaviour, and individual colloidal molecules were observed (Fig. 10A). In contrast, at 35 °C, many large aggregate structures were found in the sample, due to the transition of the PNIPAM-co-MA microgels from the repulsive to the attractive regime (Fig. 10B). These observations confirm that the interaction behaviour observed in the binary microgel mixture (Fig. 5) is conferred to the corresponding colloidal molecules, and that the constituent microgels can effectively serve as interaction sites. In summary, using temperature as an external stimulus allows us to, in a facile way, control the interactions in the patchy colloidal molecules system, with the possibility to, in a selective manner, induce attractive patch-patch-type interactions between one type of interaction site alone (Movie S2 and S3†).

## 4 Conclusions

The strive for using self-assembly to fabricate materials with improved or novel properties has led to a rapid development of colloidal building blocks with increasing complexity. In particular the synthesis of patchy or molecule-like particles has been explored by various researchers. This is for example driven by the need of obtaining low-density crystal structures in order to obtain photonic materials with a complete band gap, which is very difficult to achieve with spherical particles interacting via a centrosymmetric potential only. While a number of successful strategies for making colloidal molecules has been presented in the past, their ability to form the required low-density single-crystal structures with a large size and free of defects has been limited. This is primarily due to a lack of tunability and external control of the interactions between the attractive patches, which makes it very difficult to grow large crystals with the necessary degree of perfection, as the particles aggregate in a rather uncontrolled

way and the systems frequently become trapped in an arrested glassy or amorphous state. The lack of control over the patchy interactions then also makes it difficult to use annealing processes that can be successfully used in molecular systems. We believe that the use of colloidal molecules formed by thermoresponsive particles could offer a promising route for making such materials. Our results demonstrate that we can fabricate colloidal molecules based on the spontaneous evaporation of water-in-oil emulsion droplets. Droplet-based microfluidics allows for an exact control over the precursor particle composition and concentration, resulting in control over the number and thermoresponsive and ionic nature of the interaction sites. The inherent thermo- and pH-responsive properties of the microgels gives us the ability to finely tune the interactions between different patches/interaction sites with temperature, pH and ionic strength. While the current study has shown the feasibility of such an approach, future work will have to address the quantitative investigation of the resulting directional interactions, the phase behaviour and the self-assembly of mixtures of colloidal clusters as a function of concentration and temperature. While the currently used microgels are of limited use for making for example photonic materials due to their low optical density, there exist a number of pathways to create core-shell architectures that combine inorganic, metallic or magnetic particle cores with a thermoresponsive microgel shell<sup>60–64</sup> required for the crosslinking step and the exquisite external control over the directional patchy interactions demonstrated in this article. We believe that the use of such hybrid particles combined with the application of droplet-based microfluidics fabrication methods provides us with an exciting opportunity for the creation of novel and responsive materials.

## Acknowledgments

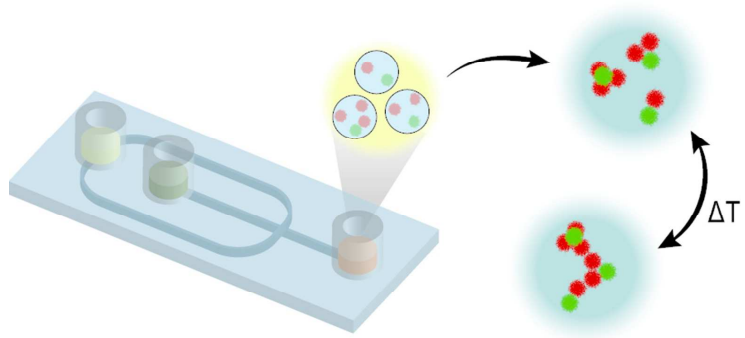
We thank Alfredo Lanzaro for helpful discussions. The authors acknowledge financial support from the European Research Council (ERC-339678-COMPASS), the Swedish Research Council (VR 2015-05426), the Knut and Alice Wallenberg Foundation (KAW 2014.0052), the Sten K. Johnson Foundation and NanoLund at Lund University. All device fabrication was carried out in Lund Nano Lab.

## References

- 1 P. N. Pusey and W. Van Megen, *Nature*, 1986, **320**, 340–342.
- 2 P. N. Pusey and W. van Megen, *Phys. Rev. Lett.*, 1987, **59**, 2083.
- 3 P. Pusey, W. Van Megen, P. Bartlett, B. Ackerson, J. Rarity and S. Underwood, *Phys. Rev. Lett.*, 1989, **63**, 2753.
- 4 W. Van Megen and P. Pusey, *Phys. Rev. A*, 1991, **43**, 5429.
- 5 A. van Blaaderen, *Science*, 2003, **301**, 470–471.
- 6 F. Li, D. P. Josephson and A. Stein, *Angew. Chem., Int. Ed.*, 2011, **50**, 360–388.
- 7 E. Duguet, A. Desert, A. Perro and S. Ravaine, *Chem. Soc. Rev.*, 2011, **40**, 941–960.
- 8 S. Sacanna and D. J. Pine, *Curr. Opin. Colloid Interface Sci.*, 2011, **16**, 96–105.
- 9 Y. Wang, Y. Wang, D. R. Breed, V. N. Manoharan, L. Feng, A. D. Hollingsworth, M. Weck and D. J. Pine, *Nature*, 2012, **491**, 51–61.
- 10 S. C. Glotzer and M. J. Solomon, *Nat. Mater.*, 2007, **6**, 557–562.
- 11 G.-R. Yi, D. J. Pine and S. Sacanna, *J. Phys.:Condens. Matter*, 2013, **25**, 193101.
- 12 J.-W. Kim, R. J. Larsen and D. A. Weitz, *Adv. Mater.*, 2007, **19**, 2005–2009.
- 13 A. Perro, E. Duguet, O. Lambert, J.-C. Taveau, E. Bourgeat-Lami and S. Ravaine, *Angew. Chem., Int. Ed.*, 2009, **48**, 361–365.
- 14 J.-G. Park, J. D. Forster, E. R. Dufresne *et al.*, *Langmuir*, 2009, **25**, 8903.
- 15 Y. Wang, Y. Wang, D. R. Breed, V. N. Manoharan, L. Feng, A. D. Hollingsworth, M. Weck and D. J. Pine, *Nature*, 2012, **491**, 51–55.
- 16 D. J. Kraft, W. S. Vlug, C. M. van Kats, A. van Blaaderen, A. Imhof, W. K. Kegel *et al.*, *J. Am. Chem. Soc.*, 2009, **131**, 1182–1186.
- 17 D. J. Kraft, J. Groenewold and W. K. Kegel, *Soft Matter*, 2009, **5**, 3823–3826.
- 18 N. B. Schade, M. C. Holmes-Cerfon, E. R. Chen, D. Aronzon, J. W. Collins, J. A. Fan, F. Capasso and V. N. Manoharan, *Phys. Rev. Lett.*, 2013, **110**, 148303.
- 19 A. F. Demirörs, J. C. P. Stiefelhagen, T. Vissers, F. Smalenburg, M. Dijkstra, A. Imhof and A. van Blaaderen, *Phys. Rev. X*, 2015, **5**, 021012.
- 20 S. Sacanna, L. Rossi and D. J. Pine, *J. Am. Chem. Soc.*, 2012, **134**, 6112–6115.
- 21 Y. Yin, Y. Lu, B. Gates and Y. Xia, *J. Am. Chem. Soc.*, 2001, **123**, 8718–8729.
- 22 V. N. Manoharan, M. T. Elsesser and D. J. Pine, *Science*, 2003, **301**, 483–487.
- 23 G. R. Yi, T. Thorsen, V. N. Manoharan, M. J. Hwang, S. J. Jeon, D. J. Pine, S. R. Quake and S. M. Yang, *Adv. Mater.*, 2003, **15**, 1300–1304.
- 24 A. P. L. Lung-Hsin Hung, *J. Med. Biol. Eng.*, 2007, **27**, 1–6.
- 25 J. H. Kim, T. Y. Jeon, T. M. Choi, T. S. Shim, S.-H. Kim and S.-M. Yang, *Langmuir*, 2014, **30**, 1473–1488.
- 26 D. T. Chiu, A. J. deMello, D. Di Carlo, P. S. Doyle, C. Hansen, R. M. Maceiczkyk and R. C. R. Wootton, *Chem*, 2017, **2**, 201–223.
- 27 P. J. Yunker, K. Chen, M. D. Gratale, M. A. Lohr, T. Still and A. Yodh, *Rep. Prog. Phys.*, 2014, **77**, 056601.
- 28 J. Wu, B. Zhou and Z. Hu, *Phys. Rev. Lett.*, 2003, **90**, 048304.
- 29 J. Zhou, G. Wang, L. Zou, L. Tang, M. Marquez and Z. Hu, *Biomacromolecules*, 2008, **9**, 142.
- 30 G. Romeo, A. Fernandez-Nieves, H. M. Wyss, D. Acierno and D. A. Weitz, *Adv. Mater.*, 2010, **22**, 3441–3445.
- 31 A. Zacccone, J. J. Crassous, B. Béri and M. Ballauff, *Phys. Rev. Lett.*, 2011, **107**, 168303.
- 32 P. Holmqvist, P. Mohanty, G. Nägele, P. Schurtenberger and M. Heinen, *Phys. Rev. Lett.*, 2012, **109**, 048302.
- 33 S. Nöjd, P. S. Mohanty, P. Bagheri, A. Yethiraj and P. Schurten-



- berger, *Soft Matter*, 2013, **9**, 9199–9207.
- 34 A. Zaccone, J. J. Crassous and M. Ballauff, *J. Chem. Phys.*, 2013, **138**, 104908.
- 35 D. Paloli, P. S. Mohanty, J. J. Crassous, E. Zaccarelli and P. Schurtenberger, *Soft Matter*, 2013, **9**, 3000–3004.
- 36 P. S. Mohanty, D. Paloli, J. J. Crassous, E. Zaccarelli and P. Schurtenberger, *J. Chem. Phys.*, 2014, **140**, 094901.
- 37 R. Liu, A. H. Milani, T. J. Freemont and B. R. Saunders, *Soft Matter*, 2011, **7**, 4696–4704.
- 38 A. V. Reis, A. R. Fajardo, I. T. Schuquel, M. R. Guilherme, G. J. Vidotti, A. F. Rubira and E. C. Muniz, *J. Org. Chem.*, 2009, **74**, 3750–3757.
- 39 G. Huang, J. Gao, Z. Hu, J. V. S. John, B. C. Ponder and D. Moro, *J. Control. Release*, 2004, **94**, 303–311.
- 40 R. K. Shah, J.-W. Kim and D. A. Weitz, *Langmuir*, 2009, **26**, 1561–1565.
- 41 P. Zhu and L. Wang, *Lab Chip*, 2017, **17**, 34–75.
- 42 W. Lee, L. M. Walker and S. L. Anna, *Phys. Fluids*, 2009, **21**, 032103.
- 43 S. L. Anna, N. Bontoux and H. A. Stone, *Appl. Phys. Lett.*, 2003, **82**, 364–366.
- 44 A. M. Gañán Calvo, *Phys. Rev. Lett.*, 1998, **80**, 285–288.
- 45 C. N. Baroud, F. Gallaire and R. Danga, *Lab Chip*, 2010, **10**, 2032–2045.
- 46 L. Rosenfeld, T. Lin, R. Derda and S. K. Y. Tang, *Microfluid. Nanofluid.*, 2014, **16**, 921–939.
- 47 Y. Xia and G. M. Whitesides, *Angew. Chem., Int. Ed.*, 1998, **37**, 550–575.
- 48 S. H. Holm, J. P. Beech, M. P. Barrett and J. O. Tegenfeldt, *Anal. Methods*, 2016, **8**, 3291–3300.
- 49 M. Beck, M. Graczyk, I. Maximov, E.-L. Sarwe, T. Ling, M. Keil and L. Montelius, *Microelectron Eng*, 2002, **61-2**, 441–448.
- 50 G. M. Conley, P. Aebischer, S. Nöjd, P. Schurtenberger and F. Scheffold, *Sci. Adv.*, 2017, in press.
- 51 A. R. Abate, L. Han, L. Jin, Z. Suo and D. A. Weitz, *Soft Matter*, 2012, **8**, 10032–10035.
- 52 I. D. Block and F. Scheffold, *Rev. Sci. Instrum.*, 2010, **81**, 123107.
- 53 M. Stieger, W. Richtering, J. S. Pedersen and P. Lindner, *J. Chem. Phys.*, 2004, **120**, 6197–6206.
- 54 M. Reufer, P. Diaz-Leyva, I. Lynch and F. Scheffold, *Eur. Phys. J. E*, 2009, **28**, 165–171.
- 55 Z. Hu and G. Huang, *Angew. Chem., Inter. Ed.*, 2003, **42**, 4799–4802.
- 56 J. Schindelin, I. Arganda-Carreras, E. Frise, V. Kaynig, M. Longair, T. Pietzsch, S. Preibisch, C. Rueden, S. Saalfeld, B. Schmid, J.-Y. Tinevez, D. J. White, V. Hartenstein, K. Eliceiri, P. Tomancak and A. Cardona, *Nat. Methods*, 2012, **9**, 676–682.
- 57 N. Boon and P. Schurtenberger, *Phys. Chem. Chem. Phys.*, 2017.
- 58 P. S. Mohanty, S. Nöjd, K. van Gruijthuijsen, J. J. Crassous, M. Obiols-Rabasa, R. Schweins, A. Stradner and P. Schurtenberger, *Sci. Rep.*, 2017, **7**, 1–12.
- 59 D. Di Carlo, D. Irimia, R. G. Tompkins and M. Toner, *Proc. Natl. Acad. Sci. U. S. A.*, 2007, **104**, 18892–18897.
- 60 R. Contreras-Cáceres, A. Sánchez-Iglesias, M. Karg, I. Pastoriza-Santos, J. Pérez-Juste, J. Pacifico, T. Hellweg, A. Fernández-Barbero and L. M. Liz-Marzán, *Adv. Mater.*, 2008, **20**, 1666–1670.
- 61 R. Contreras-Cáceres, S. Abalde-Cela, P. Guardia-Girós, A. Fernández-Barbero, J. Pérez-Juste, R. A. Alvarez-Puebla and L. M. Liz-Marzán, *Langmuir*, 2011, **27**, 4520–4525.
- 62 M. Karg and T. Hellweg, *Curr. Opin. Colloid Interface Sci.*, 2009, **14**, 438–450.
- 63 C. Dagallier, H. Dietsch, P. Schurtenberger and F. Scheffold, *Soft Matter*, 2010, **6**, 2174–2177.
- 64 J. J. Crassous, A. M. Mihut, H. Dietsch, O. Pravaz, L. Ackermann-Hirschi, A. M. Hirt and P. Schurtenberger, *Nanoscale*, 2014, **6**, 8726–8735.



75x39mm (300 x 300 DPI)

## Supplementary Figures and Videos for

### Thermoresponsive colloidal molecules prepared using droplet-based microfluidics

Feifei Peng,<sup>ac‡</sup> Stefan H. Holm,<sup>bc‡</sup> Linda K. Månsson,<sup>ac</sup> Somnath Ghosh,<sup>ac</sup> Jérôme J. Crassous,<sup>ac</sup> Peter Schurtenberger<sup>ac\*</sup> and Jonas O. Tegenfeldt<sup>bc\*</sup>

<sup>a</sup>Division of Physical Chemistry, Lund University, Lund, Sweden.

<sup>b</sup>Division of Solid State Physics, Lund University, Lund, Sweden.

<sup>c</sup>NanoLund, Lund University, Lund, Sweden.

‡ Authors contributed equally

\* Corresponding authors: Jonas O. Tegenfeldt, Peter Schurtenberger

E-mail: [jonas.tegenfeldt@ftf.lth.se](mailto:jonas.tegenfeldt@ftf.lth.se), [peter.schurtenberger@fkem1.lu.se](mailto:peter.schurtenberger@fkem1.lu.se)

#### 1. Droplet diameter analysis

In order to acquire good statistics for the droplet size analysis, an ImageJ 1.51n script was developed which was able to correctly determine the droplet size of several thousands of droplets per second. Typically, an image stack of the droplets flowing in the straight, wide channel containing 5000 frames acquired at 5000 frames per second was used. With the plug-in Stack Sorter, every 500 frame was selected in order to not image the same droplet multiple times, generating 10 frames of unique droplets. The background was subtracted by a rolling ball function, with a radius equal to the radius of the droplets. Thereafter the images were thresholded to create a binary image stack. A grey scale range of 30-255 was used to select individual particles and to avoid overlap. In order to recreate the shape of droplets which had been distorted the binary functions Fill holes and Watershed were used. Particle selection was carried out by first excluding non-circular objects by using the function Analyse particles with the area range set to 0-Infinity  $\mu\text{m}^2$  and the circularity range set to 0-0.8. The selected areas were removed by filling them white. Noise was thereafter cancelled out by removing particles which were too small to be droplets. Once again, the Analyse particle function was used, this time with the area range set to 0-50  $\mu\text{m}^2$  and the circularity range set to 0-1.0. Selected areas were once again filled white. The diameters of the particles remaining were measured by taking the mean of the major and minor axis of an ellipsoidal fit.

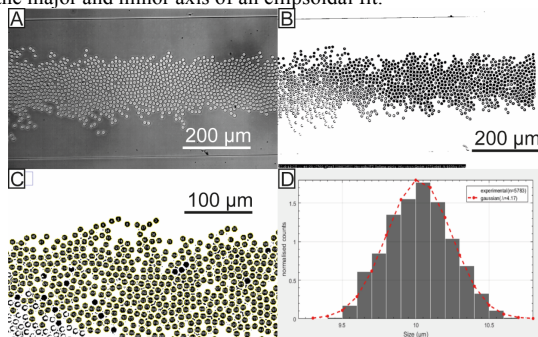


**Figure S1** Automated image processing in order to quantify the diameters of several thousands of droplets accurately. **(A)** An image stack is processed using the software Image J. **(B)** By using rolling ball background subtraction, the droplets can clearly be distinguished from the background. **(C)** By filtering the image based on area and circularity, all particles which overlap and noise in the image can be removed. The final particles which can be distinguished are then detected and measured by an ellipsoidal fit. **(D)** The mean of the major and minor ellipsoidal axis is taken as a measure of the droplet diameter and here shown in a histogram together with a Gaussian fit.

## 2 Fluidic simulation of droplet devices

COMSOL 5.3 was used to carry out computational fluid dynamics simulations in order to estimate the hydraulic resistances and the pressure drop distributions of the different devices used in this study. The CAD design of the short and the long device was directly imported into COMSOL and converted to a single block to enable CFD analysis. The finite element model was set up using the 2D Creeping Flow Module in the CFD Physics Toolbox. The inlet pressures were set to  $P_{in} = 100$  Pa with an entrance length of  $100\ \mu\text{m}$ , while the outlets were set to  $P_{out} = 0$  Pa. The mesh consisted of  $\sim 200\ 000$  elements and the PARADISO solver was used with standard settings. Water, incompressible, was used as the liquid from both inlets.

The results show that a significant part of the pressure drop across the devices occurs, as expected, over the droplet forming constriction. However, the pressure drop over this region for the short device (75% of total pressure drop) is much larger than that of the long device (10% of total pressure drop). This is beneficial as a larger part of the energy put into the system acts to form droplets (*i.e.* to create new interface between the oil and the water phase).

The resistance measurements further point to how the shorter device is better suited for high frequency droplet generation. Here, the hydraulic resistance of the short device is  $R_{\text{short}} = 1.5 \times 10^9$  Pa s m<sup>-2</sup> while the resistance of the long device is almost twice as much,  $R_{\text{long}} = 2.9 \times 10^9$  Pa s m<sup>-2</sup>.

The length of the meandering channels is around 30 cm. This means that if we want a residence time of 5 minutes the average flow velocity should be  $\sim 80\ \mu\text{m/s}$ . In our model, the corresponding pressure drop across the device to achieve this flow velocity is 11 000 Pa (110 mBar).

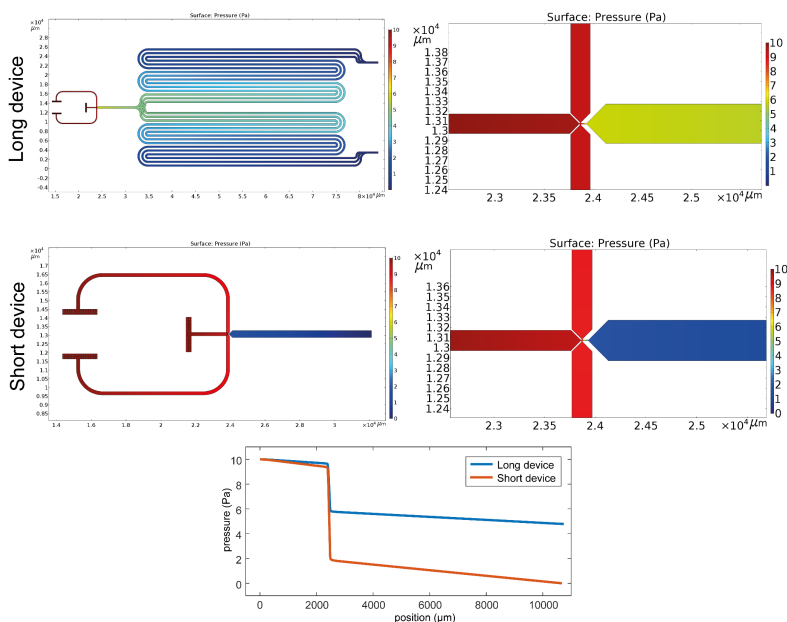


**Figure S2** Comparison between pressure drop in the long and short device using COMSOL Multiphysics to simulate the flow field. With the inlet pressure set to 10 Pa, it can be seen that for the long device (top row) the pressure drop over the droplet generating region is lower than that of the short device (centre row). This was measured from the aqueous phase inlet to the outlet of the short device, and the same distance in the long device with the results shown in the graph. Here it can be seen that for the long device only  $\sim 10\%$  of the pressure drop occurs at the droplet constriction while the corresponding number for the short device is  $\sim 75\%$ . With a larger pressure drop at the droplet formation region a higher droplet formation frequency is expected.

### 3 Droplet diameter and generation frequency as a function of pressure drop

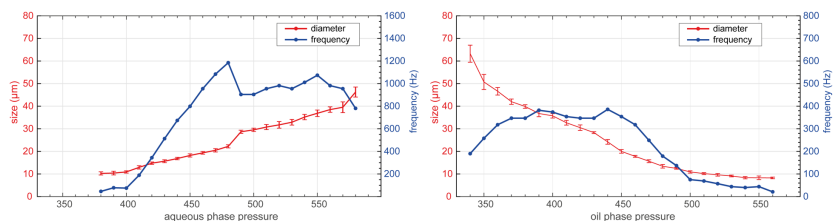


**Figure S3** Generation frequency and droplet diameter as a function of varying either the oil phase pressure (left) or the aqueous phase pressure (right) while keeping the other inlet constant at 400 mBar and 500 mBar, respectively. At a constant water phase pressure the droplet diameter decreases exponentially to around the size of the constriction (10  $\mu\text{m}$ ). This is expected since a larger oil phase pressure decreases the time it takes to pinch off the aqueous phase thread and create a droplet. The minimum droplet diameter is comparable to the constriction size due to the device operating in squeezing mode. The generation frequency when the oil phase is varied is, of course, linked to the droplet diameter. At low oil pressures the mean droplet diameter is very large, and as a consequence the generation frequency is low. At the highest oil pressures, the generation frequencies are low due to the high oil pressure decreasing the aqueous phase flow rate. Consequently, the maximum generation frequency is reached at intermediate oil inlet pressures, comparable to the water inlet pressure. When keeping the oil pressure constant and varying the water phase inlet pressure we see an increase in the droplet diameter with increasing pressure of the aqueous phase. This is expected as a larger water pressure allows for generating larger droplets before being pinched off by the oil phase. Also, the generation frequency seems to have a similar tendency as for the previous study with varying water phase pressure. Low aqueous phase pressure results in low generation frequency. Here the higher oil pressure hinders the water from entering the constriction. At very large aqueous phase pressure relative to the oil phase the time to pinch off the aqueous thread is extended significantly.

#### 4 Completely shrunken droplets – clusters in oil

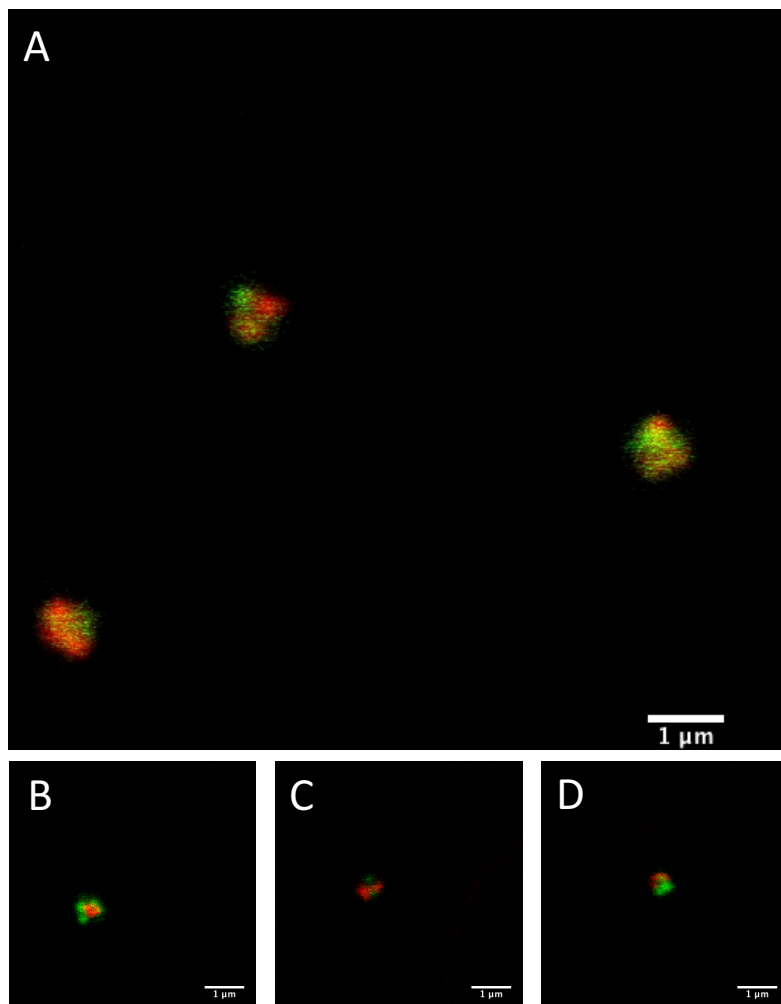
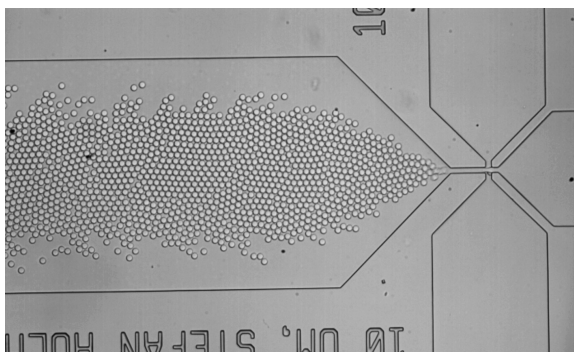


**Figure S4** CLSM images of fully evaporated microgel-containing water droplets, resulting in dense microgel clusters in oil. PNIPAM-co-MA microgels are labelled red, and PNIPMAM-co-MA microgels green, respectively. **(A)** Overview of microgel clusters in a local area. **(B) (C) (D)** Zoomed-in images of single microgel clusters. The microgel particles contain around 80% water when dispersed into water at room temperature. After the evaporation of water inside droplets, microgels are highly compressed and form dense clusters. This makes it difficult to distinguish individual microgels within a given cluster.

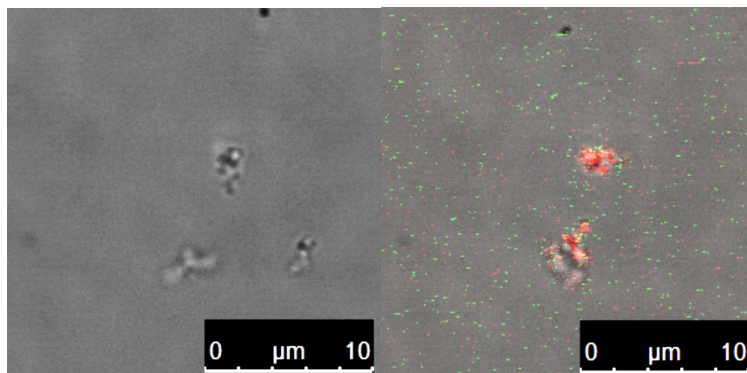
## 5 Droplet generation at high generation frequency in the short device



Video S1

In this video encapsulation of microgels in the short device can be seen. The driving pressures are  $P_w = 922$  mBar and  $P_{oil} = 956$  mBar for the water and oil pressure respectively. The resulting droplet generation frequency is around 17 kHz. The oil used is 2 wt% PicoSurf 1 in HFE-7500, and the aqueous phase contained PNIPAM microgel suspension. The droplet device is operating in squeezing mode where droplet breakup is to a large extent dependent on the geometry of the constriction where droplets are generated, as the aqueous thread blocks the oil phase creating a pressure build-up acting to pinch of a single droplet.

## 6 Attraction between microgel clusters at higher temperature with salt and acid



**Video S2 and S3**

The redispersed microgel clusters were imaged at high ionic strength (0.1 M KCl) and  $\text{pH} < \text{pK}_a$  (HCl aq. pH 3), at a temperature of 35 °C. The attraction-induced assembly of three microgel clusters was recorded using CLSM. Video S2 shows the microgel clusters in Bright Field mode, while Video S3 shows the clusters in fluorescent mode with the TRITC channel coloured red and FITC (weak signal) coloured green.







